Connectivity and Processing in the Macaque Cerebral Cortex

Marie-Alice Gariel

N°d'ordre NNT : 2017LYSE1005

THESE de DOCTORAT DE L'UNIVERSITE DE LYON
opérée au sein de
l'Université Claude Bernard Lyon 1
en cotutelle avec Vrije Universiteit Amsterdam (Pays Bas)

Ecole Doctorale N° 476
Neurosciences et cognition

Spécialité de doctorat : **Biologie**
Discipline : **Neurosciences**

Soutenue publiquement le 11/01/2017, par :
Marie-Alice Gariel

Connectivity and Processing in the Macaque Cerebral Cortex

Devant le jury composé de :

Derrington, Edmund PU Université Claude Bernard Lyon 1 Président

Fries, Pascal Professeur Université Radboud, Nimègue (Pays-Bas) Rapporteur
Martin, Kevan Professeur Ecole Polytechnique Fédérale de Zurich, Suisse Rapporteur
Lamme, Victor Professeur, Universiteit van Amsterdam (Pays-Bas) Examinateur
Kennedy, Henry Directeur de recherches, INSERM Examinateur

Knoblauch, Kenneth Directeur de recherche, INSERM Co-directeur de thèse
Roelfsema, Pieter Professeur Vrije Universiteit, Amsterdam Co-directeur de thèse

In Memoriam Jérôme Sanson
1966 – 2010

To understand how the cerebral cortex does what it does, it is necessary to elucidate both how its dynamic states are correlated with the functions it performs, and how it is organised (because, contrary to man-made computing systems, the brain has no software layer: the algorithm is in the physical design). From a computational point of view, cortical information processing is based on hierarchical abstraction: different levels deal with increasingly less detailed but more abstract representations. This allows for both localisation of functions in specialised cortical areas, and integration of extracted features into behaviourally relevant models governing the brain's output (actions) and long-term modification (learning and memory).

To contribute to the understanding of cortical computation, we have focused on the level of cortical areas, and their connections and interactions. At this level of description, many functional and anatomical gradients have been described that reflect the hierarchical abstraction at the heart of cortical computation. The most famous of these functional gradients is probably the increase in the size of neuron's receptive field and complexity of their tuning along the series of visual areas in the rostrocaudal direction. Later, it was showed that two flavours of cortical connections exist, and that in the visual cortex they happen to transport information in opposite directions along this gradient. It was also hypothesised that other modalities exhibit the same type of gradient in their respective domains. However, how these two types of inter-areal connections interact with intrinsic connectivity to give rise to more and more abstract representations along these functional gradients remains an open question, one that requires knowledge of the architecture at different levels (such as the cortical column) and a causal understanding of the functional properties of these types of connections.

We have addressed this issue in a number of ways. First, we have studied the dynamics of both feedforward and feedback propagation in the visual system of awake, behaving macaque monkeys. Using the causal method of electrical microstimulation and recording, we have found a dynamic signature of each type of projections and an asymmetry in the way each type of input interacts with ongoing activity in a given visual area. Secondly, we have "zoomed out" of the visual system to look at the properties of the whole cortical network. Thanks to a rich and systematic data set in the macaque, we have found a fundamental organisational principle of the embedded and weighted cortical network that holds also in the more detailed level of neuronal connections inside an area. Finally, we have combined known anatomical gradients with actual inter-areal connectivity into a dynamic model, which exhibits another functional gradient, this time in the temporal domain. This gradient of progressively longer timescales of the intrinsic dynamics of areas has been observed in the brain, and here we show how it relates to both the ordering of areas along a hierarchical gradient and the wiring diagram of the cortical network.

Keywords: Cerebral cortex, macaque, electrophysiology, electrical microstimulation, neuroanatomy, cortical graph, modelling, neuronal population dynamics.

Résumé

Connectivité et traitement de l'information dans le cortex cérébral du macaque

Pour comprendre comment le cortex cérébral extrait du sens et produit des actions à partir des informations sensorielles, il est nécessaire de comprendre à la fois son architecture et ses états dynamiques. Dans la présente thèse nous avons abordé cette relation structure-fonction au niveau des aires cérébrales, leurs connections et leurs interactions au sein du réseau cortical. Les aires sont connectées entre elles par deux grands types de projections axonales. D'une part, les connections « feedforward » – littéralement « antéroactives » – transmettent l'information des aires sensorielles aux aires de plus haut niveau dans la hiérarchie corticale (dont l'activité sous-tend des représentations plus abstraites). À l'inverse, les connections « feedback » (rétroactives) relient des aires dans la direction descendante de la hiérarchie corticale, vers les aires sensorielles primaires. Pour explorer les rôles respectifs des connections feedforward et feedback nous avons utilisé une triple approche chez le macaque, à la fois anatomique, électrophysiologique, et de modélisation mathématique du réseau.

Pour décrire les connexions entre les aires corticales avec une précision suffisante pour comprendre les principes d'organisation du cortex, il est nécessaire de choisir des traceurs corticaux spécifiques, d'appliquer des méthodes systématiques et de croiser les résultats de plusieurs animaux. Dans un premier chapitre, nous montrons qu'une seule injection de traceur dans une aire suffit pour établir le profil de connectivité complet de cette aire de façon fiable, y compris pour les connexions les plus faibles. La stabilité du profil de connectivité des aires corticales d'un individu à l'autre est en soi un résultat important, qui a nécessité la modélisation statistique de la variabilité de la distribution des neurones marqués par le traceur après des injections multiples. Notre méthode révèle non seulement la présence ou l'absence d'une projection entre chaque aire et l'aire injectée, et la force des connexions existantes, mais elle fournit également une mesure de leur direction, c'est-à-dire la propagation bottom-up (feedforward) ou top-down (feedback) de l'information traitée. Cette base de données obtenue par une méthode unifiée et validée statistiquement forme la base de nos travaux sur les principes d'organisation de l'anatomie corticale et des fonctions qu'elle réalise.

Dans le chapitre suivant, nous nous sommes intéressés au réseau cortical en tant que tel, en utilisant des méthodes de la théorie des graphes. Contrairement à la plupart des études précédentes essentiellement descriptives, qualitatives et basées sur des données incomplètes, nous avons tenté de construire un modèle prédictif de la connectivité corticale. En utilisant le profil de connectivité pondérée de 30 aires réparties dans tout le cortex, nous avons reconstitué un sous-graphe où chaque connexion potentielle a été testée et mesurée, ce qui permet d'inférer de façon fiable les propriétés du graphe complet. Cette approche a révélé i) que le réseau des aires corticales est extrêmement dense, mais que la grande variabilité de la force des projections donne à chaque aire sa spécificité bien plus que l'identité des aires auxquelles elle est connectée ; ii) le réseau cortical est composé d'un groupe de voies de communication à haute bande passante au milieu d'une myriade de connexions mineures, et que la majorité des neurones corticaux participent à des connexions à courte distance allouées au traitement local de l'information ; iii) le poids des connexions est gouverné par la distance parcourue par les axones à travers la matière blanche entre l'aire source et l'aire cible, avec une diminution exponentielle avec cette distance du nombre d'axones impliqués. Cette règle de distance exponentielle (EDR) est un principe fondamental d'organisation du cortex, si bien qu'un réseau aléatoire avec l'EDR comme seule contrainte de construction reproduit de près la structure du réseau réel.

En parallèle, nous avons exploré le fonctionnement électrophysiologique des connexions feedforward et feedback. Des études précédentes de stimulation magnétique transcrâniennes (TMS) suggèrent que la rétroaction d'aires de haut niveau sur les aires primaires du cortex visuel est nécessaire pour la perception visuelle consciente. Pourtant, l'influence du feedback cortico-cortical sur l'accès à la conscience visuelle et la nature des effets médiés par les connexions feedback ne sont pas élucidés. Dans le chapitre 4, nous avons abrdé cette question en micro-stimulant électriquement le cortex visuel de macaques en comportement, ce qui induit une perception lumineuse artificielle (un phosphène). En micro-stimulant le cortex visuel primaire (aire V1) et l'aire V4 à différents intervalles de temps, nous avons observé que les singes peuvent détecter les phosphènes induits par microstimulation dans V1, mais que la microstimulation de V4 sous le seuil de détection d'un phosphène n'influence pas le seuil de détection d'un phosphène dans V1. Dans une deuxième expérience nous avons étudié l'influence de la microstimulation dans V4 sur la capacité des singes à détecter un court changement de luminance d'un stimulus parmi trois présentés en vision parafovéale. Là encore, la microstimulation d'un groupe de neurones de V4 n'influence pas la perception du singe d'un stimulus dans le champ récepteur concerné.

N'ayant pas réussi à détecter l'influence de la connexion feedback entre V4 et V1 dans la perception visuelle consciente, nous avons décidé de comparer l'effet d'une connexion feedforward (V1 vers V4) et d'une connexion feedback (V4 vers V1) sur l'activité de

l'aire cible engagée ou non dans une tâche visuelle de segmentation d'une scène en objet et fond (figure-ground segregation). Dans le chapitre 5 nous avons de nouveau utilisé la technique causale de microstimulation pour tester la propagation de l'activité neuronale le long d'une connexion feedforward et feedback. Dans le sens feedforward (microstimulation dans V1, enregistrement dans V4) nous avons observé dans V4 une activation immédiate et forte suivie d'une désactivation. Dans le sens du feedback cependant (microstimulation dans V4, enregistrement dans V1), nous avons observé que la stimulation des neurones de V4 provoque seulement une désactivation dans V1, et surtout, contrairement au sens feedforward, cet effet n'a lieu que si la microstimulation a lieu durant la période plateau de la réponse à un stimulus visuel (après le pic inital d'activation). De plus, cette désactivation de l'activité des neurones cibles interagit avec la présence d'un objet visuel dans le champ récepteur, d'une façon qui suggère une contribution de la connexion feedback dans tout le champ visuel, même en l'absence d'objet (quand seul le "fond" de la scène est perçu). Ce résultat sur l'asymétrie entre l'effet d'un input feedforward ou feedback sur l'activité électrique d'une aire corticale est nouveau. De plus, il est en accord avec l'étude des propriétés oscillatoires des deux directions de propagation réalisée dans l'équipe et qui montre des différences claires dans les bandes de fréquence feedforward et feedback, ainsi que dans les couches corticales ciblées par chaque type de connexion (van Kerkoerle et al., 2014).

Dans une dernière approche, nous avons combiné des données anatomiques et fonctionnelles dans un modèle dynamique à grande échelle du cortex du macaque (chapitre 6). En stimulant ce modèle nous avons observé qu'émerge une hiérarchie de constantes de temps, où les aires sensorielles primaires ont une réponse brève, immédiate et transitoire à un stimulus, tandis que les aires de plus haut niveau intègrent les inputs sur de plus longues périodes et ont une activité plus durable. Selon la modalité de l'input (visuel, auditif, etc) différentes hiérarchies dynamiques se mettent en place, suggérant des mécanismes d'établissement de ces "fenêtres réceptives temporelles" de façon dynamique selon les tâches.

Mots-clef : Cortex cérébral, macaque, électrophysiologie, microstimulation, neuroanatomie, modélisation, population de neurones.

Samenvatting

Connectivité et traitement de l'information dans le cortex cérébral du macaque

Ici le résumé in nederlands.

List of publications

The original findings described in the present thesis have resulted in the following publications:

- Chapters 2 and 3:
  - Markov, N. T., Misery, P., Falchier, A., Lamy, C., Vezoli, J., Quilodran, R., Gariel, M. A., Giroud, P., Ercsey-Ravasz, M., Pilaz, L. J., Huissoud, C., Barone, P., Dehay, C., Toroczkai, Z., Van Essen, D. C., Kennedy, H., & Knoblauch, K. (2011b). Weight consistency specifies regularities of macaque cortical networks. *Cerebral Cortex*, *21*(6), 1254–1272
  - Markov, N. T., Ercsey-Ravasz, M. M., Gariel, M. A., Dehay, C., Knoblauch, A., Toroczkai, Z., & Kennedy, H. (2011a). The tribal networks of the cerebral cortex. In L. M. Chalupa, N. Berardi, M. Caleo, & L. Galli-Resta (Eds.) *Cerebral Plasticity: New Perspectives*, (pp. 275–290). Cambridge, Massachusetts: MIT Press
  - Markov, N. T., Ercsey-Ravasz, M. M., Ribeiro Gomes, A. R., Lamy, C., Magrou, L., Vezoli, J., Misery, P., Falchier, A., Quilodran, R., Gariel, M. A., Sallet, J., Gamanut, R., Huissoud, C., Clavagnier, S., Giroud, P., Sappey-Marinier, D., Barone, P., Dehay, C., Toroczkai, Z., Knoblauch, K., Van Essen, D. C., & Kennedy, H. (2014a). A weighted and directed interareal connectivity matrix for macaque cerebral cortex. *Cerebral Cortex*, *24*(1), 17–36
  - Gariel-Mathis, M. A., Knoblauch, K., & Kennedy, H., *The macaque connectome: a high-resolution tract tracing method for the quantitative analysis of interareal connectivity.* (review, submitted)
- Chapter 4:
  Gariel-Mathis, M. A., Dagnino, B., & Roelfsema, P. R. (2015). Microstimulation of area V4 has little effect on spatial attention and on perception of phosphenes evoked in area V1. *J. Neurophysiol.*, *113*(3), 730–739
- Chapter 5:
  Gariel-Mathis, M. A., Dagnino, B., & Roelfsema, P. R., *Microstimulation in V1 and V4 reveals asymmetric feedforward and feedback influences in texture-segregation.* (submitted)
- Chapter 6:
  Chaudhuri, R., Knoblauch, K., Gariel, M. A., Kennedy, H., & Wang, X. J. (2015). A Large-Scale Circuit Mechanism for Hierarchical Dynamical Processing in the Primate Cortex. *Neuron*, *88*(2), 419–431

The author of this thesis has also contributed to van Kerkoerle, T., Self, M. W., Dagnino, B., Gariel-Mathis, M. A., Poort, J., van der Togt, C., & Roelfsema, P. R. (2014). Alpha and gamma oscillations characterize feedback and feedforward processing in monkey visual cortex. *Proc. Natl. Acad. Sci. U.S.A.*, *111*(40), 14332–14341

Contents

List of Figures

Chapter 1

Introduction

Nel mezzo del cammin di nostra vita
mi ritrovai per una selva oscura
ché la diritta via era smarrita.

Dante Alighieri, *Inferno*

How the cerebral cortex creates actionable meaning from its environment is constrained by its exquisitely complex architecture, and retro-engineering this particular computational system might be the most fertile challenge we have ever been faced with. However, even if we could (or rather, when we will) access the complete wiring diagram of the cortex down to individual neurons, together with their activity at time t, this data would not get us closer to understanding how the brain processes information. In fact, this approach would only work for the simplest of problems and systems, like the one presented in fig. 1A: two sensors and two actuators linked by a grand total of two connections are sufficient to implement a simple attraction or repulsion behaviour. However, more complex algorithms require more components, and before long the mapping between inputs and outputs is no longer apparent in the blueprint of the system. Consider the system illustrated in fig. 1B: unless you happen to recognise the action of a piano key, chances are you cannot predict that depressing the bottom right lever will result in the damper lifting, the hammer hitting the string and springing back followed by the damper resuming contact with the string, thus effectively stopping the sound. Even a trained engineer happening upon an electrical wiring diagram may not be able to tell right away whether the resulting system is a clock radio, a bomb timer, a kitchen scale, or whether it will do anything at all. In the case of the cortex with its billions of neurons and thousands of billions of connections, the task seems hopeless. Even worse, at this point the system is too high dimensional for our man-made computing systems to handle, by many orders of magnitude. However, complex systems are hierarchical in nature: their complexity emerges from the interaction of several levels of nested subsystems, the operation of one level consisting of many more elemental operations. Thankfully, understanding the integration that occurs between one particular level and the next is a much more tractable problem than looking at the whole system in all its excruciating detail.

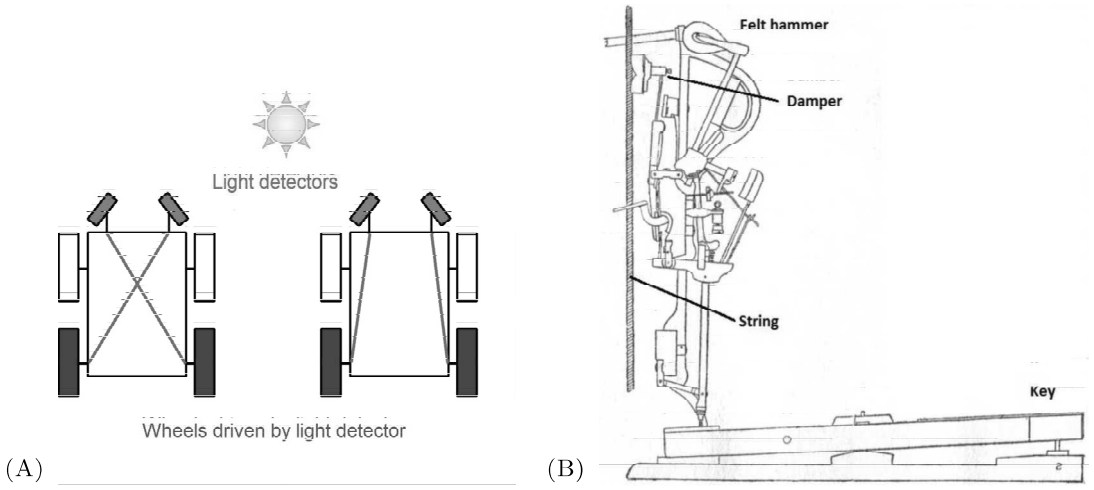

FIGURE 1: **Complexity in a system's behaviour.** **(A)** A simple mechanical implementation of an attraction/repulsion to light: the back wheels (in blue) are driven by the intensity of light that hits the detectors (in red). Depending on how the wheels and detectors are wired, it is easy to see that the system on the left, with connections (green) crossing over to the opposite side, will steer towards the light source. Without this decussation (right) a light source on the left side will steer the system to the right by increasing the speed of the left wheel. *Figure adapted from (Edelman, 2008).* **(B)** A more complex system: the key action of an upright piano. Several interacting components are needed for the key to trigger the desired behaviour from the hammer and damper. *Image by William Braid White [Public domain], via Wikimedia Commons.*

The brain may be "the most complex toy you'll ever come near, let alone get to play with" (Edelman, 2008), yet it is no exception to this rule, as evidenced by the great achievements obtained in such a recent research domain as cognitive neuroscience. In the present thesis, we have focused on the level of cortical areas (a concept first defined by Brodmann 1909) and how their interactions underlie sensory, motor and cognitive functions.

In the piano action example of fig. 1B, even if you know what the mechanism is designed to do, it is still hard to grasp how this output is produced by the interaction of the different components without watching the mechanism in action. The analogy is simple but illustrates how crucial structure-function relations are at every level of abstraction in a complex computational system like the cortex. On the one hand, the architecture of the cortex (what are the components and how they can interact) constrains the type of computation that can be performed. In turn, the functional correlates of cortical computation have to be entirely explained in terms of the interacting components: there is no software running on neuronal hardware – the algorithm is the design itself. In the present thesis we have therefore combined anatomical and functional approaches, and have tested their possible interactions through modelling.

Interestingly, cortical computation is itself hierarchical: different processing stages deal with increasingly less detailed but more abstract representations (Marr & Poggio, 1977). The pioneering work of Hubel and Wiesel in the 60's showed that in the visual system this hierarchy is implemented as a succession of specialised visual areas feeding into each other whose neurons have gradually larger receptive fields and more complex tuning, culminating with neurons in inferotemporal cortex tuned to specific objects and individual faces (fig. 2). The functional role of projections routing raw visual information through this series of processing stages is quite straightforward, but there are many more connections linking cortical areas, including pairs of

reciprocally connected areas. (Rockland & Pandya, 1979) were the first to describe a different laminar distribution of cell bodies (in the source area) and axon terminals (in the target area) between connections transporting raw visual information up the hierarchy (from V1 to higher level areas) and connections linking areas in the other direction (fig. 3). Since the latter fed processed information back to areas previously activated by the visual stimulus they were called feedback projections, and by analogy the former were dubbed feedforward. The link between this anatomical dichotomy and Hubel and Wiesel's processing stages was later systematised by Felleman and Van Essen. In their seminal paper (Felleman & Van Essen, 1991) they used the same anatomical definitions and showed that it was possible to order all the areas involved in visual processing (from V1 to the prefrontal cortex and hippocampus) in 10 levels such that nearly all known feedforward connections were ascending hierarchical levels and feedback connections were descending (fig. 4). This property is far from trivial: the two types of projections did not have to be segregated between the bottom-up and the top-down directions. Furthermore, the fact that anatomical relations between areas are in agreement with the functional processing stages of Hubel and Wiesel suggests that the bidirectional flow of information propagation (Ullman, 1995) is an important principle of cortical function. A similar structural and functional hierarchy was also found in the somatosensory and motor systems and ever since, the concept of two opposite directions of information propagation up and down a hierarchy has been central in our understanding of cortical architecture. However, how feedforward and feedback input from other hierarchical levels interact with intrinsic connectivity to give rise to more and more abstract representations remains an open question.

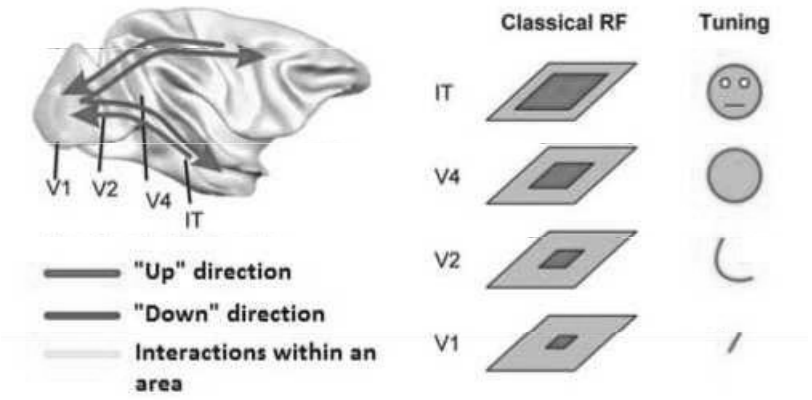

FIGURE 2: **Visual processing in the cortex is hierarchical.** A gradient in size of the neuron receptive fields and tuning complexity is evident in the series of ventral visual areas feeding into each other. Hubel and Wiesel have found that each area corresponds to a different processing stage of visual information, allowing for more and more abstract representations along this gradient. Interareal projections therefore transmit processed information up or down the hierarchy, and interact with the intrinsic connectivity of an area (yellow). Note that areas are also physically aligned with the gradient in the caudorostral direction. *Adapted from Roelfsema (2006).*

To study the architecture of the interareal network the Kennedy lab in Lyon has developed a systematic method of tract tracing to uncover the connectivity of cortical areas, detailed in chapter 2. The technique uses two highly sensitive retrograde tracers and a coherent parcellation of the cortex; it has single-neuron resolution and produces direction, strength, and laminar information. We show in chapter 2 that this method uncovers with a single injection the connectivity

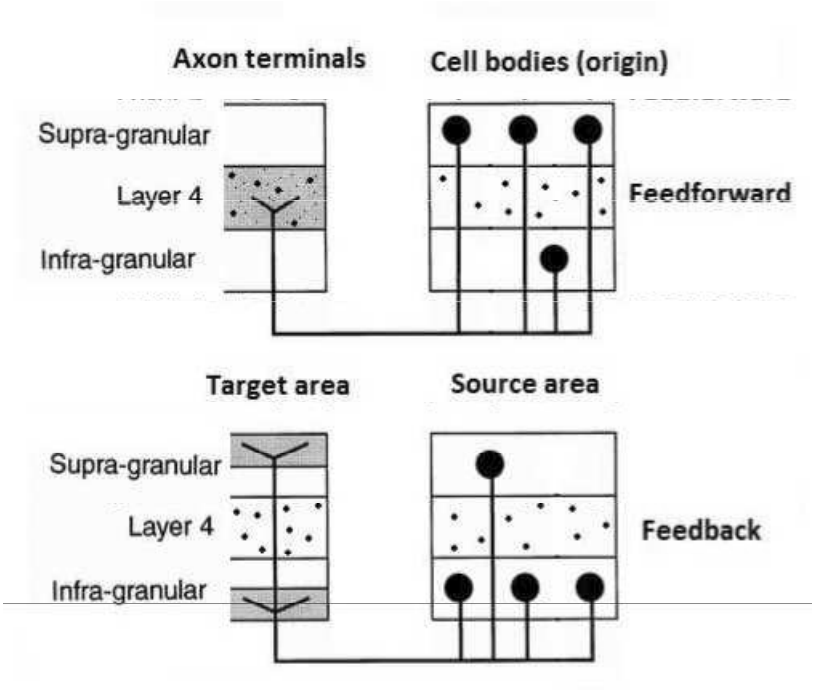

FIGURE 3: **Anatomical distinctions between interareal projections.** The two kinds of laminar profiles described by Rockland & Pandya (1979) differ in their cortical layers of origin and termination. They showed that in the early visual areas (V1, V2, V4 and IT) this anatomical dichotomy corresponds to the two directions of information propagation up and down the gradient of representational complexity. *Adapted from Felleman and Van Essen (1991).*

profile of the injected area and that, contrary to previous estimations, this areal profile is stable across individuals.

This rich, exhaustive dataset about the connectivity of 29 areas from all regions of the cortex requires an appropriate theoretical framework. Graph theory has been the language of network analysis ever since Euler addressed the famous problem of Königsberg's bridges in 1736 (and published the proof in Euler 1741), but the description of a network as a set of vertices (objects) and a set of edges connecting them didn't emerge until the late 19th century. Felleman and Van Essen used it in their 1991 paper to express the then-known connectivity of visual areas in matrix form (Felleman & Van Essen, 1991). We used an extended graph theoretical approach in chapter 3 to show that axonal wiring in the cortex occurs predominantly over short distances (indicating a preponderance of local processing), forming a backbone of strong interareal projections in a sea of weaker ones, with the full scale of strengths covering 5 orders of magnitudes. This result helped us uncover a general principle of interareal brain connectivity (that also holds at the level of single neurons), which is the exponential decay of the probability of an axonal projection between two points of the cortical surface with the distance that this axon would have to cover through the white matter to connect them. The fact that the strength of a connection depends on the geometry of cortical sulci and gyri illustrates the important idea that cortical areas are not connected in a vacuum: the network is embedded in the folded surface of the cortex and there are physical constraints to wire them. Contrary to other concepts that have been claimed to apply to the cortical network such as the Small World property, the exponential distance rule (EDR) is also constrained by cortical geometry, and it can predict connectivity from a set of

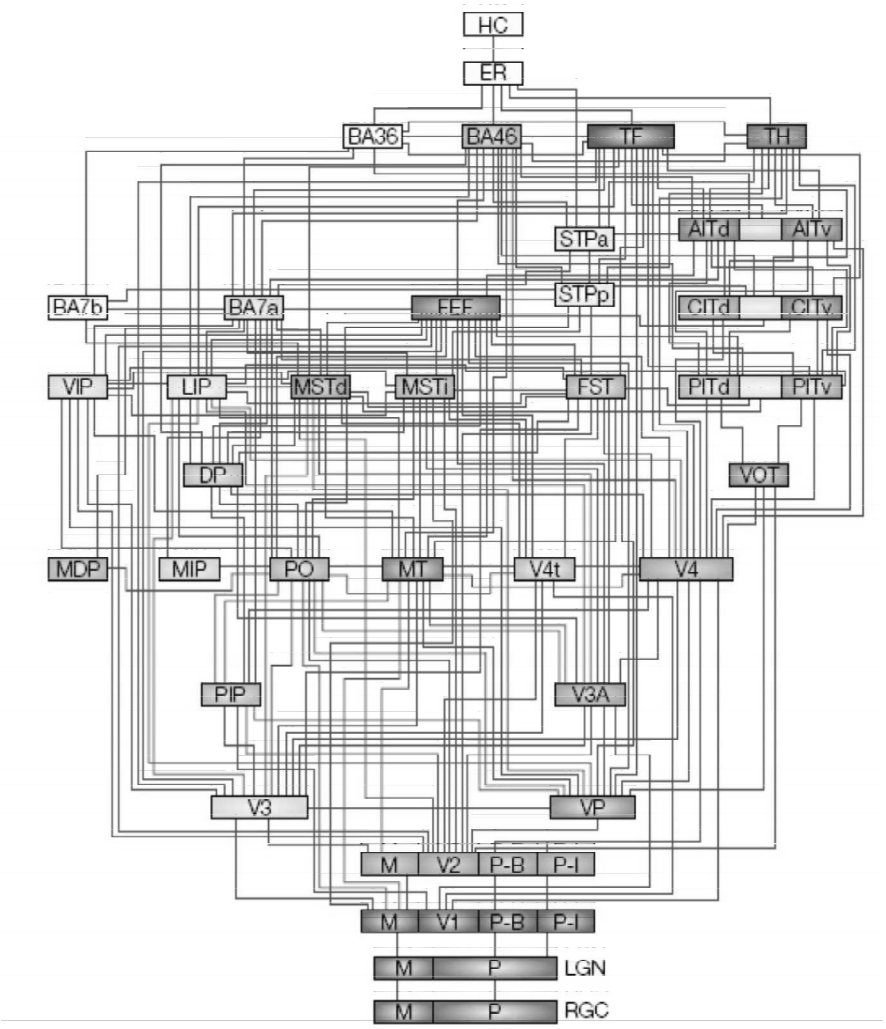

FIGURE 4: **The landmark visual hierarchy of Felleman and Van Essen.** The building rule for this ordering is simple: feedforward projections must be ascending and feedback projections must be descending. Based on the then known connectivity, there are very few violations to this rule in the resulting model that counts 10 levels and 32 visual areas from the occipital to the prefrontal lobes. Importantly, this hierarchy is not based on the properties of each area (like the size of its neurons' receptive field) but on the type of connections between areas, i.e. their relations. *Figure from Felleman & Van Essen (1991).*

distance between nodes. In the case of actual cortical distances between a subset of cortical areas, the connectivity predicted by the EDR captures many properties of the real-life macaque network. Therefore, the EDR is not a feature of the cortical network but its very architecture.

We also investigated the feedforward/feedback dichotomy from a functional point of view using electrophysiology. In particular, the question of why the brain needs feedback connections at all in sensory processing is listed as one of 23 unresolved problems in systems neuroscience (Bullier, 2006). Many aspects of cognitive processing cannot be accounted for by purely feedforward models (Moran & Desimone, 1985; Posner et al., 1980), but there is no unified theory of the interaction of feedforward and feedback input with intrinsic connectivity or how it gives rise to more and more abstract representations along the hierarchy.

One of the proposed roles of feedback processing is that it gates access of sensory information to consciousness (Dehaene & Changeux, 2011; Lamme & Roelfsema, 2000; Moran & Desimone, 1985; Super et al., 2001). In chapter 4 we have tested this hypothesis in the case of visual awareness in behaving macaque monkeys. Primates rely heavily on vision to interact with the world and the visual system has been studied in more detail than any other brain function, becoming a model system of cortical information processing. Previous transcranial magnetic stimulation studies suggested that feedback from higher to lower areas of the visual cortex allows the access of visual information to awareness (Pascual-Leone & Walsh, 2001; Silvanto et al., 2005). In the present study, we used electrical microstimulation in primary visual cortex (V1) and area V4, but contrary to our expectations, stimulating the higher area feeding back to V1 did not lower the threshold for reporting a microstimulation induced phosphene in V1, nor did it influence the monkey's ability to detect a change in one of three potential stimuli (distributed attention).

Since microstimulation of a group of V4 neurons failed to modulate the monkeys' perception of a stimulus in their receptive field, we next sought to characterise more precisely the effects of feedback and feedback inputs to an area. In chapter 5 we again used the causal technique of electrical microstimulation in macaque monkeys engaged in a visual task. We wanted to compare the effect of microstimulating the feedforward V1 to V4 pathway onto the activity of area V4 with that of microstimulating the feedback connection from V4 to V1 onto the activity of V1, as well as their interaction with the presence of a visual stimulus. We chose a figure-ground segregation task because it involves feedback influence (Poort et al., 2012) whose effect is measurable in V1 neurons after the initial response: their sustained activity is modulated depending on whether the contents of their receptive fields, although identical across trials, is part of an object or falls on the background. The choice of area V4 in particular was based on lesion studies showing that V4 damage led to impairment in complex shape recognition despite no loss in visual acuity (Merigan, 1996), so the recurrent connectivity from V4 seemed necessary to integrate local activity within V1 in order to achieve object integration. Stimulating neurons in area V1 resulted in a fast and strong activation of cells in area V4 followed by a long lasting suppression. In contrast, stimulating V4 neurons resulted only in a long lasting suppression of activity in area V1, but only during the sustained response period. Moreover, this suppression interacted with the presence of a figure in a way that suggests the presence of feedback contribution all across the visual field, even in the absence of a figure stimulus.

Another important challenge to further our understanding of cortical processing is to relate the properties of the EDR-governed weighted network to the concept of hierarchy based on feedforward and feedback connections. To address this issue we used the laminar information contained in the Kennedy dataset because it provides a measure of hierarchical distance: instead of the traditional FF/FB dichotomy, there is a gradient from strongly feedforward projections (crossing many hierarchical levels) to weakly feedforward, more lateral projections linking areas in nearby levels, to strongly feedback projections descending many levels (Barone et al., 2000; Vezoli et al., 2004). We combined these hierarchical distance with the data on strength of projections into a 2D circular model where the distance from the centre reflects the hierarchical position of an area, and the angular displacement is a measure of the bandwidth existing between two areas. This "update" of the Felleman and van Essen hierarchy, based on exhaustive data between 29 areas from all over the cortex, captures the functional clustering and highly local processing

of the cortical network: the visual and somatosensory systems are clustered in different regions of the disc, with sensory and motor areas at the periphery converging to a group of high-level association areas near the centre, in line with theoretical models of cognition (Dehaene et al., 1998).

We used this 2D embedding of the cortical network to relate cortical architecture and function by simulating the dynamics of the cortical network with a large-scale dynamical model presented in chapter 6. The aim was to probe the interplay of local microcircuitry and inter-areal connectivity that underlies global cortical dynamics, but contrary to previous dynamical models we did not treat areas as identical nodes. Instead, we used the findings of Elston and colleagues about the increase of the number of spines per pyramidal neurons across the areas of the cortical hierarchy in the macaque, culminating in the extreme anatomical specialisation of the prefrontal cortices (Elston et al., 2011). In response to a deterministic or noisy input, the model system displays a hierarchy of timescales (or “temporal receptive windows"), with rapid, transient responses in early sensory areas and persistent activation in association areas integrating information across long periods of time. Importantly, by using different sensory inputs we demonstrate the existence of multiple dynamical hierarchies subserved by the same anatomical structure. Moreover, we dissect the contributions to the generation of this hierarchy by local and long-range anatomical properties, including the role of weak feedback projections. We then show that network heterogeneity has important consequences for global dynamics measured by functional connectivity, a finding that has broad implications for interpretation of brain imaging data.

To conclude the present thesis, we compare the multiple notions of hierarchy uncovered by our results, and discuss how the different tools developed to study feedforward and feedback connectivity can inform future models of cortical processing.

Chapter 2

A tract tracing method for the quantitative analysis of interareal connectivity

Travailler sans souci de gloire ou de fortune
À tel voyage, auquel on pense, dans la lune !

Edmond Rostand, *Cyrano de Bergerac*

Introduction

Complete deciphering of cortical circuitry, in enough detail to shed light on cortical organisation, has been made possible by selecting the right anatomical tracers, applying systematic methods and testing the results across animals so as to yield significant results. In this chapter we will show how one injection per area is enough to reliably establish the complete connectivity profile of that area, down to the lightest projections. The fact that cortical areas exhibit a stable connectivity profile across injections and animals is an important result in itself, made possible by the statistical modelling of the variability of the distribution of labelled neurons following repeated injections. Our method not only reveals the presence or absence of a projection between areas, and the strength of existing pathways, it also provides information as to the nature of these projections in terms of the bottom-up or top-down flow of information during cortical processing. Such a rich data set obtained with a validated and exhaustive method, will be the basis of a unified attempt to understand the organisational principles of brain anatomy and the functions it subserves.

1 Tract tracing method and calculation of FLN and SLN

1.1 Principle

To reveal axonal pathways between cortical areas, injections of the retrograde tracers diamidino yellow (DY) and Fast Blue (FsB) were made in the cerebral cortex of macaque monkeys. These fluorescent dyes are picked up by axon terminals at the injection site and retrogradely transported back to the cell body (fig. 1A; Kuypers et al., 1980).

After appropriate survival time the brain is removed, cut on a microtome, and sections are examined for labelled neurons throughout the injected hemisphere. All labelled neurons, which have axons terminating in the dye uptake zone, are localised and counted both within the borders of the area where the injection has been made (intrinsic parent neurons) and outside this area (extrinsic neurons). The injected area is referred to as the target area and the area containing labelled neurons as the source area. The restricted region of the source area containing the labelled cells is the projection zone. Each charted neuron is then assigned to a cortical area or subcortical structure according to an atlas dividing the cortex into 91 areas (Markov et al., 2014a). In the neocortex, each labelled neuron is also assigned to either the supragranular compartment (layers 2 and 3, above the granular layer 4) or the infragranular compartment (layers 5 and 6, below layer 4) (fig. 1B). The granular layer is clearly visible on the sections, but contains no labelled neurons (layer 4 is an input layer in the cortex; its neurons project only to other layers in the same column, that are in turn the output layers projecting laterally).

Two quantitative measures are derived from the localised parent neurons. The first is the fraction of labelled neurons (FLN) attributed to a given source area, relative to the total number of labelled neurons in the hemisphere following the injection (fig. 1C). Total FLN (FLNt) is computed with all labelled neurons (both inside and outside the injected area), while extrinsic FLN (FLNe) uses only labelled neurons outside the target area to look at interareal pathways.

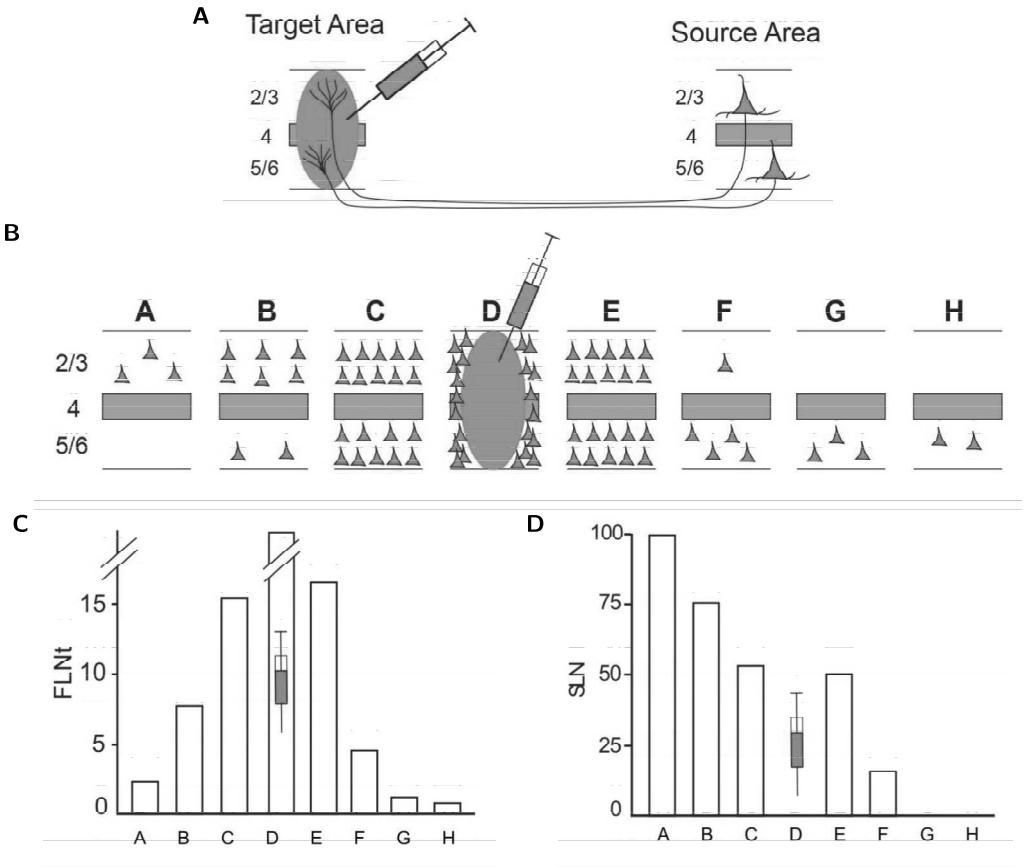

FIGURE 1: **Principle of quantitative tract tracing.** (**A**) Schematic view of the depth of the cortical sheet in the target area where the injection takes place, and a source area (with labelled cell bodies). (**B**) Mock example of the distribution of labelled neurons in the source areas following injection in target area D. (**C**) Mock neuron numbers from (B) are used to calculate the FLNt values for the pathways terminating into the target area D. The FLN percentage of pathway (A $\rightarrow$ B) is defined as the number of labelled neurons found in source area A over the total number of labelled neurons in the brain after an injection in target area B. If the labelled neurons within the injected area are excluded from the total FLN is called extrinsic (FLNe); otherwise it's the total FLN or FLNt. (**D**) Mock neuron numbers from (B) are used to calculate the corresponding SLN values for the existing pathways terminating in area D. The SLN percentage of pathway (A $\rightarrow$ B) is defined as the ratio of the number of labelled neurons above layer 4 in source area A over the total number of labelled neurons in area A (supragranular + infragranular), following an injection in target area B.

In the present thesis, unless indicated otherwise, FLN indicates this extrinsic measure. FLNe is not defined for the injected area even though there are numerous labelled neurons around the injection zone; it is equal to zero for absent pathways (areas without labelled neurons). Since FLN is the proportion of parent neurons present in each source area, it is also a measure of the strength of the pathways in number of fibres. It shows the input bandwidth to each injected area and allows us to build the weighted network of interconnected cortical areas. Figure 1B and C shows a mock example of FLNt calculation.

The second measure is called SLN for "fraction of supragranular labelled neurons". For each pathway, it is the ratio of labelled neurons in the supragranular compartment of the source area, relative to the total number of labelled neurons in the source area. Since Rockland & Pandya (1979) this laminar distribution of parent neurons has been linked to the nature of the projection,

with feedforward projections emanating predominantly from supragranular layers and feedback projections predominantly from infragranular layers (see also Barone et al., 2000; Felleman & Van Essen, 1991 and chapter 1 of this thesis). With SLN we have a graded measure of the type of projection, going from purely feedforward pathways where all parent neurons are in layers 2/3 (SLN = 100% = 1) to more lateral projections (SLN around 0.5) to purely feedback ones (SLN = 0). Figure 1B and D shows a mock example of SLN calculation .

1.2 Materials and methods

(a) Surgical procedures

A total of 39 injections of fluorescent retrograde tracers, Fast Blue (FsB) and diamidino yellow (DY), were administered to 28 macaque monkeys (27 Macaca fascicularis and 1 Macaca mulatta). The cases are listed in table 2.1 (page 40). All procedures were in accordance with national regulations concerning animal experiments, European requirements 86/609/EEC, and were approved by the competent veterinary and ethical services.

After premedication with atropine (1.25 mg, intramuscular (i.m.)) and dexamethasone (4 mg, i.m.), the monkeys were prepared for surgery under ketamine hydrochloride (20 mg/kg, i.m.) and chlorpromazine (2 mg/kg, i.m.). After intubation, anaesthesia was continued with halothane or isofluorane in a N_2O/O_2 (70:30) mixture. Heart rate was monitored, and artificial respiration was adjusted to maintain the end-tidal CO_2 at 4.5 – 6 %. The rectal temperature was maintained at 37 °C. Single injections of DY and FsB (0.1 – 60 µL) were administered with Hamilton syringes that in 4 of the 5 area V1 injections were equipped with glass pipettes (40 – 80 µm diameter). Injections were made at a shallow angle to the cortical surface to form longitudinal injection sites in the cortical grey matter. The cortex was penetrated to 2 – 4 mm and 0.1 µL of tracer injected at regular intervals as the needle was retracted, leaving a bolus of dye in the cortex.

Injection of areas in non-exposed cortical regions was aided by an image-guided stereotaxic system (Brainsight® Frameless, Rogue Research Inc.) (Frey et al., 2004). Monkeys were equipped with a bone-implanted fiducial marker screwed to the skull under anaesthesia. After recovery a 1.5 Tesla MRI scan was performed with 3 to 5 radio opaque arms fitted to the fiducial peg (IZI Medical Products, Baltimore, USA) and a 3D reconstruction of the monkey brain was obtained. During the tracer injection procedure, the Brainsight® system controlled and optimised the trajectory of the injection needle with respect to a designated target site by matching on line the position of the fiducial markers to the 3D MRI reconstruction.

In all cases, the uptake zone of the dye was characterised with respect to the retinotopic representation of the area injected, sampling of cortical layers, and possible involvement of white matter. The injections in the present study were restricted to the cortical gray matter except for case 101LH: in this V2 injection, the injection site encroached on the underlying white matter. This did not appear to influence either the FLN distribution in the cortex or the thalamus (the profile was similar to other V2 injections, and very distinct from V1 profiles), so this injection has been maintained in the study.

Following 11 to 13 days of survival, animals were deeply anaesthetised before being perfused transcardially with 4−8% paraformaldehyde/0.05% glutaraldehyde in phosphate buffer (0.1 M, pH 7.4). Cryoprotection was ensured by sucrose (Kennedy & Bullier, 1985) or glycerol perfusion gradients (Rosene et al., 1986). Brains were removed and kept in the cryoprotecting liquid overnight or until sinking. Horizontal or coronal 40 µm thick sections were cut on a freezing microtome and every third section was mounted on gelatinised glass slides and used to explore projection pathways.

(b) Charting of neurons

We refer to the injected area as the target area and the areas containing labelled neurons as the source areas. The restricted region of the source area containing the labelled cells is the projection zone (Barone et al., 2000). The extent of the uptake zone (where the dye is picked up) has been characterised (see section 2.1(b)) and is confined to the target area.

Sections were analysed without cover slips using an oil-immersion objective at a magnification of 200−250 under ultraviolet light with a Leitz or Leica fluorescent microscope equipped with a D-filter set (355−425 nm). Retrogradely labelled neurons were identified using standard criteria (Keizer et al., 1983) to distinguish FsB (cytoplasm dyed blue) and DY (yellow label mainly in nucleus) under these observation conditions.

Precise charts of labelled neuron location were acquired. For 4 injections, charts were made on an X-Y plotting table electronically coupled to the microscope stage (see column "Charts" in table 2.1, page 40). The large sheets of paper obtained with this setup were later matched to projections of the subsequently stained sections so as to locate cortical layers and landmarks. These 4 brains and all the remaining brains were subsequently investigated using the superior Mercator® software package running on ExploraNova® technology. This much-improved system digitally records and stores charts of whole-brain sections with the accurate counts and coordinates of labelled neurons, making it possible to view the charted sections at different magnifications.

After plotting, labelled neurons were assigned to a particular area and a cortical compartment (supra- or infra-granular). To do so, sections used for charting neurons were counterstained for Nissl substance and back-projected onto the charts of labelled neurons to delineate layer 4 (Batardiere et al., 1998). Areal boundaries in individual hemispheres were assigned, primarily using gyral and sulcal landmarks relative to the M132 atlas (detailed in next section), with recourse to cytoarchitectonic criteria when required. In some V1, V2 and V4 injections, the areal limits of specific areas were determined by assessment of SMI-32 immunoreactivity (Sternberger Monoclonals Incorporated, Hof et al., 1995). The limits determined by this method were the borders between areas IPa and PGa, IPa and TE, PGa and STP, LIP and V3 and DP, and their projections to V1; the border of the parahippocampal complex with TE and its projection to V2; and the borders of the perirhinal complex with the entorhinal cortex and area TE (in a V4 injection).

1.3 Cortical parcellation

The same parcellation of the cortex into areas was used throughout the study, and the cortical surface was reconstructed in 3D to allow visualisation and comparison to existing datasets and other cortical atlases.

(a) Cortical segmentation

Localisation of injection sites and labelled neurons was based on a new reference atlas of areal limits that includes 91 cortical areas mapped to the left hemisphere of case M132. The cortical parcellation was based on a combination of atlas-based landmarks (Paxinos et al., 2000; Saleem & Logothetis, 2007) and histological criteria.

For visual areas we used our previously published segmentation criteria (Barone et al., 2000; Falchier et al., 2002) as well as reported chemoarchitectonic and cytoarchitectonic criteria (Brewer et al., 2002; Gattass et al., 2005; Hof et al., 1995). We used published criteria and landmarks to delineate the separation between V4 and DP (Stepniewska et al., 2005). Region PO is split into separate areas V6 and V6A (Colby et al., 1988; Luppino et al., 2005)

We used published criteria for prefrontal areas, and included the transitional areas 9/46d and 9/46v (Barbas & Pandya, 1989; Paxinos et al., 2000; Petrides & Pandya, 1999). In the dorsal bank of the superior branch of the arcuate sulcus and extending medially, we identified area 8B (Preuss & Goldman-Rakic, 1991). In ventrolateral prefrontal cortex, area 45A is distinguished rostral to area 45B and ventral to the principal sulcus (Gerbella et al., 2010). A finer-grained subdivision of area 8 in the arcuate sulcus enabled demarcation of a small area 45B ventral to area 8/FEF and a small reported non-saccadic strip lining the caudal tip of the principal sulcus which we refer to as 8r (Gerbella et al., 2007). Area 8/FEF is subdivided into a medial large saccade-related area, area 8m, and a lateral small saccade-related area, area 8l (Schall et al., 1995; Sommer & Wurtz, 2000).

In auditory cortex, we used the nomenclature and subdivisions of the Kaas group (Hackett et al., 1998; Kaas & Hackett, 1998) and of Van Essen and Anderson for parietal cortex (Andersen et al., 1990; Lewis & Van Essen, 2000), but areas PGm and PEcg are combined into area 7m in the medial parietal cortex (Margulies et al., 2009; Morecraft et al., 2004; Pandya & Seltzer, 1982). All insular complexes were combined into a single entity we call Insula (Ins) (Jones & Burton, 1976; Mesulam & Mufson, 1982).

We subdivide the frontal cortex in areas F1−F7 (Luppino & Rizzolatti, 2000). Area 7op is located in the upper limb of the lateral sulcus caudal to area SII (Pandya & Seltzer, 1982; Preuss & Goldman-Rakic, 1991). In the superior bank of the STS, we defined STP as including cytoarchitectonic areas TAa and TPO based on published criteria using SMI-32 immunoreactivity (Padberg et al., 2003). It is further subdivided into STPr (rostral), STPi (intermediate), and STPc (caudal) (Cusick et al., 1995; Padberg et al., 2003).

In the fundus of STS rostral to FST and MST, we identified areas PGa and IPa (Seltzer and Pandya 1978). Area TE was subdivided into area TEa/m p, TEa/m a, TEpd, TEpv, TEad and TEav. The region immediately dorsal to TEO and buried in the ventral bank of STS is

identified as area TEOm. The entorhinal (ENTORHINAL) cortex is medial to the perirhinal (Amaral et al., 1987).

(b) Hemisphere reconstruction

A non injected brain (M132) was used in reconstructions for two purposes: a surface reconstruction of the left hemisphere for the constitution of a reference atlas and 3D visualisation, and an MRI scan of the right hemisphere to help areal segmentation of brains cut in the horizontal and parasagittal planes.

The majority of brains were sectioned in the coronal plane. So as to align the plane of section to that used in our atlas, a 7T MRI scan was made of the cryoprotected right hemisphere M132 brain. After acquisition of slices in a particular plane, ITK-SNAP software (`http://www.itksnap.org`) makes it possible to shade a region of interest in a given plane and view this region in an alternative plane. This proved to be an extremely powerful tool for identifying areas in horizontal and parasagittal planes with respect to the M132 atlas as well as for compensating for small deviations from the optimal coronal plane of section.

The left hemisphere of the M132 brain was cut in the coronal plane and the sections were stained with neutral red to show the cytoarchitetonic structure. The sections, with indications of areal boundary, constitute the reference atlas for segmentation of injected brains into the mosaic of cortical areas.

The folded surface of the M132 cortex was then reconstructed from the contour drawings of the sections with the Caret software suite developed in the Van Essen lab (Van Essen et al., 2001a). Caret allows visualisation (including painting areas onto the surface) and manipulation of cortical surfaces like flattening and other deformations. The midthickness representation (i.e. the surface running midway between the pial surface and the grey/white matter interface) was chosen for reconstruction because despite cortical folding, each unit of surface area is associated with a similar cortical volume for both gyral and sulcal regions (Van Essen et al., 2001a).

(c) Atlas registration

To allow comparison with other data sets of cortical parcellations, the 3D surface of M132LH was registered to the rhesus monkey F99 atlas. This atlas was obtained by scanning the brain of a single individual at high resolution (structural MRI with 0.5 mm^3 voxels). Probabilistic locations of the grey-white matter transition and the pial outer boundary (both visible on T1 weighted images) were generated on each MRI slice by the SureFit method in the Caret suite. The midthickness boundary is set midway between the most likely position of the inner and outer boundaries, and tessellated across slices to form a geometrically defined surface (Van Essen, 2004a,b; Van Essen et al., 2005).

In order to register it onto the F99 atlas, our M132 cortical surface was inflated in Caret, mapped to a sphere and deformed to fit the F99 surface using a landmark-constrained, surface-based method (Van Essen, 2005; Van Essen et al., 2005, 2001b) with a total of 24 landmarks running along geographically corresponding locations (gyri and sulci) in the M132 and F99 hemispheres.

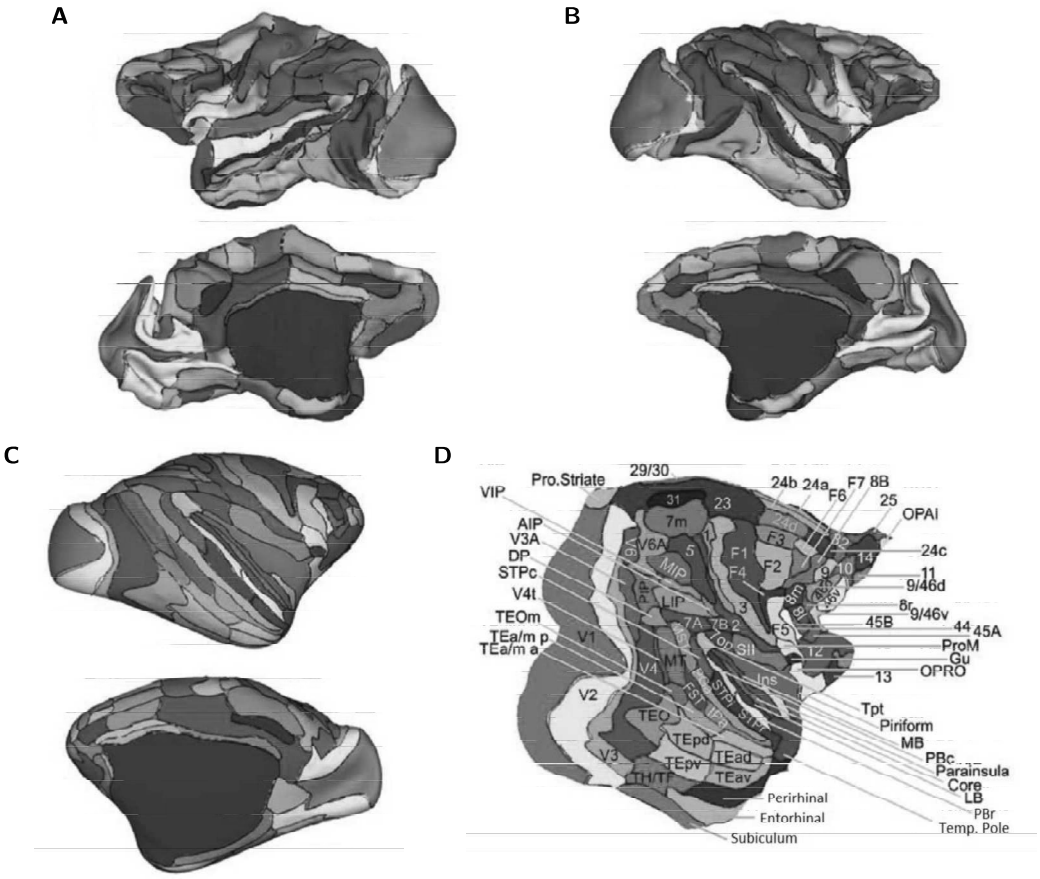

FIGURE 2: **3D surface reconstruction of the M132 atlas.** **(A)** Lateral and medial views of the M132LH midthickness surface reconstructed from section drawings, showing our 91 area parcellation. **(B)** Parcellation after registration of M132 anatomical surface onto the F99 right hemisphere reference atlas. **(C)** The inflated F99 surface shows areas buried in sulci. **(D)** Flat map of F99 atlas with our parcellation and areal identities, generated in Caret (Van Essen et al., 2001a).

The surface-based registration is the preferred method for interspecies comparison (M132 is from a cynomolgus macaque while F99 is from a rhesus), and allows the study of homologous structures in primates, both human and non human. Our areal boundaries defined on the M132 atlas were deformed accordingly so that our parcellation was fitted onto the reference F99 brain and compared to others. Caret can show the areal assignation of any point on the surface in the different registered parcellations.

Figure 2 shows our parcellation on the reconstructed M132 surface and the F99 surface (fiducial, inflated and flattened).

Each injection site was localised relative to areal boundaries and anatomical landmarks, both within the sections containing the needle track and along the axis orthogonal to the cutting plane (the distance between sections being known). These distances to different landmarks were used to position the injection sites on the M132 atlas and they were registered onto the F99 atlas along with the M132 surface. The reported coordinates are likely to be accurate within 5 mm.

Figure 3 shows the location of the 39 injections represented on the F99 atlas surface. This mapping provides each injection site with a well-defined stereotaxic location that is independent of the underlying cortical parcellation for the stereotaxic coordinates of the injection sites. This

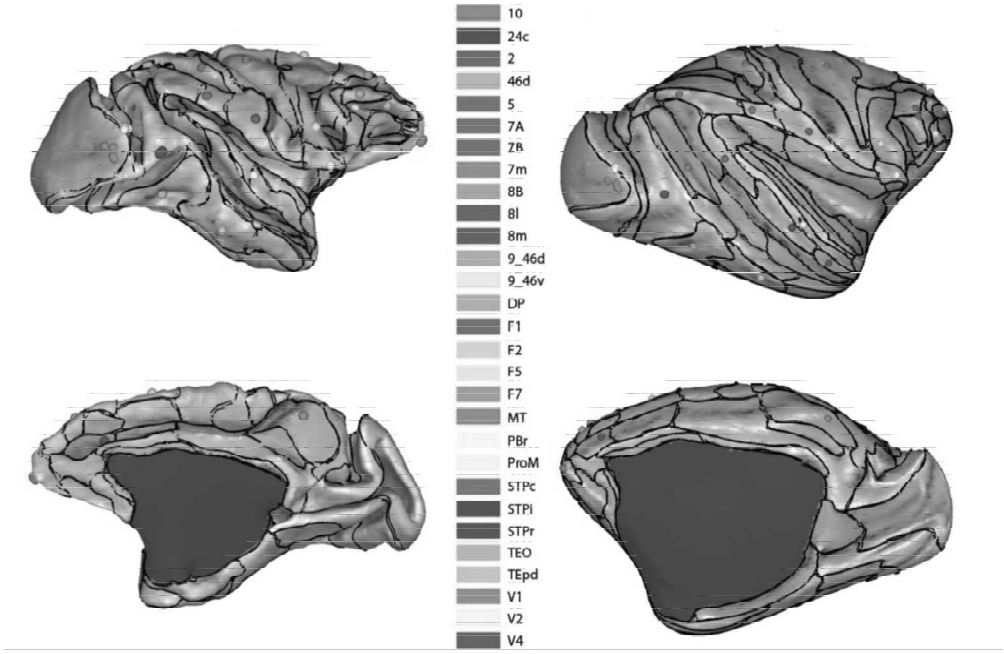

FIGURE 3: **Localisation of injection sites on the F99 atlas surface.** Each injection site centre was identified on histological section contours, and its location relative to areal boundaries used to estimate its atlas location. Colour key as in fig. 2. **Left**: The 39 injection sites are shown on the F99 reference brain on lateral (upper) and medial (lower) views. **Right**: Injections sites shown on inflated F99 surface.

way, while the focus of our analysis is on the pattern of area-to-area connectivity, these data can also be evaluated in terms of the areal inputs to a set of atlas coordinates that have well-defined locations relative to alternative parcellation schemes that have been mapped to the F99 atlas (Van Essen et al., 2012a).

The entire dataset is available in the online supplementary materials of Markov et al. (2014a), and at `http://www.core-nets.org`, including:

- all the section drawings of the M132 atlas with areal boundaries (figure S7),
- the sections containing the needle track of injections (figure S6),
- all the charts of labelled neurons with areal identities (figure S2),
- the table of number of neurons and FLN values with bibliographic references for known projections (table S6).

In these SOM the charts of labelled neurons (figure S2) show selected section contours with the injection site in solid red, the injected area in gray, and retrogradely labelled neurons as red dots; labelled neurons intrinsic to the area are not shown. Areal boundaries are indicated by black lines. Source areas representing newfound projections (NFP) are labelled in bold blue and marked by an asterisk; the sections were selected to illustrate all the NFP. In a few places, the label in a restricted region (identified by a black rectangle) comes from an adjacent section projected onto the section shown. Red lettering indicates inferred known projections, which although illustrated in previous studies listed in supplementary table 6 were not explicitly reported largely due to differences in the parcellation scheme used.

Surface-based atlas datasets are accessible on the website of the Van Essen lab at `http://sumsdb.wustl.edu/sums/directory.do?id=8287442&dir_name=MARKOV_CC12`.

2 Validity of the labelling method

Scannell et al. (2000) emphasised the importance of sampling and statistical methodologies in efforts to quantify cortical connectivity. Conventional approaches typically involve repeated injections into each cortical area and examination of connectivity using only a small fraction of the available histological sections, and averaging of connectivity data across multiple cases. We chose an alternative strategy that includes sampling histological sections at high density and across the entire hemisphere, thereby capturing as much data as is feasible. Furthermore, before basing a large scale quantitative study on retrograde labelling, the tracers had to be thoroughly characterised. In particular, it is crucial to know the spatial extent of the zone where they are picked up after injection, and precisely how they are transported in the brain, in order to unveil direct pathways to a particular target area. In this section we present evidence i) that the zone of dye uptake is very small and can be confined within an area, ii) that after transport the dyes are confined in the cell body without transynaptic labelling, iii) that it is possible to know the total number of fluorescent neurons in labelled regions through adequate sampling, and iv) that systematic parcellation and whole hemisphere charting uncover many previously unknown projections, thereby giving a much more complete picture of the cortical wiring diagram than was previously possible.

Together these results show that when injections are large, made in a stereotypical fashion and restricted to the cortical grey matter, it is possible to use DY and FsB to quantitatively characterise the population of cortical neurons sending afferents to the injected volume of cortex.

2.1 Characterisation of the tracing method

There is a large spectrum of available retrograde tracers that differ in several aspects: uptake mechanism, interactions with other tracers, method of visualisation, cell toxicity, and fading. For our present purpose we needed tracers that have a high sensitivity, are distinguishable in the same observation conditions, can co-label cells without interactions and are not toxic for the labelled cells.

(a) Choice of the dyes

The retrograde tracers Fast Blue and Diaminido Yellow have been available since the 80's (Bentivoglio et al., 1980; Kuypers et al., 1980). There are many advantages to combining them:

- DY and FsB have a high sensitivity compared to other retrograde tracers such as horseradish peroxidase, marking an estimate of 70 to 80% of parent neurons (Bentivoglio et al., 1980). Since FLN is a proportion, i.e. a relative measure of the strength of input, and because both tracers label a similar percentage of parent neurons, we can use them for a quantitative analysis of projection weights.

- The survival time necessary for efficient transport over long distances are similar (7 to 12 days).
- They both fluoresce when viewed with a D filter set (band pass 355 – 425 nm), and the two tracers accumulate in different cell compartments allowing double labelling studies.

Moreover, retrograde transport of Fsb and DY is an active process carried out by healthy neurons (FsB and DY are not toxic to the cells) during the survival time of 7 to 12 days (Bentivoglio et al., 1980). This allows an even labelling of parent neurons, whose intensity essentially does not decrease with axonal distance. Indeed we routinely observe bright labelling in parent cells even for the longest known white matter distances, and when the source and target areas are on opposite ends of the brain. Additionally, if the survival time exceeds 15 days, the quantity of labelled neurons is not markedly different, but the dye starts to leak out of the cell bodies, indicating that after normal survival time the tracer has already accumulated in the cell and more transport does not result in better labelling.

(b) Identification of the uptake zone

At the injection site, the processed brains present a crystallised deposit of dye, visible in the histological sections as a zone of dense extracellular fluorescence that extends 0.5 to 1 mm from the needle track. Examples are shown in fig. 4, and the extent of the uptake zone is characterised with respect to this dense colouring region.

A first line of evidence is to be found in the characteristic pattern of labelled cells near the injection site in the cortex. In sections perpendicular to the needle track, locally labelled neurons are found up to 3 mm away from the needle track in supra- and infra-laminar compartments, but in layer 4 they are practically confined to the region of dense colouring as seen in fig. 5. Layer 4 neurons only project very locally, while neurons in layers 2, 3, 5 and 6 send collaterals several millimetres from the cell body (Lund et al., 1981), so layer 4 labelled neurons have to be in or very near the uptake zone, while upper and lower neurons can pick up the dye from farther away. This explains the two long stripes of fluorescent cell bodies in those compartments and the absence of spread of labelled layer 4 neurons, and suggests that the uptake zone is almost reduced to the region of dense colouring in all cortical layers.

Further characterisation of the uptake zone was done by Bullier et al. (1984), who made adjacent injections (one of FsB and one of DY) at varying distances in area 17 of the cat cortex, and looked at the topography of the projection of the lateral geniculate nucleus (LGN) on to area 17. This pathway being highly point to point, injections lead to a narrow column of labeled cells spanning the layers of the LGN. When the injections were close enough for their zones of intense colouring to mix, the two columns of labelled cells in the LGN were overlapping, with intense double labelling (around 80%) in the overlap region. With gradually more distant injections, columns of parent cells showed less and less overlap and double labelling, until for injections about 2 mm apart the two columns in the LGN were separate (fig. 6). The terminal arborisation of geniculocortical neurons does spread several hundred micrometres (Bullier & Henry, 1979; Ferster & Le Vey, 1978), and yet none of these neurons could pick up both dyes when the distance between the borders of the dense colouring regions of each dye was greater than this

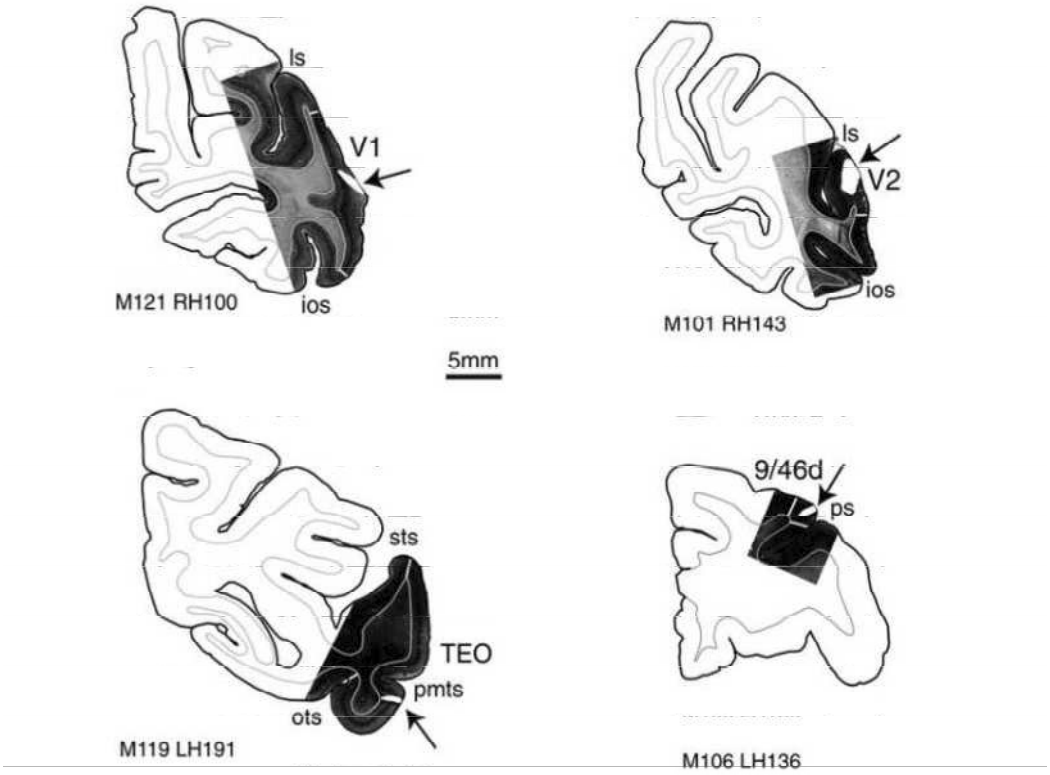

FIGURE 4: **Zone of intense colouring at the injection site.** Coronal plot charts overlaid on coronal photomontages of Nissl stain (objective 310) for exemplar injection sites. Uptake zones are indicated by arrows.

span. This indicates that the uptake zone essentially corresponds to the brightly fluorescent crystallised dye around the needle track. An independent study by Condé (1987) posits an even smaller uptake zone.

The small extent of the uptake zone even turned out to be a problem when making small, punctal injections in retinotopically equivalent regions in areas 17 and 18: despite extensive mapping, the two populations of labelled cells did not overlap in the LGN. The injection site had to span several receptive fields along a path in the visual field, with the path for the injection in area 17 crossing the one for the injection in area 18 and thus having some RFs in common, for overlap to be observed.

The experiment was repeated in the macaque in Kennedy & Bullier (1985) and again in Perkel et al. (1986). Again, the populations of parent cells were two non overlapping columns spanning all layers of LGN when the injections were 2 mm apart and the intensely fluorescent regions were separate (fig. 7). Even with two injections 1.4 mm apart and the two colouring regions lying within 0.5 mm of each other, the labelled regions in LGN are separate with some double-labelled neurons at the interface (fig. 8). The scarcity or absence of double labelling found in this study after injections in different areas is also proof that tracers do not show subpial spread, vascular uptake or spread in the cerebrospinal fluid.

It is important to note that since the uptake zone is essentially restricted to the densely coloured region, we can be sure that no uptake occurs in passing axons in the white matter as long as

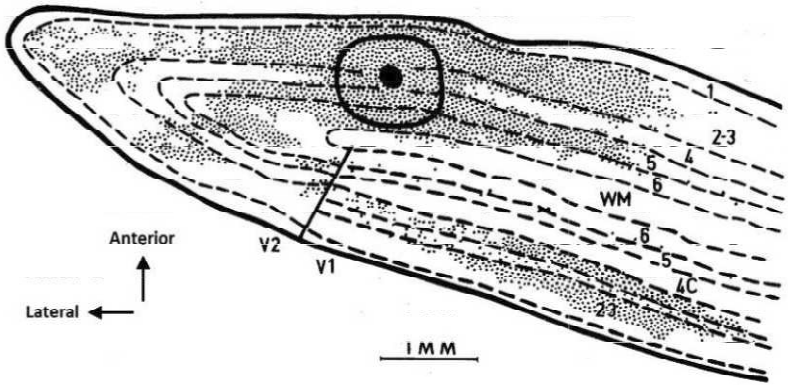

FIGURE 5: **Pattern of intrinsic labelling**: charting of neurons following a DY injection in V2 (horizontal sections). The black area represents the needle track; the region enclosed in the line around the track corresponds to the region of dense yellow colouring; the small dots are labelled neurons. Cortical layers and the V1/V2 limit are identified. WM: white matter. *Case BK5 from Bullier & Kennedy (1983), reproduced with permission.*

the extracellular fluorescence around the needle track does not reach the white matter and stays confined to the cortex. This can be achieved by inserting the needle parallel to the surface in a site spanning several millimetres, and slowly injecting the tracer while withdrawing the needle; therefore we used this method in all injections. This leads to relatively large injection sites, which though increasing the workload (more labelled neurons requires more person-months in charting their location) are necessary for the uptake zone to span the six layers of the cortex (all of which receive cortical afferents). Relatively large injection sites are also necessary to ensure that they are sufficiently large to overcome possible heterogeneity in the injected area, as speculated by Scannell, and because small injections could lead to between-injection variability (MacNeil et al., 1997; Scannell et al., 2000).

Finally, these results show that FsB and DY allow the characterisation of afferent connectivity of areas, even small ones, without contaminating the population of parent neurons with neurons projecting to regions around the target area. Since the uptake zone is defined and restricted, it is also possible to identify labelled neurons within the target area i.e. quantify the intrinsic connectivity of the volume of cortex where the dye was deposited.

(c) Absence of transynaptic labelling

Another cause for concern is the possibility that after initial retrograde transport to the cell body, the dye would not stay confined there but would cross the synapse and be transported to the cell body of a neuron that does not directly project to the injected area.

The possibility of transynaptic transport was controlled in Bullier & Kennedy (1983) by examining the retinae of an animal after a large injection in area V1. Despite heavy labelling in the LGN, no labelled neuron was found in the retina. It shows that no LGN neurons (labelled after direct axonal transport along the LGN to V1 pathway) had transported the dye across a synapse to the parent neurons of the pathway from the retina to the LGN.

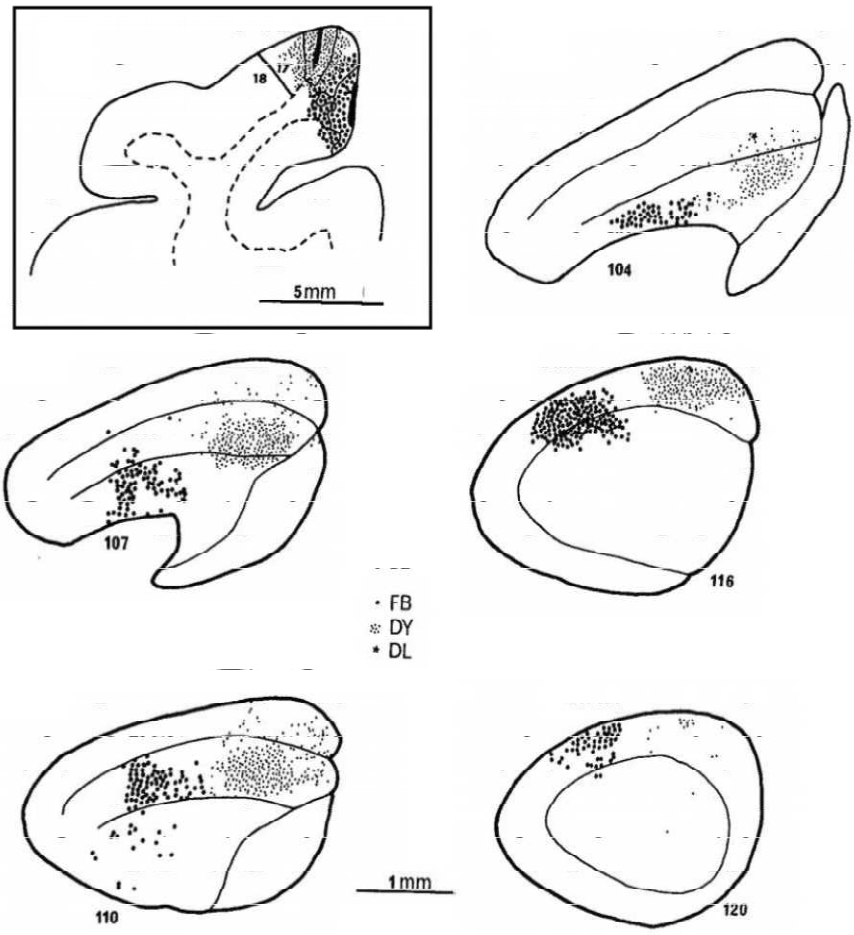

FIGURE 6: **LGN labelling in the cat following side-by-side injections in area 17.** Charted neurons in frontal sections of LGN (section numbers increase from caudal to rostral). DL: double-labelled neurons, positive for both dyes. Inset: Injection sites in area 17, with needle track in black and a line enclosing the two zones of intense colouring. *Case BK29 from Bullier et al. (1984), reproduced with permission.*

The absence of secondary uptake is further indicated by the pattern of interhemispheric labelling following injections in areas V1 and V2. It is known that area V2 on the V1/V2 border shows strong interhemispheric connectivity, while area V1 lacks callosal connections (Dehay et al. (1986, 1988) and the present study where injections in area V1 fail to label any neurons in the contralateral hemisphere). Injections in area V2 fail to label neurons in the contralateral area V1 off the V1/V2 border, while transynaptic labelling across the projection from V1 to V2 would have made it possible. The lack of contralateral labelling after V1 injections is very reliable because the density of the ipsilateral V2 labelling is extremely high (V2 projections to V1 are one of the highest densities of intra-cortical connections), so that if there was secondary uptake, one would expect some of the contralateral neurons that target the ipsilateral V2 to be labelled. They are not. One possible objection to the observation that injection in V1 fails to label contralateral V2 is that it is a long-distance connection. However, this does not hold against the fact that paracentral V4 has no input from area V1 but a strong input from area V2. Given the strong V1 to V2 projection, if transynaptic labelling were to occur, then one would find back-labelled cells in V1 following large injections of DY and FsB in V4. This is not the case.

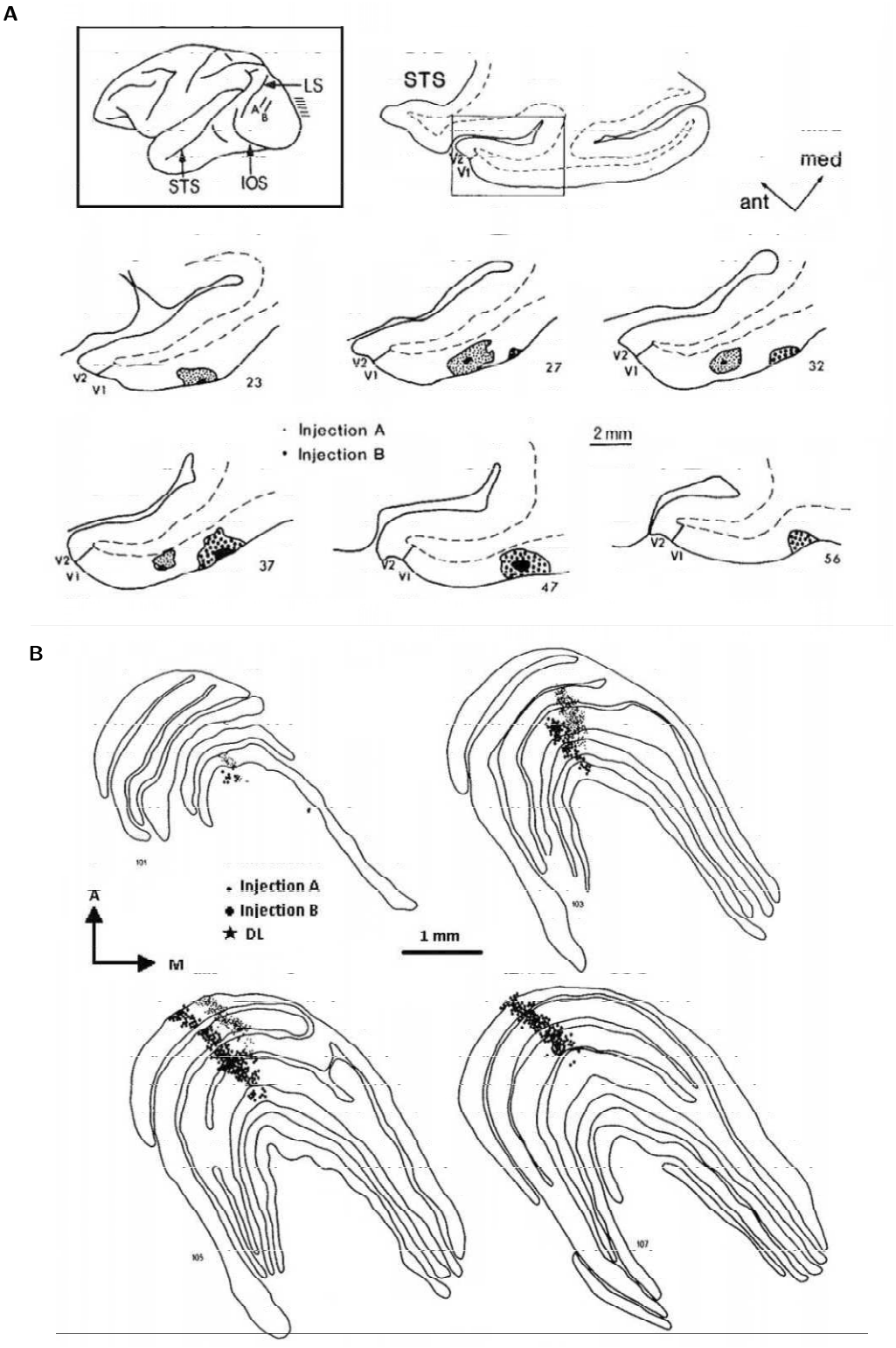

FIGURE 7: **LGN labelling after double injection in macaque V1.** (**A**) Position and extent of the two injections in V1 (horizontal sections, numbers increasing from dorsal to ventral, 120 µm of tissue between two adjacent sections). Solid regions represent the needle tracks and the surrounding areas filled with dots indicate the region of dense extracellular labelling. **Inset:** Lateral view of the brain showing the two injection sites, needle penetration, and location of the sections shown below. LS: lunate sulcus; IOS: intra occipital sulcus; STS: superior temporal sulcus. (**B**) Charted neurons in horizontal sections of LGN. Injection A: DY; injection B: FsB. DL: double-labelled neurons. *Case BK15 from Perkel et al. (1986), reproduced with permission.*

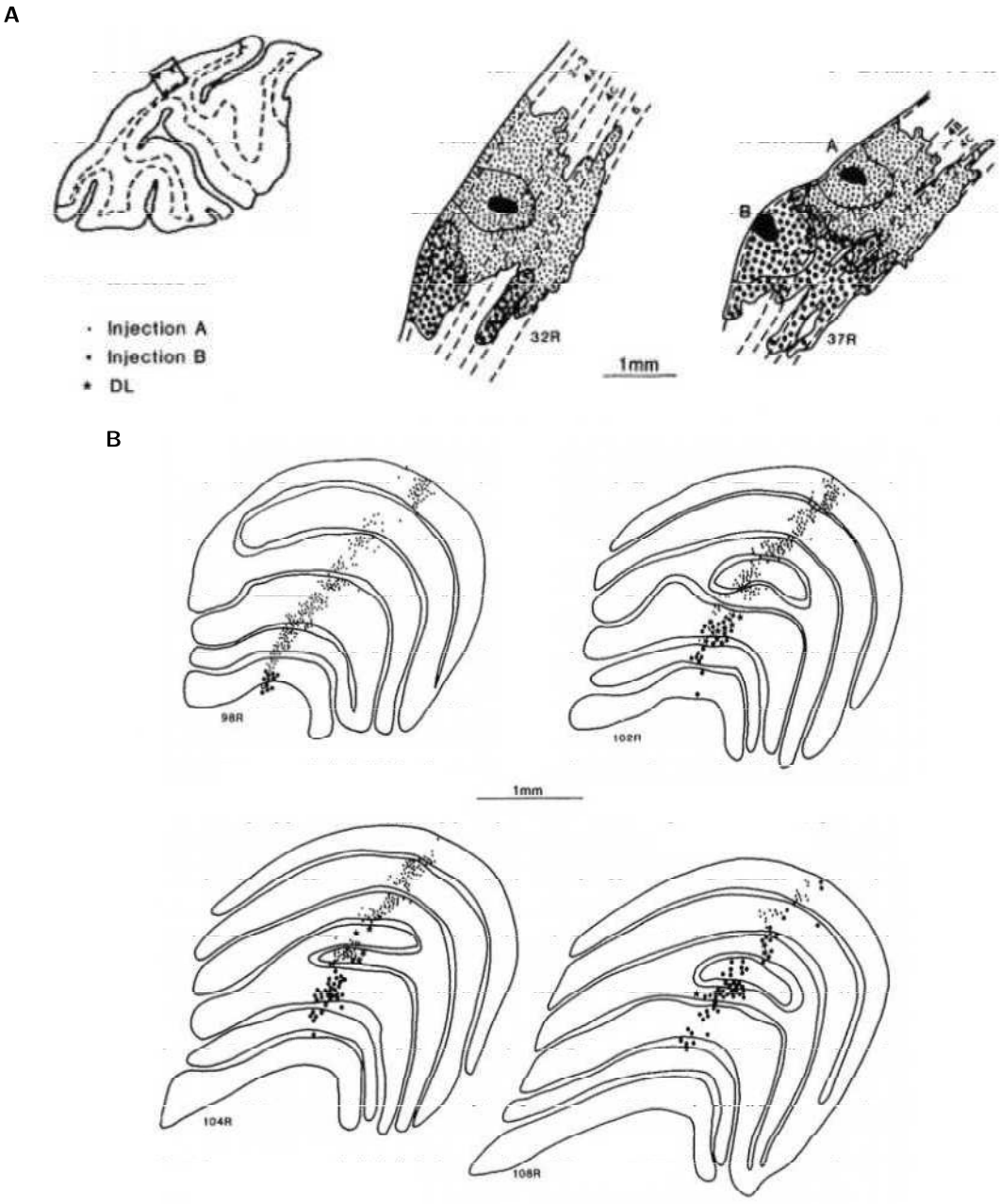

FIGURE 8: **LGN labelling after double injection in macaque V1 separated by 1.4 mm.** Same conventions as in fig. 7. **(A)** Location of both injections on a horizontal section and extent of the zone of dense extracellular labelling. **(B)** Charted neurons in horizontal sections of LGN. *Case M23RH from Perkel et al. (1986), reproduced with permission.*

Finally, here and elsewhere, we have shown that intrinsic labelling, although very dense, has a sharp drop off over two or three millimetres. If there were any transynaptic labelling at all, this could not be the case. These results, and numerous unpublished observations, mean that following their retrograde transport to the source area, these tracers are not released and picked up by neurons or by afferents to the source area in quantities sufficient to lead to secondary labelling.

2.2 Sampling of the projection zone

The extent of the projection zones (the cortical regions containing labelled neurons) is not homogeneous but has a complex shape (Barone et al., 2000; Batardiere et al., 1998; Vezoli et al., 2004). Labelled neurons are unevenly distributed in the projection zone, peaking in a central core region and gradually decreasing toward its periphery. Furthermore, the gradient is sharper for supragranular layer neurons than for infragranular layer neurons, which means the infragranular layer neurons tend to stretch further (fig. 9). Both FLN and SLN (percentage of supragranular labelled neurons) values computed within a section can vary widely from the values computed from the total numbers in the projection zone (examples of the different values of SLN across sections are given in fig. 9B). Therefore, it is necessary to count neurons at close intervals throughout the projection zones. Although laborious and time consuming, this is crucial in order to obtain stable neuron counts that do not vary according to sampling frequency. However, because of the curvature of the cortex it is complex to determine the appropriate sampling frequency.

To address this issue, Barone et al. (2000) have compared neuron counts obtained when using every section kept for labelling search (1 in 3 slices from brain cutting) or lower frequencies (1/2, 1/4 or 1/8 of these sections kept after cutting). They show that for both FLN and SLN, the minimum sampling frequency is highly dependent on the FLN values: setting the maximum acceptable error at 10%, a frequency of 1/2 is required to obtain reliable SLN values for areas with an FLN above 0.36%, and for lower FLN values, it is necessary to sample at 1/1. Importantly, when sufficient numbers of sections have been scanned the contours of the density profile (histograms of the number of labelled neurons per scanned sections) are smooth (Batardiere et al., 1998; Vezoli et al., 2004).

In the present study, we estimated the number of neurons present in the 1 in 3 slices kept after brain cutting and mounted on microscope slides, i.e. we inspected 40 µm of every 120 µm of tissue. The actual numbers in the hemisphere following the injection are therefore three times those numbers. Of course, FLN and SLN being relative indices, this does not change their values. We chose the sampling frequency by inspection of the density profiles and ensuring they were smooth across the whole projection zone, and linearly interpolated the number of neurons in the non scanned sections in between. For spare connections, all sections retained for charting neurons were explored (frequency of 1/1), whereas the sampling frequency was as low as 1/4 for the strongest projections, and typically 1/2 in the rest of the hemisphere. Outside of projection zones, a high frequency sampling was also carried out so as to not miss potential weak projections. Both FLN and SLN were computed for entire areas; the values from individual sections from fig. 9B only serve to show that the full extent of the projection zone must be sampled at a

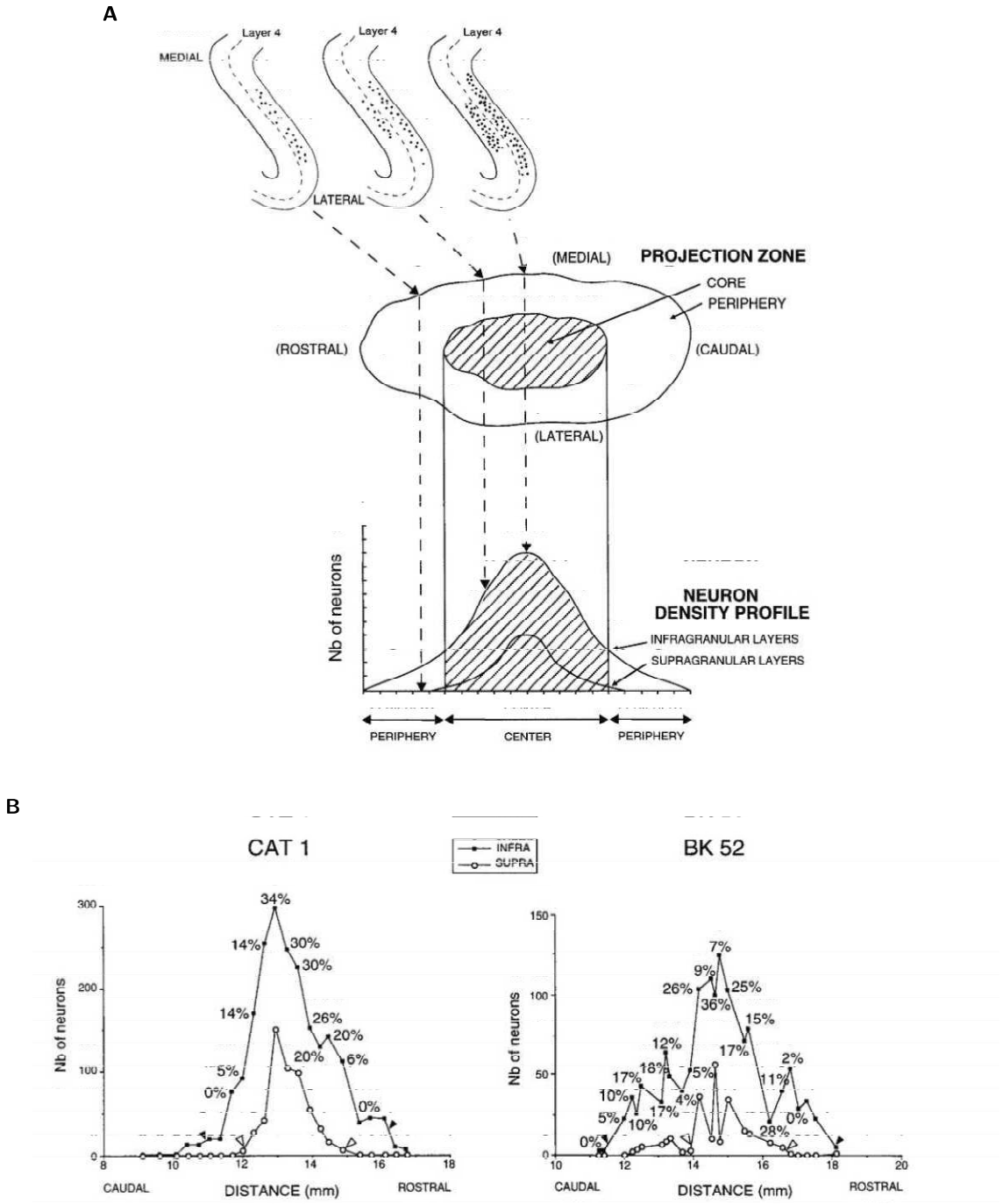

FIGURE 9: **Geometry of the projection zone and neuron counts.** (A) Schematic representation of the extent of the projection zone. **Top**: Example coronal sections from different parts of the projection zone. Dots represent retrogradely labelled neurons. **Bottom**: the density profile represents the number of labelled neurons in each section for supra- and infragranular compartments. The core of the projection zone is the region containing labelled neurons in both compartments. (B) Neuron density profiles (caudal to the left) of the PMLS area projection zone after area 17 injection in two cats, for infra- (black squares) and supragranular (open circles) layers. Percentages indicate SLN values for each individual section. Arrowheads indicate 5% of peak values used to determine the limits of the projection zone. *Cases CAT 1 and BK52 from Batardiere et al. (1998), reproduced with permission.*

high density to correctly estimate the total numbers for the area. The scale bars in the figures represent distances measured in the processed sections, without correction for tissue shrinkage.

2.3 Exhaustive mapping of projections

Since the seminal analysis of Felleman & Van Essen (1991), there has been a major increase in the number of areas reported to project to visual areas, and in our database 36% of the 1,615 interareal pathways revealed by retrograde tracers have not previously been reported. To make sure that all the projections previously unreported were indeed novel, we checked against the CoCoMac text-based connectivity database for the macaque (Stephan et al. (2001); `http://cocomac.org/`) and performed extensive literature searches (see the online supplementary material of Markov et al., 2014a). However, this database and other available datasets have been collated from multiple studies using different methods of tracing and nonmatching areas, nomenclatures, planes of section, etc., and they contain at best only a qualitative assessment of connection weights (Felleman & Van Essen, 1991; Kötter, 2004; Stephan et al., 2001).

Importantly, to assess the presence of a projection it is sufficient to find a section with labelling (as was done in many older studies), but the status of unreported pathways is unclear. As we saw in the previous section, it is not enough to provide quantitative estimates of the numbers of neurons involved, nor is it enough to rule out the presence of weak pathways: for this, a high-resolution scan of the brain is required. Moreover, many studies on which the CoCoMac database and others are based only scanned parts of the brain for projections. Typically, an experiment on the connectivity of a visual area would look at other visual areas, including parietal and some prefrontal regions, but not the rest of the hemisphere. On the contrary, we performed a complete scanning of the hemisphere to determine the full set of ipsilateral cortical source areas projecting to each injected area. This explains how "unexpected" projections like the one of the core auditory region onto the periphery of area V1 (Falchier et al., 2002) could be overlooked until our systematic method was applied. This also led Felleman & Van Essen (1991) to estimate the actual network density at around 40% of possible projections. The crucial distinction between projections checked and found absent, and unchecked pathways has led to the development of an algorithm to interpolate the unknown components of the network (Jouve et al., 1998). Such an interpolation is no longer necessary in our dataset since our connectivity matrix of 29 injected areas and 91 source areas gives complete information about the existence, strength and laminar profile of all projections to the injected area. The unprecedented scope and detail of this study, along with the high sensitivity of FsB and DY, explain the high number of new found projections (NFP) and reveal a density of the graph even higher than previously estimated, which is a result in itself.

The pattern of source areas for each injection was determined using our own parcellation of the entire cortical sheet into 91 architectonic areas drawn from published atlases (Paxinos et al., 2000; Saleem & Logothetis, 2007) and other studies, rather than any of the numerous alternative macaque cortical parcellations that are in common use (Van Essen et al., 2012b, 2005). Indeed, in many regions, these other parcellations differ substantially from ours. While this choice of parcellation obviously impacts our detailed results, use of alternative parcellations would only modestly impact our main conclusions (see fig. 13 in section section 3.2(b)). More importantly,

it is the use of the same parcellation across the whole study, rather than the choice of our particular areal boundaries, that makes the resulting quantitative results reliable. In particular, the reassessment of some areal limits with histology following some V1, V2 and V4 injections did not significantly change the areal FLNe values, thereby supporting the use of geographical delineation of areal limits for determining the FLNe of cortical projections. Since we have registered our atlas onto the F99 dataset for comparison, it would be of interest to ultimately determine a quantitative connectivity matrix using one or more alternative parcellations applied to each of the cortical injection cases. Unfortunately, technical considerations make this an enormous undertaking that was not feasible for the present study.

3 Using FLN values to study interareal connectivity

The paucity of corticocortical connectivity studies reporting quantitative neuroanatomical data largely reflects the difficulty in accurately quantifying the weight of connections between cortical areas. Even the motivation to pursue such analyses has been dampened by evidence that the connection weight of any given pathway is highly variable or overdispersed with a more than 100-fold range (MacNeil et al., 1997; Musil & Olson, 1988a,b; Olson & Musil, 1992; Scannell et al., 2000). One of these studies suggests that it might require the analysis of 10 to 20 injections to adequately characterise the profile for a given area (Scannell et al., 2000). However, these reports examining the consistency of connection weights largely relied on data compilations across laboratories, often from studies using different tracing techniques and definitions of areas; these factors may have contributed to the observed overdispersion (Scannell et al., 2000). Here, using multiple injections in the same area and ensuring minimal methodological variability, we demonstrate that while connectivity strengths do display significant overdispersion, their variability can be bracketed and their distribution characterised. With this knowledge, we have explored statistical approaches that permit appropriate treatment of the issue of overdispersion, and show that there is a specific connectivity profile for each area that can be uncovered by single injections of FsB or DY.

3.1 Modelling the variability of FLNe values

A group of 11 animals was used for repeat injections to assess variability of FLN across animals. A total of 13 injections were made in V1 (5 injections in 4 animals), V2 (3 injections and 2 animals), V4 (3 injections and 3 animals) and area 10 (4 injections in 4 animals), a higher order area with about twice as many inputs as the early visual areas. The cases are detailed in table 2.1 page 40, cases 1 to 10, 34, and 37 to 39. V1, V2 and V4 are large areas whose borders and retinotopy are well established, making it possible to make stereotypic injections of retrograde tracers in the central representation of these areas across animals (Gattass et al., 2005). Similarly, area 10 was systematically injected at the rostral tip of the brain, and 3D reconstructions of the 4 injection sites in relation to the pial surface and the grey/white border were generated from the stack of sections containing the injection site using the Module Map3D program in ExploraNova® (fig. 10). Inspection of these reconstructions, especially the medial views (far right column), confirms that the uptake zones were restricted to the frontal pole,

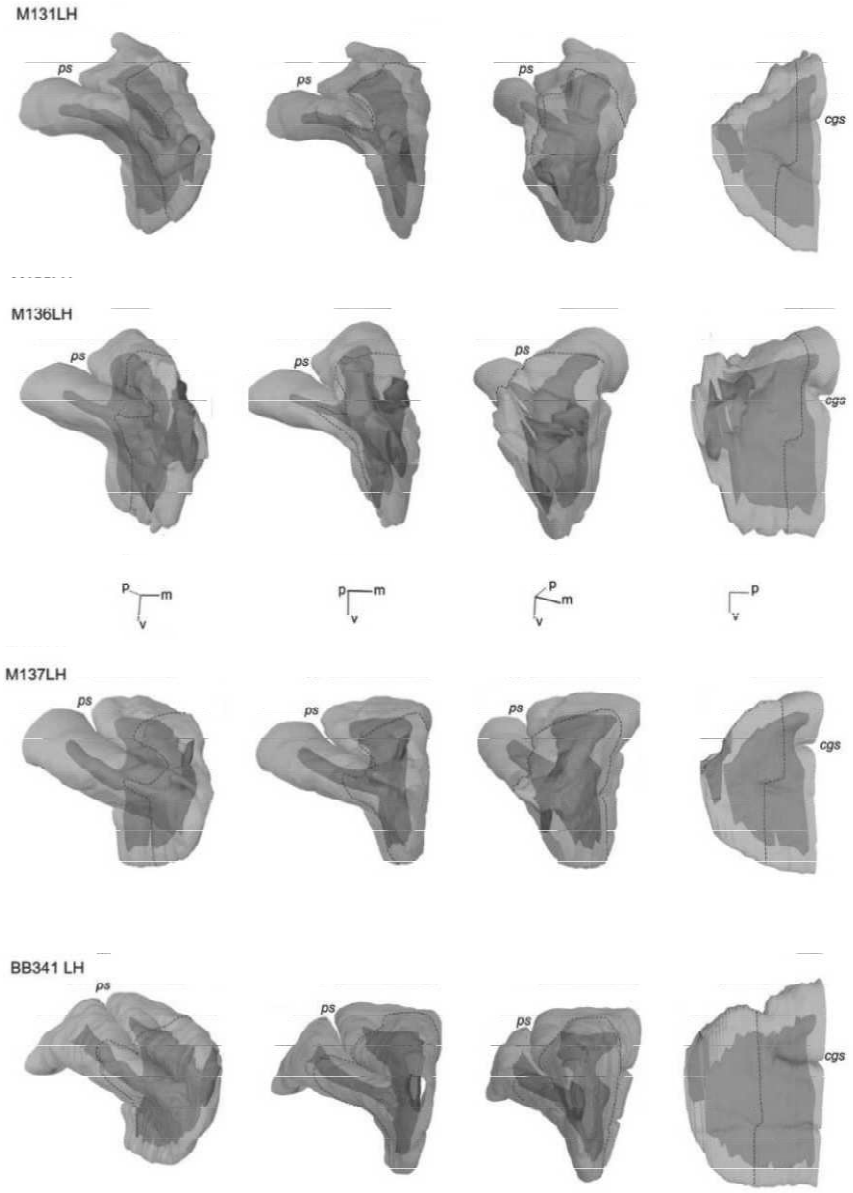

FIGURE 10: **3D reconstruction of area 10 injection sites.** For each of the 4 cases the extent of the dense colouring region is shown in red and the white matter in blue. The dotted line indicates the limits of area 10.

spanning the cortical gray matter but not encroaching on the underlying white matter. The 2 smallest injections (M131 LH and BB341 LH, panels A and D) had almost identical locations in the rostral pole. The 2 larger injections (panels B and C) also included the anterior pole but extended further ventrolaterally.

With this dataset, we analyzed the consistency of individual pathways in order to determine whether a connectivity profile exists. This entailed determining the statistical distribution that best describes the data, including the average connection strength and its variability. To do so, we used extrinsic FLN (percentage of labelled cells in each source structure but the total for the brain does not include the labelled cells inside the injected area, which make up 80% of the

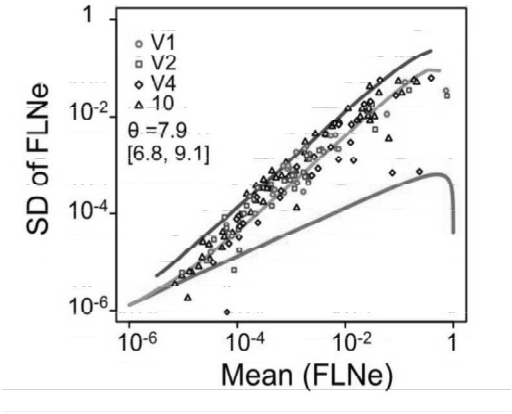

FIGURE 11: **Mean-SD relationship of FLNe values in repeated injections.** The graph shows the observed standard deviation of FLNe as a function of the observed mean. The curves are the predictions for a Poisson (red), geometric (blue), and the best-fitting negative binomial distribution (green). The dispersion parameter θ of the negative binomial distribution and its 95% confidence interval are indicated.

total). Interestingly, the full range of FLNe values still spans more than 5 orders of magnitude, and the primary source of connectivity (areas that share a border with the injected area) still make up for 80% of the total.

All statistical analyses were performed in the R statistical computing environment (R Development Core Team 2010) with additional tools from the MASS and multcomp packages (Hothorn et al., 2008; Venables & Ripley, 2002).

Count data are intrinsically heteroscedastic, that is, the standard deviation (SD) depends on the mean μ (Hilbe, 2007). In the simplest model of count data, the Poisson distribution, a single parameter determines the mean and the SD is equal to the square root of the mean: $sd = \sqrt{\mu}$. Proportions, where the count is conditioned on a fixed total sum N, then follow a binomial law where the standard deviation is $sd = \sqrt{p(1-p)/N}$, with p the mean value of the proportion (in our case the mean FLNe). The geometric distribution is an alternative model that predicts greater variation than the Poisson distribution. Under this model, the SD increases as the square root of the mean plus the mean squared: $sd = \sqrt{\mu + \mu^2}$. Both the Poisson and the geometric distributions are extreme examples from the negative binomial distribution family that has proven valuable in the analysis of over-dispersed count data (Hilbe, 2007; Lindsey, 1999; Venables & Ripley, 2002). The negative binomial can be derived as a Poisson distribution modified to have a gamma distribution of the mean. A second parameter θ controls the dispersion of the distribution, with standard deviation $sd = \sqrt{(\mu + \mu^2)/\theta}$. Note that the geometric distribution is simply a negative binomial with the dispersion parameter equal to 1.

The relation between the mean FLNe values and their SD is plotted in fig. 11 for all the pathways to the 4 areas with repeated injections. The observed values were evaluated with respect to the negative binomial family of models, with the Poisson and geometric distributions as upper and lower limits. The expected mean-SD relations are plotted for each model (Poisson in red, geometric in blue and the best-fit negative binomial in green). To derive the fit for the Poisson distribution, we set $N = 6 \times 10^{-5}$, the approximate average total number of extrinsic neurons

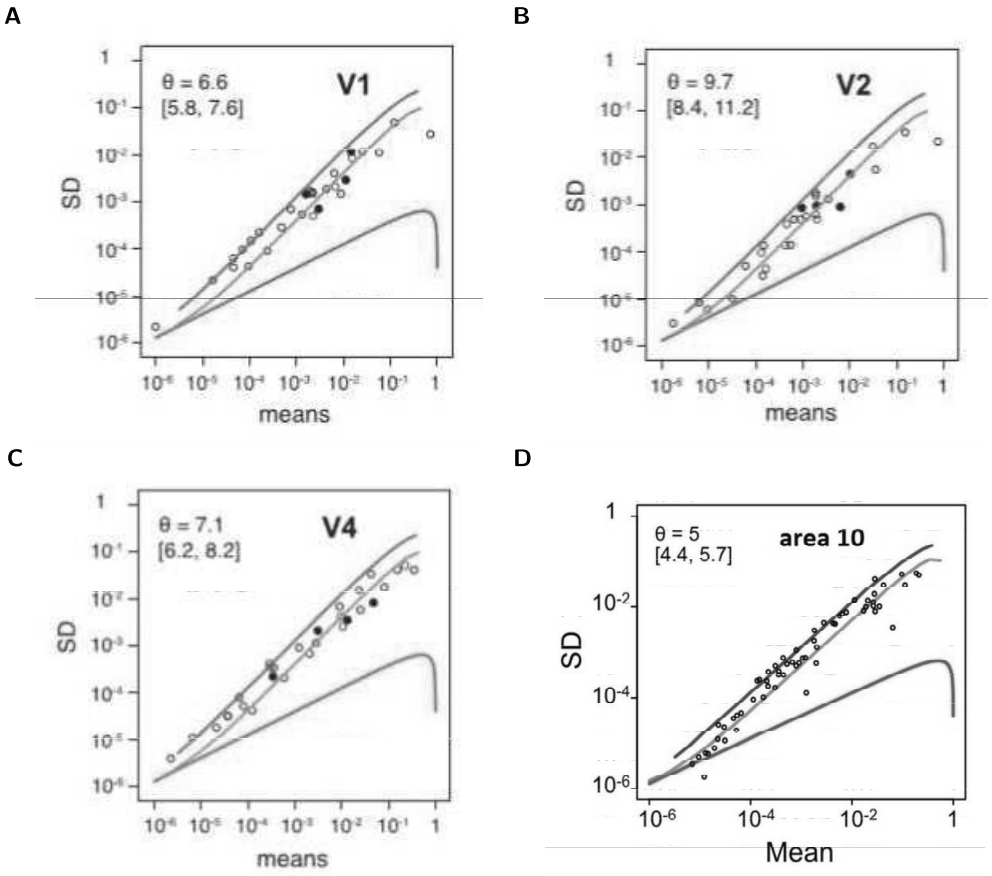

FIGURE 12: **Mean-SD relationship of FLNe values in each area with repeated injections.** Same conventions as in fig. 11: Poisson model in red, geometric in blue, best-fitting negative binomial in green with its dispersion parameter θ and 95% confidence interval indicated above the curves. **(A)** Area V1 **(B)** Area V2 **(C)** Area V4 **(D)** Area 10.

observed across injections. The negative binomial fits were obtained by simulating counts from a negative binomial distribution for mean values ranging from 2 to 106 and calculating the mean and SD of the proportions for values of θ ranging from 1 to 128. Average curves were based on a spline interpolation of the mean of 20,000 repetitions. From these simulated curves, the values of θ and 95% confidence interval were estimated that generated the best fit to the data by a least squares criterion. In fig. 11 we can see that the standard deviation of the FLNe for any given pathway is about an order of magnitude or less, but exceeds the prediction for a Poisson-distributed variable (red curve). Using the Poisson model for statistical tests would therefore lead to increased Type 1 errors (rejecting the null hypothesis when it is true). Most data points however fall below the geometric prediction (blue curve), suggesting that the geometric model predicts too much variability in the data. Using this law would tend to generate Type 2 errors, failing to reject the null hypothesis when it is false. The green curve in fig. 11 indicates the prediction of the negative binomial distribution that best fits the data (its dispersion value and 95% confidence interval are indicated in the figure). Note that the confidence interval for θ excludes 1, which would be the geometric distribution. Similar relations were found when areas are considered separately (fig. 12).

A negative binomial model can also predict the symmetry of the distribution of the data. The

95% confidence interval of the average of the median/mean of the FLNe ($0.87-0.97$) that measures this symmetry differs from the geometric prediction ($\ln(2) = 0.69$) and includes the value of the negative binomial model with parameters indicated by the SD-mean relation of fig. 11 (0.96).

By extension, we assume that a negative binomial model with similar dispersion should be valid for injections in other regions. For a negative binomial distribution with a known dispersion, there is a functional relation between the variance σ and the mean μ, that is, the variance of the negative binomial distribution is $\sigma = \mu + \mu^2/\theta$, with θ the dispersion. This relation improves our statistical power and enables us to accurately estimate the random variability of the data from repeated injections (next section). It also allows us to estimate the reliability of results obtained from a single injection as well as to model the consistency of the sparse connections (section 3.3).

3.2 Statistical analysis of connectivity profiles

(a) Existence of a connectivity profile

Overdispersion of the strength of projection from an individual area raises the issue of whether the observed variability reflects genuine individual differences or is intrinsic to the technical procedures used. Armed with our description of the distribution of the data, we can now test the minimum set of factors accounting for the differences in the data from each target area. For the 3 visual injection sites, models of the number of cells from each source area as a function of various explanatory variables were fitted with a generalised linear model (McCullagh & Nelder, 1989) with a negative binomial family. The link function was chosen to be logarithmic. The log of the total number of cells counted from each injection was used as an offset or constant component added to the model so that in fact the connection density was modelled. Four explanatory variables were evaluated for systematic effects: $AREA$ (a factor with a level for each source area), $BRAIN$ (the individual from which the counts were obtained), DYE (a 2-level factor indicating the tracer used), and $HEMISPHERE$ (the hemisphere of the injection). For example, if $AREA$ is considered as an explanatory variable, then it is treated as a factor with as many levels as source areas that contained marked cells from the injections in the target areas. Fitting to the data a model containing only this factor provides estimates of the average FLNe, and estimates of the variability associated with each level of the factor.

Including more factors and interactions will always improve the fit to the data, at the expense of the explanatory power of single, likely explanatory variables. To optimise the likelihood (quality of fit) while keeping a small number of parameters that best describe the data, we used the Akaike information criterion or AIC (H., 1993; Venables & Ripley, 2002). The AIC is equal to $-2\log(L) + 2P$ with P the number of parameters used to fit the data and L the likelihood. It introduces a penalty for additional parameters, so that the model with the lowest AIC corresponds to one in which likelihood and numbers of parameters are optimised. The best model, selected in this way, was subsequently verified by evaluating the statistical significance of adding and/or dropping additional terms. The principal hypothesis tested was whether the neural counts across areas were independent of factor $BRAIN$. For the 3 visual areas with

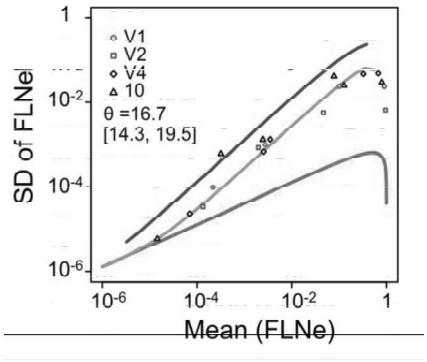

FIGURE 13: **Mean-SD relationship of FLNe values for large cortical regions.** Cortical areas were grouped into 7 possible source regions and cumulative FLNe values for these potential pathways were evaluated. Conventions as in fig. 11.

repeated injections (V1, V2, and V4), the model with the lowest AIC included no main effect of factor $BRAIN$, subsequently confirmed by likelihood ratio tests (V1: $F_{3,30} = 2.1, p = 0.1$; V2: $F_{1,29} = 0.07, p = 0.78$; V4: $F_{2,32} = 0.91, p = 0.41$). Thus, the simpler models without the $BRAIN$ term were retained. The absence of a main effect of $BRAIN$ implies that quantitative connectivity profiles do not differ significantly across cases, and therefore a robust signature (connectivity profile) exists for each area.

(b) Influence of parcellation uncertainties on FLN variability

If our analysis overestimated the overdispersion of the data, our model would be less sensitive and might lead to an underestimation of the systematic effect of the factor $BRAIN$. One possible source of overdispersion could relate to the parcellation of the cortex into individual areas, so we grouped cortical areas into 7 large regions having less uncertainty in the boundaries. Figure 13 shows that it reduces but does not eliminate overdispersion (a larger θ means a smaller dispersion). Overdispersion is therefore an intrinsic feature of the cortex and not simply a consequence of an experimental error in defining the limits of cortical areas. Significantly, even with this reduction in overdispersion, factor $BRAIN$ did not contribute a significant improvement to the fit by the source regions themselves (V1: $F_{4,25} = 0.27, p = 0.89$; V2: $F_{2,12} = 1.39, p = 0.29$; V4: $F_{2,14} = 1.12, p = 0.35$). We also considered the possibility that the overdispersion was generated by the weakest projections, which tended to be more variable. However, the results were unchanged when we repeated the analysis with the data set thresholded to eliminate projections with FLNe values less than 0.0001, that is, $BRAIN$ did not contribute a significant improvement to the fit obtained by using $AREA$ alone (V1: $F_{3,83} = 1.19, p = 0.32$; V2: $F_{1,40} = 0.02, p = 0.88$; V4: $F_{2,36} = 0.08, p = 0.93$). The result holds when adding injections in area 10 (also plotted in fig. 13).

Note that the overdispersion can in part be attributed to interindividual differences because the comparison of the standard deviations and means for the two cases of multiple injections within an animal (fig. 14) indicates a smaller dispersion (larger θ).

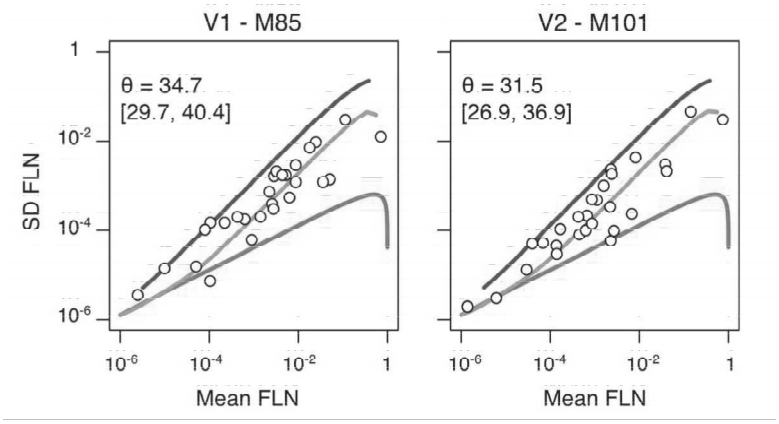

FIGURE 14: **Mean-SD relationship of FLNe values from repeated injections in the same animal.** In two animals, several injections were made in the same area using different hemispheres and/or dyes. Here we pool all the within-animal FLNe values and plot the mean-SD relationship. Conventions as in fig. 11.

(c) Distinct connectivity profiles

While the three visual areas have a great number of common sources, the orderings are quite different (fig. 15A; the inputs are sorted in descending order with respect to the V1 connection weights). There is a broad similarity in the strengths of the projections from specific areas to the 3 targets, but the confidence intervals do not overlap for many pairwise comparisons (e.g., TE projections to V4 are significantly stronger than to V1 or V2). The only case with no overlap of all three confidence intervals is area TEO, whose projections are significantly different to V1, V2, and V4. This, plus the complete absence of projections to some target areas for others, indicates an overall different signature of input areas and strengths for each target. Figure 15B shows the profiles of subcortical inputs. These are notable in terms of the small LGN input to V1 (about 1%) and the large projections from the claustrum to the 3 target areas.

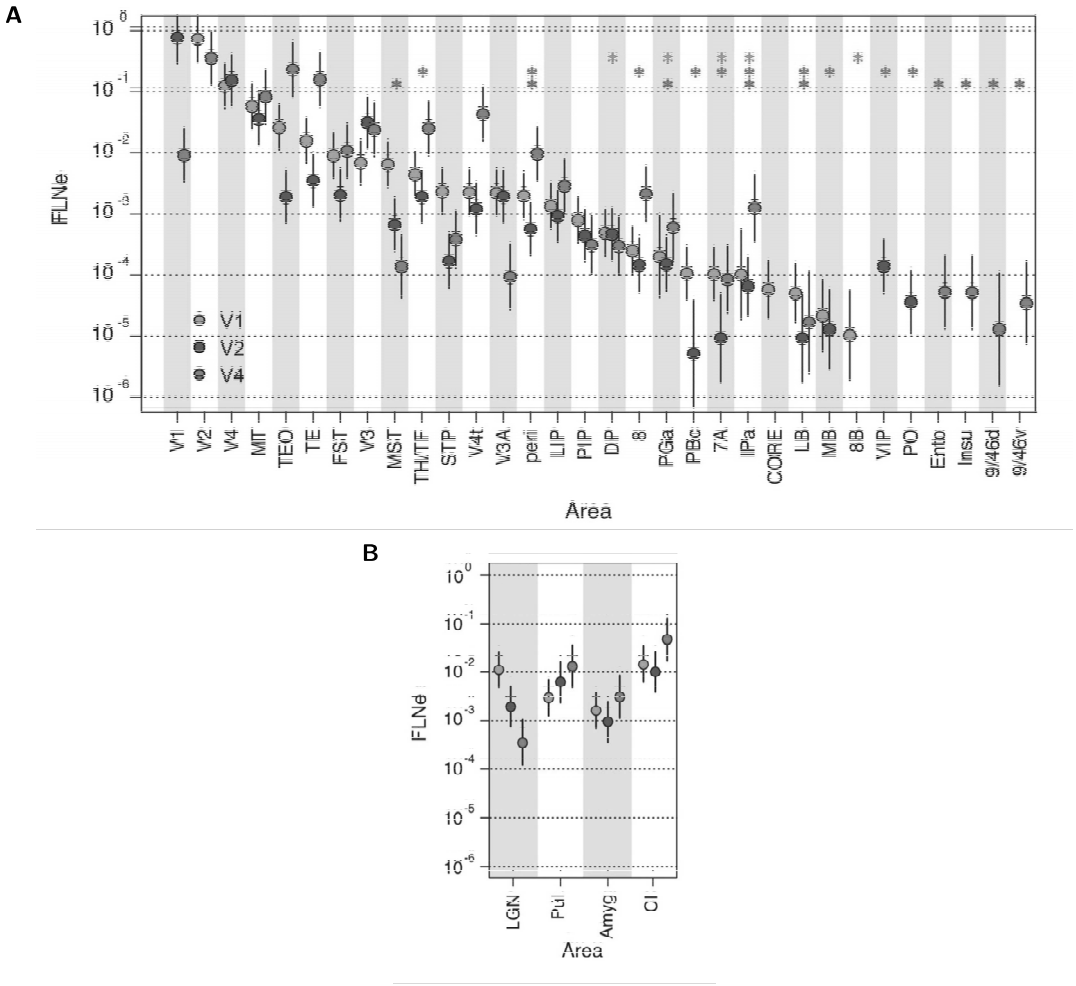

FIGURE 15: **Connectivity profiles of areas V1, V2, and V4.** (**A**) Extrinsic FLNe values of cortical projections and 95% confidence intervals for V1 (green), V2 (blue), and V4 (red) as estimated with a negative binomial model. Stars: new previously undocumented projections. (**B**) Mean $\log(FLNe)$ of subcortical projections with SDs.

The confidence intervals generally are less than an order of magnitude except for the weakest connections, which tend to be more variable. The observed range of FLNe values for the four injections in area 10 is less than one order of magnitude, except for the inputs from areas 45A, 31, 7A, and DP where the range exceeds orders of magnitude. Importantly, the confidence intervals are much smaller than the range of strengths across pathways, thus establishing significant differences between the projections onto a given target area, i.e. a distinct signature or connectivity profile for each area.

3.3 Validity of single injections to estimate FLN

One important question is how closely the weight of a pathway observed after a single injection approximates the average connection weight determined from repeat injections.

(a) Using single-injection FLNe values to predict the mean for multiple injections

To evaluate how accurately FLNe values from a single injection can predict the mean obtained from multiple injections, we compared the FLNe values from single injections to the mean FLNe from all the repeats. Figure 16A shows the ordered FLNe values from a single V1 injection (white circles), with a 95% confidence interval assuming a negative binomial distribution analysis with the dispersion observed following the multiple injections. For most pathways, the difference between the observed single-case value and the mean of 5 injections (blue circles) is quite small, and lies within the 95% confidence interval predicted by the negative binomial distribution. In this exemplar injection, the difference is smaller than the error bar for all pathways (the 5 last areas have no white dot value because the plotted injection had no labelled neurons in these pathways but some of the other repeats had). The maximum difference is 0.99 log unit, corresponding to a 9.5-fold difference between the single subject and group-average results. Another example in area 10 (fig. 16B) shows a comparably good fit for most of the data involving strong and moderate projections. However, for a few projections, the difference between individual and group average exceeds an order of magnitude. For the full set of 14 repeats involving 544 single FLNe values, the 95% confidence values included 98.5% of the observed FLNe means determined from repeated injections.

Altogether, this analysis indicates that FLNe values obtained from single injections are usually within a factor of 3 and highly likely to be within a factor of 10 of the mean value. However, exceptions can occur, especially for sparse connections, which brings us to this issue: if a given interareal pathway is observed after a single injection, what is the likelihood that the same pathway will be observed after repeat injections, and to what extent does this likelihood depend on the observed connection weight?

(b) Consistency of sparse connections

To analyze statistical characteristics of inconsistent projections, we computed the probabilities of observing no neurons under several models. For the simple case of the Poisson distributed counts, the probability of observing y neurons given the mean number of neurons μ is

$$P(y|\mu) = \frac{e^{-\mu}\mu y}{y!}$$

For $y = 0$,

$$P(y = 0|\mu) = e^{-\mu} \tag{1}$$

For the negative binomial distribution, the probability density is:

$$P(y|\mu, \theta) = \frac{\Gamma(y + \theta)}{\Gamma(\theta)\Gamma(y + 1)} \left(\frac{\theta}{\theta + \mu}\right)^{\theta} \left(\frac{\mu}{\theta + \mu}\right)^{y}$$

where Γ is the gamma function defined as $\Gamma(n) = (n - 1)!$ and θ the dispersion. Then, the probability of observing zero neurons is

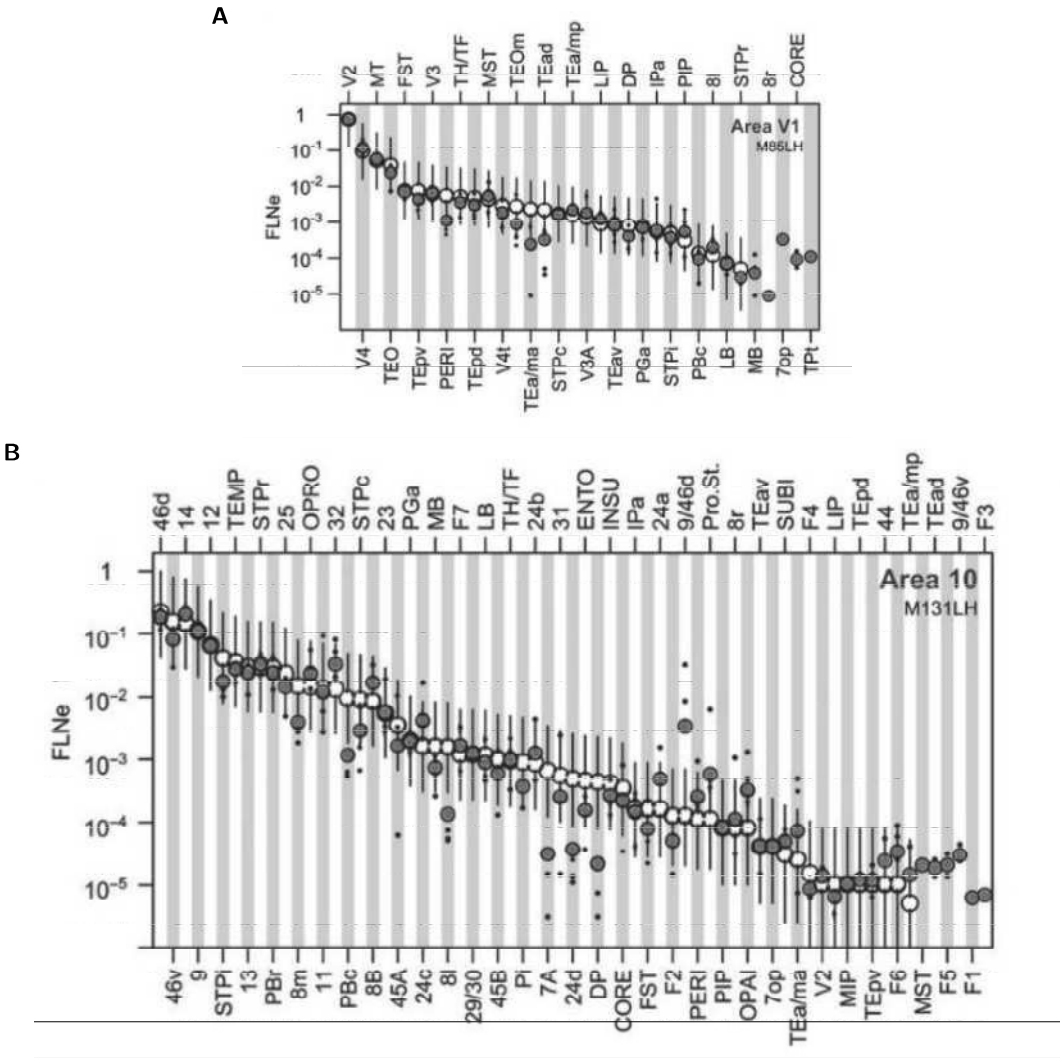

FIGURE 16: **Relationship of means from multiple injections and values from a single injection.** Ordered FLNe values from a single injection (white circles) with 95% confidence intervals expected on the basis of a negative binomial distribution with the dispersion observed in the multiple injections (error bars). The blue circles are the geometric means of all the repeats; the small black dots correspond to values obtained in the other repeats. **(A)** Injection in V1 (case 2, M85LH). Four other repeats were made (black dots). For the 5 entries on the far right, there were no labelled neurons from the plotted V1 injection used for FLNe rank ordering. **(B)** Injection M131LH in area 10 (case 34). Three other repeats were made (black dots). The 6 entries on the far right have no white circles because there were no labelled neurons from the plotted injection.

$$P(y = 0|\mu, \theta) = \left(\frac{\theta}{\theta + \mu}\right)^{\theta} \tag{2}$$

For the special case of the geometric distribution ($\theta = 1$), the probability of a null count becomes:

$$P(y = 0|\mu) = \frac{1}{1 + \mu} \tag{3}$$

Let p be the probability of observing zero neurons for a projection in a single injection, as given by any of equations (1)–(3). The probability of observing one or more neurons in a projection

(i.e. a non zero count) from a single injection is $1-p$. Since each injection is independent, the probability that some neurons are observed in each of n injections is $(1-p)^n$, and the probability of observing no neurons in at least 1 of n injections is $1-(1-p)^n$. This represents the probability of observing zero neurons in the n injection experiments performed (one or more).

For the 37 projections to areas 10, V1, V2 or V4 having interpolated mean counts fewer than 10 neurons, 31 were inconsistent, i.e. their present/absent status was not identical across all repeated injections. They are detailed in table 2.2 (page 41). Here, we want to distinguish between inconsistency attributable to sampling error (e.g. due to incomplete sampling, given that not all sections were examined) and genuine biological variability in which some pathways are present in some but not all cases.

Figure 17 shows the probability of observing zero neurons (i.e. failing to detect a connection that exists, namely a false negative) as a function of the mean (expected) number of labelled neurons, μ, after a single tracer injection for Poisson, negative binomial, and geometric distributions. These probabilities are derived from the definitions of the three distributions as detailed in equations (1)−(3). The probability of a false-negative falls below 0.05 (grey horizontal line in fig. 17A) for means as low as 4 neurons for both the negative binomial and Poisson curves, consistent with the convergence of their variance/mean ratio at small FLNe values shown in fig. 11. The probability of observing at least one false-negative decreases as a sigmoid function of the mean, as shown in fig. 17B for 2, 3, and 5 injections (spanning the range in our data set). For an injection repeated 5 times, as in our V1 injections, the false-negative probability falls below 0.05 (grey horizontal line) for a mean of 7 neurons. The probability of observing at least one false-negative after 5 injections drops much more steeply for a negative binomial than for a geometric distribution fig. 17C.

Taking the observed mean as the best estimate of the population mean (or expected value), the probability of the observed inconsistency under the negative binomial model exceeds 0.05 for 27 of 39 projections having an observed mean fewer than 10 neurons (see the penultimate column of table 2.2, page 41). Of the 12 cases with probabilities below 0.05, 3 are consistent and had an observed mean exceeding 7 neurons. After applying the Bonferroni correction for evaluating multiple probabilities (Bretz et al., 2010), only the projections of areas 7A and DP to area 10 were inconsistent despite a statistically very low probability of being so. Genuine biological variability presumably exists in the connectivity profiles for different individuals, and it is possible that some pathways are present in some individuals and altogether absent in others. However, statistical fluctuations in the data largely accounts for the observed inconsistency of very sparse projections. These observations on inconsistency depend on the fine sampling that we employed. In simulations of sparse projections having a negative binomial distribution, coarser sampling had little effect on the expected proportion of zero counts observed, but the variability in the estimates was proportional to the square root of the sampling interval (e.g. a 1/16 sampling interval results in 4 times as much variability in the estimated occurrence of zero counts compared with a 1/1 sampling).

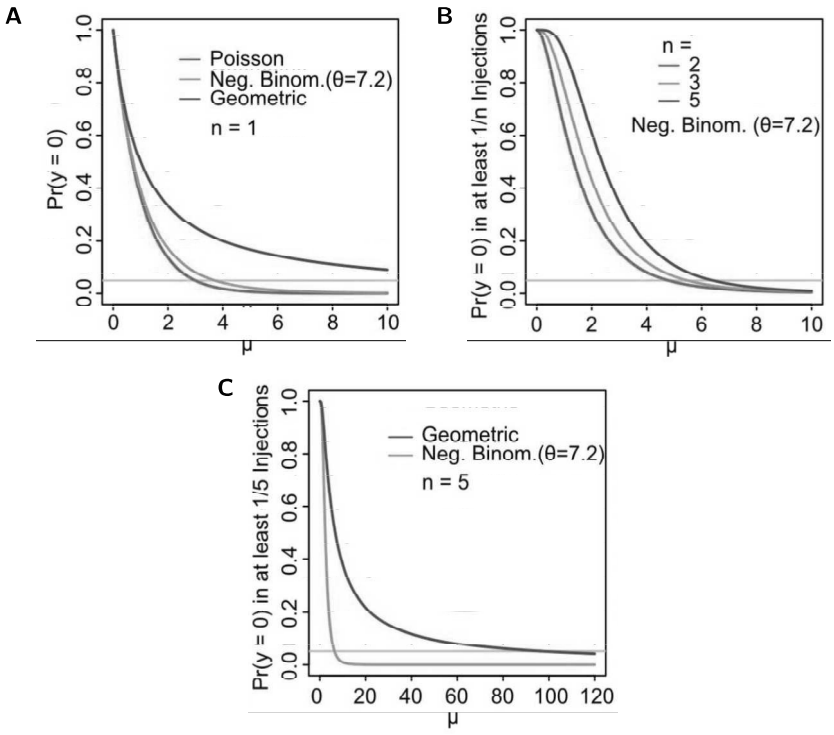

FIGURE 17: **Theoretical analysis of projection consistency.** (A) Probability of observing zero counts as a function of the true mean for Poisson (red), negative binomial (green), and geometric (blue) distributions. (B) Probability of observing at least one case of zero counts in n injections as a function of the true mean for a negative binomial distribution with dispersion parameter equal to 7.2. (C) Comparison of the probability of observing at least 1 zero count, as a function of the true mean in $n = 5$ replications for the geometric (blue) and negative binomial ($\theta = 7.2$) distributions.

Conclusion

In summary, this analysis of repeat injections provides objective constraints on what can and cannot be learned from making a single injection into any given cortical area. Specifically, a single-injection approach can 1) detect all but the most sparse projections with high probability, 2) provide a reasonable estimate of the connection weight of each pathway (generally within an order of magnitude), and 3) identify some of the sparse connections that are statistically likely to be inconsistent across multiple injections. Repeat injections enable identification of a few additional sparse projections and also provide better estimates of average connection weights. However, given the paucity of quantitative data on interareal connection weights in the macaque, the single-injection results described here have advantages in terms of the overall information gained when applied to a large number of areas. Indeed, the variability of any single projection is considerably less than the range of connectivity weights from the full complement of areas feeding into a given target area, thus permitting the connectivity profile of this area to be revealed.

TABLE 2.1: **List of cases and procedures.** LH: left hemisphere; RH: right hemisphere; planes of section: H horizontal, C coronal, Para parasagittal; M: Plots of charted neurons produced in Mercator®; P: neurons plotted on paper. For injections in V1, V2 and V4 the site is in the central representation of the visual field. The plot frequency is given within the 1 in 3 sections kept after cutting. Monkey NICO is a rhesus macaque, all the others are cynomolgus.

Case	Animal and hemisphere	Tracer	Injected area	Plane of section	Charts	Plot frequency
1	M81 LH	DY	V1	H	M	1/2
2	M85 LH	FB	V1	H	M	1/2
3	M85 RH	FB+DY	V1	H	M	1/2
4	M88 RH	FB	V1	H	M	1/2
5	M121 RH	DY	V1	C	M	1/2
6	M101 LH	DY	V2	C	M	1/2
7	M101 RH	FB	V2	C	M	1/2
8	M103 LH	DY	V2	C	M	1/2
9	M121 RH	FB	V4	C	M	1/2
10	M123 LH	DY	V4	C	M	1/2
11	M119 LH	FB	TEO	C	M	1/2
12	M106 LH	FB	9/46d	C	M	1/2
13	M106 RH	DY	F5	C	M	1/2
14	BB272 LH	DY	8m	C	M	1/2
15	BB135 LH	DY	7A	H	P/M	1/4
16	M89 LH	DY	DP	H	M	1/2
17	M89 LH	FB	area 2	C	M	1/2
18	M70 LH	FB+DY	area 5	H	P/M	1/4
19	M68 LH	DY	7B	Para	M	1/2
20	BB289 LH	FB	STPr	C	M	1/4
21	BB289 LH	DY	STPi	C	M	1/4
22	M90 RH	FB	STPc	C	M	1/4
23	M108 LH	FB	PBr	C	M	1/2
24	M128 LH	FB	TEpd	C	M	1/2
25	NICO RH	FB	24c	C	M	1/2
26	M69 LH	DY	F1	H	P/M	1/4
27	M102 LH	DY	F2	C	M	1/2
28	M102 LH	FB	F7	C	M	1/2
29	M98 LH	DY	ProM	C	M	1/2
30	BB272 RH	FB	8l	C	M	1/2
31	M116 RH	FB	9/46v	C	M	1/4
32	M116 RH	DY	46d	C	M	1/4
33	M128 LH	DY	8B	C	M	1/2
34	M131 LH	FB	area 10	C	M	1/2
35	M133 LH	DY	MT	C	M	1/2
36	M136 LH	DY	7m	C	M	1/2
37	M136 LH	FsB	area 10	C	M	1/2
38	M137 LH	FsB	area 10	C	M	1/2
39	BB341 LH	FB	area 10	C	M	1/2

TABLE 2.2: **Probability of occurrence of weak projections in repeated injections.**

Pathway	Observed mean	Occurrences of pathway	Number of inj. (n)	θ	$P(y=0)$ in all n inj.	$P(y=0)$ in ≥ 1 inj.	$P(y>0)$ in all n inj.
7A → 10	33.25	3	4	5.0	0.000	0.000	1.000
DP → 10	22.25	3	4	5.0	0.000	0.001	0.999
8r → V4	9.50	1	2	7.1	0.000	0.005	0.995
Ins → V4	8.50	2	2	7.1	0.000	0.007	0.993
V6A → V2	7.67	3	3	9.7	0.000	0.011	0.989
LB → V1	7.60	4	5	6.6	0.000	0.031	0.969
Ento → V4	7.50	2	2	7.1	0.000	0.012	0.988
9/46v → 10	6.75	3	4	5.0	0.000	0.055	0.945
8m → V2	6.67	2	3	9.7	0.000	0.019	0.981
Core → V1	6.60	2	5	6.6	0.000	0.050	0.950
44 → 10	6.50	3	4	5.0	0.000	0.061	0.939
MB → V1	5.60	3	5	6.6	0.000	0.084	0.916
PIP → 10	4.00	1	4	5.0	0.000	0.195	0.805
45B → V4	4.00	2	2	7.1	0.002	0.082	0.918
F5 → 10	3.50	2	4	5.0	0.000	0.253	0.747
TEp/v → 10	3.50	4	4	5.0	0.000	0.253	0.747
TEa/mp → 10	3.25	2	4	5.0	0.000	0.289	0.711
TEad → 10	3	2	4	5.0	0.000	0.330	0.670
STPr → V1	2.80	3	5	6.6	0.000	0.399	0.601
TEpd → 10	2.50	3	4	5.0	0.000	0.432	0.568
7op → V1	2.40	1	5	6.6	0.00	0.499	0.501
MB → V2	2.33	3	3	9.7	0.002	0.327	0.673
V2 → 10	2.00	2	4	5.0	0.001	0.561	0.439
7op → 10	2.00	1	4	5.0	0.001	0.561	0.439
F4 → 10	1.75	3	4	5.0	0.002	0.636	0.364
STPr → V2	1.67	1	3	9.7	0.010	0.516	0.484
9/46v → V4	1.50	1	2	7.1	0.066	0.447	0.553
MST → 10	1.50	1	4	5.0	0.005	0.715	0.285
LIP → 10	1.25	3	4	5.0	0.012	0.796	0.204
V6 → V2	1.00	1	3	9.7	0.058	0.769	0.231
LB → V4	1.00	1	2	7.1	0.154	0.631	0.369
TPt → V1	0.80	1	5	6.6	0.023	0.958	0.042
9/46d → V4	0.50	1	2	7.1	0.380	0.853	0.147
MIP → 10	0.50	1	4	5.0	0.149	0.979	0.021
F1 → 10	0.50	1	4	5.0	0.149	0.979	0.021
F3 → 10	0.50	1	4	5.0	0.149	0.979	0.021
PBc → V2	0.33	1	3	9.7	0.374	0.978	0.022
TPt → V2	0.33	1	3	9.7	0.374	0.978	0.022
8r → V1	0.20	1	5	6.6	0.373	1.000	0.000

Chapter 3

Organisational principles of cortical connectivity

Non quæras quis hoc dixerit: sed quid dicatur attende.

Thomas à Kempis, *De imitatione christi*

Introduction

The primate cortex is one of the largest complex networks in existence, yet it has only recently been receiving appropriate attention from a graph theoretical angle (Sporns, 2011). Many earlier studies were based on incomplete data and are primarily descriptive characterisations using various graph theoretical measures, generating qualitative inferences concerning brain function. The present study is based on consistent and coherent brain-wide tracing data at the interareal level, aiming to provide a generative model with predictive capacity.

As reported in the previous chapter, with a single DY or FsB injection it is possible to reveal the connectivity profile of a cortical area, that is, the identity of other cortical or subcortical structures projecting to it, and the weight of these projections within one order of magnitude among 6. We are confident that a pathway found with this method will be consistent across animals even if they are very sparse. However, it is still possible that a pathway not found with a single injection could in fact be present in that animal with a very low number of neurons (< 7) but have escaped detection because of statistical fluctuations inherent to even our high resolution sampling method. Such a detailed dataset necessitated a huge experimental effort (around 70 man-years of work) but in turn revealed the principles governing cortical connectivity, which are the subject of this chapter. Namely, i) the cortical network is very dense if one looks at the presence or absence of connections, but the weights of its connections give each area its specificity much more than the identities of the areas connected to it, ii) the cortical network is made of a subset of high-bandwidth information highways in a sea of weak projections, with most of the neurons being allocated to local processing and iii) these weights are governed by the distance axons have to cover to connect two areas and show an exponential decrease with this distance. Together, these weight- and distance-related features describe the structural organisation of the cortex, so much so that a random network built under these constraints closely resembles the experimental cortical interaeal network.

1 Highly local processing in the brain

Individual injections made into 25 cortical areas in addition to multiple injections in areas V1, V2, V4, and 10 provided extensive new information of several different types. This includes the identification of many previously unreported pathways, the demonstration of the lognormal distribution of FLNe and the high cortical investment in local processing.

1.1 FLN values: local, long distance and subcortical

The number of labelled neurons in a given source structure (cortical area or subcortical nuclei) relative to the total number of labelled neurons in the brain for that injection, including intrinsic neurons that are in the injected area itself, defines the FLN (FLNt) of that structure (see fig. 1 in chapter 2 and Falchier et al. 2002). The extrinsic FLN (FLNe) equals the strength of connections with the intrinsic neurons excluded.

(a) Intrinsic connectivity

FLNt (based on all labelled neurons in the brain included those in the injected area) was determined in a selected number of injected areas: V1, V2, V4, 8 (grouping areas 8r, 8l and 8m), 9/46d, F5, TEO, and 7A. The mean FLNt value of the intrinsic (within-area) connectivity was 79% (68-89%) (fig. 1A). Because the uptake zone of these tracers is defined and restricted (see chapter 2), it is possible to determine the number and spatial location of labelled intrinsic neurons. This intrinsic connectivity is highly local. With very small injections, we could accurately measure the local spatial distribution, which revealed an exponential decrease in the density of labelled neurons with distance (fig. 1B), as shown in previous publications (Barone et al., 2000). The density profiles (number of labelled neurons in each section of the projection zone) were used to measure the spatial extent of intrinsic labelling in the large injections that are required for optimal labelling of the full complements of inputs and their FLN values. This showed that 80% of intrinsic neurons arise within a distance of 1.2 mm from the injection site and 95% within 1.9 mm (fig. 1C).

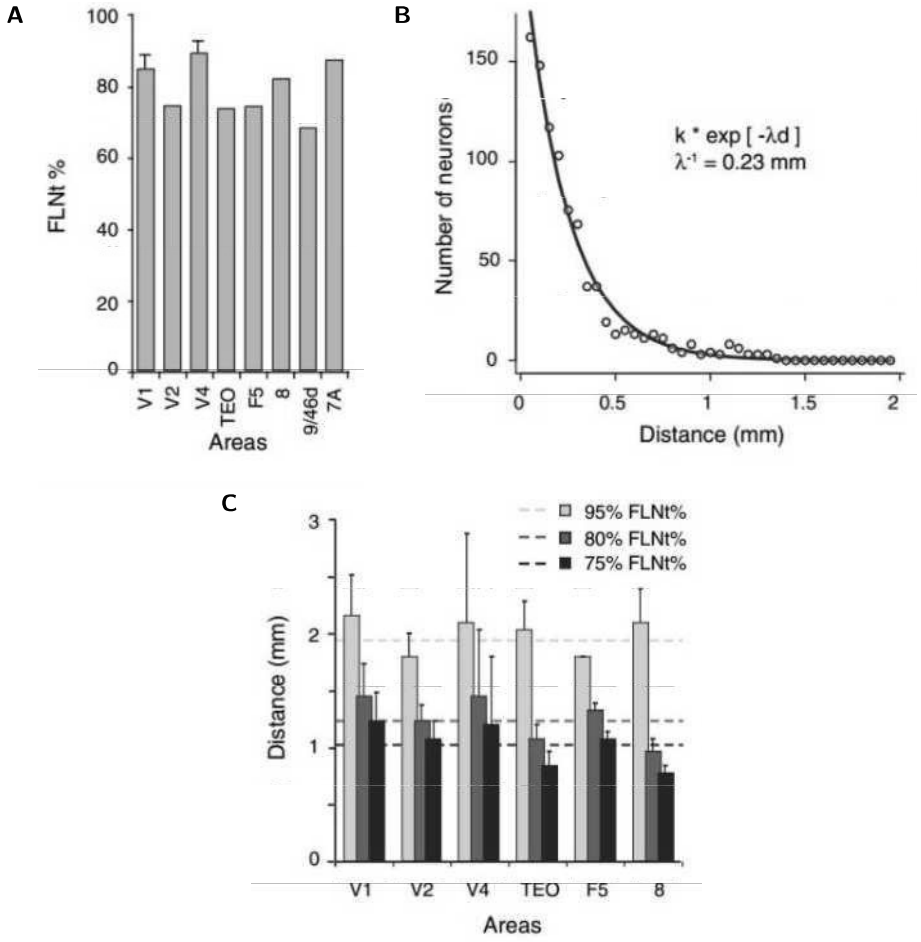

FIGURE 1: **Intrinsic and extrinsic connectivity.** (**A**) Intrinsic FLNt values of 9 areas. V1 and V4 are averages for repeated injections. (**B**) Exponential decay of density of intrinsic neurons with distance following injection in area V1. (**C**) Distances within which the 3 thresholds (75%, 80%, and 95%) of intrinsic FLNt are attained in 7 injected areas. Dashed lines indicate mean distance at which each threshold is reached. Error bars are SD.

(b) Global contributions to the input

Figure 2 compares FLNt values for intrinsic, interareal (short and long distance), and subcortical connections, averaged after injections in the same 8 areas from the occipital, parietal, temporal and frontal lobes. After the FLNt value of the intrinsic connections, the next largest contribution is from the adjoining cortical areas (i.e., areas that share a border with the injected target area and labelled "short" in fig. 2), with FLNt values on the order of 16% (2.5-39%). When only the interareal projecting neurons are considered, the neighbouring area has an average FLNe of 80%. The remaining connectivity is shared between long-range corticocortical connections (i.e. all the remaining cortical areas beyond the nearest neighbours) with a cumulative FLNt value of 5% (0.8-11%) and subcortical connections with a cumulative FLNt value of 1.1% (0.4-2.8%) (fig. 2). This pattern of high local connectivity coupled with very small sub-cortical input and weak long distance connectivity is consistent across the cortex.

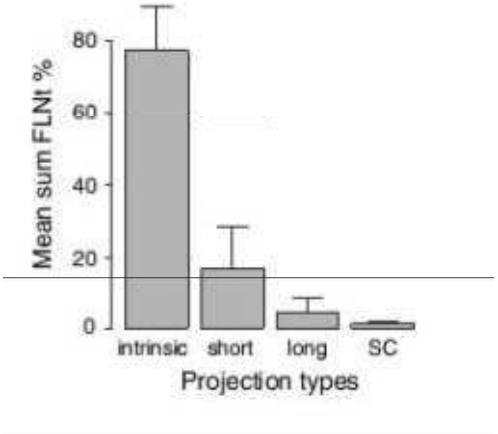

FIGURE 2: **FLNt values of the different sources.** Mean cumulated FLNt of 4 projection classes for injections to 9 exemplar areas from different lobes (V1, V2, V4, TEO, F5, 9/46d, 8l, 8r and 8m). Intrinsic: intra-areal; short: projection from immediate neighbours; long: all the remaining corticocortical projections to the target area; SC: subcortical projections. Error bars indicate the SD.

(c) Local processing in the brain

The small FLNt of the thalamic input to the cortex (fig. 2) coupled with the high FLNt values of intrinsic connectivity (fig. 1A) fits with the evidence that local recurrent excitatory networks amplify a numerically sparse feedforward signal (Douglas et al., 1995). For instance, we find that the FLNt of the lateral geniculate nucleus projection onto area V1 is 0.16% (FLNe 1.45%, see fig. 15B in previous chapter). This result is consistent with the fact that fewer than 2% of all synapses found in area V1 arise from the lateral geniculate nucleus (Latawiec et al., 2000). The intrinsic FLNt of area V1 that we observe is 85%, consistent with the vast majority of synapses in area V1 originating from local neurons (Binzegger et al., 2004, 2007). The similarly low subcortical FLNt values to various cortical areas indicate that this pattern is repeated across the cortex and reveal the high investment of the cortex in local processing. The massive allocation of the neuronal resources of the cortex to local processing and its ongoing patterned activity likewise accounts for much of the brain's energy consumption (Kenet et al., 2003; Raichle &

Mintun, 2006; Tsodyks et al., 1999). This view of the cortex emphasises the importance of intrinsic operations, so that the input to a given level of the cortical hierarchy interacts with ongoing activity.

In the connectivity matrix for area 17 of the cat, the vast majority of excitatory synapses in area 17 originate from local neurons, consistent with the intrinsic FLNt of 85% reported here (Binzegger et al., 2004, 2007). Reports from the same laboratory suggest that the synaptic input to a cortical area from a distant area is comparable numerically with the thalamic input (Anderson & Martin, 2002; Anderson et al., 1998). These results are compatible with our findings that many different sources converge on area 17 with FLN values equal or inferior to that of the LGN (fig. 15 in previous chapter). This is very relevant to experimental (Bruno & Sakmann, 2006; Gil et al., 1999; Stratford et al., 1996) and theoretical (Wang et al., 2010) analyses of how weak cortical inputs can be operationally robust and reliable. Mechanisms that ensure the reliability of the thalamic input to the cortex including synchronisation of inputs may also contribute to effective transmission between cortical areas (Tiesinga et al., 2008; Wang et al., 2010).

1.2 Interareal pathways

(a) Lognormal distribution of input weights

Next, we looked at the connectivity profiles, i.e. the distribution of projections from outside the injected area (FLNe values). Interestingly, even without the 80% of labelled neurons that are intrinsic, the full range of FLNe values still spans more than 5 orders of magnitude, and the primary source of connectivity (areas that share a border with the injected area) still make up for 80% of the total. Therefore, using logarithmic coordinates was key for visualising this distribution.

Figure 3 show the ordered average experimental values and their empirical standard deviations indicated as error bars for both cortical and subcortical projections to areas V1, V2, and V4. The black curves are the predictions for an ordered sample from a lognormal distribution with the same number of points as the data points in each area and the same mean and SD as the data. These curves fit the data reasonably well and the points and standard deviations fall within the estimated 95% confidence interval for the lognormal distribution, indicated by the grey bands around each curve.

For all 29 areas, we found that the ordered FLNe was well described by a lognormal distribution. Figure 4 show a further selection of 5 areas, chosen to illustrate a greater than 3-fold range in number of incoming projections to the target area (the remaining 21 connectivity profiles are shown in the supplementary online material of Markov et al. (2014a). Importantly, the curves in each plot are based only on the mean and SDs of the $log(FLNe)$ values and the number of projections; no free parameters were used to constrain the shape of the curves. This consistency in the weight distribution indicates a strong regularity in the cortex, because although these curves are necessarily monotonically decreasing by the way they were constructed, there is no a priori reason why the distribution must be well fit by a lognormal distribution.

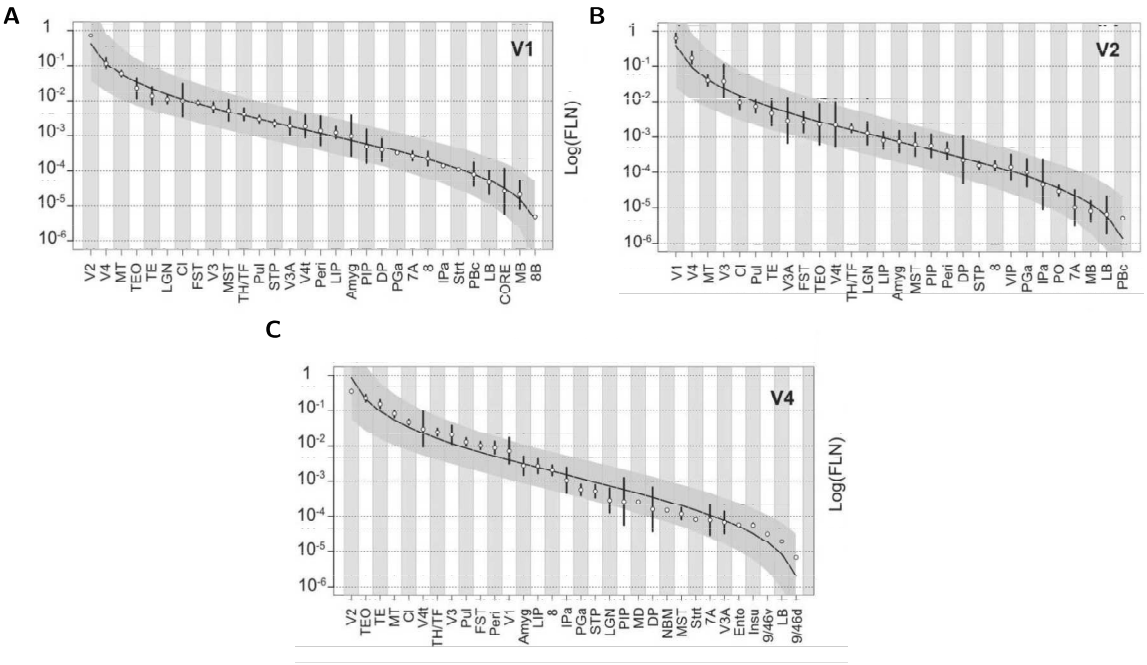

FIGURE 3: **Connectivity profiles of visual areas** Source areas are ordered by $log(FLNe)$ values. The solid curves correspond to the predicted order statistics for a lognormal distribution with the same mean and SD as the data. The error bars are 95% confidence intervals, assuming that the data follow a negative binomial distribution with dispersion equal to 7.

The curves shown in fig. 3 and fig. 4 illustrate common features in the connectivity profiles, including just how closely the single FLNe values track the lognormal distribution as well as the progressive widening of the 95% confidence interval with decreasing FLNe values. For each area, the midpoint of the distribution occurs at an FLNe of about 10^{-3}, with half the projections being stronger and half being weaker. A few areas on the upwardly curved portion on the far left represent notably strong pathways ($FLNe \gtrsim 10^{-2}$); a few on the downwardly curve portion on the far right represent notably weak pathways ($FLNe \lesssim 10^{-4}$). The majority of pathways are in the middle range ($10^{-2} > FLNe > 10^{-4}$).

(b) Possible origin of the lognormal profile

One source of lognormal distributions is via the product of independent random variables (Newman, 2005). A simple hypothesis could suppose, for example, that the distribution of weights to a given area arises from a common developmental process of neural growth in which the probability of an axon growing a given distance before making a synapse is the product of randomly varying probabilities that it will stop and make a synapse at any area along its path. This common profile of weights is likely to be the substrate for a common mechanism of information distribution or neural computation by a cortical area. Such a mechanism would suggest a very specific layout of cortical areas and could require some sort of optimisation in the location of cortical areas in the 3D structure of the brain (Cherniak et al., 2004; Kaiser & Hilgetag, 2006). Interestingly, random outgrowth models have been proposed for the formation of local connectivity, which if modified to take on board the weight distributions could be extended to concepts of interareal formation (Kaiser et al., 2009).

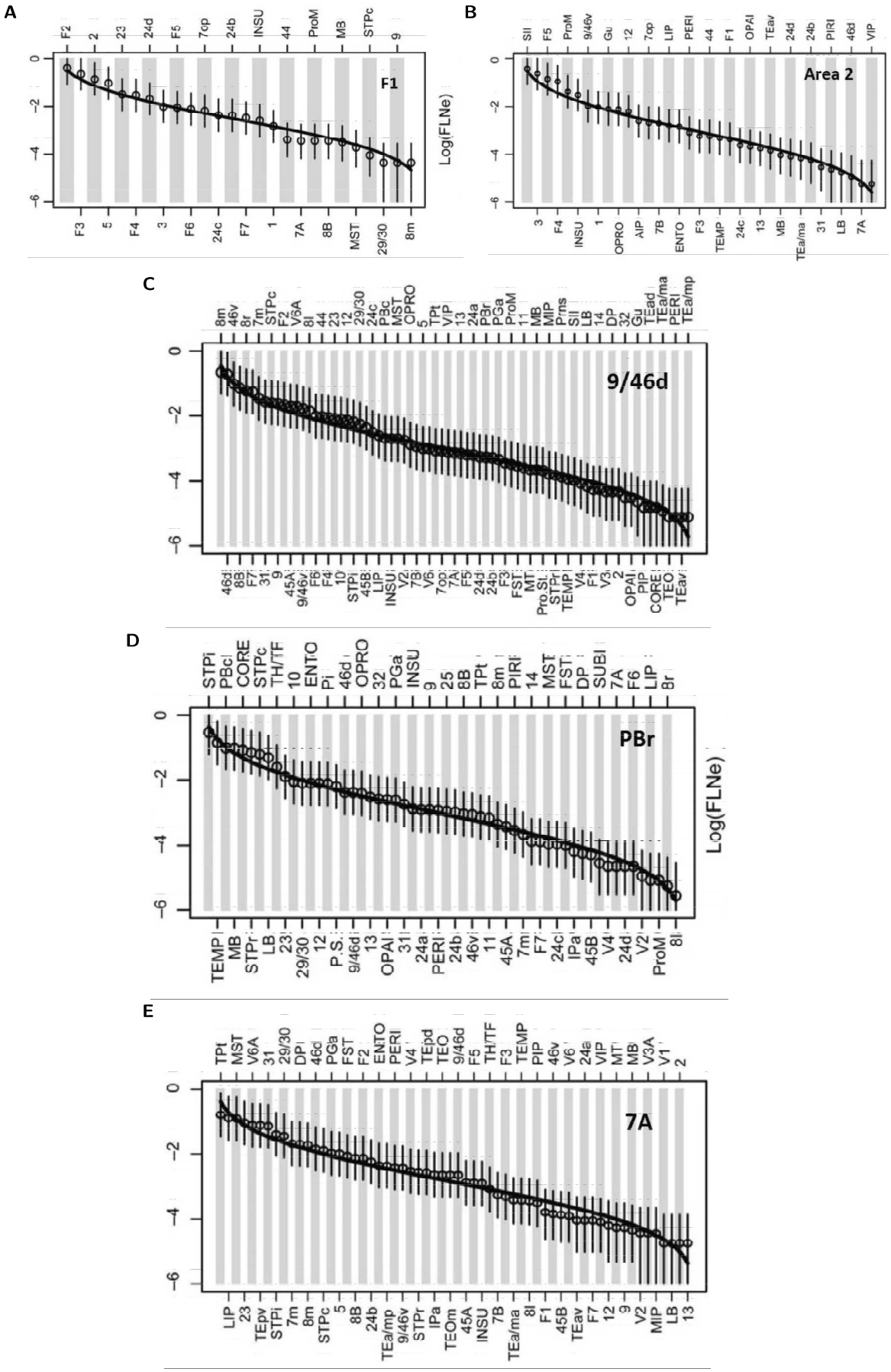

FIGURE 4: **Lognormal connectivity profiles.** Connectivity profiles for 5 injected areas, chosen to illustrate a greater than 3-fold range in number of connections. Conventions as in fig. 3.

(c) Lognormal distributions at different scales

The lognormal distribution of FLNe values that we observe is a heavy-tailed and heterogeneous distribution that is different from a power law. Lognormal distributions have been reported for a number of biological phenomena, including the nonzero synaptic strengths on single cortical neurons (Song et al., 2005). An interesting parallel can be drawn between interareal (long-range) and intrinsic (local) properties: 1) as we have shown here, local, intrinsic connectivity shows an exponential decay in density, echoing the decrease in the likelihood of synaptic contact with distance (Braitenberg & Schüz, 2012); 2) intrinsic source distributions, just like the extrinsic interareal source distributions, have a patchy character (Yoshioka et al., 1992); 3) lognormal distributions like the one described here for interareal weights have been found for the distribution of synaptic strengths of single neurons (Song et al., 2005). These parallels, at both the cellular and areal levels, suggest that similar logical principles might function over multiple scales.

1.3 Role of weak interareal projections

Interareal connections from neighbouring areas may provide inputs that interact with recurrent local connectivity very much in the same way as the feedforward inputs from the thalamus to cortex as described above. However, long-range interareal pathways have FLNe values up to 4 orders of magnitude weaker than the FLNe of the LGN. These weak corticocortical connections might contribute to long-range coordination of neuronal assemblies, possibly required for high-level representations (Buzsaki & Draguhn, 2004). Interaction of ascending activity with ongoing activity of dense local networks may contribute to multiple brain rhythms, which are in some way controlled by the long-range very sparse connections (Buzsaki, 2007; Kopell et al., 2000; Lakatos et al., 2008; Uhlhaas et al., 2009; von Stein et al., 2000). Importantly, these long-range connections are not randomly organised but instead, as shown here, link specific sets of areas with precisely determined connection weights, having weights that are typically consistent within a range of $5-8$, although some of the weakest projections have a variability exceeding 10-fold (see fig. 15 in chapter 2). The function of the long-range cortical connections may complement nonspecific corticothalamic loops (Llinas et al., 1998). In this respect, corticoclaustral loops may also be important (Crick & Koch, 2005), as an intriguing finding in the present study is that the claustrum provides the strongest subcortical input to the cortex.

2 Network density and connection weights

2.1 A dense interareal network

(a) New cortical pathways

Injections in all 29 target areas revealed a total of 1,615 cortical pathways. Of these, 579 have not been previously described (newly found projections or NFP). Each target area received projections from between 26 to 87 source areas. The evidence for the existence of the known connections is generally relatively good with most projections reported in several studies, but in

some case their existence can only be inferred from suggestive and not compelling evidence. For the target areas in each cortical region, the NFP constituted a substantial fraction of the total number of connections (limbic 13%, prefrontal 40%, frontal 30%, parietal 30%, temporal 43%, and occipital 37%). Figure 5 shows a histogram of connection weights for known projections (white bars) and NFP (red bars) in intervals of 0.5 $log(FLNe)$. Known connections are on average stronger than NFP, but the two populations overlap extensively. Remarkably, 43% of the NFP had FLNe of moderate strength, and a few (2%) are classified as strong connections. For very low FLNe values, NFP correspond up to 90% of the population, but constitute a decreasing fraction of the source areas with increasing FLNe.

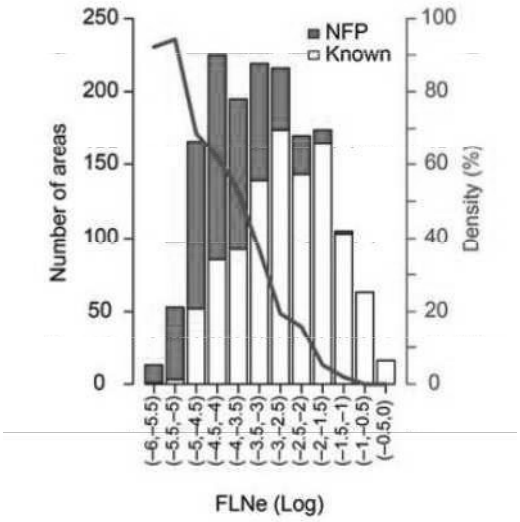

FIGURE 5: **Weight comparisons for known projections and NFP.** Distribution of known projections and NFP as a function of projection magnitude (FLNe) at intervals of half a log unit, following the injection of the 29 target areas. Blue line indicates the percentage of NFP within each interval.

In the present study, we also report some very weak connections containing a few dozens neurons or less. For a few projections we report just 1 or 2 neurons, which are found in only 1 or 2 cases. However, the numbers of neurons reported reflect only a small fraction of the total number of neurons associated with an area-to-area pathway. If the entire target area were filled with tracer, the numbers of labelled neurons would be many orders of magnitude greater than the numbers reported here.

(b) Connectivity matrix

A convenient way to encode and manipulate network information is the connectivity matrix, where rows and columns represent areas (nodes of the graph) and each cell contains connectivity data between the area of its row and the area of its column (edges of the graph, i.e. pathways linking nodes). The pathways of the cortical graph are directed because information only flows one way along axons, and retrograde tract tracing reveals incoming projections to a given area. Thus the matrix is asymmetric, in contrast to many connectivity matrices obtained using neuroimaging methods that cannot distinguish the directionality of connections. The connectivity matrix revealed by our tract tracing experiments has 29 columns for the 29 injected areas and

91 rows because our cortical parcellation contains 91 areas, i.e. 91 potential sources of pathways to the injected area.

Figure 6A shows this 29 by 91 weighted connectivity matrix where the colour of each entry represents the $log(FLNe)$ value for that pathway (brighter shades representing stronger connection weights; black represents no connection). Each column gives the FLNe profile of inputs observed for a given area and each row its outputs. The rows and columns of this matrix were clustered on the basis of similarity of connectivity profile, i.e. similar columns and rows were close. The dissimilarity between 2 rows (columns) was defined as the reciprocal of the dot product between them (Jouve et al., 1998). This measure is like a distance: the more similar the weights for two areas, the smaller it is. If the areas shared no common inputs (outputs) this distance would be infinity, but we observed no areas for which this situation arose. We then used a non-metric, multidimensional scaling (MDS) algorithm (de Leeuw & Mair, 2009) on the row (column) distances, ordering them by the first component. Visual areas are concentrated in the upper left quadrant of the matrix. Motor and somatosensory areas are concentrated in the lower right quadrant. Higher-level areas of the frontal, parietal, and temporal cortex are mainly in the middle portion. Green squares indicate the "identity" entry for the same area in a row and column. These entries are mostly located near the diagonal, suggesting that areas having a similar pattern of inputs also have a similar pattern of outputs. However, the many deviations from the diagonal suggest that some areas having similar input profiles have distinctly different output profiles, and vice versa.

(c) Estimation of cortical density

Existing databases do not provide reliable estimates of the density of the network of cortical areas, nor has there been a concerted effort to extrapolate from the existing data to the connectivity of the full interareal network (FIN). Here, we explore the classical, binary notion of graph density, i.e. the present/absent status of connections, independently of their strength (Janson et al., 2011; Newman, 2010). Graph density is a fundamental measure of the graph's overall connectedness, extensively used in network science and also in earlier analyses of cortical connectivity (Bullmore & Sporns, 2009; Sporns & Zwi, 2004).

Based on the M132 atlas parcellation (fig. 2 of chapter 2), the FIN contains $N_{FIN} = 91$ cortical areas that represent the nodes of the complete $G_{91\times91}$ graph. The directed edges of the FIN correspond to directed connections between nodes, based on the FLN. Our analysis of the FIN makes use of the $G_{29\times91}$ directed subgraph of projections within FIN, which reveals all the in-degrees (number of incoming pathways) of the 29 injected nodes. It also makes use of the $G_{29\times29}$ edge-complete subgraph of FIN, corresponding to the connections among just the 29 injected areas (fig. 6B). Both $G_{29\times91}$ and $G_{29\times29}$ contain complete information about the status of their edges and would not be influenced by injections into additional areas elsewhere in the cortex. Given that the 29 injected areas are widely distributed among the 6 lobes, the $G_{29\times29}$ subgraph is likely to reflect major characteristics of the FIN.

The density of a directed graph is given by the ratio $\rho = M/(N(N-1))$ between the number of directed edges (connections) M of the graph and the total number of possible edges, $N(N-1)$, where N is the number of nodes in the graph. The $G_{29\times29}$ graph has $M = 536$ (binary) directed

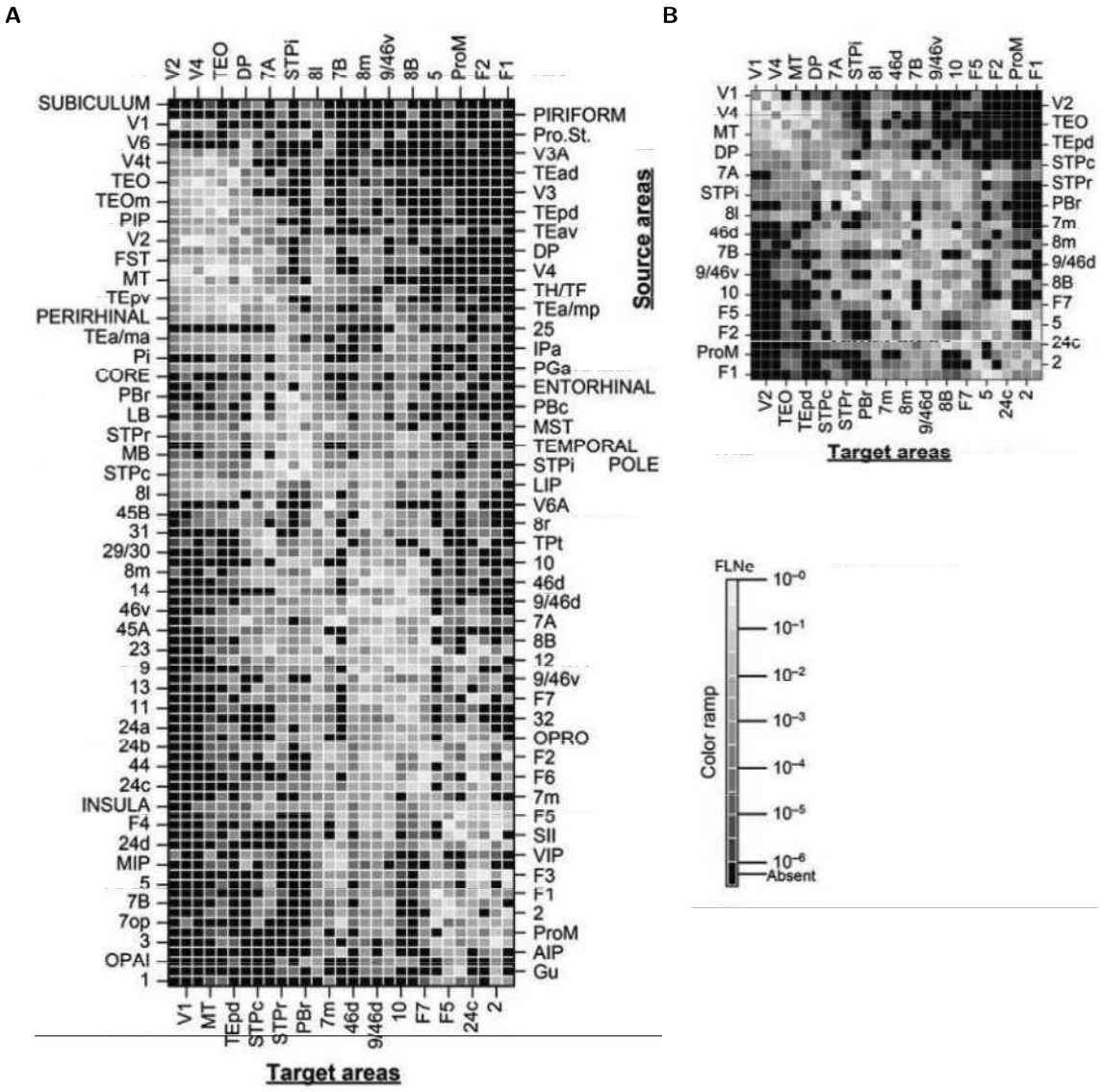

FIGURE 6: **Weighted connectivity matrix.** Each row represents 1 of the 91 source areas; each column represents 1 of the 29 injected target areas. The colour shows the strength of the projection as indicated by the colour bar. Black cells correspond to absent connections and green cells to the intrinsic projections that are not included here. For multiple injections, shading is based on geometric mean values. **(A)** The row and column ordering was determined by clustering based on similarity of the input and output profiles between areas. **(B)** Complete weighted connectivity matrix for the $G_{29\times29}$ subgraph.

links from the maximum possible of $N(N-1) = 812$, and therefore, it is strongly interconnected, with a graph density of $\rho = 0.66$ (66%). Because it is an edge-complete subgraph of the FIN, the density of $G_{29\times29}$ is expected to be comparable to that of the FIN.

The in-degrees of the $G_{29\times91}$ graph (i.e. the number of source areas projecting to each of 29 target areas, fig. 7) range from 26 to 87 with a mean of $\langle k\rangle_{in} = 55.4$; their distribution (shown as a marginal histogram in gray) is concentrated around the mean. The density of the FIN was estimated as follows. Because every directed edge is an in-link to some node, the total number of edges M_{FIN} equals the total number of in-links in the FIN. We lack data on the in-links to nodes that were not injected, but we can assume that they are characterised by the same average

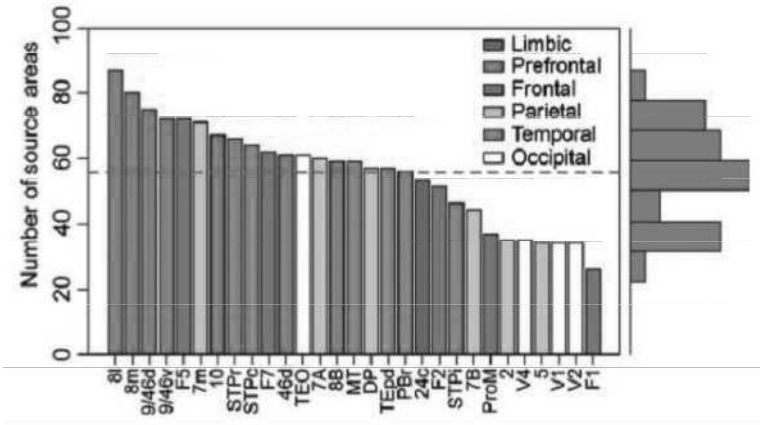

FIGURE 7: **In-degree distribution.** The number of areas projecting to each of the target areas of this study. Horizontal dashed line indicates the mean in-degree (57.4).

in-degree as the 29 injected nodes. Assuming $M_{FIN} \approx \langle k \rangle_{in}$, $N_{FIN} = 5,071$ for the FIN (that is, $G_{91\times91}$) leads to the prediction $\rho_{FIN} = M_{FIN}/(N_{FIN}(N_{FIN}-1)) \approx \langle k \rangle_{in}/(N_{FIN}-1) \approx 0.62$ (62%), which is of the same order as the density for the edge-complete graph $G_{29\times29}$.

A dominating set analysis on $G_{29\times29}$ provides further evidence that the FIN is indeed dense. In graph theory, a subset D of nodes of a graph G with node set V is said to be dominating G if all elements of V have a link to at least one node in D (Kulli & Sigarkanti, 1991). Here, we modify this definition slightly by saying that D dominates x% of the nodes of G, if x% of all nodes in V are linked to one or more nodes in D. The x% = 100% corresponds to "full" domination. This definition includes also nodes from D. The minimum dominating set (MDS) D_{min} is defined as the one that fully dominates G and has the smallest size (number of nodes). For all sets of 2 target area combinations from the 29 target areas (406 pairs), 26.6% of them dominate 90-100% of the 91 areas. One pair of areas (8l, 7m) receives projections from all 91 areas, revealing an MDS size of 2.

A low MDS indicates either a very dense graph or a scale-free graph, which is usually dominated by hubs, areas with extremely high degree $k \gg \langle k \rangle$ (Barabasi & Albert, 1999). The actual in-degree distribution of $G_{29\times91}$ (fig. 7) is inconsistent with a scale free graph (see next section), as is the fact that slightly increasing the size of dominating sets to include 3, 4, and more nodes quickly increases their number. For triplets of areas there are 69 dominating sets (1.88% of 3,654), and for sets of 4 areas, there are 1,978 (8.33% of 23,751). Moreover, all combinations of 8 sites (out of 29, $\sim$ 4.29 million) will dominate at least 90% of all the areas. As more injections add links but not new nodes, they can only enhance these strong domination effects, confirming that the FIN is indeed a dense graph when considered in terms of binary connectivity.

2.2 The binary network does not have small-world properties

(a) History of the concept of small-world networks

Recently an alternative approach to understanding cortical pathways appeals to graph theoretic analysis of cortical networks. Since the early 1990s there has been an increasing focus on network representations of complex systems with the goal of gaining an insight into the functional processes supported by these networks (Barabasi & Albert, 1999; Newman, 2003).

Among the major discoveries coming out of this approach was the recognition that many real-world networks, on the binary connectivity level, share small-world (Watts & Strogatz, 1998) and scale-free properties (Barabasi & Albert, 1999). The description of the small-world and scale-free phenomena seemed to be particularly relevant to understanding the brain (Watts & Strogatz, 1998). Small-world networks are characterised by short path lengths between nodes and high levels of clustering, which provides maximum integration with minimum wire length. Translated into anatomical terms, nodes are areas and a small world network would imply that the average number of connections forming the shortest path between any two areas would be small, even though areas are mostly linked to a few other areas that are themselves highly interconnected, forming a densely clustered neighbourhood. Minimum wire would mean that there would be multiple interconnections within a set of neighbouring areas but only some of these areas will have extensive connections that form long-distance pathways to other tightly grouped areas, thus effectively providing the shortcuts necessary to keep average path lengths optimally short.

Small world networks were initially used for describing social networks where it has been claimed that no two individuals on the planet are more than 6 handshakes from each other. This proverbial small world exists because, although most of our friends know each other (clustering), some of them plug into other social groups (and provide the shortcuts across the graph). These features provide the integrative function typical of modern society, and it is easy to imagine that they are important in cortical function (Bassett & Bullmore, 2006).

Inspired from these early studies on small worlds, and using the compilation of Felleman & Van Essen (1991), several studies have confirmed the clustering of functionally related areas and found evidence of short average path lengths suggestive of small-world architecture (Hilgetag et al., 2000; Sporns et al., 2000).

(b) Previous estimates of the graph density

In fig. 8 we show how average shortest path length relates to graph density. At 66% (that is with all observed connections included) we have a path length of 1.34 and as connections are randomly removed, there is a progressive increase of the average path length. This allows us to compare our graph density to those of earlier studies, some of which have claimed small world architectures in cortical interareal connectivity. The Felleman & Van Essen (1991) study provided a compilation of data taken from over 300 anatomical studies. The authors cautiously questioned their network and found it to have a density of 30%. They distinguished three possible states: documented (existing), not found (explored but reported absent), and unknown (non explored connections). By taking into account the unknown connections they predicted that the real density of cortex

would be around 45%. Later Jouve et al. (1998) first updated the database of Felleman and Van Essen and then implemented an algorithm that uses the properties of the network to predict if there are projections within the unknown category that are very likely to exist (Jouve et al., 1998). This led to a density prediction of 50%. All subsequent studies examining the small world properties of the cortex have used the database of Felleman and Van Essen. However, these studies firstly considered that unknown connections were non-existing and secondly, they increased the number of areas by referring to publicly available databases where the unknown category is actually higher than that in the Felleman and Van Essen database. This automatically increased the sparseness of their graphs (15-20%) (Modha & Singh, 2010; Sporns et al., 2007, 2000; Young, 1993).

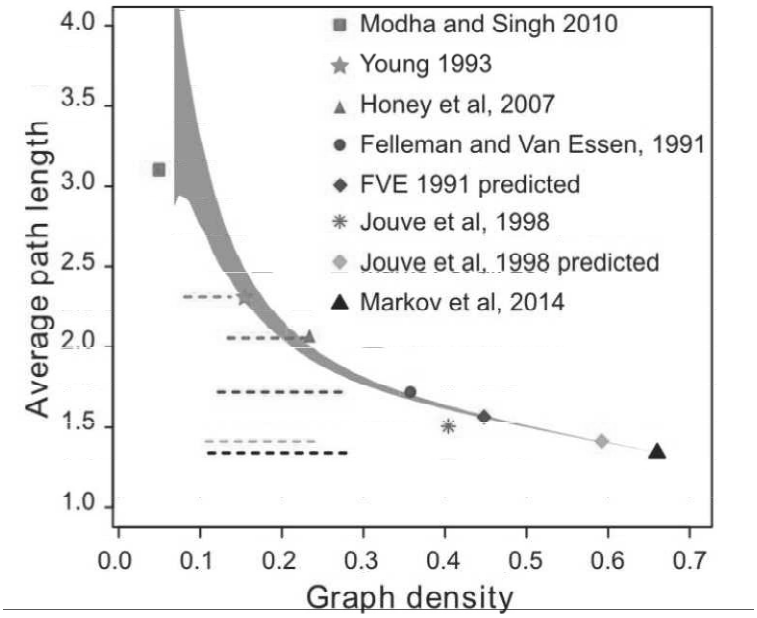

FIGURE 8: **Previous estimates of graph density.** Comparison of the average shortest path length and density of the $G_{29\times29}$ subgraph with the graphs of previous studies. Sequential removal of weak connections causes an increase in the characteristic path-length. Black triangle: $G_{29\times29}$; gray area: 95% confidence interval following random removal of connections from $G_{29\times29}$. Dotted horizontal lines indicate the 5 to 95% interval with at least one unreachable node (after repeated and graded, random edge removal). The three least dense graphs are near their 5% unreachability levels. Data incompleteness meant that some of the initial networks have unreachable nodes (the latter are removed and not considered here); 14 unreachable nodes are from Modha & Singh (2010); 1 unreachable node is from Young (1993); and 2 unreachable nodes are from Felleman & Van Essen (1991). The other references are Honey et al. (2007); Jouve et al. (1998). "Jouve et al., 1998 predicted" indicates values of the graph inferred using their published algorithm.

These earlier works claim that the interareal network is sparse, exhibits short path lengths and high clustering, and that these properties form an organisation principle of information integration in the cortex (Bassett & Bullmore, 2006; Bullmore & Sporns, 2012; Honey et al., 2007; Modha & Singh, 2010). However, in fig. 8 all the graphs this claim is based on are near or within the 95% confidence interval of progressive removal of random connections in the graph (grey trace), thus indicating that they are edge-incomplete subgraphs of our dataset. Moreover, these graphs are near unreachability, meaning that removing only a few random edges will

isolate one or more areas: they cannot be reached because not all other areas have a directed (even multi-step) path to them any more. Two of these datasets even have unreachable nodes without removing any links. In our edge-complete subgraph this is very far from being the case, and we hypothesise that this a strong property of the FIN: on the contrary, the network is highly parallel and redundant (Felleman & Van Essen, 1991). Therefore we estimate that these datasets, because of their edge-incompleteness, do not reflect the properties of the FIN as the edge-complete $G_{29\times29}$ does.

(c) The cortical graph is not a SW

The novel anatomical connectivity data, including the strengths of connections and spatial information suggest a revision of the cortical network given by previous studies. In particular, at such a high density as we have discovered, the binary features of the cortex like small world properties (average directed path length = 1.34 and diameter = 2) and hubs are not significant and provide little functional insight. Neither can the network be described as scale-free in terms of its binary connectivity, given its small number of nodes and its non-power-law degree distribution.

Small world properties were described for real world sparse graphs (typically with a density $< 0.01\%$), because at these densities it is unlikely that a random graph, obtained by rewiring existing connections, would exhibit both local high density of projections (clustering) and a short path to any other node in the graph (short average path length). A highly dense graph on the contrary, where a large part of possible connections do exist, has both these properties but cannot be rewired in a manner not to express short average path length and high clustering. In the extreme case where every node is connected to every other (density 100%), the average path length is 1 and a there is single large cluster, but there is no other possible binary wiring. In other words, short path lengths and clustering can be identified at various densities but for a dense graph they are uninformative about any architectural specificity. That is why small world properties only become interesting when the number of nodes is large and the number of links is small.

We suggest that instead of looking for hubs or Small World properties, the range of weights of connection and distance must be examined. Doing so reveals a strong regularity of the cortex, where each area has strong connections with its neighbours, and where weights of connections fall off exponentially with distance to give place to weak, mid to long distance projections. These latter connections greatly contribute to linking areas standing on very distant levels of the cortical hierarchy and yet appear to make only a poor contribution to the global efficiency of the cortex. We see a dichotomy between the circuit of few very strong connections and the myriad of weak links that do not provide channels broad enough to transfer detailed, extensive fine grain information.

A simple way to illustrate the role of connection weights is to plot the graph either using a binary or weighted, adjacency matrix. When weights are not taken in to account the algorithm converges to a layout where there is no biologically relevant node clustering. Remarkably when the weighted matrix is provided to the algorithm it converges to groupings that strongly reflect the functional lobes and suggest their functional interactions (fig. 10).

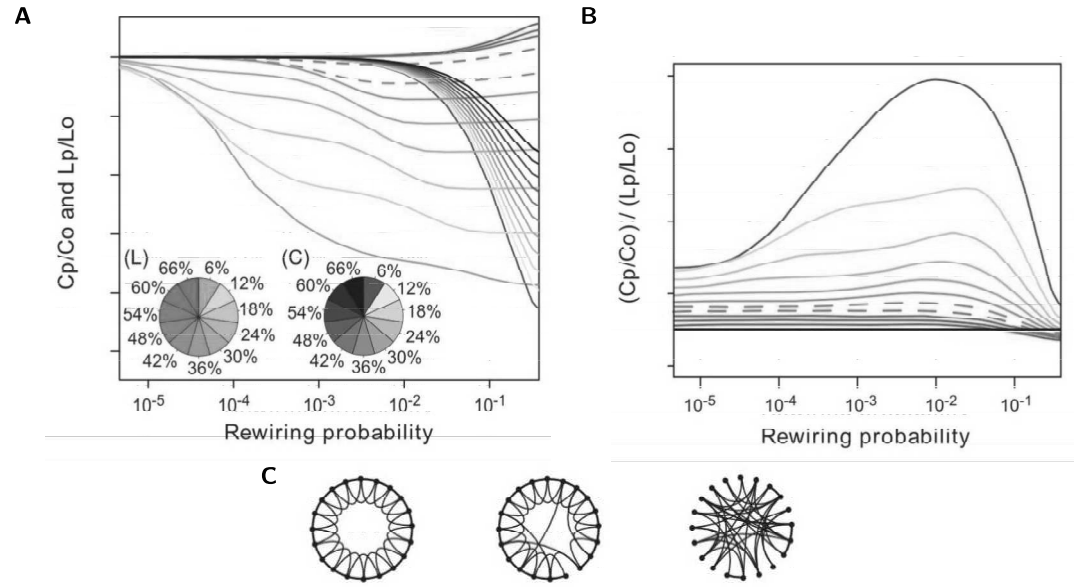

FIGURE 9: **Effect of density on Watts and Strogatz's formalisation of the small world.** (A) Clustering and average path-length variations generated by edge rewiring with probability range indicated on the x axis applied to regular lattices of 1,000 nodes in a 1D ring as in Watts & Strogatz (1998), of increasingly higher densities. The pie charts show path length L and clustering C colour-coded for graph density. On the y axis, we indicate the average path length ratio L_p/L_o and clustering ratio C_p/C_o of the randomly rewired network, where L_o and C_o are the path length and clustering of the regular lattice, respectively. L_p and C_p are the same quantities measured for the network rewired with probability p. Hence, for each density value indicated in the L and C pie charts, the corresponding L_p/L_o and C_p/C_o curves can be identified. **(B)** The small-world coefficient $(C_p/C_o)/(L_p/L_o)$ (Sporns & Honey, 2006) corresponding to each lattice rewiring. Colour code is the same as in (A). Dashed lines in (A) and (B) indicate 42% and 48% density levels. **(C)** Diagrams illustrating the lattice (left), sparsely rewired (middle), and randomised (right) networks.

2.3 A backbone of strong projections

(a) Weighted measures to characterise the graph

The five orders of magnitude range of connection weights mean that information capacity is expected to vary differently along the high-bandwidth, within-lobe pathways and the weak, interlobe connections. To investigate how differences in connection strength shape the functional structure of the cortical graph, we approach the problem from a communication efficiency point of view. The FLN f_{ij} between areas i and j can be interpreted as a measure of the capacity of information transfer between the source i and its target j. The higher f_{ij} (the stronger the projection), the higher the bandwidth of information transfer along the $i \to j$ link. Thus, to a first approximation, the probability for signals along the $i \to j$ link to induce activity in node k via the $i \to j$ link is proportional to the product $f_{ij} \times f_{jk} = \exp(\ln(f_{ij}) + \ln(f_{jk}))$. Therefore, it is more convenient to work with $w_{ij} = -\ln(f_{ij}) \geq 0$ as link weights, so that they are additive along directed paths. The w_{ij} is equivalent to link resistance, with larger w_{ij} means a weaker link or a higher resistance. For every pair of nodes (i, j), we define r_{ij} as the minimum sum of link weights (sum of w_{lk} weights taken along a path) among all paths directed from i to j . For constant weights, r_{ij} is proportional to the length (number of links) of the shortest directed path

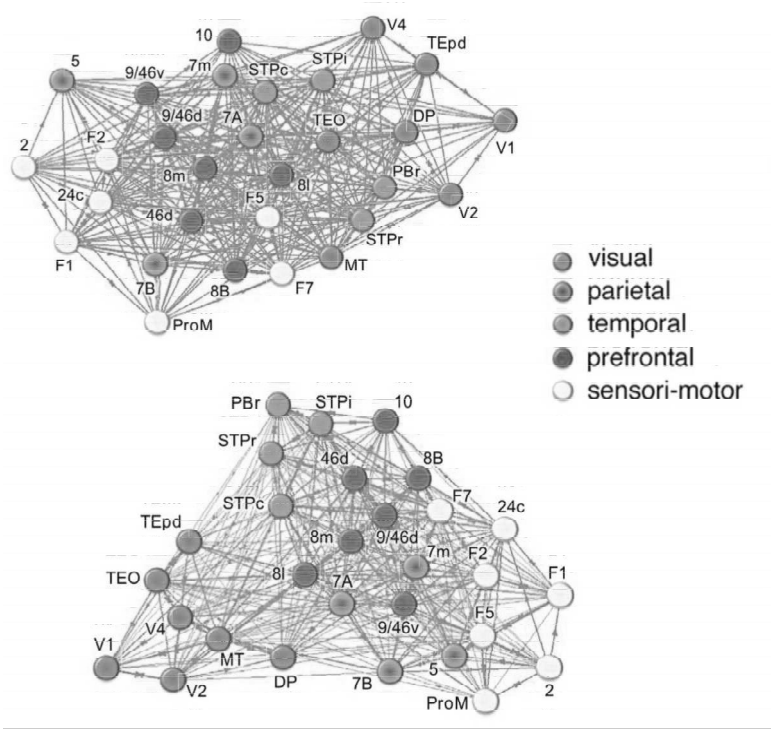

FIGURE 10: **Force-based layout of the graph.** Relative spatial placement of the areas that is optimal with respect to the weights, generated via the Kamada-Kawai (KK) force-based graph-drawing algorithm (Kamada & Kawai, 1989). **Top:** Full density (all 536 links), all weights taken as unity (binary graph). **Bottom:** Link weights given by their FLN values.

from i to j (fig. 11A). We examined two communication efficiency measures, namely a global measure E_g and a local measure E_l.

The global network communication efficiency measure E_g introduced by Latora & Marchiori (2003) is defined as:

$$E_g = \frac{1}{N(N-1)} \sum_{i \neq j} \frac{1}{r_{ij}}$$

where the summation is over all the $N(N-1)$ possible pairs (i, j) of nodes. E_g is a global conductance measure for information transfer between two arbitrary nodes, calculated as the mean of the conductance $1/r_{ij}$ over all the $N(N-1)$ possible pairs (fig. 11A).

The local network communication efficiency measure E_l introduced by Vragović et al. (2005) is defined as:

$$E_l = \frac{1}{N} \sum_{i} \frac{1}{k_i(k_i-1)} \sum_{j \neq k \in \{i\}} \frac{1}{r_{jk/i}}$$

Here a local efficiency is calculated for all pairs j, k of neighbours of node i after node i and its links are removed from the graph (obtaining $r_{jk/i}$ through the remaining graph), then this is averaged over all nodes i. The local efficiency is essentially the average conductance between all the areas connected to an area X, after removal of area X with its links (that is, through the rest of the network). It is similar to assessing how easily one can travel between the satellites of a town, without using routes passing through the town. Again, this is averaged across the entire graph (fig. 11B).

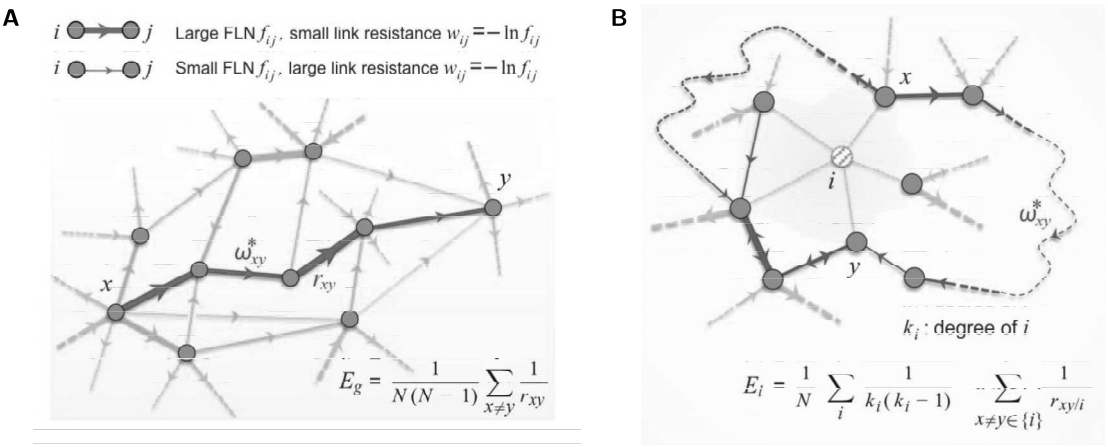

FIGURE 11: **Definition of efficiency measures.** (**A**) Link resistance and global efficiency. (**B**) Local efficiency.

(b) Few strong projections in a sea of weak ones

We explored the role of the connection weights in communication efficiency, by simulating a threshold effect via progressively deleting the weakest links (green and blue solid lines in fig. 12A). The effect on global efficiency starts to decline sharply only after 76% of links (containing 5% of total neurons) have been removed. Hence, efficiency is assured by the remaining 24% of links exhibiting the largest FLN values and accounting for 95% of neurons. These links with the highest FLN assuring global efficiency have a mean projection distance of 16 mm (SD 8.4), considerably shorter than the 27 mm mean of the removed connections. This high FLN network constitutes the global efficiency backbone of the graph, shown in fig. 12B. As more weak links are removed, regional groups of areas cluster in a connected network, forming a high-strength, high-bandwidth subgraph of the cortex. Note that given the large average path length (3.7) and the diameter of the graph (9) the efficiency backbone does not seem to correspond to a small world architecture.

Interestingly, with decaying density, global efficiency (green solid line in fig. 12A) remains virtually unchanged, while local efficiency (blue solid line) increases, peaking in the region just prior to the breakdown of the global backbone (i.e. when only the 19% strongest projections are still present in the graph).

(c) Consequences on the system's dynamics

Moreover, the differential response of the local and global efficiencies suggests interesting dynamics of the system. High activity levels in the network could raise neuron response threshold (Azouz & Gray, 2003; Braitenberg & Schüz, 2012; Destexhe & Paré, 1999), which is comparable to removing the weakest connections as we did in the data. This in turn suggests that activity dependent increases in threshold (Braitenberg & Schüz, 2012) could lead to a small decrease in global efficiency that is off-set by a large increase in local efficiencies, as has been suggested in the local microcircuit (Binzegger et al., 2004). In this way the control of assembly dynamics in the cortex will have a spatial component in large part due to the spatial and weight characteristics of the cortical network described here.

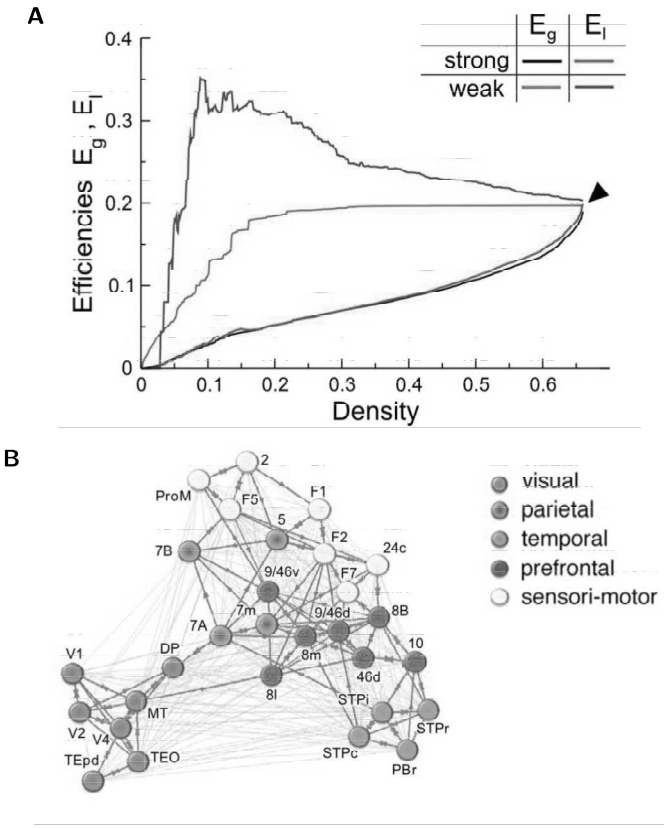

FIGURE 12: **Global and local efficiency in the graph.** (A) Effects of graph density on efficiency via sequentially deleting weak (blue, green) and strong (black, red) links. (B) Kamada-Kawai force-based layout for the backbone i.e. the 130 strongest connections (blue links, 0.16 density) left after weak link (thin gray) removal.

3 Relation between axonal distance and FLN

3.1 The exponential distance rule (EDR)

(a) Measure of distances

To measure interareal distances through the white matter we first calculated the geometric centre of each area in CARET. We then transposed them onto the reconstructed M132 surface brain (see section 1.3(b) in chapter 2) using sulcal landmarks. Except for the large visual areas V1, V2 and V4 we evaluated in CARET the shortest physical distance between geometric centres of cortical areas through the white matter. Areas V1, V2 and V4 were injected in the central representation of visual space, so for these 3 areas we measured distances to and from the injection sites (Markov et al., 2013).

(b) Definition of the rule

We have shown that for each injected area, the distribution of FLNs (incoming link weights) is lognormal. Figure 13A shows that the pooled distribution of FLN values for all the 29 injections also has a lognormal distribution, hence exhibiting a heavy tail (fig. 13B). Here we show that

the FLN decays exponentially as a function of projection distance. This allows formulation of a global distance rule as a principle of allocation of resources in the cortex. Figure 14A shows the $log(FLN)$ values for all 1,615 projections of $G_{29\times91}$ as a function of interareal projection length. In spite of the variability in the data, there is a clear decay trend (red, linear fit) with increasing distance. However, the FLNs group neuronal counts via the injected areas, thus providing a binning by areas. Projections at longer distances come at a metabolic cost for individual neurons. To better express this cost principle as a global (area-independent) property, fig. 14B shows a histogram for all retrogradely labelled neurons found from the 29 injections (a total of 6,494,974) as function of the projection distance between cortical areas. This exhibits an exponential decay that we refer to as the "exponential distance rule" (EDR). Accordingly, $p(d)$ can be interpreted as the probability of a projection length d, irrespectively of the areas involved.

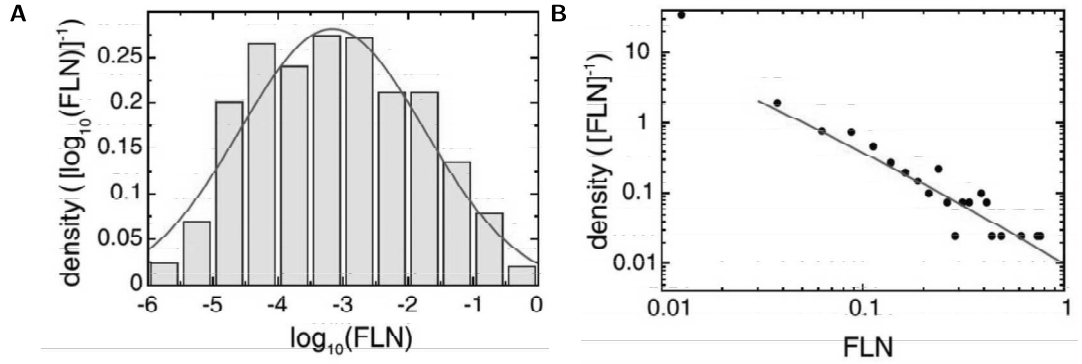

FIGURE 13: **Lognormal distribution of FLN.** (**A**) FLN values span five orders of magnitude and follow a lognormal distribution in this density plot. $log(FLN)$ values were binned (bin size 0.5 log unit), the height of each bin (ordinate) corresponds to the fraction of projections with $log(FLN)$ falling within that bin divided by the bin width. Blue, Gaussian fit with mean at $\mu_{Gauss} = -3.17$ (location parameter) and SD of $\sigma_{Gauss} = 1.42$ (scale parameter), both in units of $log(FLN)$. (**B**) Right tail (large FLN values) of the distribution exhibits a slow, power-law decay as shown by the double logarithmic plot. Blue line: right tail of the lognormal in (A). This is also a density plot, as in (A). In this case, the binning was done directly on the FLN values with a bin width of 0.025 FLN. With this choice for bin width, the right tail of the distribution is formed by those high FLN values that fall outside of one sigma ($\sigma_{Gauss} = 1.42$) in (A).

Based on fig. 14B, we express this principle as:

$$p(d) = c\, e^{-\lambda d} \tag{3.1}$$

where c is a normalisation constant and $\lambda = \lambda_d = 0.188$ mm^{-1} (obtained from least-squares fitting, fig. 14B). The blue line in fig. 14A corresponds to eq. (3.1) with $\lambda = \lambda_d$, indicating that it is a good approximation for the linear decay trend (red line with $\lambda_{f_{ij}} = 0.150$ mm^{-1} in fig. 14A) of the $log(FLN)$ values as well. Since the fraction of labelled neurons f_{ij} can be interpreted as the probability of a neuronal projection from i to j, the agreement in fig. 14A shows that, on average, we can approximate the FLN values with their distance-dependent projection probabilities, i.e., $f_{ij} \approx p(d_{ij}) = c\, e^{-\lambda\, d_{ij}}$ where d_{ij} is the distance between the areas. From this, the distance between two areas can on average be expressed in terms of the corresponding

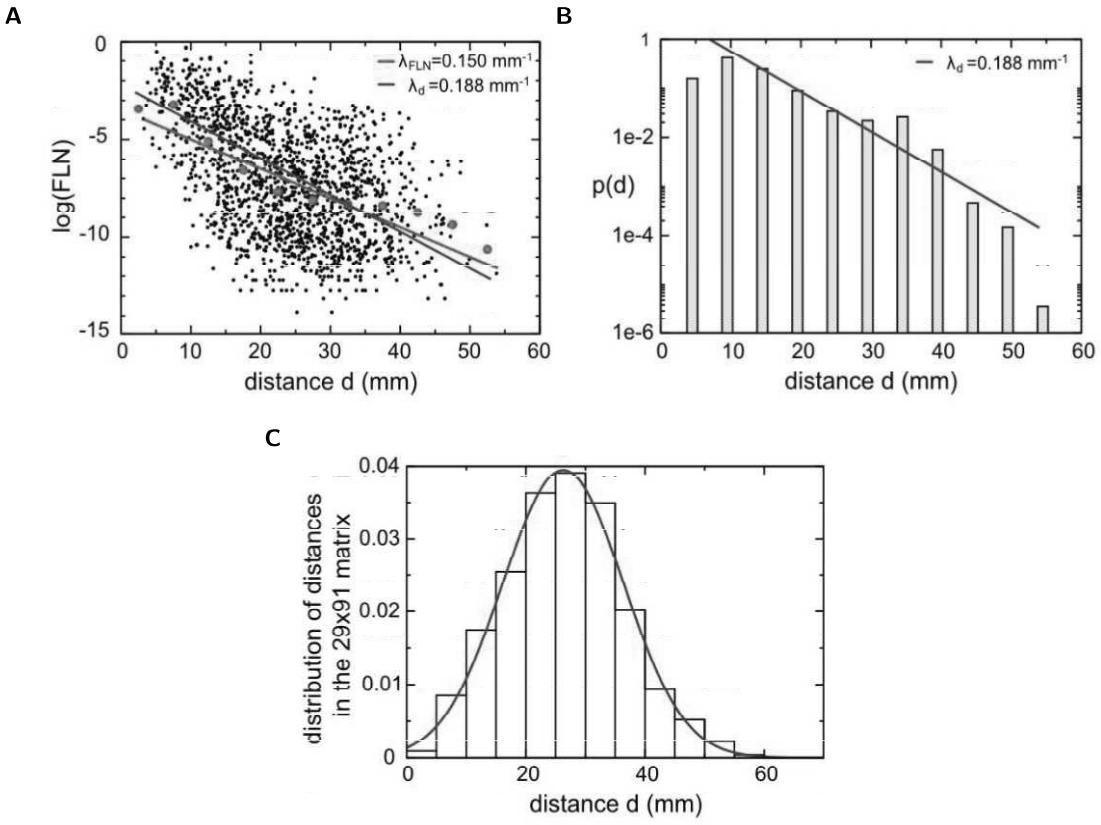

FIGURE 14: **Projection Length Distributions.** **(A)** FLNvalues ($log(f_{ij})$) for all 1,615 projections as a function of projection length (d_{ij}) estimated through the white matter. Red circles, averages within 5 mm distance bins; the red line is an exponential fit to all the black points giving a decay rate of $\lambda_{FLN} = 0.150$ mm^{-1}. **(B)** Histogram of interareal projection length for all labelled neurons (n = 6,494,974). Blue line, exponential fit with decay rate $\lambda_d = 0.188$ mm^{-1}, also shown in (A). **(C)** Distribution of interareal distances in $G_{29\times91}$ matrix, a purely geometrical property, is best approximated by a Gaussian (mean $\langle d \rangle = \mu = 26.57$ mm; SD $\sigma = 10.11$ mm).

$log(FLN)$ values (natural log) as:

$$d_{ij} \approx -\frac{1}{\lambda} log(f_{ij}) + \frac{1}{\lambda} log(c) \tag{3.2}$$

The distribution of the interareal distances (i.e., the fraction of area pairs separated by distance d) conforms to a Gaussian (see fig. 14C), i.e.

$$q(d) = \frac{1}{\sigma\sqrt{2\pi}}\ exp\left(-\frac{1}{2\sigma^2}(d-\mu)^2\right) \tag{3.3}$$

with $\mu = 26.57$ mm and $\sigma = 10.11$ mm. Note that eq. (3.3) expresses a geometrical property of the cortex, the distribution of areal separations, and is not related to neuronal counts or densities. Substituting the distance variable in eq. (3.3) with its expression in terms of $log(FLN)$ from eq. (3.2) gives an approximation to the fraction of ordered area pairs that have a given $log(FLN)$ value, i.e., an approximation to the $log(FLN)$ distribution:

$$P(log(f)) = q(d(f)) = \frac{\lambda}{\gamma\sqrt{2\pi}}\ exp\left(-\frac{1}{2\gamma^2}(log(f)-\nu)^2\right) \tag{3.4}$$

with $\gamma = \sigma\lambda$ and $\nu = \mu\lambda - log(c)$. This is indeed a Gaussian, consistent with the experimental observation that the FLN distribution is a lognormal. Note that this derivation captures only the lognormal form, as we have replaced distances in eq. (3.3) by an expression of the FLNs that holds only on average, eq. (3.2). Accordingly, the width of the Gaussian distribution in fig. 13A (data) is wider than that of eq. (3.4), due to fluctuations around the average.

(c) An EDR-Based network model of the cortex

Because the $G_{29\times29}$ graph is a densely connected network, one might expect there to be little structural specificity on the binary level (nodes connected or not). However, $G_{29\times29}$ is actually a special graph even at the binary level. This specificity follows directly from the EDR (decreasing probability of projection with distance principle), acting as a *physical* constraint and the spatial embedding of the cortex acting as a *geometrical* constraint. To explore further the role of distance in the structural properties of the cortical network, we generated two random graph models using different distance rules. One obeys the observed exponential distance rule of eq. (3.1) (EDR graphs), the other a constant distance rule $p(d) = const$, in which the probability of a projection having a distance d is a constant (CDR graphs). The CDR model can be considered a special case of EDR with $\lambda = 0$. To construct the model graphs, we first chose a connection length d according to the distance rule $p(d)$. We next pick *uniformly at random* (to avoid biases, following Jaynes' maximum entropy principle; Jaynes 1957) an area pair (i, j) from the set of area pairs in the 29 by 29 matrix of measured distances, whose separation is in the same distance bin as d, then insert a connection in the graph directed from j to i. Multiple connections from j to i are allowed, thus generating the projection's weight; the process is halted after accumulating $M = 536$ *binary* connections (i.e., the number of connections in the $G_{29\times29}$). To compare graph theoretical properties between the model and the cortical graph $G_{29\times29}$, we generated 1,000 random realisations of each model graph, averaged the measured quantity over these realisations, and compared this average to the same measure on $G_{29\times29}$.

3.2 Predictions in EDR-based random networks

(a) Frequency of uni- and bidirectional connections

Previous studies of collated data had suggested that connections between cortical areas are dominated by reciprocally interconnected pathways (Felleman & Van Essen, 1991). Markov et al. (2013) reported a higher incidence of unidirectional, nonreciprocal connections. Here we show that this feature is well captured by the EDR. If M_1 and M_2 are the number of uni- and bidirectional connections, respectively, the total is $M = M_1 + 2M_2$. The simplest quantity that we can compare between model and data graphs is the total number of unidirectional connections M_1 (because M is specified, M_2 is automatically determined). Varying λ modulates the distribution of M_1 and M_2, see fig. 15A. Since λ is the only model parameter, we set it to $\lambda = \lambda_M \approx 0.174$ mm^{-1} (fig. 15A) so that $\langle M_1\rangle(\lambda) = M_1 = 108$, the experimental number of unidirectional connections. Thus, λ_M is set by a purely binary graph theoretical measure of the data, not by weights, distances, or neuronal counts, yet it agrees closely with the decay rate

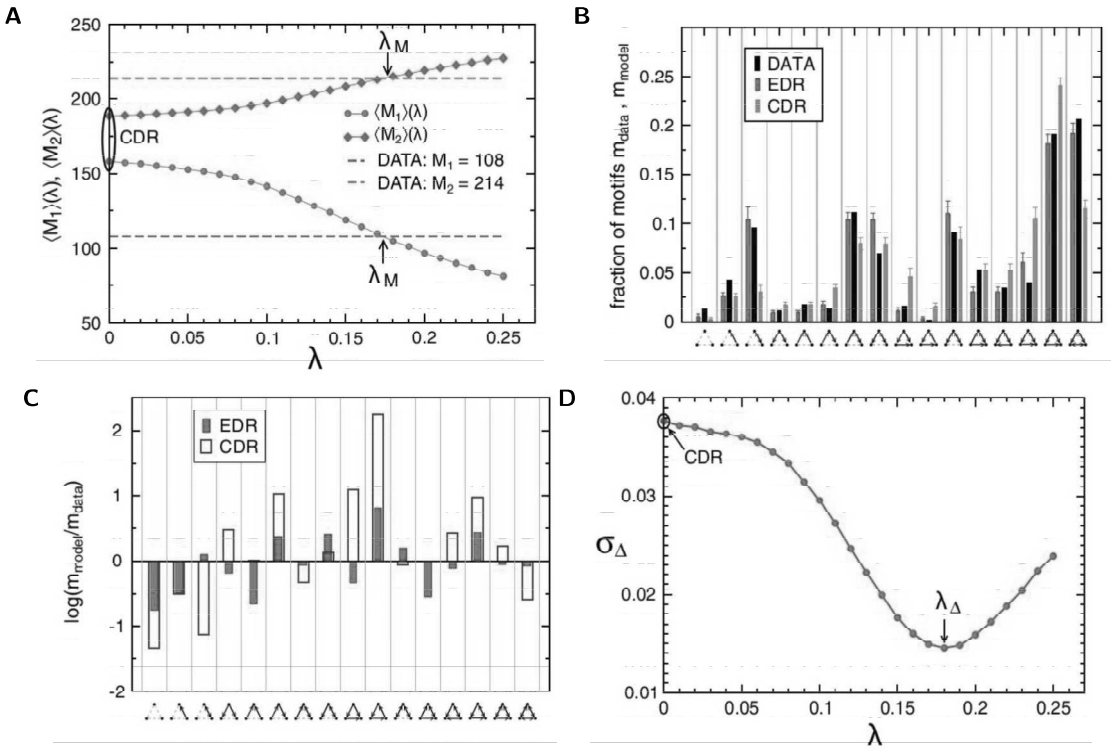

FIGURE 15: **Distance-rules-based network models of the cortex.** **(A)** The only model parameter λ here is set by setting the number of unidirectional links M_1 to that in the data. **(B)** Motif fractions in the EDR and CDR models and data. Statistics were carried out on 1,000 random graph realisations; error bars show the SD. **(C)** Logarithm of motif ratio counts between model and data. **(D)** The SD of the deviations in (C) as function of λ, optimal agreement (minimum σ_Δ) is at $\lambda_\Delta = 0.180$ mm^{-1}.

$\lambda_d = 0.188$ mm^{-1}, obtained from the histogram of projection lengths of fig. 14B. This agreement stems from the fact that the EDR rule is a strong determinant of the cortical network structure.

(b) Motif distribution

A basic binary characteristic of a directed network is its frequency distribution of directed small binary subgraphs that can be considered as network building blocks that are characteristic of different types of networks (Milo et al., 2002). For example, Milo et al. (2002) looked at three-node motifs and showed that information-processing networks were characterised by certain, abundant triangular motifs. There are 16 possible three-node motifs (abscissa symbols in panels (B) and (C) of fig. 15). The EDR model returns motif frequencies similar to those found in the data as shown in fig. 15B. Figure 15C compares the deviations by considering the log of the ratio of the model motif count to the count of the same motif in the data. Let σ_Δ denote the SD of the fluctuations in fig. 15C. Figure 15D plots σ_Δ versus λ, showing that the best agreement (minimum point) is achieved at λ_Δ. Thus, the EDR fits the data much better than the CDR: the SD σ_Δ between the experimental data and CDR is over 2.6 times larger (0.0377) than the deviation for EDR (0.0145), at $\lambda = \lambda_\Delta = 0.180$ mm^{-1}. This λ value does not necessarily equal λ_M because it is derived from an entirely different binary graph measure. The similarity of these values indicates that the EDR captures important aspects of cortical network structure. In the following, unless specified otherwise, we used λ_Δ to generate the EDR graphs (0.150 mm^{-1}

$= \lambda_{FLN} < \lambda_M < \lambda_\Delta < \lambda_d = 0.188$ mm^{-1}). Although the graphs are small (29 nodes) and the degree distributions noisy, the comparisons between models and data nevertheless show that the EDR better captures the frequency distributions than does the CDR.

(c) Global and local efficiency during removal of projections

Evidence that the differential effect of weak link removal is largely due to the distance rule is shown in fig. 16. Both local and global efficiencies decay slowly for the CDR, whereas the EDR model displays a similar behaviour as the data.

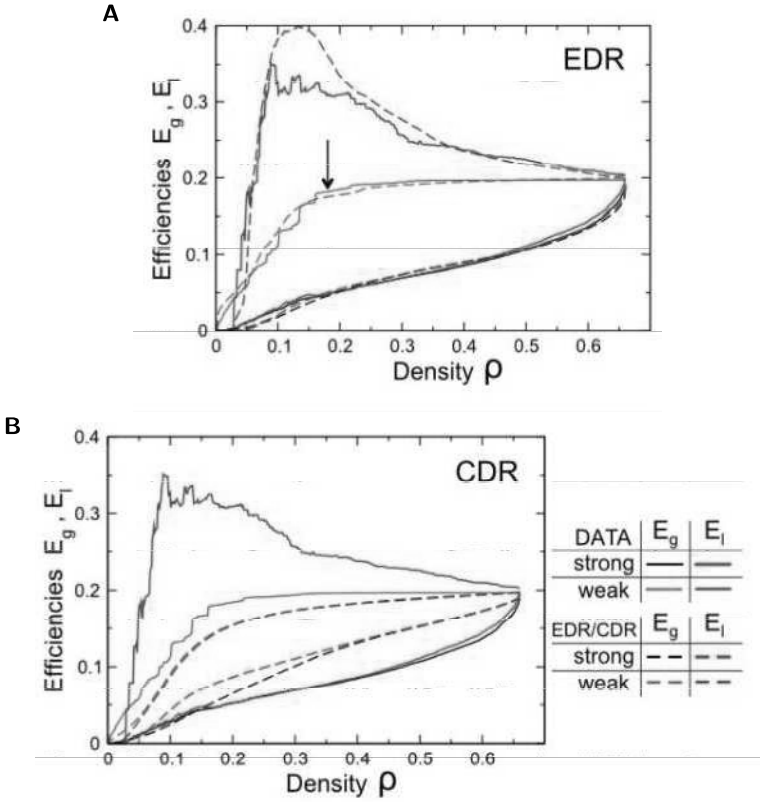

FIGURE 16: **Efficiency in the two models.** Effects of graph density on efficiency measures via sequentially deleting weak (blue, green) or strong (black, red) links. Data comparison with **(A)** EDR model, dashed lines and **(B)** CDR model, dashed lines.

The higher local, compared to global, efficiency suggests that local information processing is more voluminous and that within the clusters of areas in the backbone, the strong connections provide multiple alternative paths for functional interactions. Mathematically speaking, those terms increase in E_l for which the central node i loses a weakly connected neighbour j during the removal process. Due to the distance rule, however, if j is a weak link neighbour of i, then all its connections to the strong link neighbours of i must be weak, since j is then a node physically far from i and its immediate neighbourhood (e.g., since Lyon is far from the Hague and the Hague is close to Amsterdam, then Lyon is also far from Amsterdam).

Conclusion

Spatial information is a crucial feature of the cortical network. The EDR coupled with interareal distances generates the lognormal distribution of connection strengths as well as the basic binary connectivity properties of the interareal network. It is interesting that binary network properties are recovered from a distance rule, which is a continuous spatial property of the system. Because the EDR strongly shapes the cortical network structure, it is to be expected that it is a selector for the types of information theoretic algorithms implemented by the cortex.

Chapter 4

Microstimulating area V4 does not change phosphene detection threshold in area V1

Als Ich Kan

Jan van Eyck

Abstract

Previous transcranial magnetic stimulation (TMS) studies suggested that feedback from higher to lower areas of the visual cortex is important for the access of visual information to awareness. However, the influence of corticocortical feedback on awareness and the nature of the feedback effects are not yet completely understood. In the present study, we used electrical microstimulation in the visual cortex of monkeys to test the hypothesis that corticocortical feedback plays a role in visual awareness. We investigated the interactions between the primary visual cortex (V1) and area V4 by applying microstimulation in both cortical areas, at various delays. We report that the monkeys detected the phosphenes produced by V1 microstimulation but that subthreshold V4 microstimulation did not influence V1 phosphene detection thresholds. A second experiment examined the influence of V4 microstimulation on the monkeys' ability to detect the dimming of one of three peripheral visual stimuli. Again, microstimulation of a group of V4 neurons failed to modulate the monkeys' perception of a stimulus in their receptive field. We conclude that conditions exist where microstimulation of area V4 has only a limited influence on visual perception.

1 Introduction

The question of how visual awareness emerges in our brain is one of the major challenges that remain to be addressed in neuroscience. There is not yet a consolidated theory of how visual percepts reach awareness (Dehaene et al., 2006; Lamme, 2003; Zeki, 2003). One influential theory posits that information reaches consciousness when it ignites reciprocal interactions between multiple brain areas (Edelman, 1987) that allow sharing of information in a global workspace (Dehaene & Changeux, 2011; Dehaene et al., 2003). Feedback connections might be important for this process, as they can amplify neuronal activity in the lower areas gating the access to consciousness (Dehaene & Changeux, 2011; Lamme & Roelfsema, 2000; Super et al., 2001). Neurophysiological experiments have implicated corticocortical feedback in visual awareness (Super et al., 2001), figure-ground segregation (Lamme et al., 1998; Super et al., 2001) and shifts of visual attention (Moore et al., 2003; Moore & Fallah, 2001, 2004; Noudoost & Moore, 2011; Roelfsema et al., 1998). Specifically, neuronal responses in primary visual cortex (V1) are enhanced by feedback connections if a monkey detects a figure on a background (Lamme et al., 1998; Poort et al., 2012) but this amplification does not occur if the monkey fails to perceive the figure (Super et al., 2001).

Transcranial magnetic stimulation (TMS) experiments provided additional support for the role of feedback connections in awareness. Silvanto et al. (2005) applied TMS to V1 to evoke phosphenes, artificial percepts of light. They showed that an additional sub-threshold TMS pulse in motion-sensitive area V5 increases the probability of detecting a moving phosphene instead of a stationary one, but only if it precedes V1-TMS by 10-50ms, in accordance with a role of feedback connections. At the same time, V1-TMS can also interfere with the perception of phosphenes that are evoked by V5-TMS (Pascual-Leone & Walsh, 2001). This interference effect was only observed if V5-TMS preceded V1-TMS, again suggesting a role for feedback connections.

Our main experiment was modelled after these TMS experiments, but we applied microstimulation (MS) in two areas of the visual cortex of monkeys. The advantage of MS is that the technique activates a more circumscribed population of neurons (Histed et al., 2009; Schiller & Tehovnik, 2008; Tehovnik, 1996; Tehovnik et al., 2005). Will subthreshold MS in a higher visual area influence the perception of phosphenes evoked with MS in V1?

In a first experiment we applied subthreshold MS in area V4 in a task where monkeys had to detect a phosphene evoked by MS of V1 neurons with overlapping receptive fields (RFs). We expected that V4-MS would modulate the perception of phosphenes elicited by V1-MS. To our surprise, even though feedback connections from V4 to V1 have a strength that is comparable to that of those from MT to V1 (Markov et al., 2011b), we observed no effect of V4-MS on the phosphene detection threshold in V1. We next tested if V4-MS influences the distribution of spatial attention across a visual stimulus, in a contrast change detection task as has been observed with MS of the frontal eye fields (Moore & Fallah, 2001). However, we also did not observe any effect of V4-MS in this task. Our results imply that there are conditions where V4-MS neither influences the detection of V1-evoked phosphenes nor the distribution of visual attention.

2 Methods

2.1 Surgeries and mapping

Two male Rhesus macaques (monkeys B and C) participated in this study. In a first operation, a head holder was implanted. In a separate surgery, arrays of 4x5 or 5x5 electrodes, 80 µm thick 1 or 1.5 mm long (Blackrock Inc.) were chronically implanted in areas V1 and V4. The surgical procedures were performed under aseptic conditions and general anaesthesia. They complied with the US National Institutes of Health Guidelines for the Care and Use of Laboratory Animals, and were approved by the Institutional Animal Care and Use Committee of the Royal Netherlands Academy of Arts and Sciences. Details of the surgical procedures and the postoperative care have been described elsewhere (Poort et al., 2012; Super & Roelfsema, 2005).

We measured the receptive field (RF) dimensions of every V1 recording site by determining the onset and offset of the response to a slowly moving light bar for each of four movement directions (Kato et al., 1978). V4 RFs were mapped by presenting white squares (1x1 degree of visual angle (deg)) on a grey background at different positions of a grid (1 deg spacing).

2.2 Microstimulation

For microstimulation (MS), we used a custom-made two-channel constant current stimulator to generate trains of negative-first biphasic pulses of 400 µs duration (200 µs per phase) at a frequency of 200 Hz, through one of the electrodes in V1 or V4. We varied the amplitude and number of pulses (see below), but all currents stayed within the range of $5-250$ µA. We tested the impedance of the stimulated electrodes before every session and obtained values between 40 and 280 kΩ (mean 107 kΩ, s.d. 62 kΩ). Even though unlikely, to rule out any changes in

impedance over days due to the MS, we checked in monkey C whether there was a significant change in impedance across sessions. The mean difference was -13.7 kΩ ± 12.6 kΩ (mean ± s.e.m) and as expected, it was not significantly different from zero ($p > 0.1, t_{11} = -1.09$).

2.3 Behavioural setup

The monkeys performed both tasks while seated at a distance of 75 cm from a 21 inch CRT monitor with a refresh rate of 70 Hz (phosphene detection task) or 100 Hz (dimming detection task) and a resolution of 1024x768 pixels. The eye position was monitored with a video-based eye tracker (Thomas Recording) and sampled at 250 Hz. A trial was initiated when the monkey had maintained his gaze for 300 ms within a (virtual) fixation window, 1.5 deg in diameter, centred on the fixation point. The monkey obtained a juice reward at the end of each correct trial.

2.4 Phosphene detection task

To estimate the phosphene detection threshold we used a yes/no forced choice task with delayed saccade (fig. 1A). On each trial we presented a fixation dot in the center of the screen (0.3 deg in diameter) and a "catch dot" in the periphery (the same size as the fixation dot). We randomly selected 50% of the trials as MS trials and on those trials we delivered a train of MS pulses after 300 ms of fixation to elicit a phosphene at the location of the stimulated electrode's RF in the monkey's visual field. The other 50% of trials were catch trials without MS. In both conditions the monkeys were required to maintain fixation during an additional delay of 500 ms. After this delay the fixation dot turned blue, cueing the monkey to make a saccade. The additional delay excludes reflexive saccades that might be elicited by the direct activation of motor structures like the superior colliculus (Tehovnik et al., 2005, 2003). The monkeys reported the detection of a phosphene by making a saccade to the location of the receptive field and the absence of a phosphene by making a saccade to the catch dot. The trial was considered correct only if the monkey reported a phosphene in MS trials or made an eye movement to the catch dot in catch trials, and incorrect otherwise. The monkeys obtained a juice reward after every correct trial.

Before they could perform this task, the monkeys were trained on a very similar task, in which they had to report the presence of a visual stimulus that was flashed for 20 ms on 50% of the trials. The stimuli were presented at various positions on the screen and we decreased their luminance as the monkeys became better in the task. Once the monkeys' accuracy was higher than 80% with dim targets, we replaced the visual stimuli by MS.

To determine the threshold for the electrical stimulation we varied the amplitude of the electrical MS using a Bayesian adaptive psychometric method called QUEST (Watson & Pelli, 1983) set to determine a threshold of 80% correct. To increase the robustness of the estimation we did not use every single correct or incorrect answer as input to the QUEST but we introduced a counter for both correct and incorrect MS trials. Every time there was a correct or incorrect MS trial we incremented the corresponding counter. Once either of the counters reached a value of two the QUEST was updated and both counters were set to 0. The update of the QUEST was done in the following manner: if the correct trial counter reached 2 first, then the QUEST

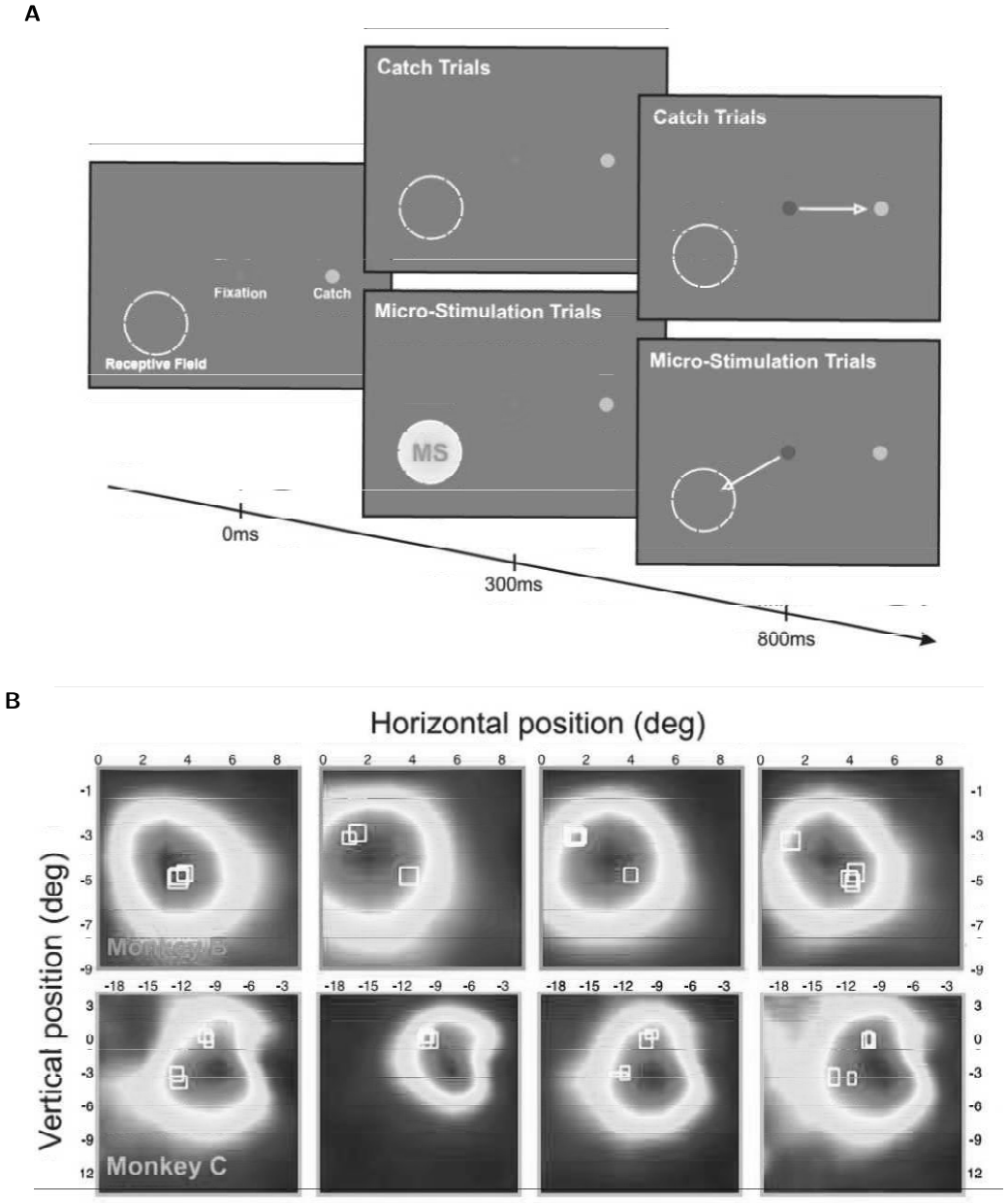

FIGURE 1: **Phosphene detection task.** (A) After an initial period of 300 ms of fixation, a train of pulses was delivered to V1 to evoke a phosphene at the retinotopic location of the RF of the stimulated cells (circle). We also presented a "catch" dot that was the target of the saccade on trials without microstimulation. After a delay of 500 ms, the fixation point changed colour, cuing the monkeys to make a saccade. Saccades to the receptive field in MS trials and to the catch dot on trials without MS were followed by a juice reward. (B) All combinations of V1 and V4 receptive fields for monkeys B and C that were tested in the phosphene detection experiment. The colour maps show V4 receptive fields and the white squares illustrate V1 receptive fields. Colour scale as in fig. 3A.

was fed with a value of 1, meaning that it should decrease the amplitude of MS. If the counter of incorrect trials was the first one to reach a value of 2, the QUEST was fed with a value of 0, indicating that it should increase the current. After 15 reversals (a reversal being a change in the monotonicity of the series of successive current amplitudes) the QUEST stopped and the threshold was computed as the mean of the last 10 reversals.

In each session we tested a combination of one V4 electrode and one V1 electrode with overlapping RFs. First we measured the threshold for phosphene detection in the V4 electrode, with 3 (monkey C) or 4 pulses (monkey B) with a separation of 5 ms (200 Hz). We used one more pulse in monkey B to keep the current thresholds below 100 µA. The average V4 threshold was 51 ± 33µA (mean ± s.d.). We then determined the phosphene detection threshold for the electrode in V1 with trains of 5 pulses. Of all trials, 50% were V1-MS trials and the other 50% were catch trials, without microstimulation in V1. There were 11 conditions for V1-MS trials. Ten of these conditions combined the train of pulses in V1 (evoking the phosphene) with V4-MS at 50% of the V4 threshold (measured at the start of the session). These 10 conditions tested 10 different stimulus-onset asynchronies (SOAs) so that V4-MS either preceded or followed V1-MS. V4-MS was between -68 ms and 22 ms after V1-MS in steps of 10 ms ("V4-V1" conditions). The 11th condition monitored the phosphene detection threshold in V1 without V4 stimulation ("V1-only" condition). The average threshold in this condition was 32±18 µA. These 11 QUEST procedures ran in parallel, in a randomly interleaved fashion.

Of the catch trials, 90% were without any MS and the animal was required to make a saccade to the catch dot. In the other 10% of catch trials we only stimulated V4 to investigate if the V4-MS at 50% of the threshold could elicit a phosphene by itself. In these trials the monkeys were also rewarded for eye movements to the catch dot (just as in the regular catch trials) and no reward was given for making a saccade toward the receptive field of the V4 stimulation site. We will refer to subthreshold V4-MS trials in which the monkey made an erroneous saccade to the overlapping V1/V4 receptive fields as "V4 false alarm responses" (keep in mind the monkeys were required to make saccades to the V1/V4 receptive field location only upon V1-MS). To investigate the influence of V4-MS on catch trials, we compute the standard false positive rate (FPR) on regular catch trials as the percentage of catch trials in which the monkeys reported a phosphene, and the V4 false positive rate (V4 FPR) as the percentage of subthreshold V4-MS trials in which monkeys reported a phosphene.

We collected a total of 15 sessions in monkey B and 16 sessions in monkey C. In average every session had 815 ± 108 trials. Figure 1B illustrates the V1-RFs (white rectangles) that have been superimposed on the V4-RFs (colour plots). On every test day we used a different electrode combination. For each SOA, threshold values either lower or higher than 5 times the standard error across sessions were considered outliers and removed from the analysis. On average, 15% of the single-session thresholds were removed.

2.5 Analysis of behavioural data

All statistical tests were performed using Matlab standard functions. Unless noted otherwise, all t-test are one-sample, two-tailed tests. Paired t-test were also two-tailed. In the phosphene detection task we used a one-way ANOVA to assess the influence of SOA and we computed

the monkey's d-prime using the Palemedes Matlab toolbox (Prins & Kingdom, 2009). For each session, we first computed the psychometric functions of two conditions by fitting the data a logistic function. The first condition grouped the trials with MS in V1 only, with the FPR as the data point for zero current (V1-only condition). The other grouped all the trials with MS in both V1 and V4 regardless of SOA (V1-V4 condition), with the V4 FPR as the data point for zero current. This way, we provided an accurate measure of the false alarm rate in each condition, and the psychometric functions expressed d-prime as a function of stimulation current. We then averaged the d-primes across sessions, clipping values larger than 4 to a value of 4 because these very high d-prime values depended strongly on the presence of one or a few errors.

2.6 Dimming detection task

To test the influence of V4 microstimulation in a distributed attention task, we trained the monkeys to perform a three-option forced-choice task in which they had to detect the dimming (transient decrease in luminance) of one of three bars (fig. 2A). Each bar was 5 deg long and 0.21 deg wide; one was presented in the RF of the tested V4 electrode and the other two at the same eccentricity but at a position rotated by 120° around the fixation point. We also presented line segments in the background (1 deg long and 0.05 deg wide) with the same luminance of 47.6 cd/m^2 as the target bars (background: 11 cd/m^2). They were randomly oriented and placed with 0.5 deg of both horizontal and vertical spacing plus a randomised jitter on their central position based on a normal distribution with a s.d. of 0.2 deg. These background line elements covered the whole screen except from a region 1 deg wide around each target bar.

We started each session by measuring the threshold for phosphene detection at the tested V4 electrode, with 20 pulse trains (200 Hz, total duration 100 ms). In the main task, after the initial 300 ms of fixation, we presented the three bars and the background. The monkey had to detect the dimming of one of the three bars and report it by making an eye movement to the relevant bar within 500 ms of the dimming. Reaction times (RTs) shorter than 100 ms were considered as false alarms and the trial was discarded. All bars were equally likely to dim, but only one did so on each trial, between 200 and 900 ms after the presentation of the stimulus. The dimming lasted for 100 ms and on MS trials (50% of the trials) the dimming was immediately preceded by the 100 ms MS train applied to a V4 electrode with a RF that overlapped with one of the bars. We used an amplitude of half the V4 phosphene detection threshold value. We also carried out a few sessions with suprathreshold V4 stimulation. In these sessions we set the current at 200% the V4 phosphene detection threshold.

The temporal expectation of an event can modulate perceptual processing (Vangkilde et al., 2012) so we maintained a constant hazard rate for the dimming event. Specifically, we used an exponential distribution of dimming times between 200 ms and 900 ms. In addition, 10% of the trials were "long" trials with a dimming time of 1200 ms. As a result, the hazard rate was constant between 200 and 900 ms, which means the dimming did not become more and more likely to occur as the time passed after stimulus presentation. If the dimming still had not occurred at 900 ms, however, the trial automatically became a long trial with dimming at 1200 ms. These long trials were not included in the analysis, they were just used to balance the hazard rate for the monkey.

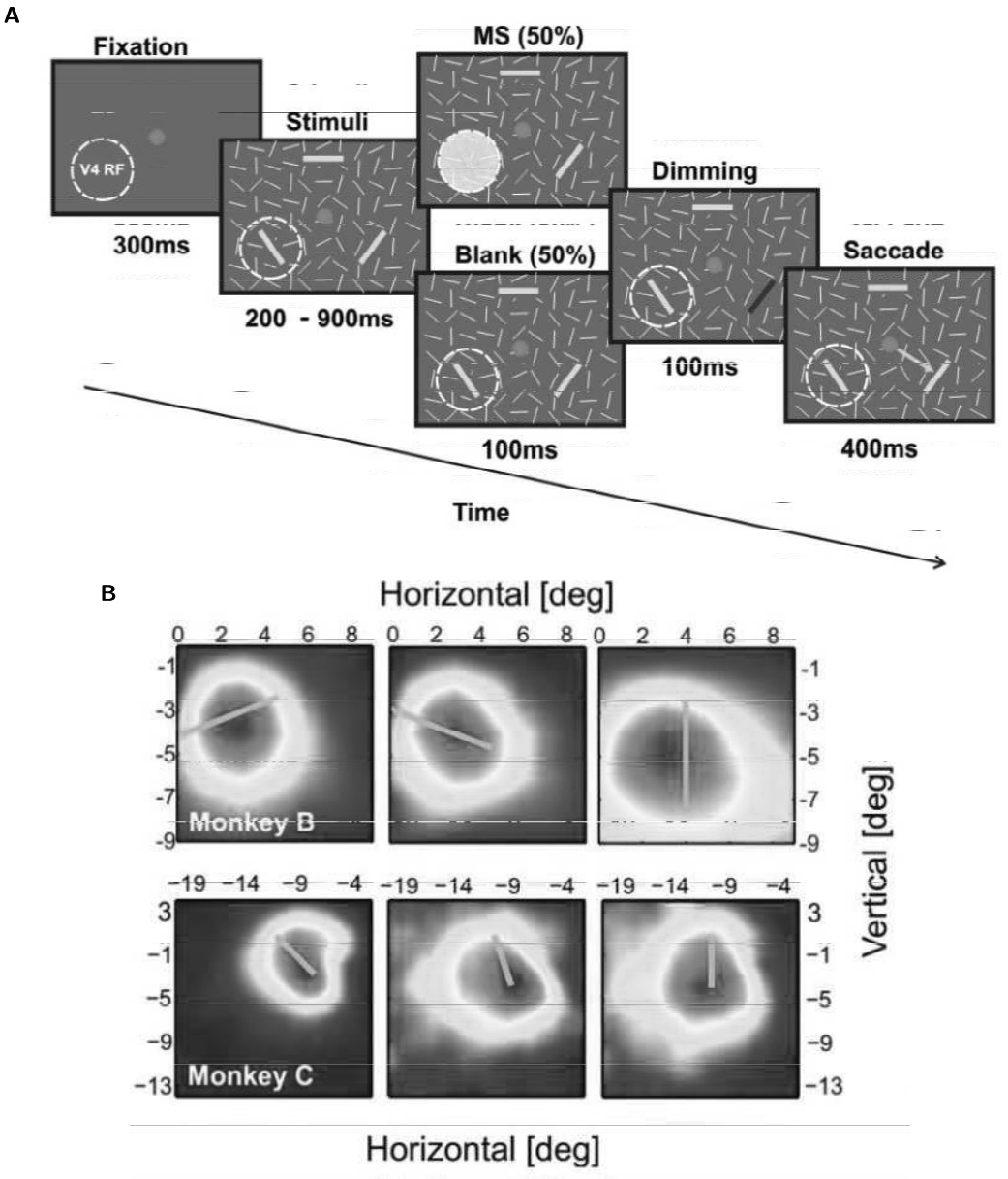

FIGURE 2: **Dimming detection task.** (A) After 300 ms of fixation, three large bars were presented among smaller distractor segments. One of the larger bars overlapped with a V4 RF. In half of the trials a train of 20 pulses (total duration 100 ms) with a current corresponding to 50% of the phosphene detection threshold was delivered to V4. After the end of the pulse train, one of the bars dimmed for 100 ms and monkeys had to make a saccade towards this bar. The luminance decrement was controlled by a staircase procedure that kept performance at 79.4%. (B) Receptive fields of V4 recording sites in the dimming detection task relative to one of the target bars (grey bars). Colour scale as in fig. 3A.

During the experiment we measured the luminance change threshold for detection of the dimming (in percentage of the bar luminance) with and without MS, separately for each bar. We used a 3 up/1 down staircase procedure. The 6 staircases (3 bars x 2 MS conditions) were run in parallel with interleaved trials. The gamma-corrected RGB luminance of the bar was 47.6 cd/m^2, and the 8 luminance values for the dimmed bars were 29.4, 31.9, 34.3, 36.7, 39.2, 41.6, 44 and 46.4 cd/m^2 respectively.

Across days, we gathered data from 25 sessions in monkey C and 24 sessions in monkey B, approximately equally distributed across three V4 electrodes per monkey (6 to 10 sessions per electrode). All the combinations of V1 and V4 RFs are shown in fig. 2B.

3 Results

3.1 Influence of V4 microstimulation on V1-induced phosphenes

Our first experiment investigated how interactions between areas of the visual cortex influence the detection of phosphenes, and was modelled after previous TMS studies on the interaction between higher and lower areas of the visual cortex (Pascual-Leone & Walsh, 2001; Silvanto et al., 2005). We trained two monkeys to detect a phosphene elicited by suprathreshold microstimulation of an electrode of one of the chronically implanted arrays in V1 and to report the phosphene by making a delayed saccade to its spatial location in the visual field. We paired V1-MS with subthreshold microstimulation of an electrode of a V4 array where neurons had overlapping receptive fields, at various stimulus-onset asynchronies (SOAs). We tested the interaction between microstimulation in V1 and V4 in 15 combinations of V1 and V4 electrodes in monkey B and in 16 combinations in monkey C (the neurons' RFs are shown in fig. 1A).

At the start of every experimental session, we determined the threshold value for the detection of a phosphene evoked by MS in a V4 electrode, and we then set the V4-MS intensity at 50% of that threshold for the remainder of the session. This choice of 50% of the threshold was inspired by previous studies using MS in frontal cortex to elicit behavioural changes (Moore & Fallah, 2001). The average V4 threshold was 51 ± 33 µA (mean ± s.d.). The threshold for evoking phosphenes with MS in V1 (in the absence of V4-MS) was 32 ± 18 µA, which is slightly higher than thresholds obtained with acutely inserted electrodes (Tehovnik et al., 2005).

We next investigated the influence of the subthreshold V4-MS on the phosphene detection threshold in V1, at various SOAs between V1-MS and V4-MS. Figure 3A shows an example electrode combination from a session with monkey C. In this session, the V4-MS threshold was 38.3 µA (we therefore stimulated with 19 µA in the rest of the session) and the threshold in V1 in the absence of V4-MS was 27.3 µA. Figure 3B illustrates the sequence of applied currents according to the QUEST staircase in the V1-only condition (in the absence of V4-MS), and in the V1-V4 condition with an SOA of -38 ms (i.e. V4-MS preceding V1-MS by 38 ms). The MS threshold in V1 for the -38 ms SOA was 22.7 µA. Thus, in this particular example, V4-MS led to a small reduction in V1 threshold.

In order to quantify the influence of V4-MS on the phosphene threshold in V1, we computed the phosphene threshold ratio (PTR) for each SOA, defined as the ratio between the threshold

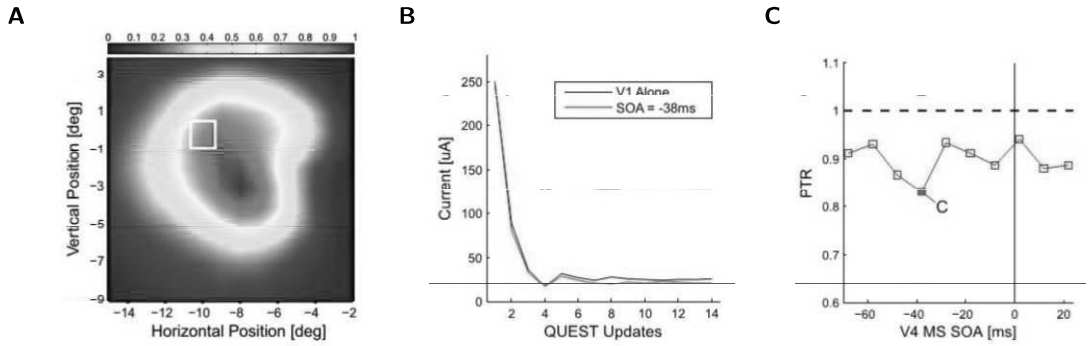

FIGURE 3: **Example session of the phosphene detection task.** **(A)** Overlap between RFs of stimulated neurons in V1 and V4 in an example session with monkey C. White square indicates the RF of the neurons in V1, the heatmap indicates the RF of the neurons in V4. **(B)** Example of QUEST staircase that was used to determine threshold of phosphenes elicited in V1 in the V1-only (black) condition and in the V1/V4-MS condition with an SOA of -38ms (red). **(C)** Relationship between the phosphene threshold ratio (PTR) in V1 and the SOA between subthreshold MS in V4 and MS in V1. Negative values on the x-axis indicate the V4 MS preceded V1 MS. Y-axis shows PTR, the ratio between V1 MS detection thresholds with and without V4-MS.

for phosphene detection in the V1-V4 condition at this SOA and the threshold in the V1-only condition. Thus, a PTR value of 1 means that V4-MS had no effect on the V1 phosphene detection threshold, a value higher than 1 indicates that V4-MS impaired V1 phosphene detection and a value lower than 1 that V4-MS facilitated V1 phosphene detection. In the example session illustrated in fig. 3C, PTR values were lower than 1 across all SOAs, indicating that V4-MS produced a general decrease of the MS threshold in V1.

To investigate the mean influence of V4-MS on V1 phosphene thresholds, we averaged values across SOAs to compute PTR_{Mean} for every session ($N = 15$ for monkey B and $N = 16$ for monkey C; fig. 4, coloured arrows on the Y-axis). PTR_{Mean} was significantly lower than 1 for monkey B ($p < 0.05$, $t_{14} = -6.34$) and there was a trend in the same direction in monkey C ($p < 0.1$, $t_{15} = -1.75$). Thus, V4-MS caused a general decrease in V1-MS thresholds. Inspection of the individual data points in fig. 4 suggests that this effect is relatively independent of the SOA, although previous studies suggested that V4-MS might interact most strongly with V1 phosphene detection if it precedes V1-MS. We therefore specifically tested the influence of SOA on the PTR with a one-way ANOVA but did not observe a significant effect of SOA on the PTR in either monkey ($F_{9,127} = 0.41$, $p > 0.1$ in monkey C; $F_{9,117} = 1.62$, $p > 0.1$ in monkey B). Thus, the effect of V4-MS on V1 phosphene detection did not depend on SOA, although we observed a general decrease in phosphene detection thresholds (fig. 4).

We suspected that this general increase in phosphene sensitivity might be caused by the detection of the V4-MS pulses themselves. Although we set the V4-MS pulse amplitude at 50% of the threshold and we did not reward the monkeys for saccades to V4 phosphenes, it is conceivable that the monkeys made saccades to phosphenes elicited by V4-MS on a fraction of the trials. To investigate the detection of V4 phosphenes, we measured a V4 false positive rate (V4-FPR) by delivering V4-MS in 10% of the catch trials without V1-MS and compared it to the false alarm rate on trials without MS in either area in the other 90% of catch trials (see Methods). V4-MS

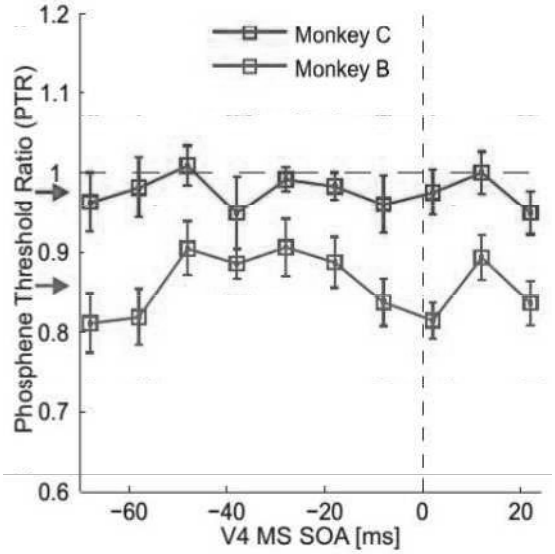

FIGURE 4: **Effect of SOA on V1 phosphene detection.** Average dependence of phosphene threshold ratio (PTR) in V1 on SOA across all sessions. Negative values on the x-axis indicate that V4 MS preceded V1 MS. PTR is defined as the threshold with V4-MS expressed as fraction of the threshold in V1 without V4 MS. Error bars indicate the s.e.m. across sessions. Coloured arrows on the Y-axis indicate PTR_{Mean}.

increased the FPR from 10% to 15% in monkey C (paired t-test; $p < 0.05$, $t_{15} = 2.8$) and from 8% to 23% in monkey B ($p < 0.01$, $t_{14} = 4.3$) (fig. 5A), which indicates that monkeys made saccades to phosphenes elicited in V4 at 50% of the threshold in some of the trials even though they were never rewarded for these saccades.

We used signal-detection theory (Green et al., 1966) to investigate if the induction of V4-phosphenes could account for the general decrease in the apparent V1-MS threshold caused by V4-MS. A genuine increase in the sensitivity for V1-phosphenes should increase the d-prime, whereas the detection of V4-phosphenes should only change the criterion, i.e. induce a general increase in the probability of reporting the presence of a phosphene. The signal-detection analysis revealed that the d-prime as function of V1-MS stimulation amplitude was hardly influenced by V4-MS in either monkey (fig. 5B). For example, the current in V1 at which d-prime reached a value of 2.12 did not differ between V1-only and V4-V1 MS trials (paired t-test, $p > 0.1$, $t_{15} = 1.65$ for monkey C and $p > 0.1$, $t_{14} = 0.68$ for monkey B: see arrows on the vertical axis of fig. 5B). In contrast, the bias was significantly different between conditions (paired t-test, $p < 0.05$, $t_{15} = -2.86$ for monkey C and $p < 0.01$, $t_{14} = -4.8$ for monkey B). As a better measure for the PTR ratio (which corrects for the influence of V4-MS on the monkeys' criterion) we computed a d-prime threshold ratio (DTR), defined as the ratio between the currents at which the d-prime reached a value of one. In this analysis we had to bin SOAs in groups of two because the number of trials per SOA bin was insufficient for a reliable determination of d-primes in individual sessions. As expected, DTR_{Mean} did not differ significantly from one ($p = 0.71$, $t_{14} = 0.38$ in monkey B; $p < 0.8$, $t_{14} = 0.25$ in monkey C; fig. 5C). Thus, although the V4 stimulation was intended to be subthreshold, the induction of V4-phosphenes on a fraction of trials accounted for the apparent decrease of the threshold for detecting V1 phosphenes, which

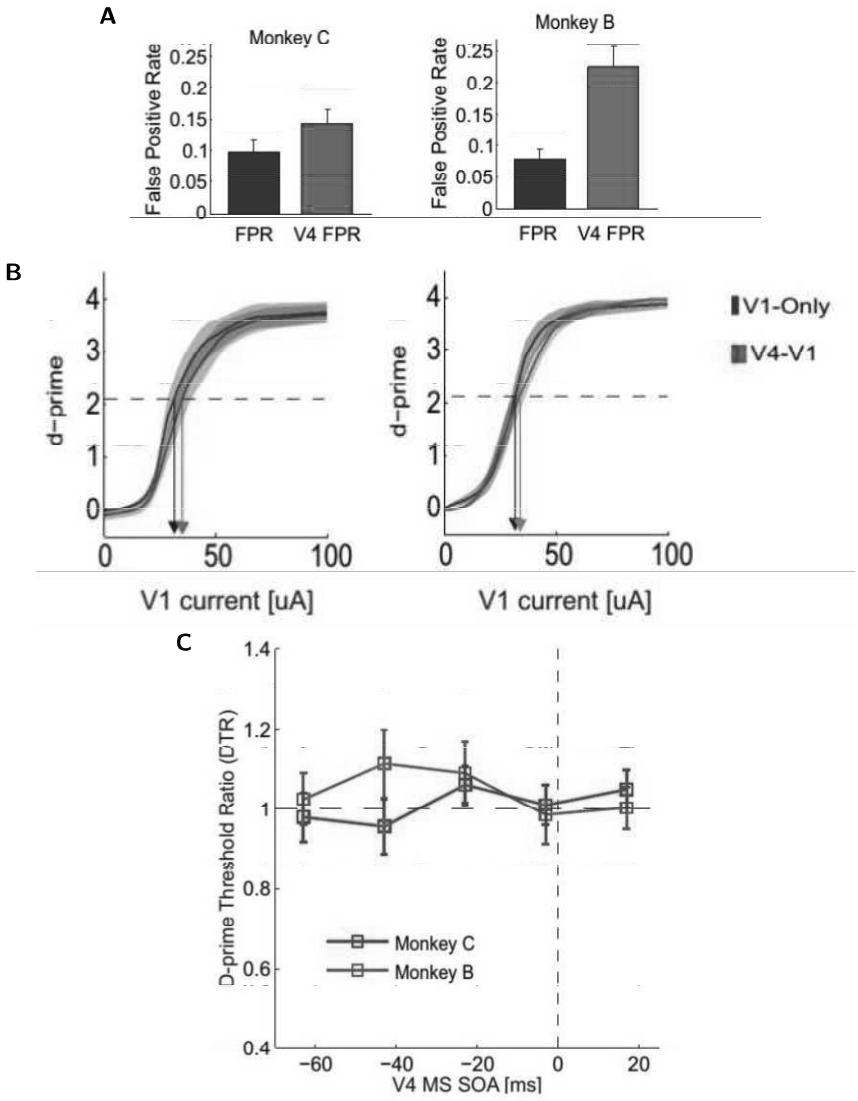

FIGURE 5: **Effect of false positive rates on d-prime.** (**A**) False positive rate is the fraction of the trials when monkeys made a saccade towards the RF in catch trials without (dark bars) or with V4 MS (coloured bars). Error bars indicate the s.e.m. across sessions. (**B**) Average d-prime as function of V1-MS current in the V1-only (dark line) and the V4/V1 combined MS condition (coloured line). Shaded areas indicate the s.e.m. across sessions. (**C**) Average dependence of V1 d-prime threshold ratio (DTR) on SOA across all sessions. Negative values on the x-axis indicate that V4 MS preceded V1 MS. DTR is defined as the current in V1 that yields a d-prime value of one in trials with V4 MS expressed as fraction of V1 current that yields a d-prime of one without V4 MS. Error bars indicate the s.e.m. across sessions. In this analysis adjacent pairs of SOAs were combined in bins to have enough data for the computation.

was independent of the SOA (fig. 4). These results, taken together, indicate that V4-MS did not influence the perception of V1-phosphenes themselves at any SOA.

3.2 Influence of V4 microstimulation on dimming detection

Despite the well-established theoretical and experimental basis for our first experiment, we did not observe a specific influence of V4-MS on the detection of phosphenes evoked in V1. One of the reasons for this negative result could be the nature of the microstimulation technique. Little is

known about the influence of V4-MS on visual perception and we therefore asked if subthreshold MS in area V4 might at the same time have influenced perception at the location of the V4 receptive fields. Such an effect of MS on perception would not be without precedent. In an elegant study, Moore & Fallah (2001) demonstrated that MS in the frontal eye fields (FEF) influences the performance of monkeys in a task in which they had to detect the contrast decrement of a stimulus in a crowded visual scene. They found that FEF-MS facilitated the detection of the contrast decrement, but only if the motor field of the stimulated neurons overlapped with the visual stimulus. One possible interpretation of this result is that the FEF-MS summoned spatial attention to the FEF motor field, thereby facilitating dimming detection at the corresponding location in the visual field while interfering with dimming detection at other locations. Could V4-MS exert a comparable facilitating influence on the detection of a small change in a visual stimulus, or conversely, might it interfere with visual perception?

To address this question we trained the monkeys to detect the dimming of one of three larger bars that were presented on a background of smaller, irrelevant line elements (fig. 2A). In half of the trials the dimming was preceded by a train of 20 MS pulses (subthreshold as determined in each session with the phosphene detection task) applied to a V4 electrode with a RF that overlapped with one of the bars. We measured the luminance change threshold for detection of the dimming (in percentage of bar luminance) with and without MS, separately for each bar. Across days, we gathered data from 25 sessions in monkey C and 24 sessions in monkey B, approximately equally distributed across three V4 electrodes per monkey (6 to 10 sessions per electrode; fig. 2B).

Does V4-MS decrease the detection threshold of the dimming at the V4 RF, perhaps at the expense of higher thresholds at other retinotopic locations? Figure 6 illustrates the effect of V4-MS on the dimming detection threshold in an example session. One of the three target bars was placed in the RF of the stimulated V4 electrode (fig. 6A). It can be seen that the staircases for the bar at the RF location in the presence and absence of V4-MS converged to a similar value of $\simeq 8.6\%$ for the luminance decrement (fig. 6B). We measured the dimming detection threshold condition as the average decrement for the last 10 reversals (fig. 3C), but did not observe a significant difference between the MS and the blank condition in the example session (comparison of the last ten reversals of the staircase, $p > 0.1$, $t_{18} = 0.59$).

We compared the contrast decrement detection thresholds with and without V4-MS across all sessions in both monkeys (fig. 7A). The average thresholds for the RF-bars were 7.74% and 5.54% (monkey C and B respectively) without V4-MS and 7.94% and 5.25% with V4-MS. For the bars outside the RF, the average thresholds were 8.88% and 6.62% with V4-MS and 9.12% and 5.49% without V4-MS. These thresholds were lower than those found by Moore & Fallah (2001), presumably because they used flashing distractors while our distractors had a constant luminance. MS did not have a significant influence on the threshold of dimming detection for any of the bars (paired t-test with Bonferroni correction for testing 2 types of bars, RF-bars and non RF-bars; monkey B: RF-bar, $p > 0.05$, $t_{23} = -2.0$; non RF-bars $p > 0.1$, $t_{47} = 0.91$; monkey C: RF-bar, $p > 0.1$, $t_{24} = 0.57$; non RF-bars $p > 0.1$, $t_{49} = -0.94$). Thus, V4 microstimulation influenced dimming detection neither in the RF of the stimulated neurons nor at the other locations far outside the RF.

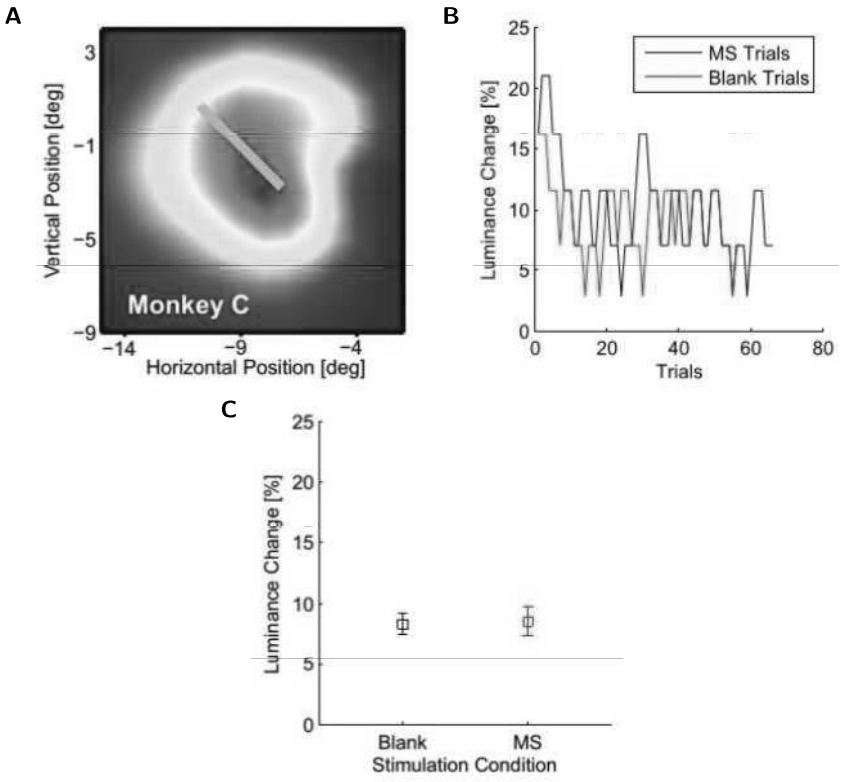

FIGURE 6: **Example session of the dimming detection task.** **(A)** Overlap between the RF of the stimulated V4 recording site and the bar in an example session. Colour scale as in fig. 3A. **(B)** Staircases of an example session; both for the blank (i.e. no MS) and the MS condition with a bar in the stimulated V4 RF. **(C)** Thresholds for blank and MS conditions of the example session computed as the mean of the last 15 reversals. Error bars indicate s.e.m. of the staircases.

Next, we investigated the possibility that MS influenced the reaction time. In monkey B, the average reaction time across sessions if the RF bar dimmed was 231.3 ± 15.6 ms (mean $\pm$ s.e.m.) in the MS condition, and 234.9 ± 10.6 ms without MS, a difference that was not significant (paired t-test, $p > 0.1$, $t_{23} = -1.3$). If one of the bars outside the RF dimmed, the average reaction time in the MS condition was 211.9 ± 10.2 ms and 212.1 ± 10.5 ms without MS (paired t-test, $p > 0.1$, 23 degrees of freedom, $t_{47} = -0.02$). Similar results were obtained in monkey C, with a mean reaction time of 275.5 ± 17.3 ms with MS and 275.9 ± 16.9 ms without MS if the dimming bar fell in the RF (paired t-test, $p > 0.1$, $t_{24} = -0.1$). If one of the other two bars dimmed, the mean response time was 258.2 ± 12.1 ms with V4-MS and 257.2 ± 13 ms without MS (paired t-test, $p > 0.1$, $t_{49} = 0.59$). Thus, subthreshold microstimulation in area V4 did not influence response time in the dimming detection task either.

To probe whether we would see an effect of V4-MS on dimming detection at higher currents, we also tested MS at 200% of V4 phosphene detection threshold in a few experiments to ensure that the MS-pulses exert an effect on activity in V4. We ran three sessions in monkey B and two in monkey C. In monkey C we did not observe an effect of V4-MS on contrast detection. However, we did observe a consistent effect in monkey B across the three sessions. MS in V4 increased the dimming detection threshold for the bar that was in the receptive field (overlap; noted "OV" in fig. 7B) and reduced the threshold for bars outside the receptive field (no overlap; noted "no OV" in fig. 7B). It should be noted however that the phosphene induced at 200% of

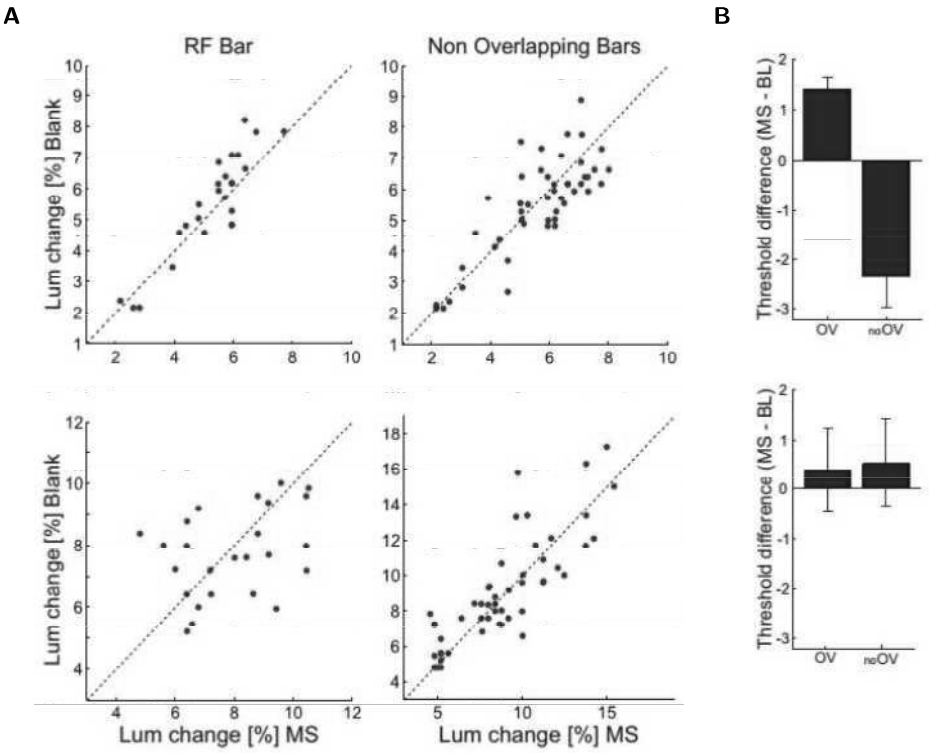

FIGURE 7: **Effect of V4 MS on dimming detection thresholds.** **(A)** Dimming detection thresholds for the V4-MS trials (x-axis) and the blank trials (y-axis) for the bar in the RF (left panels) and the two bars outside the RF (right panels) in monkey B (upper panels) and monkey C (lower panels). **(B)** Sessions with supra-threshold V4 stimulation (stimulation current was set at 200% of the threshold). We computed the difference between dimming detection thresholds (% contrast change) for bars overlapping with the stimulated V4 RF (OV) and non-overlapping bars (no OV). Shown are average results of 3 sessions in monkey B and 2 sessions in monkey C.

the threshold makes it difficult to disentangle possible effects of V4-MS on attention from the effects caused by the creation of a visual percept.

4 Discussion

In the present study we tested the hypothesis that neuronal activity in V4 may gate the access of neuronal activity in lower visual areas into awareness or may cause shifts of visual attention. To this end we electrically stimulated V4 and probed the effects on the perception of phosphenes evoked in V1 or on the perception of a contrast change of a visual stimulus. We did not observe an effect of V4 MS on behavioural thresholds in either task, which implies that subthreshold MS in V4 neither has a strong impact on the sensitivity for V1-induced phosphenes nor on the distribution of attention.

4.1 Influence of V4 microstimulation on V1 phosphene detection

Microstimulation in area V4 had little influence on the threshold for the detection of phosphenes that were elicited by MS in V1. The absence of an interaction between MS in V1 and V4 may

seem unexpected in view of previous TMS studies in areas V1 and MT (Pascual-Leone & Walsh, 2001; Silvanto et al., 2005). These studies demonstrated that a suprathreshold TMS pulse in area V1 interacts with a subthreshold TMS pulse applied to motion-sensitive area MT by decreasing the threshold for motion perception, but only if MT stimulation precedes V1 stimulation. This effect was strongest if the delay between MT and V1 TMS was approximately 50ms, which suggested the involvement of feedback connections.

Here we did not observe such a delay-specific influence of V4-MS on the threshold for phosphenes evoked by V1 stimulation, but only a general decrease of the threshold that was compatible with the detection of the V4-phosphenes on a fraction of trials. There are a number of differences between the previous TMS studies and the present study that could explain the disagreement. The most notable difference is the method used to influence neuronal activity in the cortex. TMS stimulates a large region of cortex (several millimetres to centimetres; (Walsh & Cowey, 1998, 2000). In contrast, MS influences a much smaller region of 1 mm or less around the tip of the electrode (Histed et al., 2009, 2013; Tehovnik, 1996) and allows for a much more precise control over the retinotopic overlap of stimulated neurons in the two brain areas. In the present study we only selected pairs of recording sites with overlapping receptive fields, as V4 neurons with RFs that overlap with those in V1 are predicted to exert a stronger control over V1 activity than V4 neurons with RFs that do not overlap. This difference between the present MS study and previous TMS studies raises the possibility that retinotopically non-overlapping regions targeted by TMS contributed to the interaction between the two areas. Another difference is that the TMS experiments observed that activation of MT influenced the sensory quality of the perceived phosphene rather than the threshold itself. Because we only tested if feedback from V4 influenced the threshold of phosphenes induced in V1, we cannot rule the possibility that altered feedback from V4 changed the sensory qualities of the phosphene, like its perceived shape or colour.

4.2 Influence of V4 microstimulation on the distribution of attention

We considered the possibility that the absence of a specific V4-microstimulation effect on V1 phosphene detection is related to side effects of the microstimulation procedure. For example, V4 microstimulation might interact with visually driven activity to alter visual perception. Our second experiment therefore paired subthreshold MS in V4 with the dimming of a visual stimulus. We did not observe an effect on the detection of a dimming stimulus, thus demonstrating that subthreshold V4 microstimulation does not cause gross impairments in the perception of subtle changes of visual stimuli. Previous experiments with a similar paradigm showed that microstimulation of FEF does influence dimming detection, in a manner that can be explained by an attention shift (Moore et al., 2003; Moore & Fallah, 2001, 2004) and comparable results were recently obtained in area LIP as well (Dai et al., 2014). Specifically, MS in area LIP or FEF enhanced detection of changes in the contrast of a visual stimulus, but only for stimuli inside the location of receptive field of the stimulated neurons. However, despite using a similar paradigm and the same stimulation current levels (mean of 20 µA in our experiment vs. median of 10 µA in Moore & Fallah (2001) and 40 µA in Dai et al. 2014), our second experiment also failed to reveal an effect of MS on the threshold in a dimming detection task. This second null result suggests that the influence of V4 stimulation on covert attention is limited. In contrast, stimulation of FEF or LIP appears to trigger feedback mechanisms to the visual cortex that influence the spatial

distribution of attention (Dai et al., 2014; Moore et al., 2003). The influence of microstimulation in FEF or LIP on the distribution of attention is consistent with the previously proposed role of frontal and parietal cortex in attentional control (Rossi et al., 2009). In contrast, the present results demonstrate that MS of V4 does not cause a shift of attention, which suggests that it is more involved in visual processing than in the control of spatial attention.

4.3 Orthodromic or antidromic microstimulation effects?

MS activates a sparse set of neurons that most likely have axons running in the vicinity of the tip of the stimulation electrode (Histed et al., 2009). The MS effects are specific to the stimulated area if the stimulated axons are part of neurons with cells bodies in this area. These stimulation effects can propagate to other cortical or subcortical regions such as the pulvinar (Kaas & Lyon, 2007; Purushothaman et al., 2012). Moreover, MS can also cause long-range, antidromic stimulation effects if it activates the terminals of neurons with cell bodies in another area. In our V1-V4 microstimulation experiment we therefore have to consider the possibility that V4-MS antidromically activated V1 neurons. However, there are a number of reasons why the contribution of antidromic activation of V1 cells is likely to be minor. First, at the current levels we used, most cells in the stimulated region are activated by the electrical stimulus not directly but only transynaptically (i.e. the collision test is negative for these cells) and these transynaptically activated neurons can, in turn, only cause orthodromic stimulation effects (Butovas & Schwarz, 2003). Accordingly, previous studies demonstrated that orthodromic stimulation effects are many times stronger than antidromic effects, even between areas with strong direct projections (Bullier et al., 1988; Girard et al., 2001; Movshon & Newsome, 1996). Second, the projection from V1 to V4 is relatively weak (Markov et al., 2011b) and most of the interactions between V1 and V4 are presumably mediated by intermediate area V2. If V2 cells would be activated antidromically by V4-MS, the activated V2 cells will still provide a genuine feedback signal to V1. Thus, the most likely effect of V4-MS on V1 activity is through feedback connections, although we cannot completely rule out a contribution of antidromic MS effects.

4.4 Interactions between brain areas for the perception of phosphenes

Although we did not observe an influence of V4 microstimulation on V1 phosphene thresholds, our results do not exclude the possibility that V4-MS changed the perceptual quality of the phosphenes. Schiller et al. (2011) recently trained monkeys to report the size, colour and brightness of phosphenes evoked by cortical MS. They provided evidence that V1 phosphenes evoked by currents in the same range used here have a small size (less than 0.5 deg), a relatively weak contrast (less than 10%) and in some cases have a specific colour. Future studies could use the double MS paradigm to test the influence of MS in higher visual areas on the perceived quality of phosphenes evoked in area V1. For instance, it is conceivable that subthreshold stimulation of cells tuned for colour in V4 could change in the perceived colour or shape of phosphenes evoked by MS in area V1. A similar argument can be made about the absence of an effect of V4 stimulation on the distribution of attention. We did not obtain evidence that V4 MS influences the distribution of spatial attention, but cannot exclude that V4 can exert an influence of feature-based attention. For example, MS of V4 neurons tuned to red might lead to a specific

improvement in the detection of the dimming of red bars relative to the dimming of green bars. Future experiments along these lines might further our understanding of the functional role of feedback connections between extrastriate cortex and area V1.

Chapter 5

Microstimulation of feedforward and feedback pathways

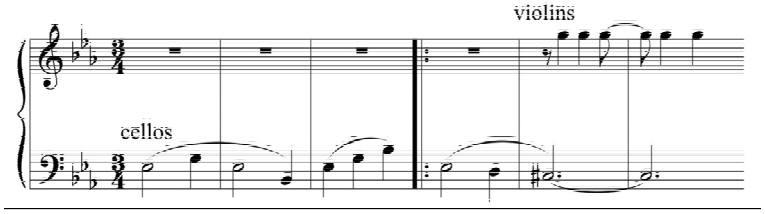

Ludwig van Beethoven,
Sinfonia eroica, composta per festeggiare il sovvenire d'un grand'Uomo

1 Introduction

Studying how visual activity propagates through the visual cortex is crucial in order to understand the mechanisms of visual perception. One of the pillars of this area of research is the distinction between feedforward and feedback propagation (Lamme & Roelfsema, 2000). Such a distinction is based in both anatomical and functional studies. From an anatomical perspective, there is a clear distinction between feedforward and feedback connections. Feedforward pathways relay information from the lower to the higher areas of the cortical hierarchy, whereas feedback connections follow the opposite direction (Felleman & Van Essen, 1991; Salin & Bullier, 1995). Interestingly, these anatomical differences have a functional counterpart. Depending on whether a stimulus is consciously perceived or not, it will engage feedforward and feedback connections differently (Dehaene & Changeux, 2011; Lamme, 2006). A similar dichotomy can be observed in different attentional tasks. Depending on the experimental conditions, a cognitive task could be solved mostly through feedforward connections or it could require the involvement of feedback connections as well (Buschman & Miller, 2007; Connor et al., 2004).

A clear example of a cognitive task that engages both types of connections is the Figure-Ground segregation task. Originally it was shown that neurons in the primary visual cortex (area V1) enhance their firing rate when their receptive field (RF) is on the figure compared to when it is on the background (Lamme, 1995; Super et al., 2001). This effect is known as figure-ground modulation (FGM). In a recent paper, Poort and colleagues (Poort et al., 2012) showed that boundary detection is computed in the lower areas in a bottom-up manner, whereas modulation on the centre of the figure depends on feedback connections. From electrophysiology (Poort et al., 2012) as well as lesion experiments (Schiller, 1995), there is evidence that V4 plays a major role on figure ground segregation and object recognition. However, despite it being known that both V1 and V4 are key cortical areas in segregating a figure from the background, the precise way they interact is not yet known.

One of the main reasons this is not yet clear is that most of the studies that analysed how neural activity propagates through the visual system use a passive approach. They engage animals or humans in different visual tasks and record with invasive or non-invasive methods how visual activity propagates. However, especially in experiments involving primates, only a small fraction of studies interfere or manipulate neural activity using techniques like micro stimulation (MS). In a recent paper Logothetis et al. (2010) showed that after electrical stimulation of the LGN, BOLD activity in higher areas was increased only in monosynaptically connected ones and decreased otherwise. However, in these experiments monkeys were either under anaesthesia or performing a passive fixation task. Thus, it remains to be explored how electrically induced changes in activity would propagate both in feedforward and feedback direction while monkeys perform a cognitive task.

In the present study, we delivered MS to the visual cortex (areas V1 and V4) while recording with chronically implanted electrodes in monkeys performing a figure ground segregation task. Will the induced changes propagate through the visual cortex under these conditions? And if so, would there be any difference between feedforward and feedback pathways? Would that propagation depend on whether the stimulated receptive field falls on the figure or on the background? And

if there is a difference, what can that tell us about the properties and dynamics of feedback as well as feedforward connections?

We found that changes in neural activity induced by MS under a demanding cognitive task propagate through the visual cortex both in feedforwad and feedback directions, but with different properties and dynamics. Moreover, the propagation is affected by the figure or ground condition in a way that suggests feedback from V4 to V1 across the whole visual field, even in the absence of a relevant stimulus.

2 Results

2.1 Effect of cortical microstimulation

It is well known that electrical stimulation of the cortex results in a brief but strong activation of neurons near the tip of the stimulating electrode (Histed et al., 2009, 2013; Ni & Maunsell, 2010; Schiller & Tehovnik, 2008; Seidemann et al., 2002; Tehovnik, 1996; Tehovnik et al., 2005). This excitatory response has been widely used as a mean to study different aspects of system neuroscience (Ekstrom et al., 2008; Houweling & Brecht, 2008; Moore & Fallah, 2001). On top of this excitatory response previous studies have shown that this brief excitation is followed by a long lasting ($\sim$ 100 ms) reduction of activity (Butovas & Schwarz, 2003; Houweling & Brecht, 2008; Seidemann et al., 2002). Despite its incredible potential in the study of cognition, this long lasting suppression of activity has been somehow neglected. In the present study we took advantage of both the excitatory and the suppressive effects of MS. Since this suppressive effect has been documented in several studies (Butovas & Schwarz, 2003; Houweling & Brecht, 2008; Seidemann et al., 2002), we did not perform a full characterisation of this effect, but rather corroborated in an example electrode that after MS of area V4 we observed both the excitatory and inhibitory phase of the MS induced changes in the vicinity of the stimulated electrode. To this effect, we delivered a single pulse of 60 µA through one of the V4 chronically implanted electrodes and recorded single unit activity from a neighbouring electrode while the monkeys were looking at a static texture (fig. 1A). After the pulse artifact was removed (see methods), the band passed signal was thresholded for single units (fig. 1B). In almost every trial there was a spike immediately after the MS pulse, followed by a clear long lasting suppression in activity (fig. 1C). Moreover, the MS-induced spikes and the texture-driven ones have the same waveform, which indicates that they belong to the same neuron (fig. 1D). Thus, as in previous studies (Butovas & Schwarz, 2003; Houweling & Brecht, 2008; Seidemann et al., 2002), we provided evidence that the MS induced changes in the cortex area of a biphasic nature. There is a strong, fast and brief excitation, followed by a long lasting suppression of activity. In the following experiments we used this fact in our favour in order to unveil differences between feedforward and feedback propagation of activity as well as to gain insight on how they are involved in a figure-ground segregation task.

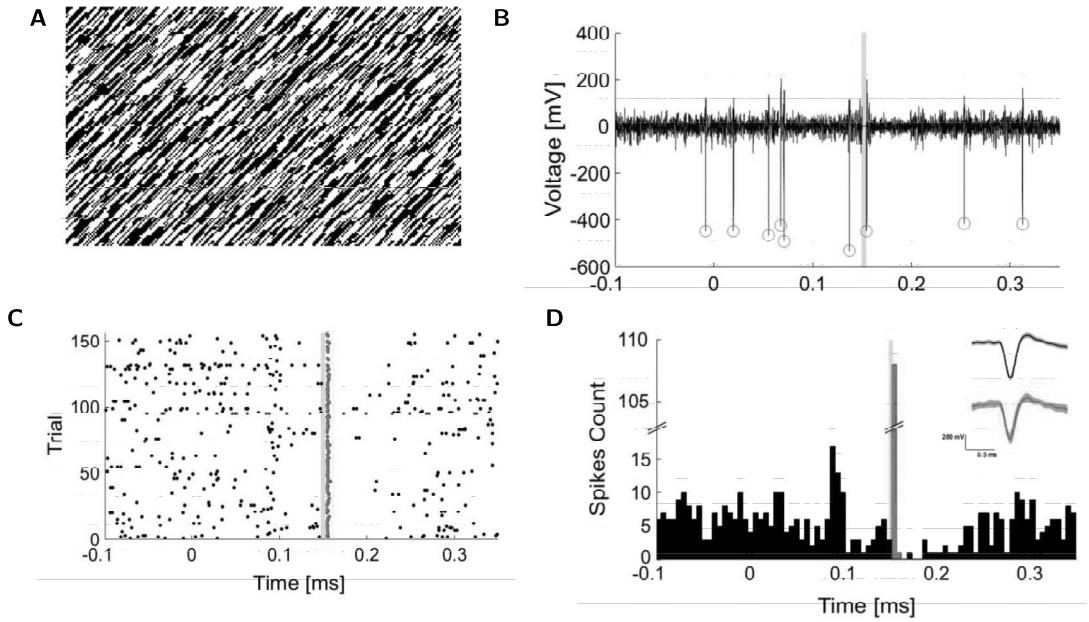

FIGURE 1: **Effect of electrical stimulation in the cortex.** (**A**) Schematic of the textured stimulus presented to the monkeys during the fixation-only task. (**B**) Band passed signal of a single trial for the fixation-only task. Circles indicate detected spikes. Yellow area indicates the period of MS. During that period data samples have been set to zero to remove the MS artifact. (**C**) Raster plot for MS trials on the fixation only task. Each dot represent a spike, red dots are spikes detected right after stimulation. Yellow area indicates the period of stimulation. (**D**) Spike count histogram for all the recorded MS trials. Red count indicates spike count right after MS pulse. Inset pictures detailed the average waveform for spikes detected right after MS (red) and the rest of the detected spikes (black).

2.2 Propagation of V1-MS effect

In the previous section we recorded from an electrode in the vicinity of the stimulation site and confirmed the biphasic nature of MS-induced changes. A natural question that follows is how do these changes in activity propagate in the feedforward direction. If we stimulate in area V1, will both phases be echoed in a higher area like V4 or will only one of them be transmitted? To answer this question we stimulated area V1 while recording in area V4. Logothetis et al. (2010) provided evidence that MS induced excitation could propagate only to monosynaptically-connected areas. In their experiments however, the monkeys were either under anaesthesia or performing a very simple fixation-only task. Thus, in the present study we engaged the monkeys in a figure-ground segregation task in order to study this propagation in the context of a cognitive task. In this figure-ground segregation task one third of the trials were Catch trials (i.e. trials in which there was no figure present and the monkeys were requested to hold fixation for an extended period of time). In the other two thirds of the trials there was a figure present at one of two locations of the visual field and the monkeys were requested to make a saccade to the figure after 350 ms. Thus, we had a two-by-to design with MS/Blank trials and Figure/Catch ones, resulting in four conditions MS-Catch, MS-Figure, Blank-Catch and Blank-Figure. In order to gain a better understanding of the propagation of MS-induced changes from V1 to V4, we analysed first only trials of the Catch condition. The exact dynamics of the visual response evoked in V4 by Catch trials differed between monkeys (fig. 2A, left and middle panels); however since both are visual

responses of area V4 to the same stimuli we worked with the average response (fig. 2A, right panel).

Next, we studied how this evoked response in V4 was affected by electrical stimulation of area V1. To this end, in each session we stimulated one of the V1 electrodes 50 ms before stimulus onset, while recording from several V4 electrodes with different degrees of overlapping between their receptive fields and the one of the stimulated electrode (fig. 2E, C). Thus, given a certain V1 electrode we had several electrodes in V4 from which we recorded. A certain unique combination of V1 and V4 electrode could occur in more than one session, in which case we averaged across sessions. An exploration of the MS effect on individual sessions revealed the presence of both an excitatory as well as an inhibitory phase on V4 (fig. 2C). In order to quantify this effect, and since the excitatory phase clearly dominated the phenomena, we computed the mean difference between the average responses to MS-Catch trials minus Blank-Catch trials over a window of 50 ms after MS onset (fig. 2D). It is important to notice that the effect starts to take place during the stimulation window and peaks right after stimulation offset. This is indicative that the effect we observed is really an excitatory phase and not an artifact of the stimulation. This can be appreciated even in more detail on the signal of individual trials when comparing MS-Catch trials with Blank-Catch ones (fig. 2E). Of all the recorded electrodes 90.1% had a significant effect (fig. 2F). Moreover, the average effect size of the significant electrodes 0.62 ± 0.03a.u. (mean $\pm$ s.e.m.) was significantly different from zero ($p < 0.01$, $t_{146} = 23.5$). It is interesting to notice that as expected, the normalised effect size (i.e. the effect size divided by the current used for that electrode) correlates positively ($r^2 = 0.1$, $p < 0.01$) with the degree of overlapping between the receptive fields (fig. 2F). All in all, after averaging across electrodes with a significant effect, we can clearly observe the presence of both an excitatory and an inhibitory phase on V4 induced by V1 MS (fig. 2G).

As a first step in studying the propagation of MS-induced changes in V1 in the feedforward direction, we started stimulating before stimulus onset. Next we studied how this changes in V4 due to V1 MS depended on the SOA between the texture and the stimulation onset.

2.3 Influence of SOA on V1-MS effect

To address this question we stimulated at 50 ms and 150 ms after stimulus onset and computed the average response to MS-Catch and Blank-Catch trials in the same manner as in the previous section (fig. 3A, C). As before, in order to compare the effect of different SOAs, we computed the difference between the MS-Catch and Blank-Catch traces. Again, in every SOA we observed a presence of both the excitatory and inhibitory phase (fig. 3D, E). Even though the suppressive phase was independent of the SOA, an ANOVA analysis revealed a significant effect of the SOA on the strength of the excitatory phase ($F_{2,384} = 61.91$, $p < 0.01$, e of both the excitatory and inhibitory phase (fig. 3D, E). Moreover, a post-hoc testing revealed significant differences between all three groups ($p < 0.01$ for all three comparisons, Bonferroni corrected).

Since the strongest effect occurred when stimulating during the baseline period, the weakest during the peak response and stimulation during the sustained period yielded an intermediate effect, we studied whether the effect size was dependent on the level of activity in V4 during the stimulation period. To that end, we computed the average response on Blank-Catch trials on the

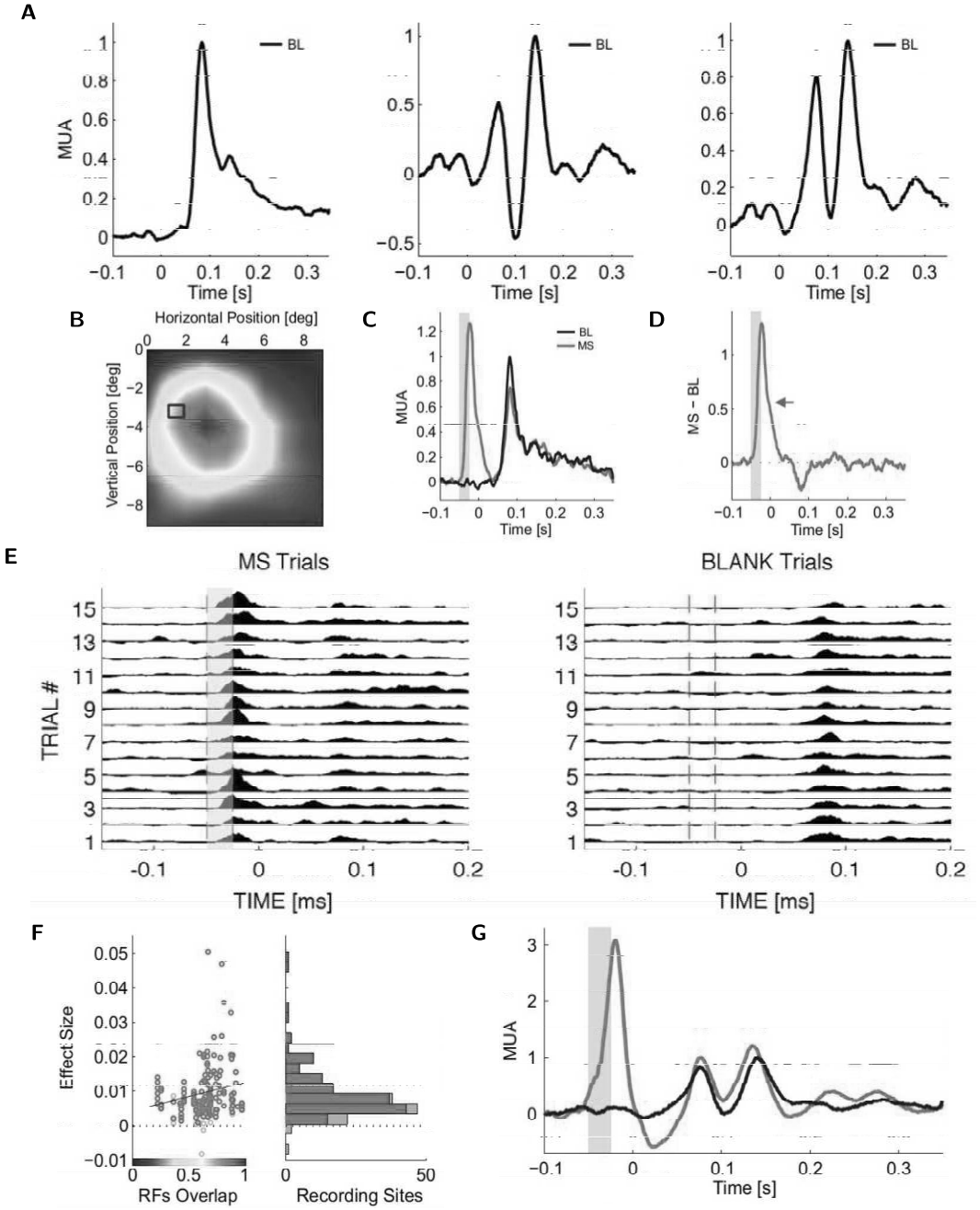

FIGURE 2: **Feedforward propagation of MS-induced changes.** (**A**) Average MUA response to Blank-Catch (catch trials without MS). **Left**: monkey B; **Middle**: monkey C; **Right**: Average. (**B**) Overlap between the RF of the stimulated V1 electrode and the RF of the V4 recording site for an example combination of electrodes. (**C**) Average MUA in response to Catch trials of an example combinations of electrodes for Blank trials (black) and MS trials with an SOA of -50 ms (red). Yellow area indicates the period of MS. (**D**) Difference between MS and Blank trials for the example traces of Fig. 2e. The arrow indicates the value of the effect size for this example. (**E**) Single trials for this example electrode for MS as well as Blank trials. Dashed lines indicate the stimulation period on MS trials and the equivalent period on Blank trials for comparison. (**F**) On the left panel, the correlation between normalised effect size (effect size/amplitude of stimulation) and the degree of overlap between the stimulated V1 RF and the RF of the corresponding V4 electrode. Dark red circles indicate significant electrodes. On the right panel: a histogram of the effect sizes. (**G**) Average MUA across monkeys and electrodes for Blank trials (black) and MS trials with an SOA of -50 ms (red). Yellow area indicates the period of stimulation.

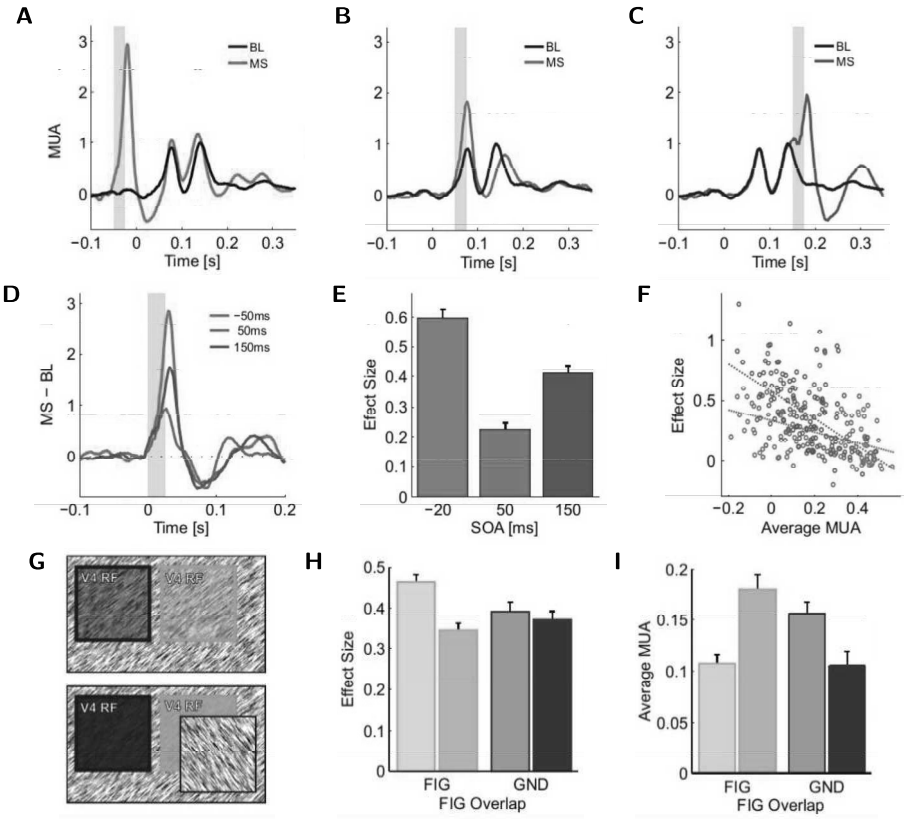

FIGURE 3: **SOA dependence of feedforward propagation of MS-induced changes and its interaction with a figure stimulus.** **(A)**-**(C)** Average MUA across monkeys and electrodes for Blank (black) and MS trials for SOAs of -50ms, 50ms and 150ms respectively. Yellow area indicates the period of stimulation. **(D)** Difference between MS-Catch and Blank-Catch trials for all SOAs aligned to stimulation onset. Yellow area indicates the period of stimulation. e, Average effect size for all SOAs. Error bars indicate s.e.m. **(F)** Correlation between effect size and the average MUA during blank catch trials for the same time window in which the effect size was computed. Green data points represent single electrodes at an SOA of 50ms. Green dashed line indicates the linear regression. Blue data points and dashed lines represent equivalent data for the SOA of 150 ms. **(G)** Schematic representation of the different conditions utilised to study the interaction between the feedforward propagation of MS induced changes and the presence of a figure stimulus. Electrodes were divided in two groups based on whether they would or not overlap with the figure on figure trials. Dark grey and dark orange represent electrodes on figure trials; whereas light grey and light orange represent those same electrodes during Catch trials (in the absence of a figure stimulus). **(H)** Average effect size for conditions in Fig. 3g. Orange bars represent electrodes that overlap (or would overlap) with the figure, while grey bars indicate electrodes that do not (or would not) overlap with the figure. Light colours indicate Catch trials, while dark ones indicate Figure trials. Error bars indicate s.e.m. **(I)** Average MUA for conditions in Fig. 3g on Blank trials measured in the same time windows utilised to compute the effect Size. Orange bars represent electrodes that overlap (or would overlap) with the figure, while grey bars indicate electrodes that do not (or would not) overlap with the figure. Light colours indicate Catch trials, while dark ones indicate Figure trials. Error bars indicate s.e.m.

same window of time in which we computed the effect size on MS-Catch trials and plotted those values against the effect size of the corresponding electrode. Since during pre-stimulus onset time the activity level will always be zero due to the normalisation of the data, we computed this correlation only for positive SOAs. For both SOAs, the effect size was inversely correlated with the level of activity during Blank-Catch trials ($r^2 = 0.17$, $p < 0.01$ for SOA 50 ms; $r^2 = 0.28$, $p < 0.01$ for SOA 150 ms; fig. 3F). In other words, the level of excitation induced in V4 due to V1 MS depends on the activity level. The higher the activity in V4, the lower the induced excitation will be.

So far we have only analysed the effect of MS on trials of the Catch condition. Since we wanted to shed some light on how feedforward and feedback signals are involved in the perception of a visual stimulus, we next analysed how this excitatory phase of the MS-induced changes interacted with the presence of a figure on Figure trials. To this end, we divided V4 electrodes based on whether they were overlapping or not with the figure. As an internal control, we kept the same division also for Catch trials even though there was not a figure present in them. This allowed us to directly compare how the effect size on a given electrode was affected by the presence of the figure compared to when there was only a texture (fig. 3G). Since we wanted to study the interaction with the figure, we only included trials with MS SOA of 150 ms (i.e. during the sustained activity period). For electrodes overlapping with the figure, the effect size was significantly reduced on Figure trials compared to Catch trials ($p < 0.01$, $t_{201} = 7.01$). However, for non-overlapping electrodes there was no significant difference between conditions ($p > 0.3$, $t_{98} = 1.04$, fig. 3H). Since the effect size is inversely correlated with the level of activity, and we know from previous studies that the presence of a figure enhances the firing of the neurons (Lamme, 1995; Poort et al., 2012; Roelfsema et al., 1998), this reduction of effect size in the presence of a figure is somehow expected. To check that indeed the level of activity increased in the presence of the figure, we computed the mean activity during Blank trials in the same time window in which we computed the effect size. As expected, the activity for the overlapping electrodes is higher in the presence of the figure compared to the activity during Catch trials ($p < 0.01$, $t_{201} = -3.8$). On the non-overlapping electrodes we observed the opposite effect. The presence of a figure in the vicinity of the electrode resulted in a reduction in activity ($p < 0.01$, $t_{98} = 7$, fig. 3I).

As we previously showed, the effect size in the feedforward direction is inversely correlated with the level of activity. Thus, the changes in the presence of the figure for the RFs that fall on the figure can be explained by the increase in activity induced by the figure. When the figure is present and it overlaps with the electrode, the activity increases and hence the effect size is reduced. On the ground however we did not observed the same pattern. Even though the activity level in V4 was reduced in the presence of the figure, the effect size did not change, suggesting that either V1 cells are less susceptible to MS-induced changes when they fall on the background or that connections from V1 to V4 in that condition are less effective. All in all, the propagation of excitatory MS-induced changes in the feedforward direction is at least to some extent dependent on the activity level in V4 at the moment of the stimulation, whereas inhibitory effects are independent. Thus, suggesting that this late suppression is a local reaction to the excitatory phase, probably due to the recruitment of nearby inhibitory cells.

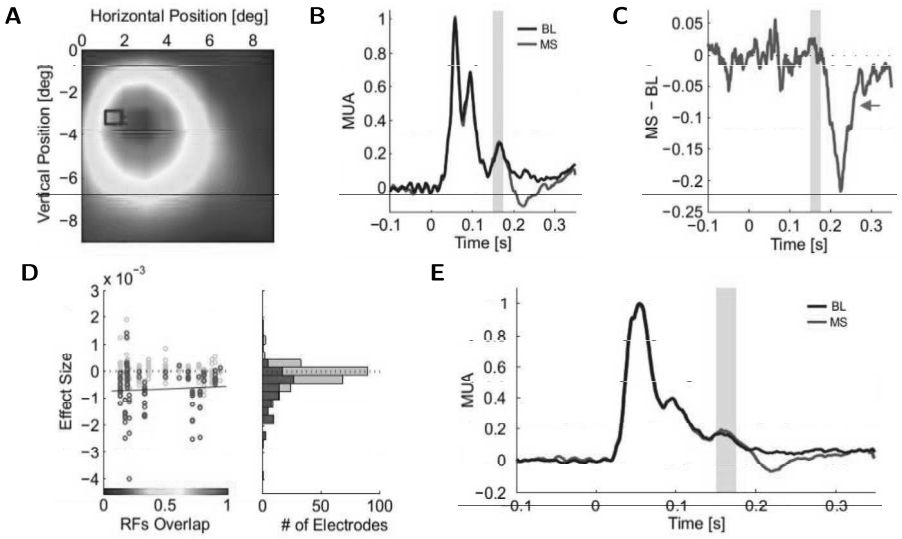

FIGURE 4: **SOA dependence of feedforward propagation of MS-induced changes and its interaction with a figure stimulus.** **(A)** Overlap between the RF of the stimulated V4 electrode and the RF of the V1 recording site for an example combination of electrodes. Colour scale as in (D). **(B)** Average MUA for electrodes combination in (A) in response to Blank-Catch trials (black) and MS-Catch trials with an SOA of 150 ms (blue). Yellow area indicates the period of MS. **(C)** Difference between MS and Blank trials for the example traces of (B). The arrow indicates the value of the effect size for this example. **(D)** On the left panel, the correlation between normalised effect size (effect size/amplitude of stimulation) and the degree of overlap between the stimulated V4 RF and the RF of the corresponding V1 electrode. Dark blue circles indicate significant electrodes. On the right panel: a histogram of the effect sizes. **(E)** Average MUA across monkeys and electrodes for Blank-Catch trials (black) and MS-Catch trials with an SOA of 150 ms (blue). Yellow area indicates the period of stimulation.

Next, we wondered what happened in the opposite direction. If we stimulated in V4 while recording in V1, will we see both phases as well or will it be that only one of the phases (either the excitatory or the inhibitory one) is reflected in V1?

2.4 Propagation of V4-MS effect

To study how MS induced changes in area V4 were reflected in area V1, we did the inverse experiment. We recorded from electrodes in area V1 while stimulating one of the chronically implanted electrodes in area V4 (fig. 4A). Since a specific combination of V4-V1 electrodes was repeated in more than one session, we averaged across days in order to obtain the average response of an electrode. As we were analysing propagation in the feedback direction we started analysing MS-induced changes during the sustained activity period (i.e. SOA of 150 ms). An exploration of the individual electrodes yielded a surprising result. After stimulation of V4 there was no replication in V1 of the excitatory phase. However in a significant amount of the sessions there was a reflection of the inhibitory phase (fig. 4B). To quantify this effect we computed the difference between the average of MS-Catch trials minus the average of Blank-Catch trials and computed the size effect as the average difference over a 175 ms window after stimulation offset (fig. 4C). Out of the 268 electrodes combinations from which we recorded, 108 showed a significant effect. Unlike the V1 stimulation experiments, in this case there is no correlation between the

overlap between stimulation and recording RFs ($r^2 = 0.01$, $p > 0.4$, fig. 4D). This might sound counter-intuitive, however it is important to notice that the feedback connections from V4 to V1 are not as localised as the ones that run from V1 to V4 (Salin & Bullier, 1995). Thus, the spread of the inhibition in V4 could be reflected in V1 electrodes nearby the stimulated V4 RF even though they are a couple of degrees away form the V4 hotspot. All in all, the average effect size for the electrodes with a significant effect is -0.03 ± 0.003 a.u. (mean $\pm$ s.e.m., $p < 0.01$, $t_{107} = -9.7$, fig. 4D, E).

This is quite an intriguing result. Even though MS in V4 elicits both an excitatory and an inhibitory phase, we only observed a reflection of the inhibitory one in V1. In one hand, the lack of an excitatory effect in V1 reveals a clear asymmetry in the system. While on the feedforward direction both fast (excitatory) and slow (inhibitory) changes propagated, on the feedback direction only the slow changes did. These results provide evidence that feedback connections are more susceptible to propagate slow "modulatory-like" signals. Fast signals seemed to get filtered out.

Regarding the suppressive phase, there are two ways in which it could be explained. One option is that the activation of V4 cells with axons reaching V1 triggers inhibitory neurons in V1, which in turn suppress the activity of V1 excitatory cells. Another possible explanation is that due to the inhibition in V4 generated by the MS V1 cells get less feedback input from V1, thus decreasing their firing. However, before discussing these possibilities, it is important to study how this suppression depends on the SOA and furthermore, how it is affected by the presence of a figure.

2.5 Influence of SOA on V1-MS effect

To study how the effect depended on the SOA, we stimulated also 50 ms after and 20 ms before stimulus onset. As before, we first analysed the results of the Catch trials alone. Even though there was a significant amount of suppression in all SOAs, an ANOVA analysis confirmed an effect of SOA on the effect size ($F_{2,351} = 50.97$, $p < 0.01$). Moreover, the effect size between SOAs of -20 ms and 50 ms were not significantly different ($p > 0.017$), while for the SOA of 150 ms the effect size was significantly bigger than for the other two SOAs ($p < 0.01$, fig. 5A-E) . These results provide clear evidence that the suppression of activity in V4 is strongly linked to the dynamics of feedback connections. During baseline period, in which there is little or no contribution of feedback connections from V4 to V1 there was only a mild suppression. In contrast, during the sustained activity period (in which feedback connections are known to play a major role (Khayat et al., 2004; Lamme, 1995; Lamme & Roelfsema, 2000; Poort et al., 2012; Roelfsema et al., 2002) we observed a much stronger suppression effect.

Next, we studied how the amount of suppression depended on the level of activity in V4 at the moment of the suppression. The first indication that the effect size and the level of activity might not be correlated comes from the population traces. Even though the activity level for the 50 ms SOA is much higher than for the 150 ms SOA, its effect size is considerably smaller. Nonetheless, to properly address this question we looked at the correlation between effect size and activity level of Blank-Catch trials for SOAs of 50 ms and 150 ms. If it is the case that the amount of suppression in V1 depends on the level of activity at the moment and during the stimulation,

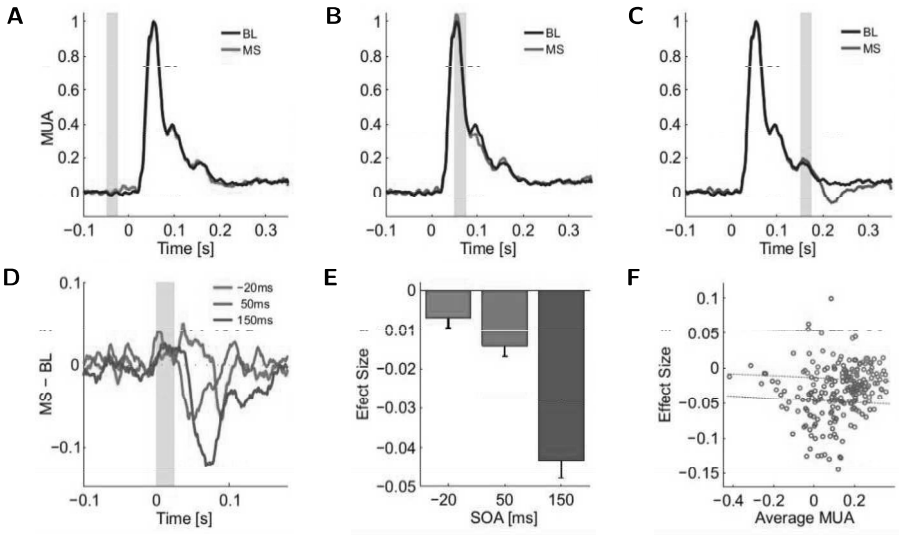

FIGURE 5: **SOA dependence of feedforward propagation of MS-induced changes and its interaction with a figure stimulus.** **(A)**-**(C)** Average MUA across monkeys and electrodes for Blank-Catch trials (black) and MS-Catch trials for SOAs of -20 ms, 50 ms and 150 ms respectively. Yellow area indicates the period of stimulation. **(D)** Difference between MS-Catch and Blank-Catch trials for all SOAs aligned to stimulation onset. Yellow area indicates the period of stimulation. **(E)**Average effect size for all SOAs. Error bars indicate s.e.m. **(F)** Correlation between effect size and the average MUA during blank catch trials for the same time window in which the effect size was computed. Green data points represent belong to single electrodes at an SOA of 50 ms. Green dashed line indicates the linear regression. Blue data points and dashed lines represent equivalent data for the SOA of 150 ms.

then these two measures should be correlated. However, in support of our hypothesis, they were not correlated ($r^2 = 0.004$, $p > 0.4$ for SOA 50 ms, $r^2 = 0.002$, $p > 0.5$ for SOA 150 ms; fig. 5F).

These results provide evidence that the propagation of the suppressive phase of the MS-induced changes form V4 to V1 is strongly linked to the dynamics of feedback connections. Knowing this and knowing that feedback connections are heavily involved in figure-ground tasks, we next studied how this effect would be affected by the presence of a figure, either overlapping or non-overlapping with the V1 RF.

2.6 Interaction of V4-MS effect and figure-ground task

We divided electrodes in three groups depending on their position relative to the figure on Figure trials. We defined different regions based on the radial distance from the centre of the figure to the center of the V1 RF, with boundaries at 3 and 6 degrees of visual angle (deg) (fig. 6). Thus, we had three groups: electrodes that on Figure trials would overlap with the figure (FIG condition), electrodes that will be in the near ground (i.e. in the vicinity of the figure; NEAR condition) and electrodes in the far-ground (i.e. far away from the figure; FAR condition). As expected, the activity of electrodes that overlapped with the figure increased in Figure trials compared to Catch trials (fig. 7A), while the activity of electrodes far away from the figure remained unchanged between conditions (fig. 7C). The activity of electrodes in the vicinity of the figure deserves a special mention. Consistent with recent literature (Poort et al., 2012), we observed that the activity of these electrodes decreased when compared to their activity during

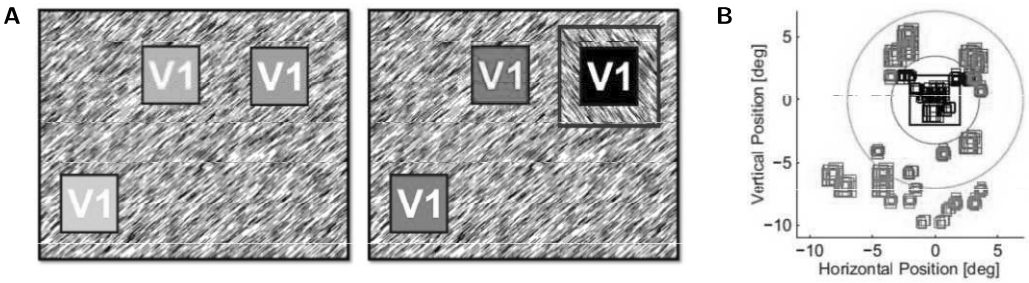

FIGURE 6: **RFs and figure configuration.** **(A)** Schematic representation of the different conditions utilised to study the interaction between the feedback propagation of MS induced changes and the presence of a figure stimulus. Electrodes were divided into three groups (FIG, NEAR and FAR) based on what their distance would be to the centre of the figure on Figure trials. Dark boxes represent electrodes on Figure trials; while light ones represent those same electrodes during Catch trials (in the absence of a figure stimulus). **(B)** Distribution of V1 electrodes with respect to the centre of the figure. Dashed circles indicate the boundaries for the groups' categories. Black circle has a radius of 2 degrees of visual angle whereas the red one has a radius of 6 degrees of visual angle.

Catch trials (fig. 7B). This result, even though it is not novel per se, reinforces the idea that the neurons close to the figure either receive less input from higher areas or get actively suppressed by them.

Next, we studied the interaction between these different conditions (i.e. FIG, NEAR and FAR) and the reduction of activity during the sustained activity period observed in the last section. For FIG electrodes, the effect size increased when comparing Figure trials with Catch trials ($p < 0.01$, $t_{118} = 2.9$, fig. 7D, F), while for NEAR electrodes the effect size was completely abolished ($p < 0.01$, $t_{111} = -5.7$, fig. 7D, G). On the FAR condition the effect size was not affected by the presence of a figure ($p > 0.05$, $t_{142} = -1.7$, fig. 7D, H). Thus, the effect size is correlated with the difference in activity between catch and Figure trials. In we consider this difference in activity to be the feedback contribution form higher areas to lower areas, we can conclude that the amount of suppression is positively correlated with the amount of feedback from V4 to V1.

However, as we just pointed out, activity levels on the near-ground condition on Figure trials is decreased when compared to Catch trials, while it is increased on the figure condition. Thus, it could be that we did not observe suppression on near-ground electrodes because their activity was already so low that they could not go any lower. To test this potential confound we plotted the effect size of each electrode for the two conditions against the mean level of activity (fig. 7E). Especially interesting were the electrodes with a positive mean value (i.e. activity during the sustained activity period was higher than during baseline, meaning that their activity level could have been lower). From this plot we can see that the mean effect size for the figure condition is significantly bigger than for the near-ground one, even for identical levels of activity.

3 Discussion

In the present study we analysed how electrically-induced changes propagates through the visual cortex. We first corroborated that electrical stimulation of the cortex results in a biphasic

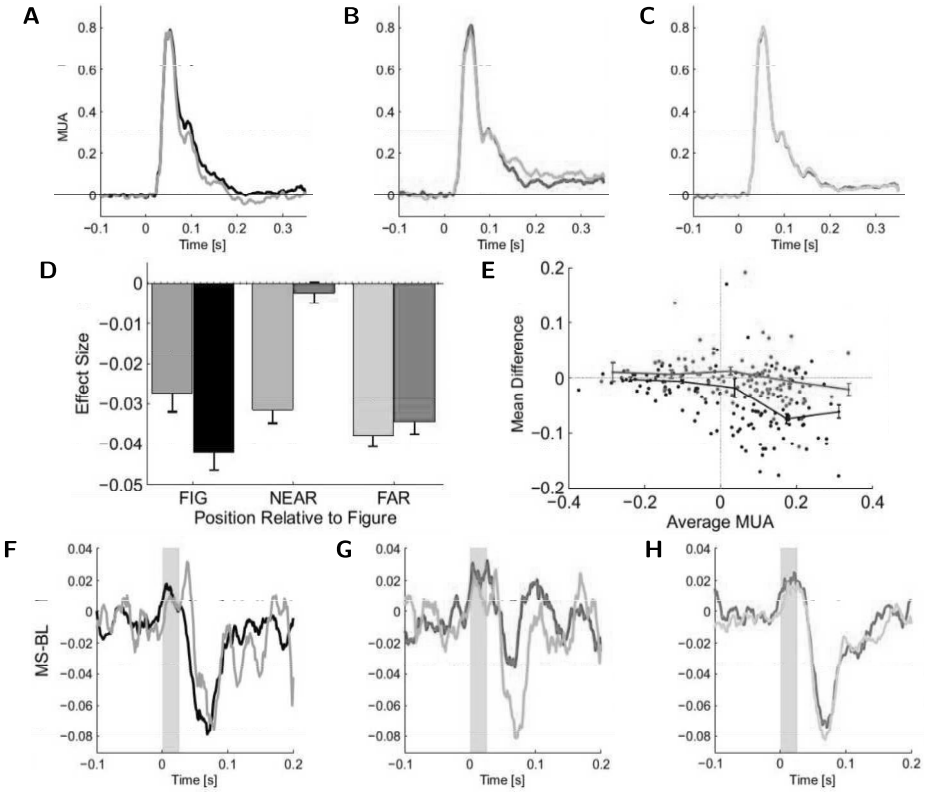

FIGURE 7: **Interaction between the feedback propagation of MS-induced changes in the cortex and a figure stimulus.** **(A)**-**(C)** Average MUA response for Catch trials (light traces) and Figure trials (dark traces) for the three conditions FIG, NEAR and FAR respectively. **(D)** Average effect size for the different conditions at an SOA of 150 ms. Grey bars represent electrodes that overlap (or would overlap) with the figure. Red bars indicate electrodes that are (or would be) on the near surrounds of the figure. Green bars represent electrodes that are (or would be) far away from the figure. Light colors indicate Catch trials, while dark ones indicate Figure trials. Error bars indicate s.e.m. **(E)** Relationship between effect size and mean MUA response in Catch trials during the same time window utilised to compute the effect size. Dots represent single electrodes, while the continuous line corresponds to the average effect size for 5 equispaced bins. Error bars indicate s.e.m. Red dot and continuous line represent electrodes from the NEAR condition; while black ones represent electrodes from the FIG condition. **(F)**-**(H)** Difference between MS and Blank trials aligned to stimulation onset at an SOA of 150ms for Catch trials (light traces) and Figure trials (dark traces) for the three conditions FIG, NEAR and FAR respectively. Yellow area indicates the period of stimulation.

phenomenon composed of a fast and brief excitatory phase, followed by a long lasting suppression of activity. Next, we studied how these two phases would propagate from V1 to V4 (feedforward) as well as from V4 to V1 (feedback). When stimulating in V1, we observed that both phases were replicated in V4, while when we stimulated V4 only the suppressive phase was present in V1. Finally, we tested whether these effects interact with the presence of a figure in the visual field. In both cases we observed an interaction with the figure. On the feedforward direction the effect was correlated with the amount of activity in V4 at the moment of the stimulation, while in the feedback direction results indicate that the effect size depends on the amount of feedback input from V4 to V1. Moreover, the results presented here suggest the presence of feedback contribution all across the visual field, even in complete absence of a figure stimulus.

3.1 Feedforward and feedback pathways

Both in the feedforward and in the feedback direction we observed a suppression of the activity due to MS. However, we only observed a propagation of the excitatory phase in the feedforward direction. This excitation is likely due to the propagation of excitatory activity from V1 to V4, which triggers a very similar response as the one that would be evoked by a visual stimulus. The reasons behind the inhibitory phase that follows the excitatory one in V4 are less clear. One possible explanation for this suppression is the reduction in activity in V1 caused by the MS. If there is less activity in V1 there is less input to V4 cells, thus resulting in a reduction of activity in V4. Another plausible explanation is that inhibitory cells in V4 are recruited by the excitatory phase. By the time that inhibition arrives the electrical stimulation is over and there is much more inhibition than excitation which also results in an increased amount of suppression. If this would be the case then the amount of suppression should be proportional to the amount of excitation, however this is not what we observed. Thus, even though we cannot rule out any of these two hypotheses we believe the data presented here argues in favour of the first alternative.

These results do not give us new insight into the mechanisms and dynamics of feedforward connections, however they are very interesting when compared to what happened on the feedback direction. We observed that feedforward pathways are sensitive to both fast and slow changes in neural activity. In contrast, when stimulating in V4 we only observed a reflection of the slow, suppressive phase in V1. Even though there are direct connections from V4 to V1 and it is very likely that they are being activated as a consequence of the MS, the activation does not trigger a fast and strong activation of excitatory cells in V1. V4 MS is reflected in V1 only through the long lasting suppression in activity. In a way it acts as a low pass filter: only slow and long lasting changes in activity are transmitted through feedback connections. This result is consistent with previous work that showed that feedforward connections are linked to AMPA receptors, which have fast dynamics, while feedback pathways involve NMDA receptors, which have slower reaction times (Self et al., 2012).

One possible explanation for this reduction in activity is that the cells activated in V4 target inhibitory cells in V1 (or in intermediate areas like V2), thus provoking local suppression that results in a reduction of activity in V1. Since we did not see any signs of excitatory signals in V1, it seems somehow unlikely that there would be only activation of inhibitory cells but not of excitatory ones. Even though it is not known for primates, there is evidence in rat visual cortex that feedback connections target approximately the same amount of inhibitory cells as excitatory ones (Wang & Burkhalter, 2013). If a similar results hold across species, then we should have seen at least as much excitation as suppression. Moreover, even though there is evidence of inhibitory effects of feedback connections (Chen et al., 2008; Nassi et al., 2013), most of the effects of feedback pathways are thought to have a net excitatory effect. Even though we cannot completely rule out this mechanism, we believe that a more likely explanation is that the suppression we see in V1 is a consequence of the reduction in activity in V4. Thus, the reduction of activity in V1 would not be caused by the fast excitatory effect induced by MS in V4, but rather by the long lasting suppression that follows. This hypothesis would be in agreement with the vast body of literature that reported excitatory effects of feedback connections and would also explain why the suppression in V1 occurs even in the absence of a previous excitatory effect.

Moreover, it would also explain why we observed an effect mostly during the sustained activity period and not so much during the baseline period or during the peak response.

An interesting consequence of this interpretation is that since the reduction in activity also occurred during Catch trials, it implies that there is a feedback contribution from V4 to V1 even in the absence of a relevant stimulus. This is a very interesting observation, since the normal interpretation is that feedback contributions only take place during the segmentation of the figure from the background. There have been some propositions that this might not be the case (Lamme, 2006; Super et al., 2001). However, as far as we know, this is the first experimental evidence that can contribute to this proposal.

3.2 Figure-ground interactions – Feedforward

To gain understanding on the role of feedforward and feedback connections in a figure ground segregation task, we leveraged on the effects triggered by MS.

In the feedforward direction we divided V4 electrodes in two groups depending on whether the centre of the figure overlapped or not with their corresponding receptive field. On the overlapping electrodes we observed a reduction of the effect size when the figure was present compared to Catch trials. We were not surprised to see such a reduction because we knew that there is a negative correlation between the activity level that would have been evoked by the textured background and the amount of excitation that can be induced in V4 due to V1-MS. We observed that the higher the activity level in V4 the smaller the amount of excitation that can be induced. In other words, the reduction of effect size when the figure is present can be explained by the extra activity it induced in V4.

More interesting are the electrodes whose receptive field did not overlap with the figure. In these electrodes we did not observe a difference in effect size, although we did observe a significant reduction in activity on Figure trials. This result is rather odd since in all the other cases there was a negative correlation between levels of activity in V4 and the effect size. Since activity in V4 during Figure trials without MS is reduced by the presence of the figure in the surroundings, we expected to observe an increase in effect size. This change in the properties of the propagation could be due to a change in the efficiency of the connections or because V1 itself is less susceptible to MS-induced changes. It is not possible to decide from the data presented here which one is the correct answer. It is however clear that the presence of the figure modifies the properties of the network on the surroundings of the figure.

3.3 Figure-ground interactions – Feedback

To study how feedback connections are involved in a figure-ground segregation task we divided V1 electrodes in three groups depending on their distance to the centre of the figure on Figure trials (FIG: on the figure, NEAR: on the surroundings of the figure and FAR: far away from the figure). As expected, the activity of V1 with RFs that overlapped with the figure increased their activity while activity in electrodes far away from the figure did not change. However, activity in the intermediate electrodes decreased during Figure trials. The same pattern is observed when

quantifying the effect size: it increases in overlapping electrodes, stays the same on distant ones and is completely absent on the intermediate ones.

As discussed previously, the most likely explanation for the reduction of activity in V1 is a reduction in the amount of feedback received from V4. Thus for the role of feedback connections in a figure-ground segregation task, this result suggests that cells that overlap with the figure get increased feedback while cells in the vicinity of the figure do not get any feedback at all. This could be expected, however the surprising part is that it suggests that cells far away from the figure keep getting a substantial amount of feedback from V4. This contribution of V4 to lower areas in regions of the visual field which in principle are not involved in the task at hand are a unique contribution to the field and could have not been predicted based on previous studies.

There is one potential confound with this interpretation and it is that the only case in which we observed a complete reduction in effect size is also the one in which the level of activity is the lowest. To address this issue we studied whether it was not a flooring effect by plotting the effect size against the mean level of activity in Blank trials during the same time window for both FIG and NEAR electrodes. Since electrodes with positive average activity have completely different effect sizes dependent on whether they are from the FIG or the NEAR group, we can conclude that the reduction of the effect size on the NEAR electrodes is not very likely to be due to a flooring effect.

There is a general agreement that feedback connections are involved in the increase of activity at the location of the figure, however there is debate in what happens both on the vicinity of the figure and at distant locations. Our results confirmed the involvement of feedback connections at the figure locations as well as provided new insight on what happens at the other locations. We provide conclusive evidence that there is V4 input to V1 through out all the visual field, even at locations that are far away from the figure. When there is a figure present, that input is increased at the location of the figure and completely reduced in its surroundings.

This lack of feedback in the nearby location could also explain why we observed a reduction in efficacy transmission of activity in the feedforward connection. If feedback from V4 to V1 is reduced on the vicinity of the figure it could have consequences on how susceptible those cells are to stimulation coming from area V1.

3.4 Antidromic vs orthodromic effects

In this study we used microstimulation to perturb activity in one area and to investigate the influence on activity in another area. Microstimulation activates axons in the vicinity of the electrode tip (Butovas & Schwarz, 2003; Histed et al., 2009) and can cause orthodromic and antidromic stimulation effects. By combining microstimulation in a lower area with recording in higher areas, we aimed to investigate the orthodromic influence of feedforward connections and we combined microstimulation in a higher area with recording in a lower area to investigate the orthodromic effects of feedback connections. However, there is one important caveat. We also have to consider antidromic effects, which occur if axon terminals of projection neurons are stimulated and action potentials travel back to their cell bodies in another area. These antidromic effects might blur the distinction between feedforward and feedback influences. We

took a number of measures to reduce the contribution of antidromic stimulation. Firstly, we used current levels that cause most neurons to be stimulated transynaptically (Butovas & Schwarz, 2003), which in previous studies between areas with strong direct projections caused orthodromic stimulation effects that were several times stronger than antidromic effects (Girard et al., 2001; Movshon & Newsome, 1996). Secondly, we chose two areas, V1 and V4, with relatively sparse direct connectivity (Markov et al., 2011b). Most of the interactions between neurons in these areas are therefore presumably mediated by intermediate area V2, which is strongly interconnected with both V1 and V4. Antidromic activation of V2 neurons by V1 microstimulation can only cause transynaptic, feedforward effects in V4. Vice-versa, if V4 stimulation antidromically activates of V2 neurons, these cells can, in turn, only cause genuine feedback effects in V1. Thirdly, the direct comparison of V1 and V4 microstimulation provides an internal control for the purity of the feedforward and feedback effects. If the influence of microstimulation in both directions would have been the same, it would have indicated that antidromic influences blurred the distinction. However, since there is a clear asymmetry it provides support for the predominance of orthodromic influences. All in all, even though is not possible to rule it out completely, we believe that any possible contribution of an antidromic effect is either negligible or non-existent.

3.5 Conclusions

As a mean to study how visually-evoked activity propagates through the cortex as well as how it gives rise to perception we stimulated the visual cortex while recording in other areas. We found that electrical activity evoked by MS under a demanding cognitive task propagates through the visual cortex both in feedforwad and feedback directions, but with different properties and dynamics. Feedforward pathways are susceptible to both fast and slow changes in activity while feedback connections filter out fast changes and convey only slow modulations of neural activity. In particular V4 MS resulted in a reduction of activity in V1, most likely as a result of a reduction of activity in V4 itself. In addition, the propagation in both feedback and feedforward directions showed an interaction with the figure stimulus in a figure-ground segregation task. All together, these results suggest that during a figure-ground segregation task there is a feedback contribution from V4 to V1 all over the visual field even in the absence of a relevant stimulus. Moreover, in the presence of a figure that feedback input is increased at the figure location and decreased in the surroundings of the figure while it remains unchanged on distant locations.

4 Methods

4.1 Surgery and mapping

Two monkeys (monkeys B and C) participated in this study. In a first operation, a head holder was implanted. In a separate surgery, arrays of 4x5 or 5x5 electrodes (Blackrock Inc.) with a thickness of 80 µm and a length of 1 or 1.5 mm were chronically implanted in areas V1 and V4. The surgical procedures were performed under aseptic conditions and general anaesthesia and complied with the US National Institutes of Health Guidelines for the Care and Use of

Laboratory Animals and were approved by the Institutional Animal Care and Use Committee of the Royal Netherlands Academy of Arts and Sciences. Details of the surgical procedures and the postoperative care have been described elsewhere (Poort et al., 2012; Super & Roelfsema, 2005). We measured the receptive field dimensions of every V1 recording site by determining the onset and offset of the response to a slowly moving light bar for each of four movement directions (Kato et al., 1978). V4 RFs were mapped by presenting white squares (1x1 deg) on a grey background at different positions of a grid (1 deg spacing).

4.2 Behavioural setup

The monkeys performed the task while seated at a distance of 75 cm from a 21 inch CRT monitor with a refresh rate of 100 Hz and a resolution of 1024x768 pixels. The eye position was monitored with a video based eye tracker (Thomas Recording) and sampled at 250 Hz. A trial was initiated when the monkey had maintained his gaze for 300 ms within a (virtual) fixation window, 1.5 deg in diameter, centred on the fixation point. The monkey obtained a juice reward at the end of each correct trial.

4.3 Fixation only task

To measure the neural changes induced by MS of the visual cortex we requested the monkeys to perform a simple fixation task while exposed to a texture. On each trial we presented a fixation point in the centre of the screen (0.3 deg in diameter) and the monkeys were requested to fixate on it for 300 ms in order to begin the trial. After that period, a texture of white lines on a black background (fig. 1A) was presented on the screen for a period of 500 ms, period in which the monkeys were requested to maintain fixation. After each correctly completed trial, a juice reward was delivered. In half of the trials MS was delivered to the cortex but monkeys did not had to react to it or report it in any way.

4.4 Figure-Ground task

To measure how the changes induced by MS in neural activity propagate through the cortex, we requested the monkeys to perform a figure-ground segregation task. A trial began with the fixation point (a red circle of 0.3 degrees of visual angle in diameter) presented on a grey background and the monkey triggered the beginning of the trial by directing gaze to a one degree fixation window centred on the fixation point. After 300 ms of fixation the texture stimulus was presented. After a further 350 ms, the fixation circle changed colour and the monkey was required to make a saccadic eye-movement into a target-window (2 deg in diameter) centred on the figure position. In this type of trials (figure condition), the figure could appear at two different locations. These locations changed across recording session. Correct responses were rewarded with juice. Trials in which the animal broke fixation before the fixation point was extinguished were aborted. On 33% of trials we presented a homogeneous texture without a figure (catch condition) and the animals were rewarded for carrying on fixating within the fixation window for a further 400 ms. All stimulus conditions were presented in a pseudorandom order.

The figure-ground stimuli were full-screen bitmaps of textures consisting of black oriented line elements (45 and 135 deg of orientation) on a white background. Two bitmaps of each texture orientation (i.e. two leftwards oriented and two rightwards oriented textures) were made with randomly placed elements. To make the figure stimuli, a square region of one bitmap of 4x4 deg was copied onto the same position of a full-screen bitmap of the orthogonal orientation.

In half of the trials MS was delivered to the cortex but monkeys did not have to react to it or report it in any way.

4.5 Microstimulation

We used negative-first biphasic pulses of 400 µs duration (200 µs per phase) at a frequency of 200 Hz, through one of the V1/V4 electrodes using a custom-made two-channel constant current stimulator. During the "fixation only" task only one pulse 150 ms after stimulus onset, with amplitude of 60 µA, was delivered through a V4 electrode. In the "figure-ground" task, we delivered a train of 5 pulses at -50 ms, 50 ms and 150 ms with respect to stimulus onset. To study the propagation in the feedback direction MS was delivered through one of the V4 chronically implanted electrodes, whereas to study feedforward propagation electrodes in V1 were used.

4.6 Data acquisition and artifact removal algorithm

Recordings were made with microelectrode grids in V1 and V4. Neuronal data was collected with TDT (Tucker Davis Technology) recording equipment using a high-impedance headstage (RA16AC) and a preamplifier (either RA16SD or PZ2) and sampled with a rate of 24.4 kHz.

For the "fixation only task" the data was band-pass filtered (500 Hz,–,5 kHz) and thresholded for spikes. On trials with MS the average ERP across trials was removed before the band-pass filter and a period of 1 ms (24 samples) was removed from the signal before thresholding.

For the "figure-ground task", on trials without MS, the digitised signals were band-pass filtered (500 Hz,–,5 kHz), full-wave rectified and low-pass filtered (200 Hz) to produce an envelope of the multi-unit activity (MUA). On trials with MS a modified version of this procedure was applied. Firstly, in each recording session, the average ERP across trials was subtracted from each individual trial. Then, after the signal was band-passed and rectified, a period of 1 ms (24 samples) centred around each pulse was removed from the signal. Consequently, the signal was low-pass filtered and finally missing samples were linearly interpolated. This procedure was not applied to non-MS trials because MUA obtained by both procedures did not differ.

This MUA signal provides an average of spiking activity of a number of neurons in the vicinity of the tip of the electrode and the population response obtained with this method is therefore expected to be identical to the population response obtained by pooling across single units. For the spectral properties of neuronal activity MUA gives a higher signal-to-noise ratio than single unit data (Super & Roelfsema, 2005).

Chapter 6

A Large-Scale Dynamical Model of Hierarchical Processing in the Primate Cortex

Hüter, ist die Nacht bald hin?

(Isaiah 21:11)
Felix Mendelssohn Bartholdy, symphony-cantata *Lobgesang*

Abstract

We developed a large-scale dynamical model of the macaque neocortex, which is based on recently acquired directed and weighted connectivity data from tract-tracing experiments, and which incorporates heterogeneity across areas. A hierarchy of timescales naturally emerges from this system: sensory areas show brief, transient responses to input (appropriate for sensory processing), whereas associative areas integrate inputs over time and exhibit persistent activity (suitable for decision-making and working memory). The model displays multiple temporal hierarchies, as evidenced by contrasting responses to visual versus somatosensory stimulation. Moreover, slower prefrontal and temporal areas have a disproportionate impact on global brain dynamics. These findings establish a circuit mechanism for "temporal receptive windows" that are progressively enlarged along the cortical hierarchy, suggest an extension of time integration in decision making from local to large circuits, and should prompt a re-evaluation of the analysis of functional connectivity (measured by fMRI or electro/magnetoencephalography) by taking into account interareal heterogeneity.

1 Introduction

The receptive field is a central concept in neuroscience, defined as the spatial region over which an adequate stimulus solicits rigorous response of a neuron (Sherrington, 1906). In the primate visual cortical system, the receptive field size of neurons progressively enlarges along a hierarchy (Hubel, 1988; Hubel & Wiesel, 1962; Wallisch & Movshon, 2008). As a result, higher areas can integrate stimuli over a greater spatial extent, which is essential for such functions as size-invariance of object recognition in the ventral ("what") stream for visual perception (Kobatake & Tanaka, 1994).

Accumulating evidence suggests that the brain also displays a hierarchy in the temporal domain. This allows neurons in higher areas to respond to stimuli spread over a greater temporal extent and to integrate information over time, while neurons in early sensory areas rapidly track changing stimuli. In human studies, preserving the short timescale structure of stimuli while scrambling long timescale structure changes responses in association areas but not early sensory areas (Gauthier et al., 2012; Hasson et al., 2008; Honey et al., 2012; Lerner et al., 2011; Stephens et al., 2013). Notably, using electrocorticography (ECoG), Honey et al. (2012) found that cortical areas sensitive to long time structure in the stimulus also shows lower decays in their temporal autocorrelation (and hence slower dynamics), and Stephens et al. (2013) made a similar observation with fMRI. In the macaque, Murray et al. (2014) found a hierarchical organisation in the timescales of spontaneous fluctuations of single neurons across 7 cortical areas, and an area's timescale was well predicted by its position in the anatomical hierarchy of Felleman & Van Essen (1991). Similarly, temporal correlations in neural activity reveal slower decay rates in the frontal eye fields than area V4 (Ogawa & Komatsu, 2010), the timescales of reward memory lengthen from parietal to dorsolateral prefrontal to anterior cingulate cortex (Bernacchia et al., 2011), and, more generally, persistent activity after a brief stimulus can last for seconds, even across inter-trial intervals, in association areas (Amit et al., 1997; Curtis & Lee, 2010; Histed et al., 2009). Finally, normative theories of predictive coding suggest that a hierarchy of timescales

would allow animals to form a nested sequence of predictions about the world (Kiebel et al., 2008). What underlying neurobiological mechanisms might give rise to such a range of temporal dynamics? For example, spatial patterns of convergence can produce increasing receptive field sizes in the visual hierarchy. Are there basic anatomical motifs that produce a hierarchy of timescales?

Here we report a large-scale circuit mechanism for the generation of a hierarchy of temporal receptive windows in the primate cortex. This hierarchy naturally emerges in a dynamical model based on a recent quantitative anatomical dataset containing directed and weighted connectivity for the macaque neocortex (Ercsey-Ravasz et al., 2013; Markov et al., 2013, 2014a, 2011b). The data were obtained using the same experimental conditions and measures, ensuring a consistent database (Kennedy et al., 2013), and include both the number of projections between areas and their laminar origins. Based on a separate anatomical study (Elston, 2000; Elston et al., 2011), we introduced heterogeneity across cortical areas in the form of a gradient of excitatory connection strengths. Strong recurrent excitation has been proposed as a mechanism by which prefrontal cortex could implement "cognitive-type" computations, such as information integration and memory-related delay activity; we hypothesized that differences in recurrent excitation might allow the generation of a temporal hierarchy.

The model thus incorporates anatomically constrained variation in both within-area and interareal connectivity and enables us to probe the interplay of local microcircuitry and long-range connectivity that underlies a hierarchy of timescales. Using different sensory inputs, we demonstrate the existence, in our model, of multiple dynamical hierarchies subserved by a single integrated global and local circuit. We then investigate the implications of local circuit heterogeneity for macroscopic dynamics measured by functional connectivity (i.e., correlations in activity across areas). Here we find a disproportionate role for slow dynamics in the prefrontal and other association cortices in shaping resting-state functional connectivity. This role is not predicted by long-range connections, suggesting that interpretations of brain imaging data will need to be revised to account for interareal heterogeneity.

While we have used the model to investigate the origin of a hierarchy of timescales, it can be a platform for future models relating connectivity to dynamics and the functions of cortical areas. Most statistical analyses of connectivity (Bullmore & Sporns, 2009; Sporns, 2014) and computational models (Deco & Corbetta, 2011; Deco et al., 2014; Ghosh et al., 2008; Honey et al., 2007, 2009) have lacked comprehensive high-resolution data, relying either on collating qualitative tract-tracing data across disparate experiments and conditions or on diffusion tensor imaging, which is noisy and cannot reveal the direction of a pathway. Moreover, such models typically treat cortical areas as identical nodes in a network, distinguished by connection patterns but not by local properties or computational capabilities. Although this approach is reasonable for certain purposes, it is doubtful that functional specialization of cortical areas can be elucidated without considering heterogeneity. Our model provides a framework to explore how dynamical and functional specialization can emerge from inter-areal pathways coupled with local circuit differences.

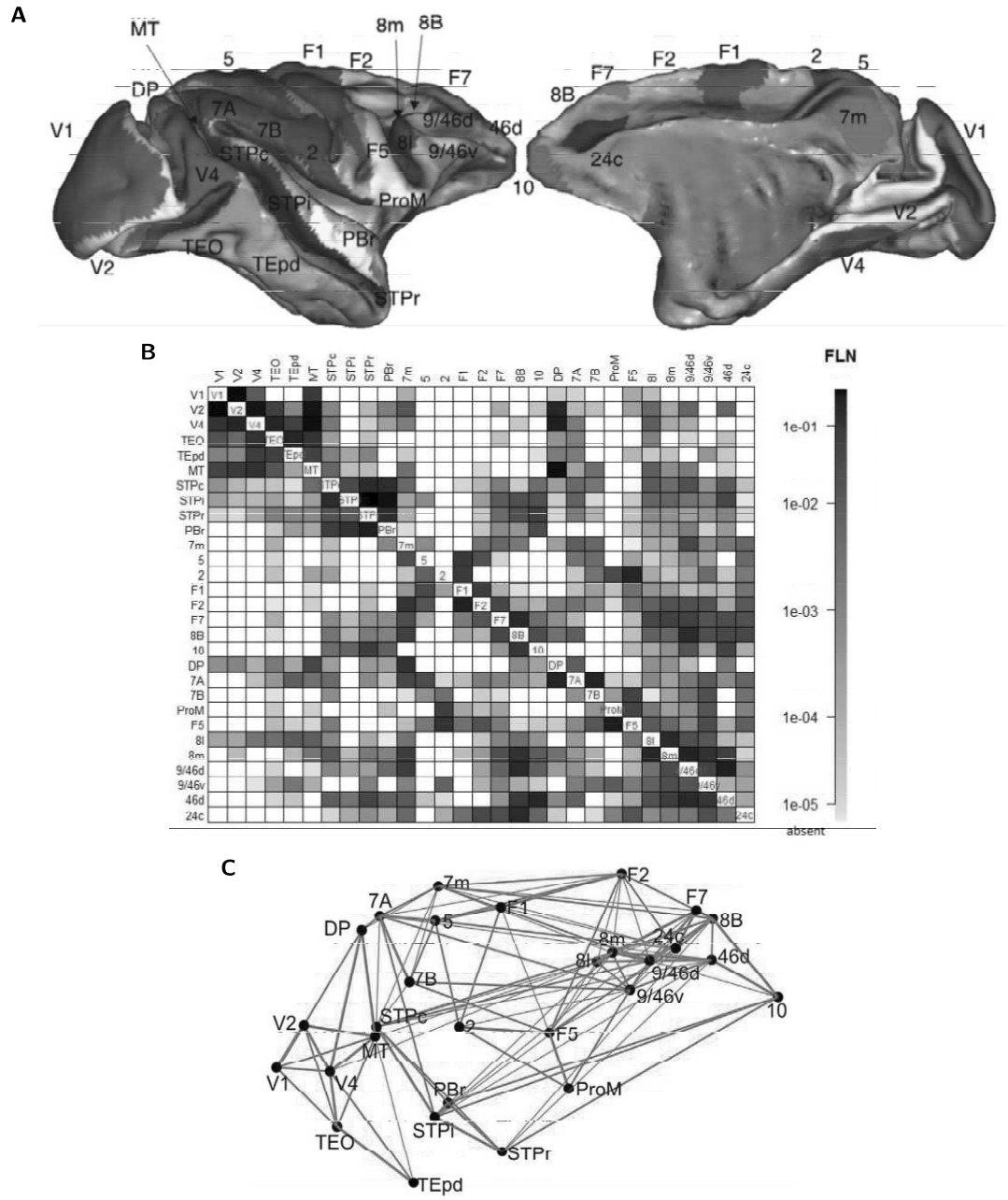

FIGURE 1: **The network consists of 29 widely distributed cortical areas.** The connectivity between this subset of the 91 areas is entirely known. **(A)** Lateral (left) and medial (right) plots of the macaque cortical surface with areas in colour. Plots generated with Caret (Van Essen et al., 2001a). **(B)** Connection strengths between all 29 areas. The strength of the projection from area A to area B is measured by the Fraction of Labelled Neurons or FLN (see section 4.1 of the Methods and table A.1). **(C)** Three-dimensional positions of areas along with strongest connections between them (FLN > 0.005). Connection strength is indicated by line width.

2 Results

2.1 Model design

We developed the model in three steps. First, we used recent connectivity data for the macaque neocortex (Markov et al., 2014a), designed to overcome the limitations of collated anatomical

datasets, and collected by the same group under similar conditions, with quantitative measures of connectivity. The connectivity weights are directionally specific and cover 29 widely distributed cortical areas, with 536 connections whose strengths span five orders of magnitude (fig. 1). The presence or absence of all projections in this network has been established; thus, there are no unknown pathways.

Second, each cortical area was described by a threshold linear recurrent network with interacting excitatory and inhibitory populations and calibrated by the neurophysiology of the primary visual cortex (Binzegger et al., 2009), but rescaled as described below. This is a highly simplified description of the dynamics of an area and ignores most within-area variability. In particular, note that the model is large-scale in that it addresses macroscopic cortical dynamics but is not large-scale in the sense of having millions of neurons or very high-dimensional activity. However, this level of complexity allows us to parsimoniously capture essential requirements for a hierarchy of timescales. We extend our results in fig. 7 and suggest further extensions in the discussion section.

Third, we hypothesised that the local microcircuit is qualitatively canonical (Douglas & Martin, 1991), i.e., the same across areas, but that quantitative inter-areal differences are crucial in generating the timescales of areas. Specifically, the number of basal dendritic spines on layer three pyramidal neurons increases sharply from primary sensory to prefrontal areas (Elston, 2000; Elston et al., 2011). Taking spine count as a proxy for excitatory synapses per pyramidal cell, we introduced a gradient of excitatory input strength across the cortex. We modelled this by scaling the strength of excitatory projections in an area according to the area's position in the anatomical hierarchy described below.

2.2 Gradient of excitation along the cortical hierarchy

The laminar pattern of interareal projections can be used to place cortical areas in a hierarchy: neurons mediating feedforward connections from one area to another tend to originate in supragranular layers of the source area, whereas feedback projections tend to originate in infragranular layers (Barbas & Rempel-Clower, 1997; Felleman & Van Essen, 1991). This was quantified by Barone et al. (2000), who observed that the fraction of projecting neurons located in the supragranular layers of the source area defines a hierarchical distance between two areas; this allowed them to reproduce the hierarchy of Felleman & Van Essen (1991) using data from connections to only two areas (V1 and V4).

The laminar data included with this paper (table A.1 page 167) contain hierarchical distance measured this way for all pairs of cortical areas included in the model (fig. 2A). We follow the approach of Markov et al. (2014b), and use these to estimate each area's position in an underlying hierarchy. We found that an area's position in this anatomical hierarchy is strongly correlated with counts of spines on pyramidal neurons in that area (Elston, 2007). This allowed us to introduce a systematic gradient of excitatory connection strength per neuron along the cortical hierarchy, and to explore how such heterogeneity interacts with the pattern of long-range projections to produce large-scale dynamics.

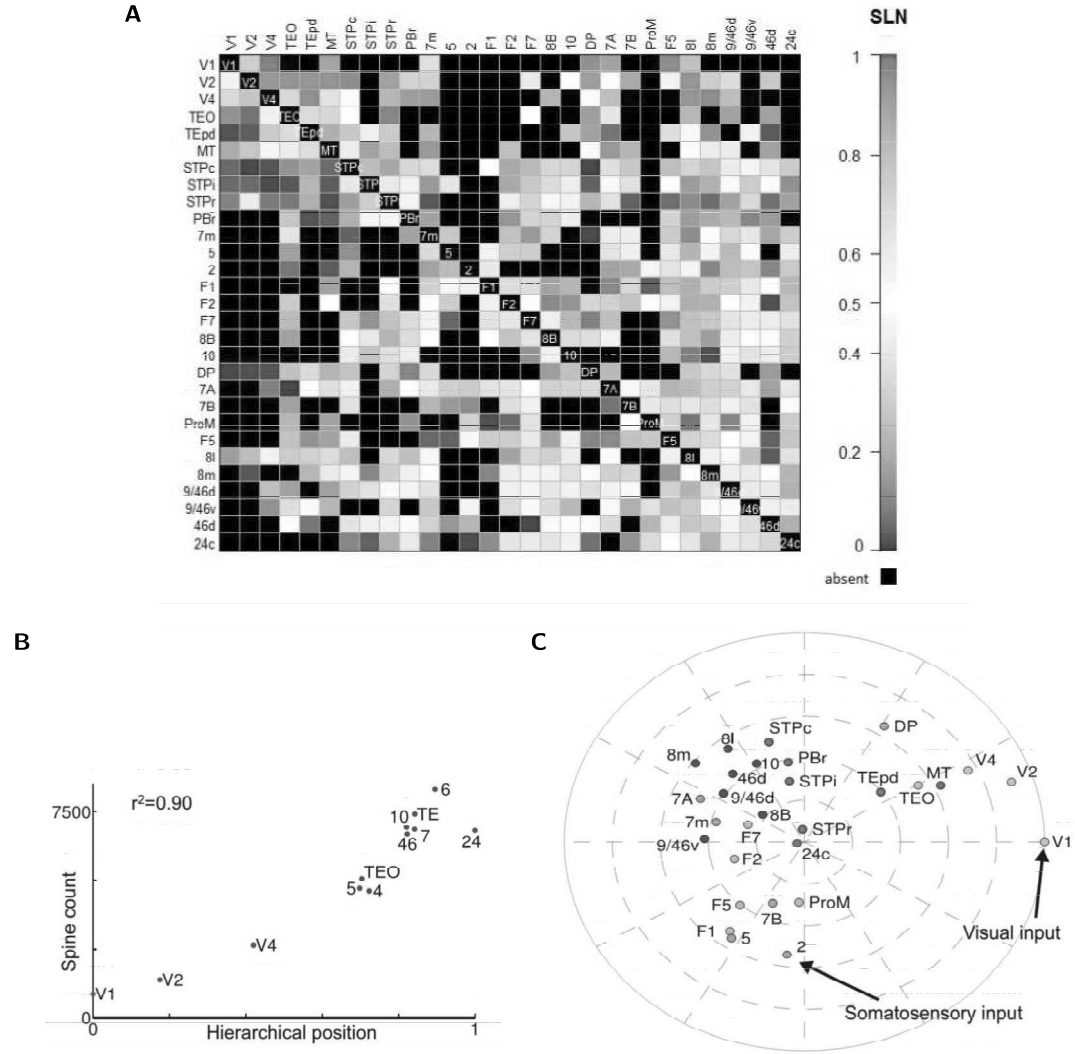

FIGURE 2: **Hierarchical organisation of the cortex.** **(A)** Fraction of neurons in a projection originating from the supragranular layers of the source area (SLN). Areas are arranged by hierarchical position. Thus, most feedforward projections (SLN > 0.5) lie below the diagonal and most feedback projections (SLN < 0.5) lie above the diagonal. Absent projections are shown in black. (see section 4.1 of the Methods and table A.1) **(B)** Hierarchical position of an area is well correlated with the number of spines on pyramidal neurons in that area (Elston, 2007). For details on area labels in this image, see section 4.2(b) of the methods. **(C)** Two-dimensional plot of areas determined by long-range connectivity and hierarchy. The distance of an area from the edge corresponds to its hierarchical position, while the angular distance between two areas is inversely related to their connection strength (see section 4.2(c) of the methods). Areas are coloured by cortical lobe.

As a visual and conceptual aid, in fig. 2C we use a two dimensional embedding to plot hierarchy and connectivity for the 29 areas. The angle between two areas reflects connection strength (closer areas have stronger connections), and the distance of an area from the centre reflects hierarchy (higher areas closer to the centre). The low-dimensional embedding is approximate but captures broad features of cortical organization and provides intuitive understanding of the model's behaviour. It suggests two hierarchical streams of sensory input originating in area V1 (primary visual cortex) and area 2 (part of primary somatosensory cortex) respectively, and converging on densely connected association areas. We next explored the response of the network

to these sensory inputs.

2.3 Response to visual inputs

We simulated the response of the network to a pulsed input to primary visual cortex (area V1). The response is propagated up he visual hierarchy, progressively slowing as it proceeds (fig. 3A). Early visual areas, such as V1 and V4, exhibit fast, short-lived responses. Prefrontal areas, on the other hand, exhibit slower responses and longer integration times, with traces of the stimulus persisting several seconds after stimulation. As with the response to a pulse of input, white-noise input is integrated with a hierarchy of timescales: the activity of early sensory areas shows rapid decay of autocorrelation with time whereas cognitive areas are correlated across longer periods (fig. 3B and 3C). Thus, a hierarchy of widely disparate temporal windows or timescales emerges from this anatomically calibrated model system.

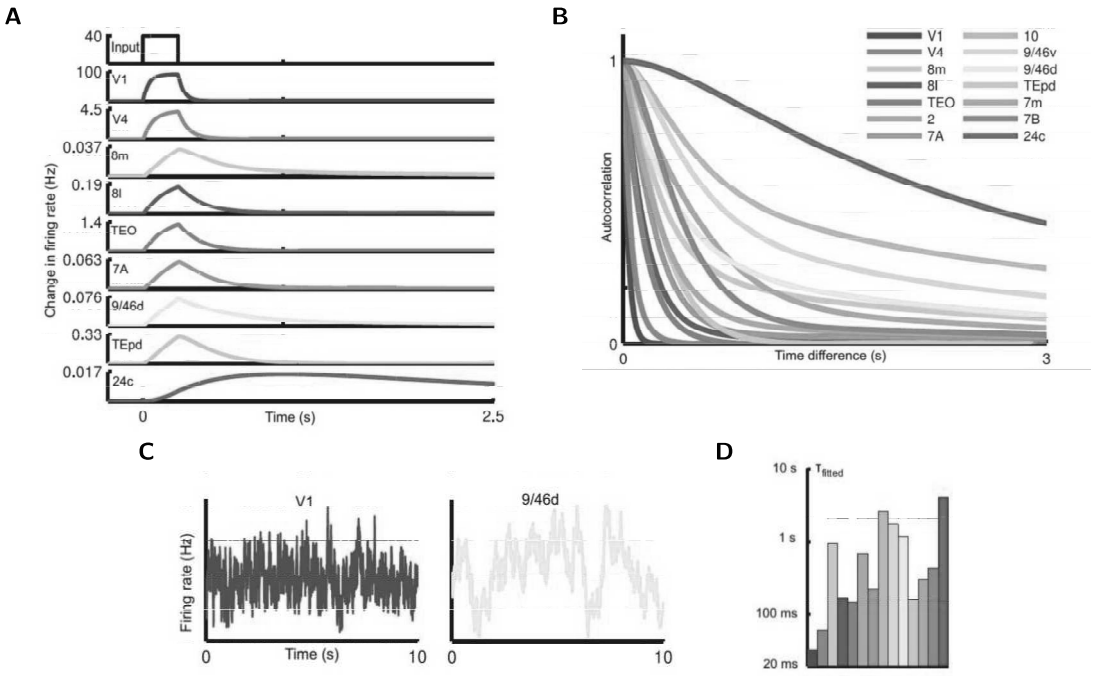

FIGURE 3: **A hierarchy of timescales in response to visual input.** **(A)** A pulse of input to area V1 is propagated along the hierarchy, displaying increasing decay times as it proceeds. In all images, areas are arranged (and coloured) by position in the anatomical hierarchy. **(B)** Autocorrelation of area activity in response to white-noise input to V1. The autocorrelation decays with different time constants in different areas, showing a functional hierarchy ranging from area V1 at the bottom to prefrontal areas at the top. **(C)** Traces contrasting the activity of area V1 and dorsolateral prefrontal cortex in response to white-noise input to area V1. **(D)** The dominant time constants in various areas of the network, extracted by fitting exponentials to the autocorrelation (colours as in (B)). Time constants tend to increase along the hierarchy but depend on the influence of long-range projections (for example, contrast area 8m with area TEpd). See also fig. 10 and fig. 11.

To quantitatively compare areas, we fit single or double exponentials to the decay of each area's autocorrelation function (see fig. 10 for plots of the fits). These fits capture a dominant characteristic timescale for each area in our model in response to visual stimulation. The time constants from the fits are plotted in fig. 3D, with areas ordered by position in the anatomical hierarchy.

As can be seen from the bar plot, the dominant timescale of an area tends to increase along the hierarchy (i.e., left to right), suggesting an important role for a gradient of excitation in generating the temporal hierarchy.

Nevertheless, an area's timescales are not entirely determined by its hierarchical position, and the plotted timescales do not increase monotonically with hierarchy. To gain some intuition for the role of long-range projections in the model, consider area 8m (part of the frontal eye fields), which is low in the hierarchy and would show a rapid decay of correlation in the absence of long-range projections (far-right graph of fig. 5A) but instead demonstrates long timescales in the model (and in the empirical observations Hasson et al. (2008). As can be seen from fig. 2C, area 8m participates in a strongly-connected core of prefrontal and association areas (Ercsey-Ravasz et al., 2013; Markov et al., 2013), allowing it to show long timescales that emerge from inter-areal excitatory loops (these timescales are strongly attenuated in the absence of feedback projections). The shared slower timescales are particularly characteristic of prefrontal areas in our model (see fig. 10, especially areas best fit by two timescales). Conversely, whereas area TEpd is high in the hierarchy, it does not participate in this core and is instead strongly coupled to ventral stream visual areas. Thus, it reflects the faster timescales of visual input.

2.4 Multiple functional hierarchies

The response to visual input reveals an ascending hierarchy of timescales in the visual system. We next stimulated primary somatosensory cortex (area 2), which is weakly connected to the visual hierarchy and strongly connected to other somatosensory and motor areas (fig. 2C). As previously, input propagates up a hierarchy of timescales (fig. 4A). However, the somatosensory response uncovers a different dynamical hierarchy to visual stimulation. Primary somatosensory cortex shows the fastest timescale, followed by primary motor cortex (area F1) and somatosensory association cortex (area 5). Parietal and premotor areas show intermediate timescales and, as with visual stimulation, prefrontal areas show long timescales. Visual areas demonstrate much weaker responses than before and are mostly driven by top-down projections from association areas. Thus, in the absence of direct input, they reflect the slower timescales of a distributed network state. In fig. 4B, we contrast time constants for visual and somatosensory stimulation across areas.

An area's timescales emerge from a combination of local circuit properties, the specificity of long-range projections, and the particular input to the network. Our model allows us to examine the contribution of each. These can be intuitively summarized by noting that each area in fig. 2C shows timescales approximately determined by its distance from the periphery (hierarchical position), proximity to the central clusters (long-range connectivity), and distance from the source of input.

2.5 Role of local and long-range projections

To further dissect the contributions of local and long-range projections, we examined time constants in response to visual input after removing either differences in local microcircuitry or interareal projections. In the second graph of fig. 5A, we show that the range of timescales

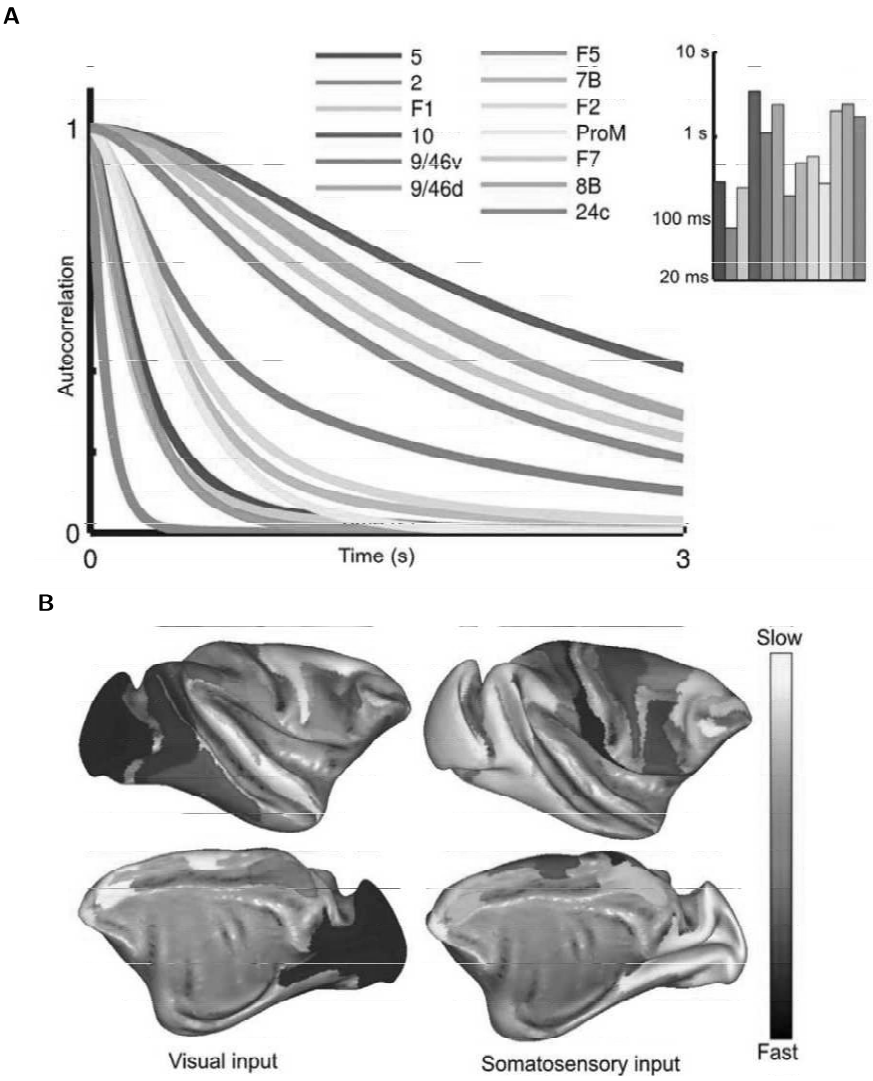

FIGURE 4: **The response to somatosensory input reveals a different functional hierarchy subserved by the same anatomical network.** **(A)** Autocorrelation of activity for areas that show strong responses to input to area 2 (part of primary somatosensory cortex). Area labels are arranged according to position in the underlying anatomical hierarchy. Inset: time constants fitted to the autocorrelation function for each area. **(B)** Timescales in response to visual (left) and somatosensory input (right) shown with lateral (top) and medial (bottom) views of the cortex. See also fig. 12.

is drastically reduced in the absence of differences in the microcircuit across areas. Moreover, there is no longer a relationship to an area's position in the anatomical hierarchy. Thus, while differences in long-range inputs and outputs to each area are significant, they are insufficient to account for disparate timescales and local heterogeneity is needed.

In the third graph of fig. 5A , we show the effect of removing long-range feedback projections, and for the far right image, we remove all long-range projections and stimulate individual areas separately. The range of time constants is lower, reflecting the propensity of slow areas to form long-range excitatory loops with each other. More significantly, once long-range projections are removed, an area's time constant simply reflects its position in the hierarchy.

We extend our investigation of the role of long-range projections by contrasting the resting-state

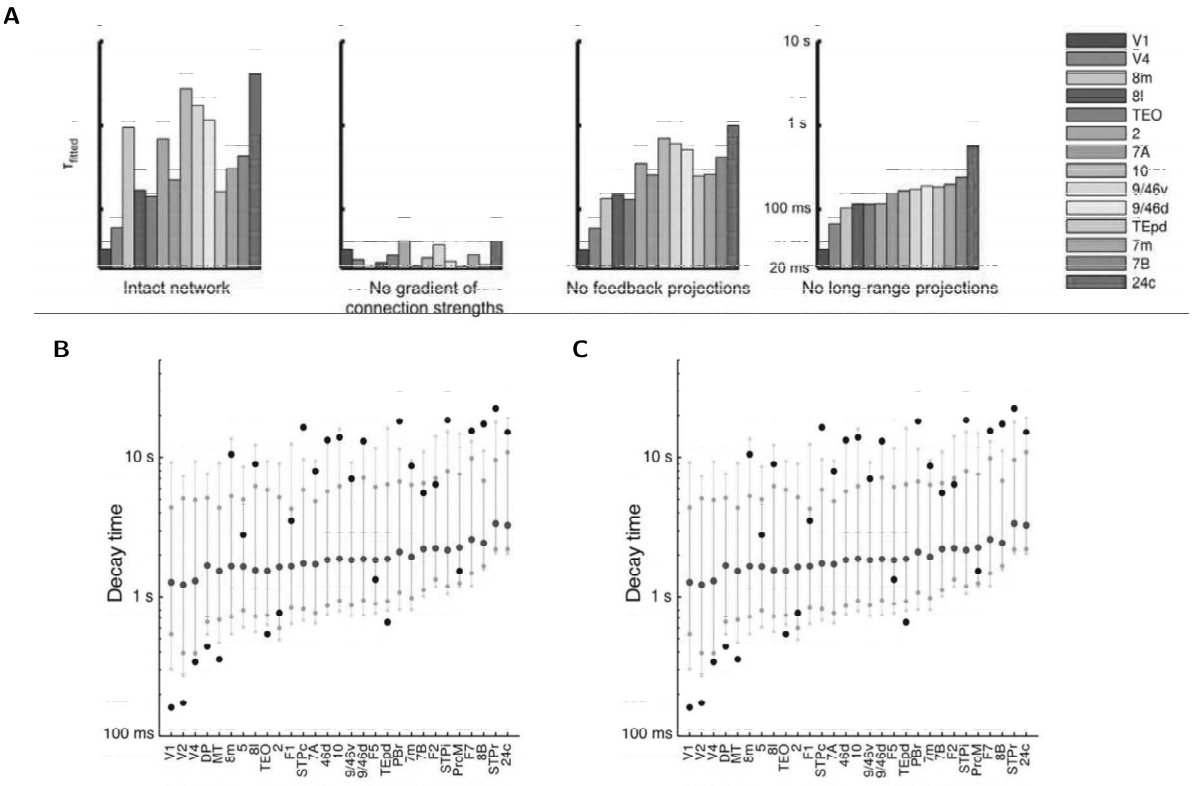

FIGURE 5: **Role of local and long-range projections in determining timescales.** **(A)** Time-constants fit to network activity after removing gradient of excitation or long-range projections. Far left: time constants for intact network. Centre left: network with no gradient of excitatory synapses across areas. Centre right: network with feedback projections lesioned. Far right: network with all long-range projections lesioned. **(B)** Effect of scrambling long-range connectivity on resting-state network dynamics, measured by the time taken for an area's activity to return to 5% of baseline after a 250 ms pulse of input. Distribution of timescales when all connection strengths are randomly permuted. Dark blue, lighter blue and very light blue circles indicate median value, 10^{th} to 90^{th} percentiles and 5^{th} to 95^{th} percentiles respectively. Intact network shown in black for comparison. Timescales for scrambled networks are much more similar to each other (compare black to blue), and fast visual areas show the greatest disruption. **(C)** Distributions when only non-zero connection strengths are permuted, thus preserving the connectivity pattern but not strengths.

response (i.e., equal white-noise input to all areas) of the intact network to networks where long-range connections are scrambled while preserving the gradient of excitation. A number of these networks show responses that are poorly fit by exponentials, so we measure time scale non-parametrically as the time after pulse offset for activity to decay to within 5% of baseline. In fig. 5B , we show that scrambling almost entirely removes the hierarchy of timescales, further confirming that a gradient of excitation alone is insufficient to separate timescales.

The connectivity data show specificity in which projections exist and in their strengths, and both connection probability and strength decay exponentially with inter-areal distance (Ercsey-Ravasz et al., 2013; Markov et al., 2013, 2014a, 2011b). In fig. 5C, we preserve network topology (i.e., which areas are connected), but scramble the strengths of non-zero projections. Here the separation of timescales is strongly attenuated for most areas, suggesting that specificity in projection strengths and not just network topology is required for the timescales we see.

2.6 Localised eigenvectors and separated timescales

The model for a single area is threshold-linear, meaning we ignore non linearities besides the constraint that firing rates be positive. This allowed us to explore the genesis of separated timescales with linear systems analysis. The activity of a linear network is the weighted sum of characteristic activity patterns, called eigenvectors (Rugh, 1995). Each eigenvector evolves on a timescale given by a corresponding eigenvalue and is differently driven by different inputs.

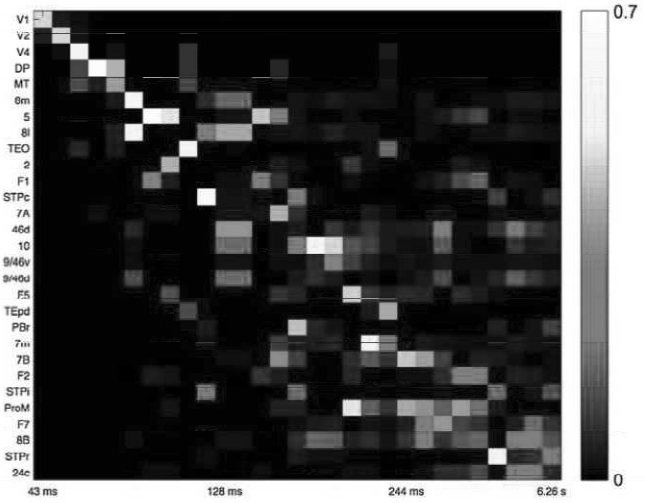

FIGURE 6: **Eigenvectors of the network coupling matrix are weakly localized, corresponding to segregated temporal modes.** Each column shows the amplitude of an eigenvector at the 29 areas, with corresponding timescale labelled below. The 29 slowest eigenvectors of the system are shown.

The eigenvectors of the linearised network are localised: those with short timescales are broadly concentrated around sensory areas and those with long timescales are concentrated at frontal areas (fig. 6). In general, if an eigenvector is small at a node, then its amplitude at that node in response to input will also be small, and the corresponding timescale will be weakly expressed. Thus, localisation means that for most inputs network dynamics will be dominated by rapid timescales at sensory areas and slower timescales at cognitive areas. In previous theoretical work, we have shown how localised eigenvectors can arise in networks with gradients of local properties and produce a diversity of timescales (Chaudhuri et al., 2014).

2.7 Extension to nonlinear dynamics and multistability

The threshold-linear local circuit let us highlight the requirements for a hierarchy of timescales and provide intuition from linear systems theory. Moreover, many systems can be linearly approximated, and neural responses are often near linear over a wide range of inputs (Chance et al., 2002; Wang, 1998), making linear and threshold-linear models used for neural circuits (Dayan & Abbott, 2001).

Nevertheless, linear models show limited dynamics and cannot capture features such as persistent activity or multistability, which are thought to be important for cognitive capabilities in higher areas (Wang, 2013). We thus replaced our local circuit with a firing rate ("mean-field") version

of a spiking network with more realistic synaptic dynamics (Wang, 2002; Wong & Wang, 2006). When isolated, an area in this network can display qualitatively different regimes (fig. 7A). For relatively weak recurrent connections, an area shows a single stable state. As recurrent excitation is increased, there is a transition to a regime with two stable states, with low and high firing rates that correspond to a resting state and a self-sustained persistent activity state. In this regime, an area can integrate inputs over time and maintain activity in the absence of a stimulus. Such dynamical regimes have been proposed to underlie "cognitive-type" computations such as working memory and decision-making (Wang, 2002, 2013).

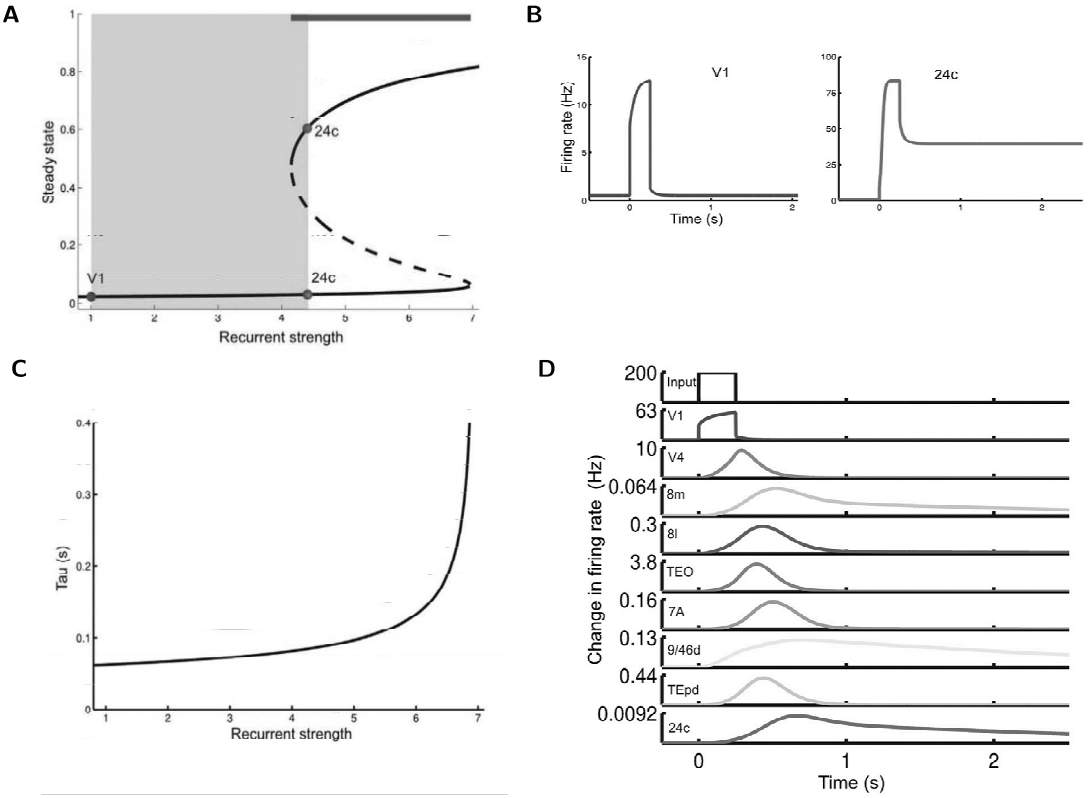

FIGURE 7: **Hierarchy of timescales in a nonlinear model.** (**A**) Possible steady states (bifurcation diagram) for an area as a function of recurrent strength (normalised by value at V1). Stable steady states are shown with solid lines. Areas with comparatively low recurrent strength display only a single steady state. Increasing the recurrent strengths leads to a regime with a high-activity steady state. The dashed line is an unstable intermediate steady state. The thick blue line shows the parameter range supporting bistability, while the light blue shaded region indicates the range used for areas in the model. Steady states are shown as fractional activation of NMDA conductance. (**B**) Response of disconnected areas to a strong pulse of input. As in (A), V1 only shows a single stable state, whereas area 24c shows sustained delay activity. (**C**) The timescales of responses to a small perturbation serve as a probe of the recurrent strength of a local area. These timescales are much smaller than those in response to a larger input but emerge from the same underlying gradient in recurrent strengths. (**D**) Response of connected network to a brief pulse of input to area V1. As in fig. 3, the input is propagated up the hierarchy, slowing down as it proceeds. Note that the input is not strong enough to switch any area into the high-activity stable state.

With this model for each area in the large-scale network, we introduced the previous gradient of excitation. Consequently, sensory areas show single stable states while areas further up the

hierarchy can also show persistent activity when driven by strong inputs (fig. 7B). Small perturbations are insufficient to shift the state of a node but take longer to decay away in areas further up the hierarchy (fig. 7C).

For small inputs, the network response resembles the threshold-linear model: a brief input to V1 is propagated up the hierarchy, with rapid decays in sensory areas and slow decays in association areas (fig. 7D). Thus, the previous results extend to a nonlinear model with a larger dynamical repertoire. Exploring the complex dynamical behaviours that this network can show is beyond the scope of this paper, but one interesting consequence of the extended model is that the timescales of small fluctuations around baseline predict the ability of an area to show much longer timescales in response to larger inputs (fig. 7C and see the discussion), as observed in Honey et al. (2012) and Murray et al. (2014).

We now investigate the implications of local heterogeneity for network organization as measured by correlations in resting state activity (resting- state functional connectivity). In our model, frontal and association areas reflect a slowly varying network state, and we hypothesized that this state should strongly shape functional connectivity.

In fig. 8A, we show functional connectivity in our threshold linear model with heterogeneity in local area properties, or without it (as typically assumed in models relating functional to anatomical connectivity). The inclusion of a gradient of local excitation reduced the correlation (r^2) between functional and anatomical connectivity from 0.83 to 0.53 (fig. 14 shows results using a BOLD kernel as in Boynton et al. (1996)).

2.8 Functional connectivity

Multiple studies find that the strength of an anatomical connection between areas ("structural connectivity") partially predicts correlations in neurophysiological signals from those areas (functional connectivity), but there are significant differences (Damoiseaux & Greicius, 2009; Deco & Corbetta, 2011; Deco et al., 2014; Hagmann et al., 2008; Honey et al., 2009). Our results also suggest that interareal connections are insufficient to predict functional connectivity. However, we find that heterogeneity in local connectivity could help account for the previously unexplained variance. In our model, slower frontal and temporal areas in particular show enhanced functional connectivity. Consequently, areas with slow timescales play a predominant role in the network, as shown by "lesioning" individual areas (fig. 8B, left panel). For the simple case of identical input to each area, the effect of lesioning an area is well predicted by the time constant of intrinsic fluctuations (fig. 8B, right panel). Note that areas most important for functional connectivity are not simply those at the highest positions in the hierarchy (i.e. with the most recurrent connections), and hierarchy alone poorly predicts impact on functional connectivity ($r^2 = 0.18$). For instance, the caudal superior temporal polysensory region (STPc) and the rostral parabelt (PBr) are at intermediate hierarchical positions but have strong connections to other parts of STP (darker lines in fig. 8B) forming a cluster that shapes functional connectivity. In general, areas combining intermediate to high hierarchical position and strong connections to slow areas have the strongest influence on global activity patterns.

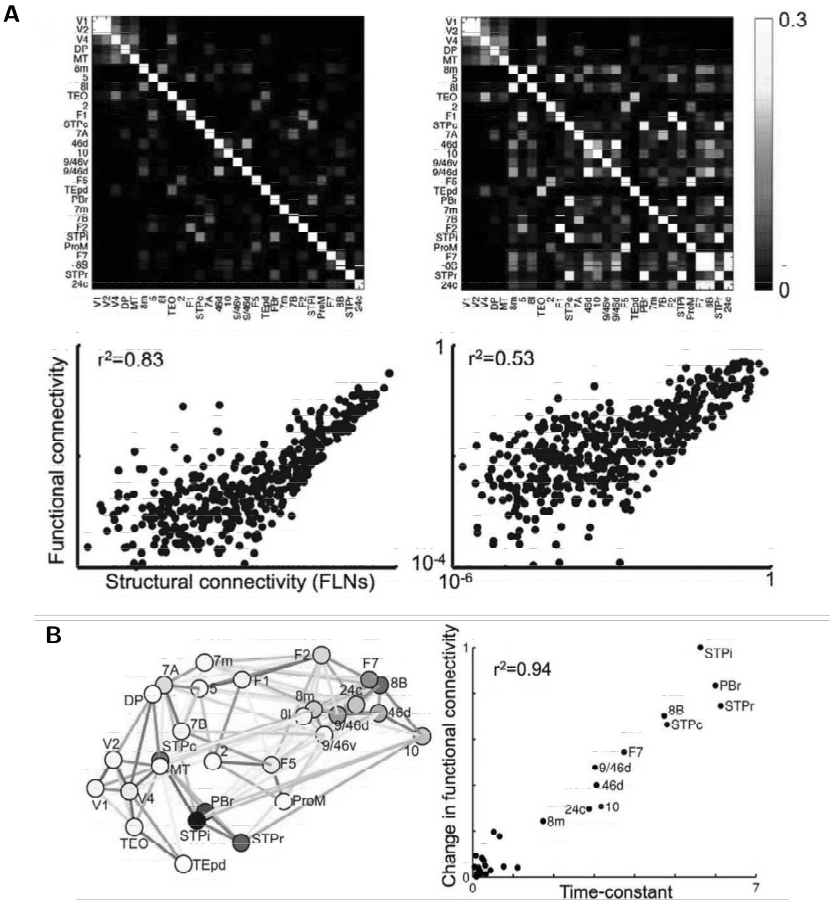

FIGURE 8: **Functional connectivity depends on local microcircuitry.** (**A**) Functional connectivity for two networks with identical long-range connectivity. The network on the left has the same properties at each area, while that on the right has a gradient of local recurrent strengths. Top panel: correlations in area activity for uncorrelated background input to each area. Bottom panel: functional connectivity (correlation) versus structural connectivity (FLN) for non-zero projections. The network with a gradient of local recurrence has enhanced functional connectivity for slow areas, and a smaller overall correlation between functional and anatomical connectivity (showing that long-range connections alone cannot predict global brain activity patterns). (**B**) Effect of lesioning areas, one at a time, on functional connectivity. Left panel: darker areas are those with a greater influence on resting-state functional connectivity. Right panel: the effect of lesioning an area on functional connectivity is well correlated with the time constant of spontaneous fluctuations in that area. See also fig. 13 and 14.

3 Discussion

The main findings of this work are 3-fold. First, it establishes a circuit mechanism for a hierarchy of temporal receptive windows, which has received empirical support in recent human (Gauthier et al., 2012; Hasson et al., 2008; Honey et al., 2012; Lerner et al., 2011; Stephens et al., 2013) and single-unit monkey experiments (Murray et al., 2014). The model extends time integration in decision making from local circuits (Wang, 2008) to a large-scale system across multiple timescales (Hasson et al., 2015). Second,interareal heterogeneity implies that areas cannot be treated as identical nodes of a network and slow dynamics in association areas can play a disproportionate role in determining the pattern of functional connectivity. This suggests that functional connectivity analyses be revised. Third, this is the first large-scale dynamical

model of the macaque cortex based on weighted and directed connectivity and incorporating heterogeneity across areas.

The ability to integrate and hold information across time is critical for cognition. On the other hand, the brain must rapidly and transiently respond to changing stimuli. Complex behaviour thus requires a multitude of coexisting timescales. We demonstrate how such timescales (or temporal receptive windows) naturally emerge in a model of primate cortex built with quantitative anatomical data. Our work reveals multiple functional hierarchies converging on a slow distributed network of densely connected frontal and other association areas.

A long-standing observation is that strong recurrent connections can produce slower dynamics (Wang, 2008), and we show how this basic anatomical motif can interact with the pattern of long-range connections to produce a hierarchy of timescales. The hierarchies we observe with different stimuli thus emerge from a combination of heterogeneity in excitatory connection strengths across areas and the profile of long-range connectivity (which is highly specific to each area, (Markov et al., 2013)), and neither alone can predict an area's timescales. For example, while differences in local recurrence play a crucial role in generating timescales, the correlation between anatomical hierarchy and timescale is relatively weak (r^2 = 0.25, 0.14, 0.22 in the visual, somatosensory, and resting-state conditions respectively). Moreover, areas can show quite different timescales in response to different inputs: as seen in fig. 4B, even early visual areas with relatively weak recurrence can have slower timescales. To characterise the dependence of timescales on local and long-range properties, we first removed the gradient of local properties and observed that the hierarchy of timescales vanishes. Separately, we preserved the local properties of areas and either removed (fig. 5A, right panels) or scrambled the long-range projections both globally and while preserving network topology (fig. 5B and 5C).

It will be important to further probe the interaction of local and long-range connectivity. This will require additional anatomical and physiological data, and our model can be a platform to explore the consequences of these data for large-scale dynamics. For example, following the finding of Markov et al. (2011b) that the proportion of local to long-range synapses is roughly conserved across areas, we have chosen to scale both local and long-range projections by an area's position in the hierarchy. Nevertheless, local and long-range synapses may have different strengths and properties and may differentially target cell types and dendritic locations. Relatedly, long-range inputs may be differentially gated depending on task demands and the local circuit regime. Conversely, in the nonlinear model, long-range input can shift the dynamical regime of the local circuit: an area that lacks persistent activity when isolated may show persistent activity in the presence of a weak long-range control signal. These interactions can provide the network with an enhanced computational repertoire.

To examine timescales in the clearest way possible, we modelled individual areas with a threshold-linear rate model, where time constants are mathematically well defined. However, the results hold for a nonlinear local circuit with multiple stable states. Note that this work did not focus on the latency of neural responses (Bullier, 2001; Schmolesky et al., 1998), for which a spiking model is needed. Nevertheless, single neurons in the monkey cortex display slow responses during stimulus presentation as shown in the model; for example, in decision tasks prefrontal and parietal neurons can show quasi-linear ramping with a time constant that may appear effectively infinite

(Brunton et al., 2013; Gold & Shadlen, 2007; Smith & Ratcliff, 2004; Wang, 2008). Thus, the model is the simplest that is adequately designed to reveal a hierarchy of timescales in the cortex.

We systematically introduced heterogeneity into our model by assigning each cortical area a hierarchical position determined by its pattern of feedforward and feedback projections. A priori, there is no reason why excitatory input would vary systematically along this anatomical hierarchy. However, we find that hierarchical position correlates very strongly with the number of spines per neuron in an area (fig. 2B). This suggests an underlying cortical organizational principle, which could be explored in future (see Scholtens et al. (2014) for a similar observation and Barbas & Rempel-Clower (1997) and Hilgetag et al. (2002) for correlation of hierarchy with lamination and relative density of an area).

There are no systematic measurements of the timescales of areas in response to different stimuli, but recent studies have compared temporal responses and integration timescales across areas and report a hierarchical organization (Bernacchia et al., 2011; Gauthier et al., 2012; Hasson et al., 2008; Honey et al., 2012; Lerner et al., 2011; Murray et al., 2014; Ogawa & Komatsu, 2010; Stephens et al., 2013). Notably, Honey et al. (2012) connected a functional hierarchy in the timescales of preferred stimuli to a dynamical hierarchy in the timescales of correlation in network activity, and found autocorrelation timescales similar to those we model (in particular, see Figure 6 of Honey et al. (2012)). Similarly, Murray et al. (2014) found that autocorrelation traces were well-described by exponentials, the hierarchical ordering of areas they observe agrees with our model, and the timescales of small fluctuations in that study are close to the intrinsic time constants of areas in the model (i.e., in the absence of long-range projections such as in fig. 5A, far right panel).

Our model has several testable predictions. Though there are multiple combinations of local time constants and network connection strengths that could produce a particular set of observed timescales, the model suggests that timescales of small fluctuations should reflect the intrinsic properties of areas (far right panel of fig. 5A), while larger responses should reflect time constants that emerge from the entire system (far left panel of fig. 5A). In the model, slow network timescales corresponding to a slowly varying global state. Inactivating these areas should decrease slow dynamics in connected areas lower in the hierarchy. The differential responses to visual and somatosensory input suggest that when a particular input is not involved in a task, the corresponding sensory areas better reflect slow changes in global cortical state. This may explain decreases in low-frequency ECoG power (i.e., slow modes) when a subject engages in a task (He et al., 2010; Honey et al., 2012), as well as the observation of Stephens et al. (2013) that, despite fast timescales in response to visual input, early visual areas have slow timescales during auditory processing. Finally, we predict that areas with longer timescales, such as prefrontal and superior temporal areas, can shape functional connectivity to a greater degree. This highlights the importance of incorporating heterogeneous local dynamics in studying the determinants of functional connectivity and, intriguingly, suggests that functional connectivity might be used to probe local properties. Whereas there is some evidence that frontal and association areas show enhanced functional connectivity (Sepulcre et al., 2010) and of a correlation between enhanced functional connectivity and slow timescales (Baria et al., 2013), it would be interesting to use functional imaging to better understand the link between functional connectivity and response timescales (for example, as determined by the approach of Gauthier et al. (2012); Hasson et al.

(2008); Honey et al. (2012); Lerner et al. (2011)). The link between slow timescales and enhanced functional connectivity might also explain observations that functional connectivity is greater at low frequencies (Salvador et al., 2005). Moreover, because distant areas tend to lack strong direct connections, their functional connectivity will be primarily driven by slow distributed network modes and will be further biased toward low frequencies, as previously observed (Salvador et al., 2005).

We mostly used a threshold-linear model for local areas, but the hierarchy of timescales holds when areas are modelled by a nonlinear microcircuit, similar to one proposed as a model for general "cognitive-type" computations (Wang, 2002, 2013). Depending on connectivity and input parameters, such networks show a single stable state, multistability with persistent firing, or continuous slow fluctuations between metastable states. While we do not explore this broader range of behaviours, note that in the nonlinear model the timescales of small fluctuations around baseline predict an area's ability to show much longer timescales in response to larger inputs. This can be seen by comparing the timescales of fig. 7C with the steady states of fig. 7A, and by contrasting responses to large and small perturbations in fig. 7B and 7D (note that timescales in response to large perturbations tend to be slower than those from small perturbations even if the area is not bistable). This may explain why the timescales of spontaneous fluctuations in an area (on the order of hundreds of milliseconds) correlate with its sensitivity totemporal structure in stimuli across seconds (Honey et al., 2012) as well as with slow drifts in baseline neural activity and the timescales of reward memory (Murray et al., 2014).

Our model is parsimonious, designed to capture a basic mechanism underlying a hierarchy of timescales, and can be extended in several ways. First, the local area model could be made more complex, and an interesting direction is using the SLNs to incorporate a laminar structure. Second, in our model activity propagates along the hierarchy with significant attenuation. This attenuation can be substantially decreased by changing model parameters (M. Joglekar and X.-J. Wang, unpublished data) and may be removed by synchronous firing (Diesmann et al., 1999) or more sophisticated feedback projections (Moldakarimov et al., 2015). Third, we only consider cortico-cortical connections. Whereas these form the major input to a cortical area (Markov et al., 2011b), subcortical projections will play an important role. For example, incorporating thalamocortical projections would allow us to more realistically model input and may help set network state and gate inter-areal interactions, whereas neuromodulators such as acetylcholine might modulate the excitability of local populations and enhance information transmission at other synapses. Fourth, as a first step, we used two global parameters to scale long-range connection strengths but emerging data relating long-range anatomy and physiology should be incorporated. Fifth, extensions should include other interareal heterogeneities, such as in interneuron types and densities (Medalla & Barbas, 2009) and in neuromodulatory signalling (Hawrylycz et al., 2012). For example, it would be interesting to model the higher numbers of dopaminergic projections to prefrontal areas. Finally, while we have focused on how areas are able to accumulate incoming information on different timescales, processing input requires synthesising it with previous input. Future work should explore how different areas in our model integrate information from more realistic time-varying stimulation such as a movie or a song and to probe how these responses change when the correlation structure of the input is disrupted (for example, by scrambling).

In conclusion, we report a novel, quantitatively calibrated, dynamical model of the macaque cortex with directed and weighted connectivity. The identification of a specific circuit mechanism for a hierarchy of timescales (temporal receptive windows) represents a key advance toward understanding specialized processes and functions of different (from early sensory to cognitive-type) cortical areas. Our findings demonstrate the importance of heterogeneity in local areal properties, as well as the specific profile of long-range connectivity, in sculpting the large-scale dynamical organization of the brain.

4 Methods

4.1 Anatomical data

The connectivity data are from an ongoing project to quantitatively measure all connections between cortical areas in the macaque, with areas defined according to a 91 area parcellation scheme (Markov et al., 2014a) (fig. 1). Briefly, connection strengths between areas are measured by counting the number of neurons labelled by retrograde tracer injections. The number of neurons labelled in a projection ranges from a few neurons to on the order of 100,000 neurons. To control for injection size, these counts are then normalised by the total number of neurons labelled in the injection, yielding a fractional weight or FLN (Fraction of Labelled Neurons) for each pathway, defined as:

$$FLN_{B\to A} = \frac{\#\text{ neurons projecting to area A from area B}}{\text{total neurons projecting to area A from all areas}}.$$

The retrograde tracing technique only uncovers the inputs to an area, but within the subnetwork of the 29 injected areas all the output pathways are also input pathways to another injected area. Therefore the presence or absence of every connection is known bidirectionally. This is why used this particular subnetwork of 29 nodes distributed across the entire cortex to represent the full 91x91 graph. In this subnetwork, of all the possible connections, 66% are present, though with widely varying strengths. The connectivity matrix of this subgraph (pathways and connections weights) is shown in fig. 1B.

We also use data on the fraction of neurons in each projection that originate in the upper layers of the source area, which we call the SLN, for Supragranular Layer Neurons (Markov et al., 2014b). These are defined as:

$$SLN_{B\to A} = \frac{\#\text{ supragranular neurons projecting to area A from area B}}{\text{total neurons projecting to area A from area B}}.$$

The whole dataset is included in table A.1 (page 167), and all data can be downloaded from `www.core-nets.org`. Further details of data collection can be found in (Markov et al., 2014a, 2011b). All the procedures used in the study followed the national and European regulations concerning animal experiments (EC guidelines 86/609/EC) and were approved by the authorised national and veterinary agencies.

4.2 Hierarchy and low-dimensional connectivity embedding

(a) Building the hierarchy from connectivity data

In the visual system, projections directed from early visual areas to higher-order areas (i.e. increasing size of receptive field, position-invariance, and so on) tend to originate in the supragranular layers of the cortex and terminate in layer 4 (Barone et al., 2000; Felleman & Van Essen, 1991). Conversely, projections from higher-order areas to early visual areas originate in the infragranular layers and terminate outside of layer 4. This observation was systematized Felleman & Van Essen (1991), who used these anatomical constraints to place cortical areas in a hierarchical ordering.

Felleman and Van Essen used a discrete classification of projections: in their framework projections are either feedforward, feedback or lateral depending on where the majority of projections originate and terminate. However, such binary relations are typically insufficient to specify a unique hierarchy (Hilgetag et al., 1996). Subsequently, it was observed that rather than classifying a projection as feedforward, feedback or lateral, the fraction of neurons in a projection originating in the supragranular layers (the SLN) could be used as a continuous measure of hierarchical displacement: the difference of the SLN from 50% is positive for feedforward projections and negative for feedback projections, and its magnitude gets larger as a projection moves further away from lateral (Barone et al., 2000). For example, a projection with an SLN of 90% would be very strongly feedforward, while a projection with an SLN of 65% would be only moderately feedforward. Using these values, the Felleman and van Essen hierarchy could be reproduced using observations of connections to only two areas (V1 and V4) (Barone et al., 2000).

To construct the hierarchy from the data in fig. 2A we follow the framework of (Markov et al., 2014b) and use a generalised linear model. We assign hierarchical values to each area such that the difference in values predicts the SLN of a projection. Specifically, we assign a value H_i to each area A_i such that

$$SLN_{A_j \to A_i} \approx g^{-1}(H_i - H_j)$$

We choose g^{-1} to be a logistic function (logistic regression), which is standard for probabilities and fractional values, but we note that other functions yield similar values (see fig. 9A). We have one such constraint for each projection (536 in total), and we find the set of hierarchical values that best fit these constraints. In the fit we weight the contribution of each projection by the log of its FLN to preferentially match stronger and less noisy projections. We then normalise by the maximum hierarchical value, yielding $h_i = H_i/H_{max}$. The result is shown in fig. 9

(b) Adding local heterogeneity from spine counts data

Regional variations in the pyramidal cell phenotype have been studied across cortical areas and species by Elston and colleagues (Elston, 2007, 2002; Elston et al., 2005, 2011, 2006; Elston & Rockland, 2002). They have found a remarkable specialisation of L3 pyramidal neurons in the primate that is linked to higher cognitive functions (Elston, 2000; Elston et al., 2011, 2006). Unlike in the rodent, the size, complexity and spine density of the terminal dendritic

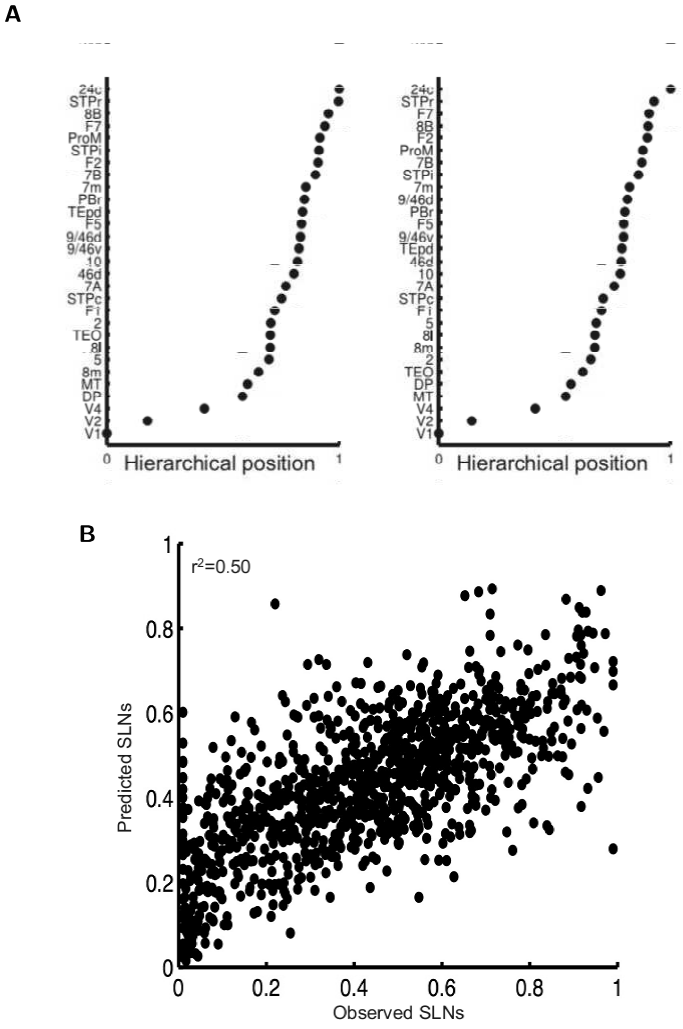

FIGURE 9: **Hierarchy fitted from pairwise SLN relationships.** (**A**) Left panel: Hierarchy fitted from logistic regression (and used in main text). The hierarchical position of an area is normalised to lie between 0 and 1. Right panel: Hierarchy fitted from beta regression (Cribari-Neto & Zeileis, 2010). (**B**) SLN values predicted from logistic regression compared to observed SLNs.

arbours of L3 neurons of the macaque increase from sensory areas to higher order areas, and reach maximum complexity and variability in the pre-frontal cortex (Elston, 2007). Given the evolutionary significance of this phenotype we based areal heterogeneity in our model on spine counts data. Spines receive at least one excitatory input, so we scaled the strength of excitatory projections to an area according to the number of spines of pyramidal (excitatory) neurons in this area.

We extract the spine counts in fig. 2B from (Elston, 2007) and plot the areas in common with our data set. The parcellation in that paper is coarser than the parcellation we use, so we report the results in terms of that parcellation. For area 7 we average together the hierarchical positions of 7A, 7B and 7m; for 6 we average F2, F5 and F7; and for 46 we average together 46d, 9/46d and 9/46v.

(c) A new hierarchical model: 2D circular embedding

As seen in the previous chapters of this thesis, the strength of projections between two areas reflects their proximity both in terms of physical position in the brain and in terms of function, as evidenced by the force-directed graph representation in fig. 10 from chapter 3. When weighted projections are used instead of binary relations (presence/absence of a projection), areas group by modalities and pathways, mirroring the physical organisation of areas in the cortex. This is linked to Felleman and Van Essen's proposal that each cortical modality has its own hierarchy (Felleman & Van Essen (1991) also describes the somatosensory and motor hierarchy) and Dehaene's global workspace model for the activation of these modalities in effortful cognitive tasks (Dehaene et al., 1998). Following this, we built a two-dimensional circular embedding of the cortical graph that maps hierarchical positions onto the radial axis and connection strengths onto angular displacement.

To construct this two-dimensional embedding we first convert the FLN to a measure of dissimilarity according to

$$D(A_i, A_j) = \begin{cases} -log(FLN(A_i, A_j)) & \text{for} \quad FLN(A_i, A_j) > 0 \\ -log(FLN_{min}) & \text{for} \quad FLN(A_i, A_j) = 0 \end{cases}$$

Here, A_i is the ith area, and FLN_{min} is some value less than the smallest FLN in the network. We use $FLN_{min} = 10^{-7}$ but the results are robust to the precise choice of this value.

We then assign angles θ_i to each area such that

$$d(A_i, A_j) \approx R \min(|\theta_i - \theta_j|, 2\pi - |\theta_i - \theta_j|)$$

where R is a free parameter and area V1 is constrained to have $\theta = 0$. Finally, we plot the areas on a 2-dimensional polar plot with $\theta(A_i) = \theta_i$ and $R(A_i) = \sqrt{(1 - h_i)}$.

The resulting circular hierarchy of the 29 areas is presented in fig. 2C. In the dynamic model we directly include the radial position to scale the excitatory input but the angular distance of the embedding is not directly used, only the connection weights.

4.3 Model architecture

The network has 29 nodes (areas), each consisting of an excitatory and an inhibitory subpopulation, which summarise the effective dynamics of the area. Their firing rate depends on input current in a threshold-linear fashion, with a rectifying threshold at 0. Long-range connectivity is excitatory and targets both subpopulations. Connectivity weights are proportional to the anatomical strength of the connection, with one scaling parameter for excitatory-excitatory and another for excitatory-inhibitory projections. Excitatory connections within an area, both local and long-range, are scaled by the area's position in the hierarchy.

The variation of firing rate is defined as:

$$\begin{cases} \tau_E \dfrac{d\nu_E}{dt} = -\nu_E + \beta_E [I_E]_+ \\ \tau_I \dfrac{d\nu_I}{dt} = -\nu_I + \beta_I [I_I]_+ \end{cases}$$

where ν_E is the firing rate of the excitatory population, with time constant τ_E and input current I_E, and for which the firing rate vs. input (f-I) curve is a straight line of slope β_E. $[I_E]_+ = max(I_E, 0)$. The inhibitory population has corresponding parameters τ_I, I_I and β_I. These values are taken from Binzegger et al. (2009): $\tau_E = 20$ ms; $\tau_I = 10$ ms, $\beta_E = 66 \times 10^{-3}$ Hz/pA and $\beta_I = 351 \times 10^{-3}$ Hz/pA.

At each node, the input current to each subpopulation has a component from itself, one from the other subpopulation (those are the local input), and another that comes from other areas (long range input). All excitatory connections are scaled according to the area's position in the hierarchy. The input current to area a is defined as follows:

$$\begin{cases} I_E^i = -w_{EI}\nu_I^i + \left(w_{EE}\nu_E^i + I_{lr,E}^i\right)(1 + \eta h_i) + I_{ext,E}^i \\ I_I^i = -w_{II}\nu_I^i + \left(w_{IE}\nu_E^i + I_{lr,I}^i\right)(1 + \eta h_i) + I_{ext,I}^i \end{cases}$$

The w_{EE} and w_{EI} terms are couplings from the excitatory population to the excitatory and inhibitory population respectively; we use $w_{EE} = 24.3$ pA/Hz and $w_{EE} = 19.7$ pA/Hz. $I_{lr,E}^i$ is the long-range input to the excitatory population and both depend on the area's position in the hierarchy, h_i (normalised between 0 and 1). The effect of hierarchy in the model is controlled by the parameter η; by setting $\eta = 0$ we remove intrinsic differences between areas. $I_{ext,E}^i$ is external input (both stimulus input and any noise we add to the system). The w_{IE}, w_{II}, $I_{lr,I}^i$ and $I_{ext,I}^i$ terms are corresponding parameters for the inhibitory population; we use $w_{IE} = 12.2$ pA/Hz and $w_{II} = 12.5$ pA/Hz. Note that unlike $I_{lr,I}^i$ (excitatory input from other areas to the inhibitory subpopulation) and local excitatory input, local inhibitory connections are not scaled by hierarchical position.

Following Binzegger et al. (2009), we write $w_{ij} = \alpha_i S_{ij}$, where i and j can be E or I; α_E (resp. α_I) measures the charge introduced per excitatory (inhibitory) spike times the transmitter release probability. Both are slightly modified from Binzegger et al. (2009): $\alpha_E = 0.007$ pC and $\alpha_I = 0.025$ pC. S_{ij} is the number of synapses from cells of type j to cells of type i, taken from the counts for layer 2/3 cells (Binzegger et al., 2004). Inhibitory values are weighted averages of basket, double bouquet and chandelier cells, with weights chosen according to their projections to the excitatory population.

We scale the excitatory inputs to an area, both local and long-range, by its position in the hierarchy, h_i. h_i is normalized between 0 and 1, and η is a scaling parameter that controls the effect of hierarchy. By setting $\eta = 0$ we remove intrinsic differences between areas. Note that we scale both local and long-range projections with hierarchy, rather than just local projections, in accordance with the observations of Markov et al. (2011b), who find that the proportion of local to long-range connections is approximately conserved across areas.

Long-range input to area a is modelled as the sum of excitatory currents from all other areas, scaled by the strength of each pathway, to both excitatory and inhibitory cells:

$$\begin{cases} I^i_{lr,E} = \mu_{EE} \sum_j FLN_{ij}\ \nu^j_E \\ I^i_{lr,I} = \mu_{IE} \sum_j FLN_{ij}\ \nu^j_E \end{cases}$$

Here j ranges over all other areas. $I^i_{lr,E}$ and $I^i_{lr,I}$ are the inputs to the excitatory and inhibitory populations, ν^j_E is the firing rate of the excitatory population in area j and FLN_{ij} is the FLN from area j to area i. Global parameters μ_{EE} and μ_{IE} control the strengths of long range input to the excitatory and inhibitory populations, respectively (they do not vary between connections; all the specificity comes from the FLNs).

The network thus has three parameters: μ_{EE} and μ_{IE} control the connection strengths of long-range projections, and η maps the hierarchy into excitatory connection strengths. For our simulations, we use $\mu_{EE} = 33.7$ pA/Hz, $\mu_{IE} = 25.3$ pA/Hz and $\eta = 0.68$. We choose the background input for each area so that the excitatory population has a firing rate of 10 Hz and the inhibitory population has a rate of 35 Hz.

We can choose the excitatory to inhibitory ratio of an input current, $\gamma = I_{inp,E}/I_{inp,I}$, such that the steady-state firing rate of the excitatory population does not change when the current is present. Given input of $I_{inp,E}$ to the excitatory population, an input of $\gamma I_{inp,E}$ to the inhibitory population increases the inhibitory firing rate sufficiently to cancel out the additional input to the excitatory population. We call such inputs balanced. Our values for μ_{EE} and μ_{IE} give a ratio slightly above this value so that projections are weakly excitatory.

4.4 Pulse input, autocorrelation, and fitted time constants

For figs. 3 to 5 and 8, we choose the background input for each area so that the excitatory and inhibitory populations have rates of 10 and 35 Hz respectively.

In fig. 3A, V1 receives a 150 ms pulse of input that drives its rate to 100 Hz. For the remaining images of this figure and fig. 5A, the stimulus to V1 is white noise with a mean of 2 Hz and a standard deviation of 0.5 Hz. The other areas receive a small amount of background input (SD of the order of 10^{-5}), but are primarily driven by long-range input propagating out from area V1. For fig. 4, the currents are the same except that area 2 receives the stimulus rather than V1.

For each area, we extract time constants by fitting both one and two exponentials to the part of the autocorrelation function that decays from 1 to 0.05. If the sum of squared errors of the single exponential fit is less than eight times that of the double exponential, then we report that time-constant. Otherwise, we use the sum of time constants from the double exponential fit, with each weighted by its amplitude. Fits in response to V1 and area 2 input and for resting state activity are shown in figs. 10, 12 and 13.

For fig. 4B, we map the time constants logarithmically to a heatmap and plot them using Caret (Van Essen et al., 2001a).

4.5 Network with conduction delays

In our simulations we ignore conduction delays between areas. While these will be important for oscillations, synchronisation and other fine temporal structure, the timescales we consider are typically slow enough that conduction delays do not play an important role.

In fig. 11 we demonstrate that our results hold in a network with realistic conduction delays. We use distances from the same data set as the connectivity strengths (Ercsey-Ravasz et al., 2013) and, to ensure a fair comparison, assume a relatively low conduction velocity of 1.5 m/s (Deco et al., 2009). As shown in fig. 11B, the response of this network to a pulse of input to area V1 is almost identical to that of a network without conduction delays.

4.6 Scrambled connectivity

For the simulations shown in fig. 5B, we scramble the connectivity matrix by permuting all entries of the matrix randomly. For fig. 5C, we preserve the absent entries and permute the non-zero entries. Note that the connectivity data show specificity both in terms of which projections exist and in their strengths, and both the probability of a connection and its strength decay exponentially with distance between areas (Ercsey-Ravasz et al., 2013; Markov et al., 2013, 2014a, 2011b). In particular, nearby areas tend to be strongly connected and to have similar timescales (see fig. 2C); thus scrambling projections should reduce the separation of timescales.

We examine the response of these scrambled networks to a pulse of input to all areas, similar to the "resting-state" condition. In the intact network, areas are dominated by a few timescales and are well fit by one or two summed exponentials. However, a number of the scrambled networks show responses that consist of many mixed timescales and are not well described by two exponentials. Thus we use a non-parametric measure of timescale: we compute the time taken after pulse offset for the area's activity to decay to within 5% of its value at baseline. Scrambling the connection strengths makes about 20% of networks unstable, meaning that responses to input grow instead of decaying, and we exclude these networks. We then compute the median and the 5^{th}, 10^{th}, 90^{th} and 95^{th} percentile of the decay time distribution for each area, and contrast it with values for the intact network.

4.7 Functional connectivity for a linear network

To highlight the effect of intrinsic hierarchy, in fig. 8A we contrast a network hierarchy with a network that has a gradient of local excitatory connections but unlike in the remaining figures, no gradient in the long-range projection strengths (thus, these networks have the same long-range

connection strengths and differences emerge from local properties). We replace

$$(1+\eta h_i)\left(w_{EE}\nu_E^i + \mu_{EE}\sum_{j=1}^{N} FLN_{ij}\nu_E^j\right)$$

with

$$(1+\eta h_i)w_{EE}\nu_E^i + \mu_{EE}\sum_{j=1}^{N} FLN_{ij}\nu_E^j$$

for the excitatory population, and similarly for the inhibitory population. For fig. 8B, we use the same network as elsewhere, so that all incoming excitatory projections are scaled by an area's hierarchical position.

If a linear network is driven by white noise input then, away from the threshold, it evolves according to the equation

$$\dot{x}(t) = Ax(t) + I + B\xi(t),$$

where I is the mean of the noise, B is its covariance matrix and A is the coupling matrix, which includes any intrinsic leak of activity.

In the steady state the covariance, C, of this matrix is the solution to the equation (Gardiner et al., 1985)

$$AC = CA^\dagger + BB^\dagger = 0.$$

This equation can be solved given the eigenvector basis (Deco et al., 2013). In the eigenvector decomposition, $A = V\Lambda V^{-1}$, where Λ is the diagonal matrix of eigenvalues and the columns of V are the right eigenvectors of A. Define

$$\tilde{Q} = V^{-1}BB^\dagger V$$
$$M_{ij} = -\frac{\tilde{Q}_{i,j}}{(\lambda_i + \lambda_j^*)},$$

then $C = VMV^\dagger$.

As an aid to intuition, assume that A is a normal matrix so that $V^{-1} = V^\dagger$. Then $\tilde{Q} = V^\dagger BB^\dagger V$, and the covariance matrix of the network is a rescaled version of the covariance structure of the input noise.

We calculate functional connectivity as the correlation matrix of area activity in response to equal white-noise input to all areas. For fig. 8B, we determine this correlation matrix analytically: since the input noise is independent and identical at each node, then the covariance matrix of the noise is diagonal with constant entries (and all correlations come from the structure of the network). If this has the value σ^2 at each node then, for a normal matrix, $\tilde{Q}_{ij} = \sigma^2\delta_{ij}$, and M is diagonal with i^{th} entry $\tau_i\sigma^2/2$, where $\tau_i = -1/\lambda_i$. Hence the covariance of the i^{th} eigenmode is proportional to its corresponding timescale.

Now $C = VMV^\dagger$, meaning that the matrix is rotated out of the eigenvector basis giving a non-diagonal matrix. Thus eigenvectors that are more broadly shared contribute more to the functional connectivity. In this case $C \propto A^{-1}/2$.

We also note that Baria et al. (2013) conduct a similar analysis on a linear network with nodes having identical properties and binary connectivity, and find that nodes with more anatomical connections and, consequently, higher functional connectivity show greater activity at low frequencies (i.e., slower timescales).

For fig. 14, we convolve the firing rates of the excitatory population at each node with a hemodynamic response function of the form:

$$H(t) = \frac{(t-d)e^{-(t-d)/\tau_h}}{\tau_h^2},$$

with timescale $\tau_h = 1.25$ and delay $d = 2.25$ s (Boynton et al., 1996). This yields a simulated BOLD signal, and we calculate the functional connectivity as the correlation matrix of this activity.

The effect of lesioning an area, A, is measured as $\parallel C_{I,A} - C_{rs,A} \parallel / \parallel C_{rs,A} \parallel$ where $C_{I,A}$ is the correlation matrix after lesioning A, $_{rs,A}$ s the intact correlation matrix without the row and column corresponding to A, and the double lines indicate the norm. The values are then scaled to lie between 0 and 1.

4.8 Nonlinear network

The single area model is a variant of the model developed in Wong & Wang (2006) as a simplified mean-field version of the spiking network of Wang (2002). There the dynamics were assumed to be dominated by the slow time-constant of NMDA synapses, and the activity of the inhibitory population was incorporated into the effective connection strengths between the excitatory populations. As in that study, we assume that the dynamics of the excitatory population are modelled by a dimensionless gating variable, s_N, reflecting the fractional activation of the NMDA conductance, with timescale set by the slow MDA time-constant. However, we also consider an inhibitory population, modelled with a threshold-linear differential equation (as in the previous sections).

The equation for the excitatory population is:

$$\nu_E^i = \phi\left(I_E^i\right) = \phi\left((1+\eta h_i)\left(w_{EE}s_N^i + I_{lr,E}^i\right) - w_{EI}\nu_I^i + I_{ext,E}^i\right)$$
$$\tau_N \frac{ds_N^i}{dt} = -s_N^i + \gamma\tau_N(1-s_N^i)\nu_E^i$$

Here ν_E is the excitatory firing rate and s_N is the NMDA gating variable, which is bounded between 0 and 1. ϕ models the firing rate-current dependence of a leaky integrate-and-fire neuron (Abbott & Chance, 2005) and is defined as:

$$\phi(I_{syn}) = \frac{aI_{syn} - b}{1 - e^{-d(aI_{syn}-b)}}$$

with $a = 0.27$ Hz/pA, $b = 108$ Hz and $d = 0.154$ s.

The inhibitory population is described with a threshold-linear equation as before:

$$\tau_I \frac{d\nu_I^i}{dt} = -\nu_I^i + \beta_I \left[I_I^i\right]_+ = -\nu_I^i + \beta_I \left[(1+\eta h_i)\left(w_{IE} s_N^i + I_{lr,I}^i\right) - w_{II}\nu_I^i + I_{ext,I}^i\right]_+ .$$

Parameter values are: $\tau_N = 60$ ms, $\tau_I = 10$ ms, $\gamma = 0.641$, $w_{EE} = 250.2$ pA, $w_{EI} = 8.110$ pA/Hz, $w_{IE} = 303.9$ pA and $w_{EI} = 12.5$ pA/Hz.

5 Supplementary figures

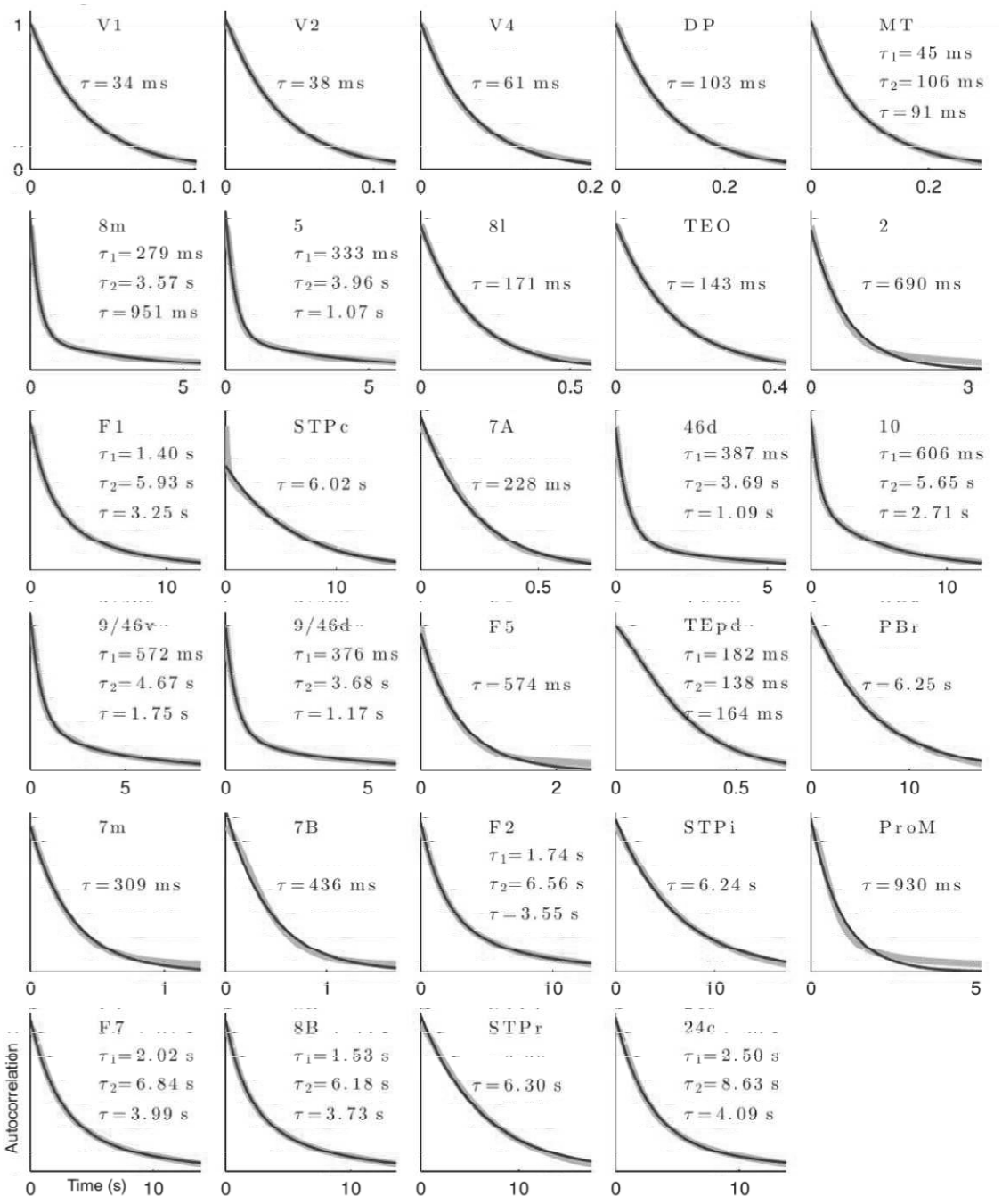

FIGURE 10: **Timescales in response to white-noise input to V1.** Data shown in grey, single exponential fits in blue and double exponential fits in dark red. For double exponential fits, τ_1 et τ_2, with weights given by the amplitudes of the exponentials.

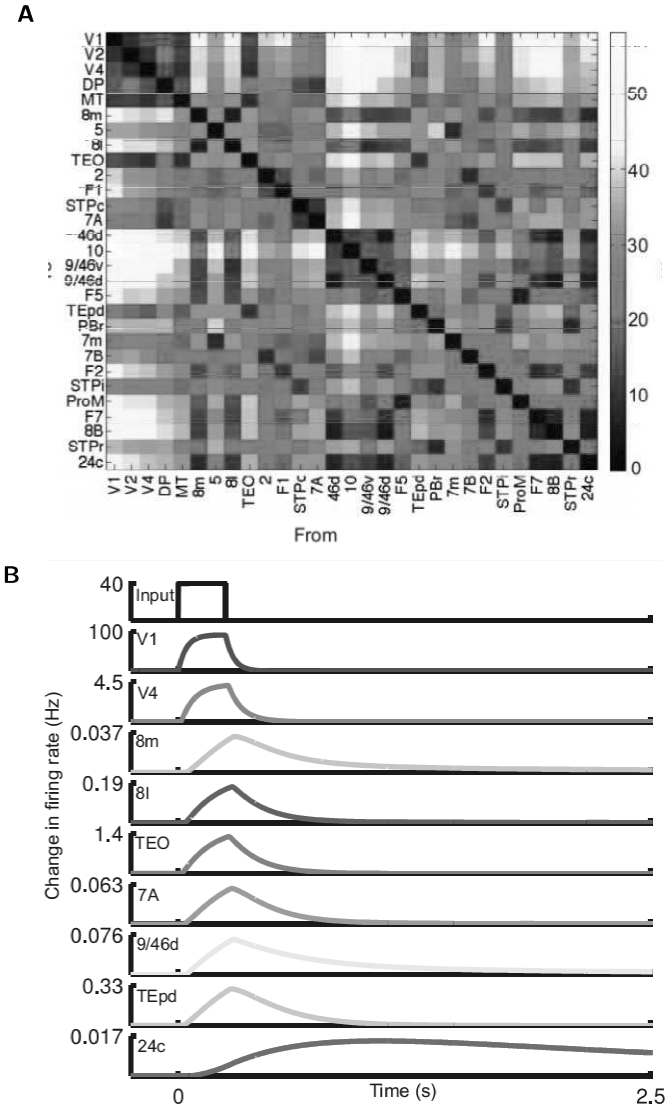

FIGURE 11: **Response of a network with interareal conduction delays.** **(A)** Distances (in mm) between the nodes of the network (Ercsey-Ravasz et al., 2013). **(B)** Response of the network to a pulse of input to area V1. Conduction delays between nodes are imposed using the distances in (A) and a conduction velocity of 1.5 m/s (Deco et al., 2009).

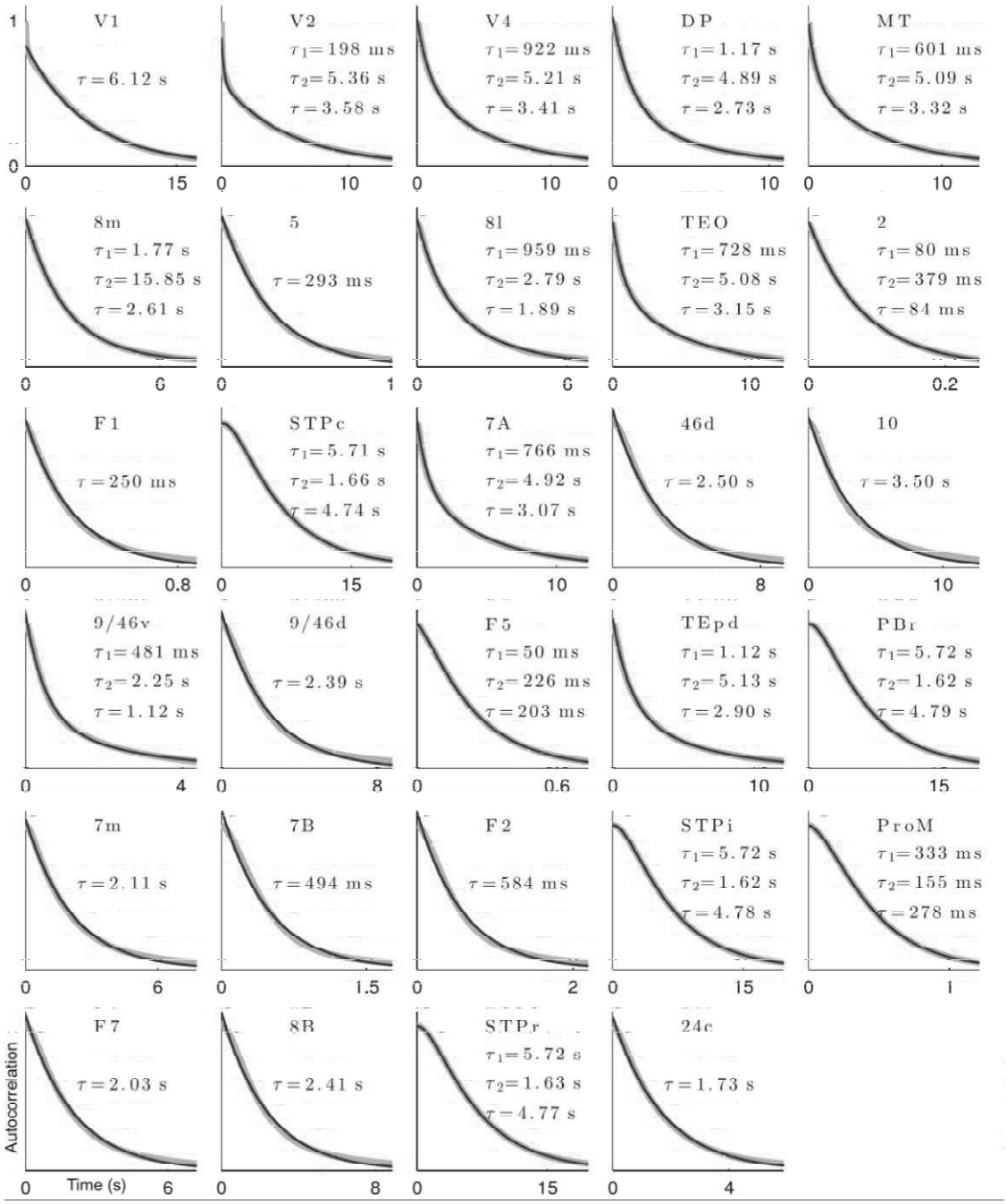

FIGURE 12: **Timescales from exponential fits of activity in response to white-noise input to Area 2.** Colours as in fig. 10.

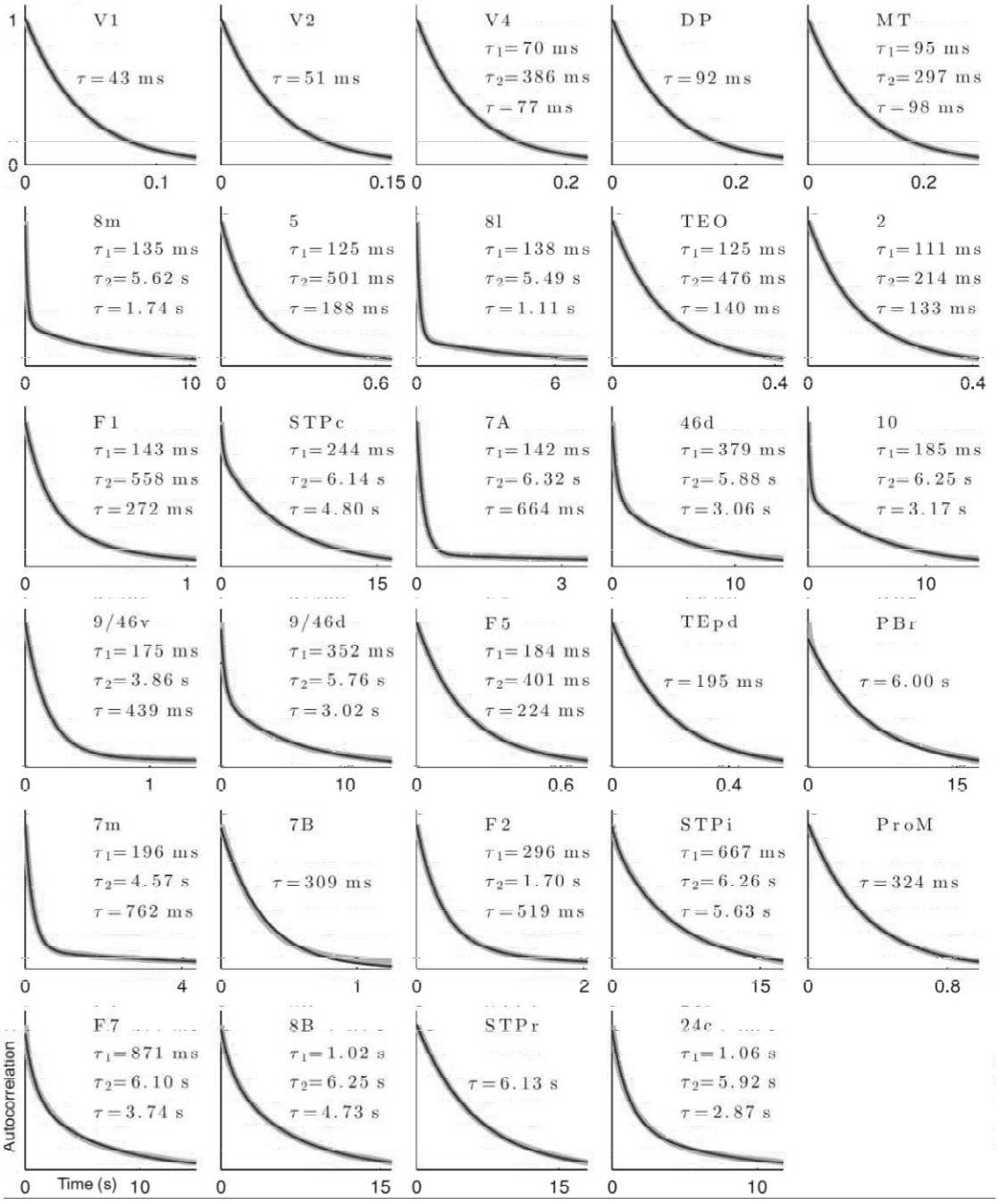

FIGURE 13: **Timescales from exponential fits of resting-state activity.** (i.e., equal white-noise input to all areas). Colours as in fig. 10.

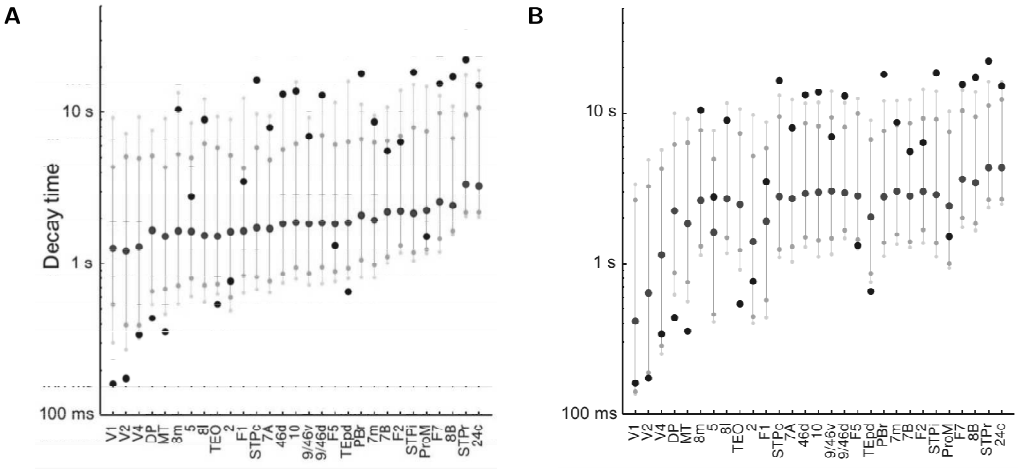

FIGURE 14: **Effect of scrambling long-range connectivity on resting-state network dynamics,** measured by the time taken for an area's activity to return to within 5% of baseline after a 250 ms pulse of input. **(A)** Distribution of timescales when all connection strengths are randomly permuted. Dark blue circles indicate median value, lighter blue circles mark the 10^{th} and 90^{th} percentiles, and the very light blue circles mark 5^{th} and 995^{th} percentiles. Values for intact network are shown in black, for comparison. Areas in scrambled networks are much more similar to each other (compare black to blue), and fast visual areas show the greatest disruption. **(B)** Distributions when only non-zero connection strengths are permuted, thus preserving the connectivity pattern but not strengths. As before, median shown in dark blue, $10\%-90\%$ range in lighter blue, and $5\%-95\%$ in very light blue, along with intact times in black.

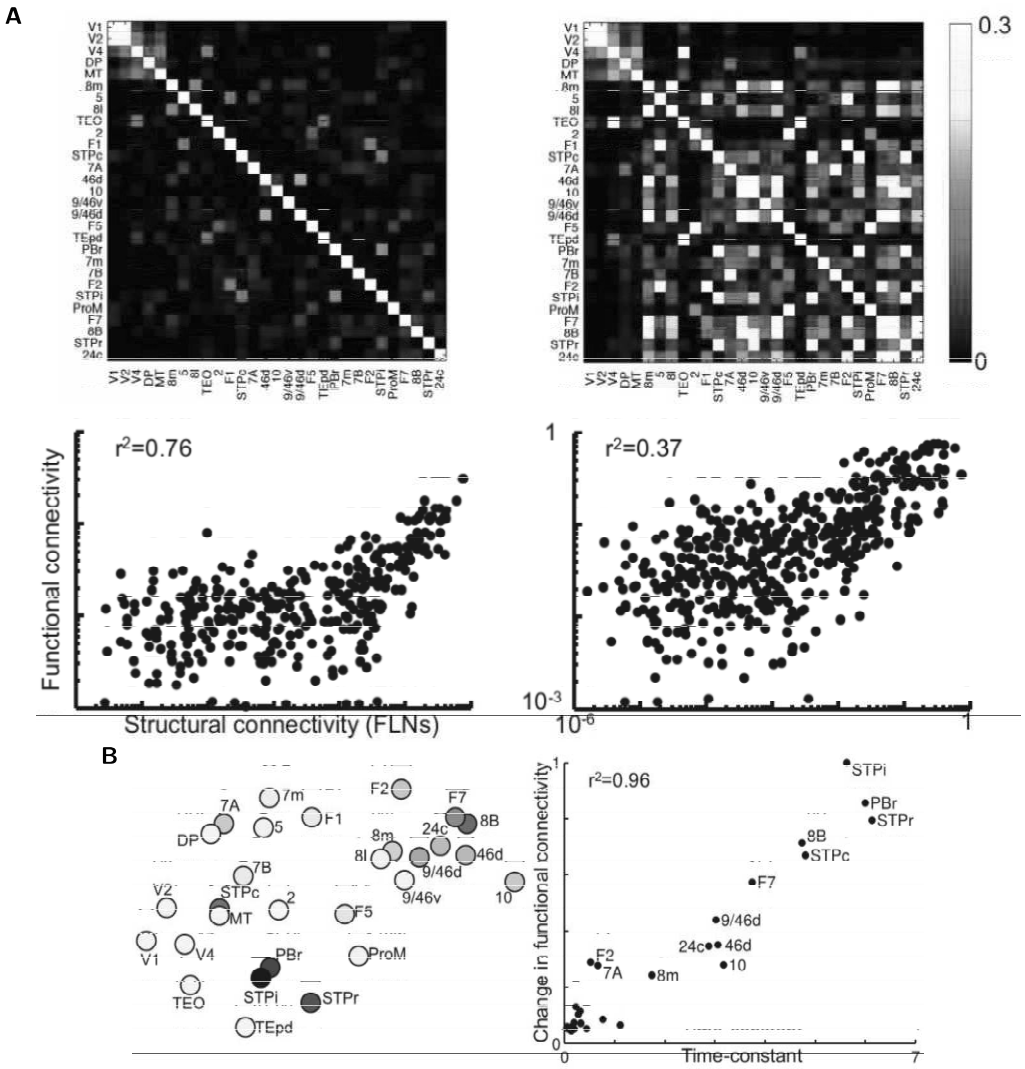

FIGURE 15: **Functional connectivity of simulated BOLD signal.** (A) As in Colours as in fig. 7A, the network on the left has the same local properties at each node, while the network on the right has a gradient of local recurrent strengths. Firing rate is convolved with a gamma function to generate a simulated BOLD signal (Boynton et al., 1996). Top panel: functional connectivity in response to background white noise input to each node. Bottom panel: functional connectivity (correlations in BOLD) vs. structural connectivity (FLN) for non-zero projections. (B) Effect of lesioning areas on functional connectivity measured via simulated BOLD signal. Plots are as in fig. 7B.

Chapter 7

Outlook

Let Hercules himself do what he may,
The cat will mew and dog will have his day.

William Shakespeare, *Hamlet*

In this thesis we have studied the anatomy and dynamics of interareal connections in the cerebral cortex, motivated by open questions linked to the well-established notions of hierarchical organisation and feedforward vs. feedback propagation. While the presence of both types of projections throughout the brain has been long known, compelling evidence for the specific roles that these different paths play in cortical function and perception has been harder to attain.

To further our understanding of this issue we have microstimulated and performed electrophysiological recordings in the visual system of the macaque monkey, while the animals were engaged in an attention-demanding visual task. We have chosen areas V1 and V4 because of their clearly established "canonical" relationship, with a feedforward pathway from V1 to V4 in the bottom-up direction, reciprocated by a descending feedback projection from V4 to V1. The main paradigm we used (the figure-ground segregation of a texture) is well established and the modulation observed in V1 involves feedback from V4 (Lamme et al., 1998). Furthermore, we were able to artificially activate these two pathways with electrical microstimulation, which is to our knowledge the first causal evidence of FB influence on a target area. Although contrary to our working hypothesis we did not find evidence that V4 influences whether or not activity in V1 triggers a percept (chapter 4), we did uncover an important functional asymmetry between FF input in V4 and FB input in V1 (chapter 5). In particular, MS in V1 always activated the corresponding RFs in V4 but MS in V4 did not evoke a visual response in V1, and V4 influence on V1 was only detected when V1 was engaged in the visual task, after the initial response to the texture, during the modulation period. Without sustained input from V4 however, the figure-ground modulation disappears in V1, and we have shown that during the task V4 input is increased at the figure location and decreased in the surroundings of the figure while it remains unchanged on distant locations. These findings are in line with the results of reversible inactivation of macaque area MT on figure-ground discrimination in areas V1, V2 and V3 (Hupé et al., 1998). Interestingly, the authors of this study show that this potentiation of the centre/surround effects mediated by feedback inputs into early visual areas is greater for low salience stimuli. It makes sense that when the task is made easy by high-salience stimuli the influence of FB is smaller and therefore more difficult to detect. For this reason we suggest that future work could evaluate V4 influence on V1 for different saliencies.

In parallel, other work from the Amsterdam team further explored this pivotal asymmetry of feedforward and feedback effects in the early visual system by investigating the hypothesis that these two types of processing result in oscillatory activity at different frequencies (Engel et al., 2001; Wang et al., 2010). In van Kerkoerle et al. (2014) (see the list of publications), laminar electrodes were used to record from all cortical layers of V1 and V4 during two visual tasks (figure-ground segregation and curve tracing). It showed that within an area, gamma waves are initiated in feedforward input layer 4 and propagate to the deep and superficial layers of cortex, whereas alpha waves propagate in the opposite direction, starting in layers targeted by feedback projections. Simultaneous recordings from V1 and downstream area V4 confirmed that gamma and alpha waves propagate between areas in the feedforward and feedback direction, respectively. This oscillatory signature of feedforward and feedback processing will likely prove useful when it comes to disentangle the influence of horizontal and feedback projections during processing. Moreover, using microstimulation as in chapters 4 and 5 of this thesis, we showed

that the propagation of alpha oscillations was stimulus-dependent: it was blocked by the presence of a task-relevant stimulus in the recorded receptive field. On the contrary, gamma oscillations propagated in the feedforward direction whether or not the stimulus was task-relevant, thus confirming the asymmetry of feedback and feedforward influence that we uncovered in chapter 5.

From a functional point of view, the idea that feedforward projections are driving the activity of their target area while feedback can only modulate ongoing activity (Sherman & Guillery, 1998) has shaped our understanding of cortical processing. This dichotomy is based on the clearcut difference between thalamocortical and corticothalamic connections, a difference that has been extended to corticocortical pathways (Crick & Koch, 1998) based on the anatomical similarities in the layers of origin and termination. Of course, there is strong evidence, that FF projections are of the driver type: inactivation of macaque area V1 leads to a complete absence of response to visual stimuli in area V2, and a cessation of activity in many downstream areas including the inferotemporal cortex. However, even after complete V1 inactivation there is residual activity in area MT, and weak motion perception in humans with V1 lesions (reviewed in Bullier et al. 1994). More importantly, Bullier (2006) notes that in the macaque all the evidence about the strong driving property of FF projections come from inactivation of area V1, which also happens to be the virtually unique entry point into the cortex for visual information. Given the strong reciprocal connections between areas V2 and V4, it would be interesting to test whether area V4 stops responding when V2 instead of V1 is inactivated.

For this reason we suggest that future work using our MS technique should test the FF projections from V1 to V2 (the most massive in the cortex) as well as the one from V2 to V4. This is especially relevant because in the parafoveal representation where we recorded there is no direct projection from V1 to V4 (although there is one for the central representation), so the pathway we have looked at is a two-step FF path through V2. Thus microstimulating V2 while recording V4 in the parafoveal representation would allow us to test the FF input from V2 without interference from the FF input from V1. Ideally, we would also study the simultaneous FF and FB inputs to an area during a task, to understand how these inputs interact with the ongoing activity in the local circuitry. Again, V2 would be the target of choice to record while simultaneously microstimulating the parafoveal representations of V1 and V4.

Hierarchies in the cortex

The notion that the cortex is hierarchically organised is widely accepted, but it is used in many more or less abstract ways so it is important to define what we mean by it. The word hierarchy comes from the Greek ἱεραρχία (hierarchia) which means "rule of a high priest", itself from ἱεράρχης (hierarkhes), a "leader of sacred rites". It is an arrangement of items (objects, names, values, categories, etc.) in which the items are represented as being "above," "below," or "at the same level as" one another. In our case, the items are the cortical areas, and after Felleman and Van Essen's building rule, if area A projects in a feedforward fashion onto area B, then A is below B. Conversely if B is above A the projection from B to A should be feedback. Finally if two areas are connected by a lateral projection they are at the same level as one another. Of course, there are both anatomical and functional definitions of feedforward and feedback, but both the items and the relations are identified. On the other hand, some hierarchical models like Fuster's famous diagram of the double hierarchy of perception and action (Fuster, 2004) are more abstract. This plot represents components of the mind/brain complex system such as "primary

(lower) associative", but what the arrows connecting the boxes represent is left to the reader to devise. This is not to say that this concept of hierarchy is not useful as a general framework to guide experimentation. It means however that it must not be confused with the hierarchy we are looking for in the present thesis. It should not be confused either with the hierarchical structure of actions performed (or problems solved) by the brain. Hierarchically structured behaviour can be decomposed in nested levels from long term goals to immediate motor plans (Botvinick, 2008) but although it is tempting to assume as much, it does not mean that the system performing it has a hierarchical structure itself.

There are also two ways to derive a hierarchy. One is from data about the relations between items (the feedforward or feedback nature of interareal connections), but being "above" or "below" can also be determined by a gradient, i.e. a measurable property of the items themselves that makes it possible to order them. From anatomical data, the former is what the GLM method computes based on each projection's SLN, while an example of the latter is Elston's data on the number of spines per pyramidal neurons across areas. As we have shown in chapter 6, the hierarchical ordering given by these two datasets yield very similar results, which indicates that the anatomical hierarchy first devised by Felleman and Van Essen is a strong feature of the cortex. It is, however, not perfectly hierarchical: in the edge-complete subgraph of the 29 injected areas there are many violations to the building rule. However, since the Kennedy dataset provides weighted connectivity and a graded measure of hierarchical distance, we need a weighted approach to quantify the extent of these "anti hierarchical" components in the network. For this, the approach by Ispolatov & Maslov (2008) to find the dominant direction of flow of information in dense networks looks promising.

Regarding functional data, the technique designed by the Roelfsema lab (van Kerkoerle et al., 2014) provides a novel way to identify feedforward and feedback projections from the frequency of their oscillations. The evidence is based on areas V1 and V4 but we hypothesise that this feature will hold across the cortex. Indeed, a different approach by Pascal Fries' lab in Frankfurt has uncovered the same frequency signatures for feedforward and feedback processing in different areas (Bastos et al., 2015). They used grids of cortical surface electrodes which cannot pinpoint the layers of origin and direction of propagation of alpha and gamma waves within an area as the probes that were used in (van Kerkoerle et al., 2014); however they allow simultaneous recording of several areas (8 in this case). From this data and using Granger causality as in van Kerkoerle's approach, they characterised the feedforward or feedback nature of each directed relation, and found a hierarchical ordering of the 8 areas that is in general agreement with our anatomically derived hierarchy. This is a particularly exciting outcome as it seems to provide a functional correlate associated with the previously demonstrated anatomical hierarchy. Other studies provide hierarchical orderings based on functional properties of areas: the intrinsic timescale of resting state activity measured in 7 regions (Murray et al., 2014) or the implication in cognitive control or more and more abstract representations in human prefrontal cortex based on fMRI data (Badre, 2008; Badre & D'Esposito, 2007; Koechlin et al., 2003). In the latter case the ordering is clearly rostro-caudal all the way up to area 10 at the tip of the brain. This disagrees with our hierarchical ordering of the 29 areas where area 10 occupies an intermediate level and not the top of the hierarchy (or the centre in the 2D circular embedding).

A possible insight into these discrepancies is to be found in the multiplicity of functional hierarchies subserved by the same structural hierarchies. Indeed, in chapter 6, the intrinsic timescale of primary sensory areas varied greatly depending on the sensory modality of the input. Furthermore, Fries' team has been able to build slightly different functional hierarchies based on areal interaction at three epochs of the task (Bastos et al., 2015). This makes sense in the light of the dynamic changes in the RF properties of V1 neuron during a visual task (Roelfsema, 2006): after recurrent connections have fed back the processed information into V1, its activity reflects the result of progressively higher processing stages, making it effectively a high order area itself. Moreover, since the dorsal stream exhibits smaller latencies, it is likely that the results of dorsal processing are fed into the slower ventral stream from primary areas like V1 and V2.

In the light of this parallels between the structural hierarchy (with its potentially interesting violations) and the multiple functional hierarchies, we deem it necessary in future studies to generalise the comparison with our large scale anatomical hierarchy (and the exhaustive parcellation that we have developed in collaboration with David Van Essen and made available through the 2nd edition of the CoCoMac database at `http://cocomac.g-node.org/`, Bakker et al. 2012). Indeed, although it is normal for a primary sensory area to be in "slow mode" when its modality is not directly involved with the current task, still we expect that identifying those areas whose hierarchical level varies a lot with the task and task epoch will prove fruitful in the quest for a comprehensive explanation of cortical processing.

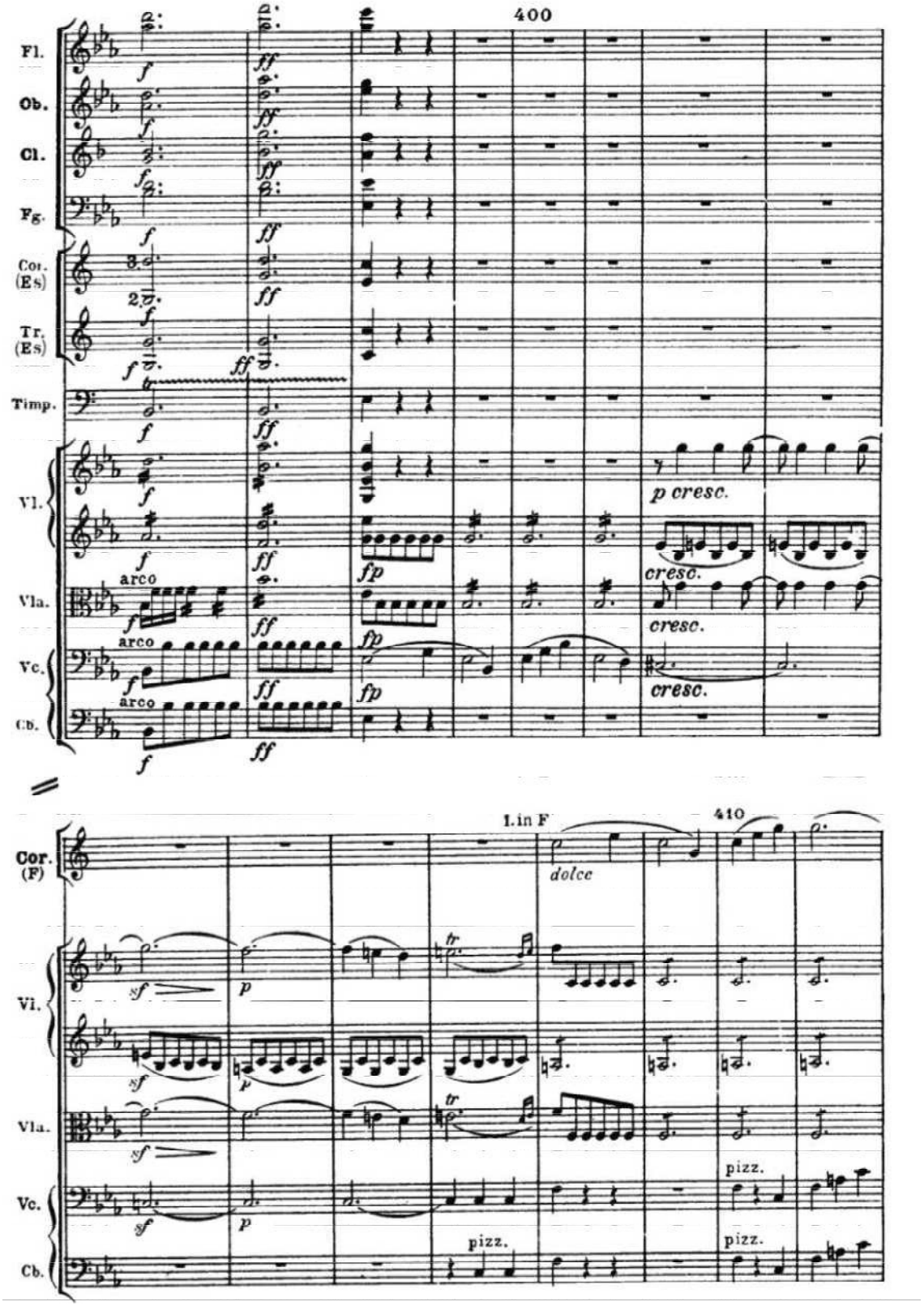
400
Fl.
Ob.
Cl.
Fg.
Cor. (Es)
Tr. (Es)
Timp.
Vl.
Vla.
Vc.
Cb.
arco
p cresc.
cresc.
1. in F
410
Cor. (F)
dolce
pizz.

Bibliography

Abbott, L. F., & Chance, F. S. (2005). Drivers and modulators from push-pull and balanced synaptic input. *Prog. Brain Res.*, *149*, 147–155.

Amaral, D. G., Insausti, R., & Cowan, W. M. (1987). The entorhinal cortex of the monkey: I. Cytoarchitectonic organization. *Journal of Comparative Neurology*, *264*(3), 326–355.

Amit, D. J., Fusi, S., & Yakovlev, V. (1997). Paradigmatic working memory (attractor) cell in IT cortex. *Neural Comput*, *9*(5), 1071–1092.

Andersen, R. A., Asanuma, C., Essick, G., & Siegel, R. M. (1990). Corticocortical connections of anatomically and physiologically defined subdivisions within the inferior parietal lobule. *Journal of Comparative Neurology*, *296*(1), 65–113.

Anderson, J., & Martin, K. (2002). Connection from cortical area V2 to MT in macaque monkey. *Journal of Comparative Neurology*, *443*(1), 56–70.

Anderson, J. C., Binzegger, T., Martin, K. A. C., & Rockland, K. S. (1998). The connection from cortical area V1 to V5: a light and electron microscopic study. *The Journal of neuroscience*, *18*(24), 10525–10540.

Azouz, R., & Gray, C. M. (2003). Adaptive coincidence detection and dynamic gain control in visual cortical neurons in vivo. *Neuron*, *37*(3), 513–523.

Badre, D. (2008). Cognitive control, hierarchy, and the rostro-caudal organization of the frontal lobes. *Trends in Cognitive Sciences*, *12*(5), 193–200.

Badre, D., & D'Esposito, M. (2007). Functional magnetic resonance imaging evidence for a hierarchical organization of the prefrontal cortex. *J Cogn Neurosci*, *19*(12), 2082–2099.

Bakker, R., Wachtler, T., & Diesmann, M. (2012). CoCoMac 2.0 and the future of tract-tracing databases. *Frontiers in Neuroinformatics*, *6*.

Barabasi, A. L., & Albert, R. (1999). Emergence of scaling in random networks. *Science*, *286*(5439), 509–512.

Barbas, H., & Pandya, D. N. (1989). Architecture and intrinsic connections of the prefrontal cortex in the rhesus monkey. *Journal of Comparative Neurology*, *286*(3), 353–375.

Barbas, H., & Rempel-Clower, N. (1997). Cortical structure predicts the pattern of corticocortical connections. *Cereb. Cortex*, *7*(7), 635–646.

Baria, A. T., Mansour, A., Huang, L., Baliki, M. N., Cecchi, G. A., Mesulam, M. M., & Apkarian, A. V. (2013). Linking human brain local activity fluctuations to structural and functional network architectures. *Neuroimage*, *73*, 144–155.

Barone, P., Batardière, A., Knoblauch, K., & Kennedy, H. (2000). Laminar distribution of neurons in extrastriate areas projecting to visual areas V1 and V4 correlates with the hierarchical rank and indicates the operation of a distance rule. *The Journal of Neuroscience*, *20*(9), 3263–3281.

Bassett, D. S., & Bullmore, E. (2006). Small-world brain networks. *The Neuroscientist*, *12*(6), 512–523.

Bastos, A. M., Vezoli, J., Bosman, C. A., Schoffelen, J. M., Oostenveld, R., Dowdall, J. R., De Weerd, P., Kennedy, H., & Fries, P. (2015). Visual Areas Exert Feedforward and Feedback Influences through Distinct Frequency Channels. *Neuron*, *85*(2), 390–401.

Batardiere, A., Barone, P., Dehay, C., & Kennedy, H. (1998). Area-specific laminar distribution of cortical feedback neurons projecting to cat area 17: quantitative analysis in the adult and during ontogeny. *Journal of Comparative Neurology*, *396*(4), 493–510.

Bentivoglio, M., Kuypers, H. G., Catsman-Berrevoets, C. E., Loewe, H., & Dann, O. (1980). Two new fluorescent retrograde neuronal tracers which are transported over long distances. *Neuroscience Letters*, *18*(1), 25–30.

Bernacchia, A., Seo, H., Lee, D., & Wang, X. J. (2011). A reservoir of time constants for memory traces in cortical neurons. *Nat. Neurosci.*, *14*(3), 366–372.

Binzegger, T., Douglas, R. J., & Martin, K. A. C. (2004). A quantitative map of the circuit of cat primary visual cortex. *The Journal of Neuroscience*, *24*(39), 8441–8453.

Binzegger, T., Douglas, R. J., & Martin, K. A. C. (2007). Stereotypical bouton clustering of individual neurons in cat primary visual cortex. *The Journal of Neuroscience*, *27*(45), 12242–12254.

Binzegger, T., Douglas, R. J., & Martin, K. A. C. (2009). Topology and dynamics of the canonical circuit of cat V1. *Neural Networks*, *22*(8), 1071–1078.

Botvinick, M. M. (2008). Hierarchical models of behavior and prefrontal function. *Trends in Cognitive Sciences*, *12*(5), 201–208.

Boynton, G. M., Engel, S. A., Glover, G. H., & Heeger, D. J. (1996). Linear systems analysis of functional magnetic resonance imaging in human V1. *J. Neurosci.*, *16*(13), 4207–4221.

Braitenberg, V., & Schüz, A. (2012). *Cortex: Statistics and Geometry of Neuronal Connectivity*. Springer, 2nd ed. 1998 ed.

Bretz, F., Hothorn, T., & Westfall, P. (2010). *Multiple comparisons using R*. CRC Press.

Brewer, A. A., Press, W. A., Logothetis, N. K., & Wandell, B. A. (2002). Visual areas in macaque cortex measured using functional magnetic resonance imaging. *The Journal of Neuroscience*, *22*(23), 10416–10426.

Brodmann, K. (1909). *Vergleichende Lokalisationslehre der Grosshirnrinde in ihren Prinzipien dargestellt auf Grund des Zellenbaues*. Barth.

Bruno, R. M., & Sakmann, B. (2006). Cortex is driven by weak but synchronously active thalamocortical synapses. *Science*, *312*(5780), 1622–1627.

Brunton, B. W., Botvinick, M. M., & Brody, C. D. (2013). Rats and humans can optimally accumulate evidence for decision-making. *Science*, *340*(6128), 95–98.

Bullier, J. (2001). Integrated model of visual processing. *Brain Research Reviews*, *36*(2), 96–107.

Bullier, J. (2006). What is fed back? In L. Hemmen, & T. Sejnowski (Eds.) *23 Problems in Systems Neuroscience*, (pp. 103–132). Oxford University Press.

Bullier, J., Girard, P., & Salin, P.-A. (1994). The role of area 17 in the transfer of information to extrastriate visual cortex. In *Primary visual cortex in primates*, (pp. 301–330). Springer.

Bullier, J., & Henry, G. H. (1979). Laminar Distribution of First-Order Neurons and Merent Terminals in Cat Striate Cortex.

Bullier, J., & Kennedy, H. (1983). Projection of the lateral geniculate nucleus onto cortical area V2 in the macaque monkey. *Exp Brain Res*, *53*(1), 168–172.

Bullier, J., Kennedy, H., & Salinger, W. (1984). Bifurcation of subcortical afferents to visual areas 17, 18, and 19 in the cat cortex. *Journal of Comparative Neurology*, *228*(3), 309–328.

Bullier, J., McCourt, M. E., & Henry, G. H. (1988). Physiological studies on the feedback connection to the striate cortex from cortical areas 18 and 19 of the cat. *Exp Brain Res*, *70*(1), 90–98.

Bullmore, E., & Sporns, O. (2009). Complex brain networks: graph theoretical analysis of structural and functional systems. *Nature Reviews Neuroscience*, *10*(3), 186–198.

Bullmore, E., & Sporns, O. (2012). The economy of brain network organization. *Nature Reviews Neuroscience*, *13*(5), 336–349.

Buschman, T. J., & Miller, E. K. (2007). Top-down versus bottom-up control of attention in the prefrontal and posterior parietal cortices. *Science*, *315*(5820), 1860–1862.

Butovas, S., & Schwarz, C. (2003). Spatiotemporal effects of microstimulation in rat neocortex: a parametric study using multielectrode recordings. *J. Neurophysiol.*, *90*(5), 3024–3039.

Buzsaki, G. (2007). The structure of consciousness. *Nature*, *446*(7133), 267.

Buzsaki, G., & Draguhn, A. (2004). Neuronal oscillations in cortical networks. *Science*, *304*(5679), 1926–1929.

Chance, F. S., Abbott, L. F., & Reyes, A. D. (2002). Gain modulation from background synaptic input. *Neuron*, *35*(4), 773–782.

Chaudhuri, R., Bernacchia, A., & Wang, X. J. (2014). A diversity of localized timescales in network activity. *Elife*, *3*, e01239.

Chaudhuri, R., Knoblauch, K., Gariel, M. A., Kennedy, H., & Wang, X. J. (2015). A Large-Scale Circuit Mechanism for Hierarchical Dynamical Processing in the Primate Cortex. *Neuron*, *88*(2), 419–431.

Chen, Y., Martinez-Conde, S., Macknik, S. L., Bereshpolova, Y., Swadlow, H. A., & Alonso, J. M. (2008). Task difficulty modulates the activity of specific neuronal populations in primary visual cortex. *Nat. Neurosci.*, *11*(8), 974–982.

Cherniak, C., Mokhtarzada, Z., Rodriguez-Esteban, R., & Changizi, K. (2004). Global optimization of cerebral cortex layout. *Proc. Natl. Acad. Sci. U.S.A.*, *101*(4), 1081–1086.

Colby, C. L., Gattass, R., Olson, C. R., & Gross, C. G. (1988). Topographical organization of cortical afferents to extrastriate visual area PO in the macaque: a dual tracer study. *Journal of Comparative Neurology*, *269*(3), 392–413.

Condé, F. (1987). Further studies on the use of the fluorescent tracers fast blue and diamidino yellow: effective uptake area and cellular storage sites. *The Journal of Neuroscience Methods*, *21*(1), 31–43.

Connor, C. E., Egeth, H. E., & Yantis, S. (2004). Visual attention: bottom-up versus top-down. *Curr. Biol.*, *14*(19), R850–852.

Cribari-Neto, F., & Zeileis, A. (2010). Beta Regression in R. *Journal of Statistical Software*, *34*(1), 1–24.

Crick, F., & Koch, C. (1998). Constraints on cortical and thalamic projections: the no-strong-loops hypothesis. *Nature*, *391*(6664), 245–250.

Crick, F. C., & Koch, C. (2005). What is the function of the claustrum? *Philos. Trans. R. Soc. Lond., B, Biol. Sci.*, *360*(1458), 1271–1279.

Curtis, C. E., & Lee, D. (2010). Beyond working memory: the role of persistent activity in decision making. *Trends in cognitive sciences*, *14*(5), 216–222.

Cusick, C. G., Seltzer, B., Cola, M., & Griggs, E. (1995). Chemoarchitectonics and corticocortical terminations within the superior temporal sulcus of the rhesus monkey: evidence for subdivisions of superior temporal polysensory cortex. *Journal of Comparative Neurology*, *360*(3), 513–535.

Dai, J., Brooks, D. I., & Sheinberg, D. L. (2014). Optogenetic and electrical microstimulation systematically bias visuospatial choice in primates. *Curr. Biol.*, *24*(1), 63–69.

Damoiseaux, J. S., & Greicius, M. D. (2009). Greater than the sum of its parts: a review of studies combining structural connectivity and resting-state functional connectivity. *Brain Struct Funct*, *213*(6), 525–533.

Dayan, P., & Abbott, L. F. (2001). *Theoretical neuroscience*, vol. 806. Cambridge, MA: MIT Press.

de Leeuw, J., & Mair, P. (2009). Multidimensional Scaling Using Majorization: SMACOF in R. *Journal of Statistical Software*, *31*(3), 1–30.
URL `http://www.jstatsoft.org/v31/i03`

Deco, G., & Corbetta, M. (2011). The dynamical balance of the brain at rest. *The Neuroscientist*, *17*(1), 107–123.

Deco, G., Jirsa, V., McIntosh, A. R., Sporns, O., & Kotter, R. (2009). Key role of coupling, delay, and noise in resting brain fluctuations. *Proc. Natl. Acad. Sci. U.S.A.*, *106*(25), 10302–10307.

Deco, G., Ponce-Alvarez, A., Hagmann, P., Romani, G. L., Mantini, D., & Corbetta, M. (2014). How local excitation-inhibition ratio impacts the whole brain dynamics. *J. Neurosci.*, *34*(23), 7886–7898.

Deco, G., Ponce-Alvarez, A., Mantini, D., Romani, G. L., Hagmann, P., & Corbetta, M. (2013). Resting-state functional connectivity emerges from structurally and dynamically shaped slow linear fluctuations. *The Journal of Neuroscience*, *33*(27), 11239–11252.

Dehaene, S., & Changeux, J. P. (2011). Experimental and theoretical approaches to conscious processing. *Neuron*, *70*(2), 200–227.

Dehaene, S., Changeux, J. P., Naccache, L., Sackur, J., & Sergent, C. (2006). Conscious, preconscious, and subliminal processing: a testable taxonomy. *Trends Cogn. Sci*, *10*(5), 204–211.

Dehaene, S., Kerszberg, M., & Changeux, J. P. (1998). A neuronal model of a global workspace in effortful cognitive tasks. *Proc. Natl. Acad. Sci. U.S.A.*, *95*(24), 14529–14534.

Dehaene, S., Sergent, C., & Changeux, J. P. (2003). A neuronal network model linking subjective reports and objective physiological data during conscious perception. *Proc. Natl. Acad. Sci. U.S.A.*, *100*(14), 8520–8525.

Dehay, C., Kennedy, H., & Bullier, J. (1986). Callosal connectivity of areas V1 and V2 in the newborn monkey. *Journal of Comparative Neurology*, *254*(1), 20–33.

Dehay, C., Kennedy, H., Bullier, J., & Berland, M. (1988). Absence of interhemispheric connections of area 17 during development in the monkey. *Nature*, *331*(6154), 348–350.

Destexhe, A., & Paré, D. (1999). Impact of network activity on the integrative properties of neocortical pyramidal neurons in vivo. *J. Neurophysiol.*, *81*(4), 1531–1547.

Diesmann, M., Gewaltig, M. O., & Aertsen, A. (1999). Stable propagation of synchronous spiking in cortical neural networks. *Nature*, *402*(6761), 529–533.

Douglas, R. J., Koch, C., Mahowald, M., Martin, K., & Suarez, H. H. (1995). Recurrent excitation in neocortical circuits. *Science*, *269*(5226), 981–985.

Douglas, R. J., & Martin, K. A. (1991). A functional microcircuit for cat visual cortex. *J. Physiol. (Lond.)*, *440*, 735–769.

Edelman, G. M. (1987). *Neural Darwinism: The theory of neuronal group selection.*. Basic Books.

Edelman, S. (2008). *Computing the mind: How the mind really works*. Oxford University Press.

Ekstrom, L. B., Roelfsema, P. R., Arsenault, J. T., Bonmassar, G., & Vanduffel, W. (2008). Bottom-up dependent gating of frontal signals in early visual cortex. *Science*, *321*(5887), 414–417.

Elston, G. (2007). Specialization of the neocortical pyramidal cell during primate evolution. In J. Kaas, & T. Preuss (Eds.) *Evolution of Nervous Systems: A Comprehensive Reference*, vol. 4, (pp. 191–242). New York: Elsevier.

Elston, G. N. (2000). Pyramidal cells of the frontal lobe: all the more spinous to think with. *The Journal of Neuroscience*, *20*(18), RC95.

Elston, G. N. (2002). Cortical heterogeneity: implications for visual processing and polysensory integration. *J. Neurocytol.*, *31*(3-5), 317–335.

Elston, G. N., Benavides-Piccione, R., & DeFelipe, J. (2005). A study of pyramidal cell structure in the cingulate cortex of the macaque monkey with comparative notes on inferotemporal and primary visual cortex. *Cerebral Cortex*, *15*(1), 64–73.

Elston, G. N., Benavides-Piccione, R., Elston, A., Manger, P. R., & Defelipe, J. (2011). Pyramidal cells in prefrontal cortex of primates: marked differences in neuronal structure among species. *Front Neuroanat*, *5*, 2.

Elston, G. N., Benavides-Piccione, R., Elston, A., Zietsch, B., Defelipe, J., Manger, P., Casagrande, V., & Kaas, J. H. (2006). Specializations of the granular prefrontal cortex of primates: implications for cognitive processing. *Anat Rec A Discov Mol Cell Evol Biol*, *288*(1), 26–35.

Elston, G. N., & Rockland, K. S. (2002). The pyramidal cell of the sensorimotor cortex of the macaque monkey: phenotypic variation. *Cerebral Cortex*, *12*(10), 1071–1078.

Engel, A. K., Fries, P., & Singer, W. (2001). Dynamic predictions: oscillations and synchrony in top-down processing. *Nature Reviews Neuroscience*, *2*(10), 704–716.

Ercsey-Ravasz, M., Markov, N. T., Lamy, C., Van Essen, D. C., Knoblauch, K., Toroczkai, Z., & Kennedy, H. (2013). A predictive network model of cerebral cortical connectivity based on a distance rule. *Neuron*, *80*(1), 184–197.

Euler, L. (1741). Solutio problematis ad geometriam situs pertinentis. *Commentarii academiae scientiarum Petropolitanae*, *8*, 128–140.

Falchier, A., Clavagnier, S., Barone, P., & Kennedy, H. (2002). Anatomical evidence of multimodal integration in primate striate cortex. *The Journal of Neuroscience*, *22*(13), 5749–5759.

Felleman, D. J., & Van Essen, D. C. (1991). Distributed hierarchical processing in the primate cerebral cortex. *Cerebral Cortex*, *1*(1), 1–47.

Ferster, D., & Le Vey, S. (1978). The axonal arborisation of lateral geniculate neurons in the striate cortex of the cat. *Journal of Comparative Neurology*, *182*, 923–944.

Frey, S., Comeau, R., Hynes, B., Mackey, S., & Petrides, M. (2004). Frameless stereotaxy in the nonhuman primate. *Neuroimage*, *23*(3), 1226–1234.

Fuster, J. M. (2004). Upper processing stages of the perception–action cycle. *Trends in cognitive sciences*, *8*(4), 143–145.

Gardiner, C. W., et al. (1985). *Handbook of stochastic methods*, vol. 3. Springer Berlin.

Gariel-Mathis, M. A., Dagnino, B., & Roelfsema, P. R. (2015). Microstimulation of area V4 has little effect on spatial attention and on perception of phosphenes evoked in area V1. *J. Neurophysiol.*, *113*(3), 730–739.

Gattass, R., Nascimento-Silva, S., Soares, J. G., Lima, B., Jansen, A. K., Diogo, A. C., Farias, M. F., Botelho, M. M., Mariani, O. S., Azzi, J., & Fiorani, M. (2005). Cortical visual areas in monkeys: location, topography, connections, columns, plasticity and cortical dynamics. *Philos. Trans. R. Soc. Lond., B, Biol. Sci.*, *360*(1456), 709–731.

Gauthier, B., Eger, E., Hesselmann, G., Giraud, A. L., & Kleinschmidt, A. (2012). Temporal tuning properties along the human ventral visual stream. *The Journal of Neuroscience*, *32*(41), 14433–14441.

Gerbella, M., Belmalih, A., Borra, E., Rozzi, S., & Luppino, G. (2007). Multimodal architectonic subdivision of the caudal ventrolateral prefrontal cortex of the macaque monkey. *Brain Struct Funct*, *212*(3-4), 269–301.

Gerbella, M., Belmalih, A., Borra, E., Rozzi, S., & Luppino, G. (2010). Cortical connections of the macaque caudal ventrolateral prefrontal areas 45A and 45B. *Cerebral Cortex*, *20*(1), 141–168.

Ghosh, A., Rho, Y., McIntosh, A. R., Ktter, R., & Jirsa, V. K. (2008). Noise during rest enables the exploration of the brain's dynamic repertoire. *PLoS Comput. Biol.*, *4*(10), e1000196.

Gil, Z., Connors, B. W., & Amitai, Y. (1999). Efficacy of thalamocortical and intracortical synaptic connections: quanta, innervation, and reliability. *Neuron*, *23*(2), 385–397.

Girard, P., Hupe, J. M., & Bullier, J. (2001). Feedforward and feedback connections between areas V1 and V2 of the monkey have similar rapid conduction velocities. *J. Neurophysiol.*, *85*(3), 1328–1331.

Gold, J. I., & Shadlen, M. N. (2007). The Neural Basis of Decision Making. *Annual Review of Neuroscience*, *30*(1), 535–574. PMID: 17600525.
URL `http://dx.doi.org/10.1146/annurev.neuro.29.051605.113038`

Green, D. M., Swets, J. A., et al. (1966). *Signal detection theory and psychophysics*, vol. 1. Wiley New York.

H., A. (1993). Information theory and an extension of the maximum likelihood principle. In C. F. Petrov BN (Ed.) *Second International Symposium on information theory*, (pp. 267–281). Budapest, Hungary: Akademiai Kiado.

Hackett, T. A., Stepniewska, I., & Kaas, J. H. (1998). Subdivisions of auditory cortex and ipsilateral cortical connections of the parabelt auditory cortex in macaque monkeys. *Journal of Comparative Neurology*, *394*(4), 475–495.

Hagmann, P., Cammoun, L., Gigandet, X., Meuli, R., Honey, C. J., Wedeen, V. J., & Sporns, O. (2008). Mapping the structural core of human cerebral cortex. *PLoS Biol.*, *6*(7), e159.

Hasson, U., Chen, J., & Honey, C. J. (2015). Hierarchical process memory: memory as an integral component of information processing. *Trends Cogn. Sci. (Regul. Ed.)*, *19*(6), 304–313.

Hasson, U., Yang, E., Vallines, I., Heeger, D. J., & Rubin, N. (2008). A hierarchy of temporal receptive windows in human cortex. *The Journal of Neuroscience*, *28*(10), 2539–2550.

Hawrylycz, M. J., Lein, E. S., Guillozet-Bongaarts, A. L., Shen, E. H., Ng, L., Miller, J. A., van de Lagemaat, L. N., Smith, K. A., Ebbert, A., Riley, Z. L., Abajian, C., Beckmann, C. F., Bernard, A., Bertagnolli, D., Boe, A. F., Cartagena, P. M., Chakravarty, M. M., Chapin, M., Chong, J., Dalley, R. A., Daly, B. D., Dang, C., Datta, S., Dee, N., Dolbeare, T. A., Faber, V., Feng, D., Fowler, D. R., Goldy, J., Gregor, B. W., Haradon, Z., Haynor, D. R., Hohmann, J. G., Horvath, S., Howard, R. E., Jeromin, A., Jochim, J. M., Kinnunen, M., Lau, C., Lazarz, E. T., Lee, C., Lemon, T. A., Li, L., Li, Y., Morris, J. A., Overly, C. C., Parker, P. D., Parry, S. E., Reding, M., Royall, J. J., Schulkin, J., Sequeira, P. A., Slaughterbeck, C. R., Smith, S. C., Sodt, A. J., Sunkin, S. M., Swanson, B. E., Vawter, M. P., Williams, D., Wohnoutka, P., Zielke, H. R., Geschwind, D. H., Hof, P. R., Smith, S. M., Koch, C., Grant, S. G., & Jones, A. R. (2012). An anatomically comprehensive atlas of the adult human brain transcriptome. *Nature*, *489*(7416), 391–399.

He, B. J., Zempel, J. M., Snyder, A. Z., & Raichle, M. E. (2010). The temporal structures and functional significance of scale-free brain activity. *Neuron*, *66*(3), 353–369.

Hilbe, J. M. (2007). *Negative binomial regression*. Cambridge University Press.

Hilgetag, C. C., Burns, G. A., O'Neill, M. A., Scannell, J. W., & Young, M. P. (2000). Anatomical connectivity defines the organization of clusters of cortical areas in the macaque monkey and the cat. *Philos. Trans. R. Soc. Lond., B, Biol. Sci.*, *355*(1393), 91–110.

Hilgetag, C. C., Dombrowski, S. M., & Barbas, H. (2002). Classes and gradients of prefrontal cortical organization in the primate. *Neurocomputing*, *44*, 823–829.

Hilgetag, C. C., O'Neill, M. A., & Young, M. P. (1996). Indeterminate organization of the visual system. *Science*, *271*(5250), 776–777.

Histed, M. H., Bonin, V., & Reid, R. C. (2009). Direct activation of sparse, distributed populations of cortical neurons by electrical microstimulation. *Neuron*, *63*(4), 508–522.

Histed, M. H., Ni, A. M., & Maunsell, J. H. (2013). Insights into cortical mechanisms of behavior from microstimulation experiments. *Progress in neurobiology*, *103*, 115–130.

Hof, P. R., Morrison, J. H., & Bloom, F. E. (1995). Neurofilament protein defines regional patterns of cortical organization in the macaque monkey visual system: a quantitative immunohistochemical analysis. *Journal of Comparative Neurology*, *352*(2), 161–186.

Honey, C. J., Kötter, R., Breakspear, M., & Sporns, O. (2007). Network structure of cerebral cortex shapes functional connectivity on multiple time scales. *Proc. Natl. Acad. Sci. U.S.A.*, *104*(24), 10240–10245.

Honey, C. J., Sporns, O., Cammoun, L., Gigandet, X., Thiran, J. P., Meuli, R., & Hagmann, P. (2009). Predicting human resting-state functional connectivity from structural connectivity. *Proc. Natl. Acad. Sci. U.S.A.*, *106*(6), 2035–2040.

Honey, C. J., Thesen, T., Donner, T. H., Silbert, L. J., Carlson, C. E., Devinsky, O., Doyle, W. K., Rubin, N., Heeger, D. J., & Hasson, U. (2012). Slow cortical dynamics and the accumulation of information over long timescales. *Neuron*, *76*(2), 423–434.

Hothorn, T., Bretz, F., & Westfall, P. (2008). Simultaneous inference in general parametric models. *Biom J*, *50*(3), 346–363.

Houweling, A. R., & Brecht, M. (2008). Behavioural report of single neuron stimulation in somatosensory cortex. *Nature*, *451*(7174), 65–68.

Hubel, D. H. (1988). Eye, brain, and vision (scientific american library). *New York*.

Hubel, D. H., & Wiesel, T. N. (1962). Receptive fields, binocular interaction and functional architecture in the cat's visual cortex. *J. Physiol. (Lond.)*, *160*, 106–154.

Hupé, J. M., James, A. C., Payne, B. R., Lomber, S. G., Girard, P., & Bullier, J. (1998). Cortical feedback improves discrimination between figure and background by V1, V2 and V3 neurons. *Nature*, *394*(6695), 784–787.

Ispolatov, I., & Maslov, S. (2008). Detection of the dominant direction of information flow and feedback links in densely interconnected regulatory networks. *BMC bioinformatics*, *9*(1), 424.

Janson, S., Luczak, T., & Rucinski, A. (2011). *Random graphs*, vol. 45. John Wiley & Sons.

Jaynes, E. T. (1957). Information theory and statistical mechanics. *Physical review*, *106*(4), 620.

Jones, E., & Burton, H. (1976). Areal differences in the laminar distribution of thalamic afferents in cortical fields of the insular, parietal and temporal regions of primates. *Journal of Comparative Neurology*, *168*(2), 197–247.

Jouve, B., Rosenstiehl, P., & Imbert, M. (1998). A mathematical approach to the connectivity between the cortical visual areas of the macaque monkey. *Cerebral Cortex*, *8*(1), 28–39.

Kaas, J. H., & Hackett, T. A. (1998). Subdivisions of auditory cortex and levels of processing in primates. *Audiol. Neurootol.*, *3*(2-3), 73–85.

Kaas, J. H., & Lyon, D. C. (2007). Pulvinar contributions to the dorsal and ventral streams of visual processing in primates. *Brain Res Rev*, *55*(2), 285–296.

Kaiser, M., & Hilgetag, C. C. (2006). Nonoptimal component placement, but short processing paths, due to long-distance projections in neural systems. *PLoS Comput. Biol.*, *2*(7), e95.

Kaiser, M., Hilgetag, C. C., & van Ooyen, A. (2009). A simple rule for axon outgrowth and synaptic competition generates realistic connection lengths and filling fractions. *Cerebral Cortex*, *19*(12), 3001–3010.

Kamada, T., & Kawai, S. (1989). An algorithm for drawing general undirected graphs. *Information processing letters*, *31*(1), 7–15.

Kato, H., Bishop, P. O., & Orban, G. A. (1978). Hypercomplex and simple/complex cell classifications in cat striate cortex. *J. Neurophysiol.*, *41*(5), 1071–1095.

Keizer, K., Kuypers, H., Huisman, A., & Dann, O. (1983). Diamidino yellow dihydrochloride (DY· 2HCl); a new fluorescent retrograde neuronal tracer, which migrates only very slowly out of the cell. *Experimental Brain Research*, *51*(2), 179–191.

Kenet, T., Bibitchkov, D., Tsodyks, M., Grinvald, A., & Arieli, A. (2003). Spontaneously emerging cortical representations of visual attributes. *Nature*, *425*(6961), 954–956.

Kennedy, H., & Bullier, J. (1985). A double-labeling investigation of the afferent connectivity to cortical areas V1 and V2 of the macaque monkey. *The Journal of Neuroscience*, *5*(10), 2815–2830.

Kennedy, H., Knoblauch, K., & Toroczkai, Z. (2013). Why data coherence and quality is critical for understanding interareal cortical networks. *Neuroimage*, *80*, 37–45.

Khayat, P. S., Spekreijse, H., & Roelfsema, P. R. (2004). Correlates of transsaccadic integration in the primary visual cortex of the monkey. *Proc. Natl. Acad. Sci. U.S.A.*, *101*(34), 12712–12717.

Kiebel, S. J., Daunizeau, J., & Friston, K. J. (2008). A hierarchy of time-scales and the brain. *PLoS Comput. Biol.*, *4*(11), e1000209.

Kobatake, E., & Tanaka, K. (1994). Neuronal selectivities to complex object features in the ventral visual pathway of the macaque cerebral cortex. *J. Neurophysiol.*, *71*(3), 856–867.

Koechlin, E., Ody, C., & Kouneiher, F. (2003). The architecture of cognitive control in the human prefrontal cortex. *Science*, *302*(5648), 1181–1185.

Kopell, N., Ermentrout, G. B., Whittington, M. A., & Traub, R. D. (2000). Gamma rhythms and beta rhythms have different synchronization properties. *Proc. Natl. Acad. Sci. U.S.A.*, *97*(4), 1867–1872.

Kulli, V., & Sigarkanti, S. (1991). Inverse domination in graphs. *Nat. Acad. Sci. Lett*, *14*(12), 473–475.

Kuypers, H. G., Bentivoglio, M., Catsman-Berrevoets, C. E., & Bharos, A. T. (1980). Double retrograde neuronal labeling through divergent axon collaterals, using two fluorescent tracers with the same excitation wavelength which label different features of the cell. *Exp Brain Res*, *40*(4), 383–392.

Kötter, R. (2004). Online retrieval, processing, and visualization of primate connectivity data from the CoCoMac database. *Neuroinformatics*, *2*(2), 127–144.

Lakatos, P., Karmos, G., Mehta, A. D., Ulbert, I., & Schroeder, C. E. (2008). Entrainment of neuronal oscillations as a mechanism of attentional selection. *Science*, *320*(5872), 110–113.

Lamme, V. A. (1995). The neurophysiology of figure-ground segregation in primary visual cortex. *The Journal of Neuroscience*, *15*(2), 1605–1615.

Lamme, V. A. (2003). Why visual attention and awareness are different. *Trends in Cognitive Sciences*, *7*(1), 12–18.

Lamme, V. A. (2006). Towards a true neural stance on consciousness. *Trends in Cognitive Sciences*, *10*(11), 494–501.

Lamme, V. A., & Roelfsema, P. R. (2000). The distinct modes of vision offered by feedforward and recurrent processing. *Trends Neurosci.*, *23*(11), 571–579.

Lamme, V. A., Super, H., & Spekreijse, H. (1998). Feedforward, horizontal, and feedback processing in the visual cortex. *Curr. Opin. Neurobiol.*, *8*(4), 529–535.

Latawiec, D., Martin, K. A. C., & Meskenaite, V. (2000). Termination of the geniculocortical projection in the striate cortex of macaque monkey: a quantitative immunoelectron microscopic study. *Journal of Comparative Neurology*, *419*(3), 306–319.

Latora, V., & Marchiori, M. (2003). Economic small-world behavior in weighted networks. *The European Physical Journal B-Condensed Matter and Complex Systems*, *32*(2), 249–263.

Lerner, Y., Honey, C. J., Silbert, L. J., & Hasson, U. (2011). Topographic mapping of a hierarchy of temporal receptive windows using a narrated story. *J. Neurosci.*, *31*(8), 2906–2915.

Lewis, J. W., & Van Essen, D. C. (2000). Corticocortical connections of visual, sensorimotor, and multimodal processing areas in the parietal lobe of the macaque monkey. *Journal of Comparative Neurology*, *428*(1), 112–137.

Lindsey, J. K. (1999). Models for repeated measurements. *OUP Catalogue*.

Llinas, R., Ribary, U., Contreras, D., & Pedroarena, C. (1998). The neuronal basis for consciousness. *Philos. Trans. R. Soc. Lond., B, Biol. Sci.*, *353*(1377), 1841–1849.

Logothetis, N. K., Augath, M., Murayama, Y., Rauch, A., Sultan, F., Goense, J., Oeltermann, A., & Merkle, H. (2010). The effects of electrical microstimulation on cortical signal propagation. *Nat. Neurosci.*, *13*(10), 1283–1291.

Lund, J. S., Hendrickson, A. E., Ogren, M. P., & Tobin, E. A. (1981). Anatomical organization of primate visual cortex area VII. *Journal of Comparative Neurology*, *202*(1), 19–45.

Luppino, G., Ben Hamed, S., Gamberini, M., Matelli, M., & Galletti, C. (2005). Occipital (V6) and parietal (V6A) areas in the anterior wall of the parieto-occipital sulcus of the macaque: a cytoarchitectonic study. *Eur. The Journal of Neuroscience*, *21*(11), 3056–3076.

Luppino, G., & Rizzolatti, G. (2000). The Organization of the Frontal Motor Cortex. *News Physiol. Sci.*, *15*, 219–224.

MacNeil, M. A., Lomber, S. G., & Payne, B. R. (1997). Thalamic and cortical projections to middle suprasylvian cortex of cats: constancy and variation. *Exp Brain Res*, *114*(1), 24–32.

Margulies, D. S., Vincent, J. L., Kelly, C., Lohmann, G., Uddin, L. Q., Biswal, B. B., Villringer, A., Castellanos, F. X., Milham, M. P., & Petrides, M. (2009). Precuneus shares intrinsic functional architecture in humans and monkeys. *Proc. Natl. Acad. Sci. U.S.A.*, *106*(47), 20069–20074.

Markov, N. T., Ercsey-Ravasz, M., Lamy, C., Ribeiro Gomes, A. R., Magrou, L., Misery, P., Giroud, P., Barone, P., Dehay, C., Toroczkai, Z., Knoblauch, K., Van Essen, D. C., & Kennedy, H. (2013). The role of long-range connections on the specificity of the macaque interareal cortical network. *Proc. Natl. Acad. Sci. U.S.A.*, *110*(13), 5187–5192.

Markov, N. T., Ercsey-Ravasz, M. M., Gariel, M. A., Dehay, C., Knoblauch, A., Toroczkai, Z., & Kennedy, H. (2011a). The tribal networks of the cerebral cortex. In L. M. Chalupa, N. Berardi, M. Caleo, & L. Galli-Resta (Eds.) *Cerebral Plasticity: New Perspectives*, (pp. 275–290). Cambridge, Massachusetts: MIT Press.

Markov, N. T., Ercsey-Ravasz, M. M., Ribeiro Gomes, A. R., Lamy, C., Magrou, L., Vezoli, J., Misery, P., Falchier, A., Quilodran, R., Gariel, M. A., Sallet, J., Gamanut, R., Huissoud, C., Clavagnier, S., Giroud, P., Sappey-Marinier, D., Barone, P., Dehay, C., Toroczkai, Z., Knoblauch, K., Van Essen, D. C., & Kennedy, H. (2014a). A weighted and directed interareal connectivity matrix for macaque cerebral cortex. *Cerebral Cortex*, *24*(1), 17–36.

Markov, N. T., Misery, P., Falchier, A., Lamy, C., Vezoli, J., Quilodran, R., Gariel, M. A., Giroud, P., Ercsey-Ravasz, M., Pilaz, L. J., Huissoud, C., Barone, P., Dehay, C., Toroczkai, Z., Van Essen, D. C., Kennedy, H., & Knoblauch, K. (2011b). Weight consistency specifies regularities of macaque cortical networks. *Cerebral Cortex*, *21*(6), 1254–1272.

Markov, N. T., Vezoli, J., Chameau, P., Falchier, A., Quilodran, R., Huissoud, C., Lamy, C., Misery, P., Giroud, P., Ullman, S., Barone, P., Dehay, C., Knoblauch, K., & Kennedy, H. (2014b). Anatomy of hierarchy: feedforward and feedback pathways in macaque visual cortex. *Journal of Comparative Neurology*, *522*(1), 225–259.

Marr, D., & Poggio, T. (1977). From understanding computation to understanding neural circuitry. *Neurosciences Res. Prog. Bull.*, *15*, 470–488.

McCullagh, P., & Nelder, J. A. (1989). Generalized linear models.

Medalla, M., & Barbas, H. (2009). Synapses with inhibitory neurons differentiate anterior cingulate from dorsolateral prefrontal pathways associated with cognitive control. *Neuron*, *61*(4), 609–620.

Merigan, W. H. (1996). Basic visual capacities and shape discrimination after lesions of extrastriate area V4 in macaques. *Visual neuroscience*, *13*(01), 51–60.

Mesulam, M. M., & Mufson, E. J. (1982). Insula of the old world monkey. I. Architectonics in the insulo-orbito-temporal component of the paralimbic brain. *Journal of Comparative Neurology*, *212*(1), 1–22.

Milo, R., Shen-Orr, S., Itzkovitz, S., Kashtan, N., Chklovskii, D., & Alon, U. (2002). Network motifs: simple building blocks of complex networks. *Science*, *298*(5594), 824–827.

Modha, D. S., & Singh, R. (2010). Network architecture of the long-distance pathways in the macaque brain. *Proc. Natl. Acad. Sci. U.S.A.*, *107*(30), 13485–13490.

Moldakarimov, S., Bazhenov, M., & Sejnowski, T. J. (2015). Feedback stabilizes propagation of synchronous spiking in cortical neural networks. *Proc. Natl. Acad. Sci. U.S.A.*, *112*(8), 2545–2550.

Moore, T., Armstrong, K. M., & Fallah, M. (2003). Visuomotor origins of covert spatial attention. *Neuron*, *40*(4), 671–683.

Moore, T., & Fallah, M. (2001). Control of eye movements and spatial attention. *Proc. Natl. Acad. Sci. U.S.A.*, *98*(3), 1273–1276.

Moore, T., & Fallah, M. (2004). Microstimulation of the frontal eye field and its effects on covert spatial attention. *J. Neurophysiol.*, *91*(1), 152–162.

Moran, J., & Desimone, R. (1985). Selective attention gates visual processing in the extrastriate cortex. *Science*, *229*(4715), 782–784.

Morecraft, R. J., Cipolloni, P. B., Stilwell-Morecraft, K. S., Gedney, M. T., & Pandya, D. N. (2004). Cytoarchitecture and cortical connections of the posterior cingulate and adjacent somatosensory fields in the rhesus monkey. *Journal of Comparative Neurology*, *469*(1), 37–69.

Movshon, J. A., & Newsome, W. T. (1996). Visual response properties of striate cortical neurons projecting to area MT in macaque monkeys. *The Journal of Neuroscience*, *16*(23), 7733–7741.

Murray, J. D., Bernacchia, A., Freedman, D. J., Romo, R., Wallis, J. D., Cai, X., Padoa-Schioppa, C., Pasternak, T., Seo, H., Lee, D., & Wang, X. J. (2014). A hierarchy of intrinsic timescales across primate cortex. *Nat. Neurosci.*, *17*(12), 1661–1663.

Musil, S. Y., & Olson, C. R. (1988a). Organization of cortical and subcortical projections to anterior cingulate cortex in the cat. *Journal of Comparative Neurology*, *272*(2), 203–218.

Musil, S. Y., & Olson, C. R. (1988b). Organization of cortical and subcortical projections to medial prefrontal cortex in the cat. *Journal of Comparative Neurology*, *272*(2), 219–241.

Nassi, J. J., Lomber, S. G., & Born, R. T. (2013). Corticocortical feedback contributes to surround suppression in V1 of the alert primate. *The Journal of Neuroscience*, *33*(19), 8504–8517.

Newman, M. (2010). *Networks: an introduction*. Oxford University Press.

Newman, M. E. (2003). The structure and function of complex networks. *SIAM review*, *45*(2), 167–256.

Newman, M. E. (2005). Power laws, Pareto distributions and Zipf's law. *Contemporary physics*, *46*(5), 323–351.

Ni, A. M., & Maunsell, J. H. (2010). Microstimulation reveals limits in detecting different signals from a local cortical region. *Curr. Biol.*, *20*(9), 824–828.

Noudoost, B., & Moore, T. (2011). Control of visual cortical signals by prefrontal dopamine. *Nature*, *474*(7351), 372–375.

Ogawa, T., & Komatsu, H. (2010). Differential temporal storage capacity in the baseline activity of neurons in macaque frontal eye field and area V4. *J. Neurophysiol.*, *103*(5), 2433–2445.

Olson, C. R., & Musil, S. Y. (1992). Topographic organization of cortical and subcortical projections to posterior cingulate cortex in the cat: evidence for somatic, ocular, and complex subregions. *Journal of Comparative Neurology*, *324*(2), 237–260.

Padberg, J., Seltzer, B., & Cusick, C. G. (2003). Architectonics and cortical connections of the upper bank of the superior temporal sulcus in the rhesus monkey: an analysis in the tangential plane. *Journal of Comparative Neurology*, *467*(3), 418–434.

Pandya, D. N., & Seltzer, B. (1982). Intrinsic connections and architectonics of posterior parietal cortex in the rhesus monkey. *Journal of Comparative Neurology*, *204*(2), 196–210.

Pascual-Leone, A., & Walsh, V. (2001). Fast backprojections from the motion to the primary visual area necessary for visual awareness. *Science*, *292*(5516), 510–512.

Paxinos, G., Huang, X.-F., & Toga, A. W. (2000). *The Rhesus Monkey Brain in Stereotaxic Coordinates*. Academic Press.

Perkel, D. J., Bullier, J., & Kennedy, H. (1986). Topography of the afferent connectivity of area 17 in the macaque monkey: a double-labelling study. *Journal of Comparative Neurology*, *253*(3), 374–402.

Petrides, M., & Pandya, D. N. (1999). Dorsolateral prefrontal cortex: comparative cytoarchitectonic analysis in the human and the macaque brain and corticocortical connection patterns. *Eur. The Journal of Neuroscience*, *11*(3), 1011–1036.

Poort, J., Raudies, F., Wannig, A., Lamme, V. A., Neumann, H., & Roelfsema, P. R. (2012). The role of attention in figure-ground segregation in areas V1 and V4 of the visual cortex. *Neuron*, *75*(1), 143–156.

Posner, M. I., Snyder, C. R., & Davidson, B. J. (1980). Attention and the detection of signals. *J Exp Psychol*, *109*(2), 160–174.

Preuss, T. M., & Goldman-Rakic, P. S. (1991). Myelo- and cytoarchitecture of the granular frontal cortex and surrounding regions in the strepsirhine primate Galago and the anthropoid primate Macaca. *Journal of Comparative Neurology*, *310*(4), 429–474.

Prins, N., & Kingdom, F. (2009). Palamedes: Matlab routines for analyzing psychophysical data. `http://www.palamedestoolbox.org`.

Purushothaman, G., Marion, R., Li, K., & Casagrande, V. A. (2012). Gating and control of primary visual cortex by pulvinar. *Nat. Neurosci.*, *15*(6), 905–912.

Raichle, M. E., & Mintun, M. A. (2006). Brain work and brain imaging. *Annu. Rev. Neurosci.*, *29*, 449–476.

Rockland, K. S., & Pandya, D. N. (1979). Laminar origins and terminations of cortical connections of the occipital lobe in the rhesus monkey. *Brain Research*, *179*(1), 3–20.

Roelfsema, P. R. (2006). Cortical algorithms for perceptual grouping. *Annu. Rev. Neurosci.*, *29*(30), 203–227.

Roelfsema, P. R., Lamme, V. A., & Spekreijse, H. (1998). Object-based attention in the primary visual cortex of the macaque monkey. *Nature*, *395*(6700), 376–381.

Roelfsema, P. R., Lamme, V. A., Spekreijse, H., & Bosch, H. (2002). Figure-ground segregation in a recurrent network architecture. *J Cogn Neurosci*, *14*(4), 525–537.

Rosene, D. L., Roy, N. J., & Davis, B. J. (1986). A cryoprotection method that facilitates cutting frozen sections of whole monkey brains for histological and histochemical processing without freezing artifact. *J. Histochem. Cytochem.*, *34*(10), 1301–1315.

Rossi, A. F., Pessoa, L., Desimone, R., & Ungerleider, L. G. (2009). The prefrontal cortex and the executive control of attention. *Exp Brain Res*, *192*(3), 489–497.

Rugh, W. J. (1995). *Linear System Theory*. Prentice Hall, New Jersey.

Saleem, K. S., & Logothetis, N. K. (2007). *A Combined MRI and Histology Atlas of the Rhesus Monkey Brain in Stereotaxic Coordinates, Second Edition*. Academic Press.

Salin, P. A., & Bullier, J. (1995). Corticocortical connections in the visual system: structure and function. *Physiol. Rev.*, *75*(1), 107–154.

Salvador, R., Suckling, J., Schwarzbauer, C., & Bullmore, E. (2005). Undirected graphs of frequency-dependent functional connectivity in whole brain networks. *Philos. Trans. R. Soc. Lond., B, Biol. Sci.*, *360*(1457), 937–946.

Scannell, J. W., Grant, S., Payne, B. R., & Baddeley, R. (2000). On variability in the density of corticocortical and thalamocortical connections. *Philos. Trans. R. Soc. Lond., B, Biol. Sci.*, *355*(1393), 21–35.

Schall, J. D., Morel, A., King, D. J., & Bullier, J. (1995). Topography of visual cortex connections with frontal eye field in macaque: convergence and segregation of processing streams. *The Journal of Neuroscience*, *15*(6), 4464–4487.

Schiller, P. H. (1995). Effect of lesions in visual cortical area V4 on the recognition of transformed objects. *Nature*, *376*(6538), 342–344.

Schiller, P. H., & Tehovnik, E. J. (2008). Visual prosthesis. *Perception*, *37*(10), 1529–1559.

Schmolesky, M. T., Wang, Y., Hanes, D. P., Thompson, K. G., Leutgeb, S., Schall, J. D., & Leventhal, A. G. (1998). Signal timing across the macaque visual system. *J. Neurophysiol.*, *79*(6), 3272–3278.

Scholtens, L. H., Schmidt, R., de Reus, M. A., & van den Heuvel, M. P. (2014). Linking macroscale graph analytical organization to microscale neuroarchitectonics in the macaque connectome. *J. Neurosci.*, *34*(36), 12192–12205.

Seidemann, E., Arieli, A., Grinvald, A., & Slovin, H. (2002). Dynamics of depolarization and hyperpolarization in the frontal cortex and saccade goal. *Science*, *295*(5556), 862–865.

Self, M. W., Kooijmans, R. N., Super, H., Lamme, V. A., & Roelfsema, P. R. (2012). Different glutamate receptors convey feedforward and recurrent processing in macaque V1. *Proc. Natl. Acad. Sci. U.S.A.*, *109*(27), 11031–11036.

Sepulcre, J., Liu, H., Talukdar, T., Martincorena, I., Yeo, B. T., & Buckner, R. L. (2010). The organization of local and distant functional connectivity in the human brain. *PLoS Comput. Biol.*, *6*(6), e1000808.

Sherman, S. M., & Guillery, R. W. (1998). On the actions that one nerve cell can have on another: distinguishing "drivers" from "modulators". *Proc. Natl. Acad. Sci. U.S.A.*, *95*(12), 7121–7126.

Sherrington, C. S. (1906). Observations on the scratch-reflex in the spinal dog. *J. Physiol. (Lond.)*, *34*(1-2), 1–50.

Silvanto, J., Cowey, A., Lavie, N., & Walsh, V. (2005). Striate cortex (V1) activity gates awareness of motion. *Nat. Neurosci.*, *8*(2), 143–144.

Smith, P. L., & Ratcliff, R. (2004). Psychology and neurobiology of simple decisions. *Trends Neurosci.*, *27*(3), 161–168.

Sommer, M. A., & Wurtz, R. H. (2000). Composition and topographic organization of signals sent from the frontal eye field to the superior colliculus. *J. Neurophysiol.*, *83*(4), 1979–2001.

Song, S., Sjostrom, P. J., Reigl, M., Nelson, S., & Chklovskii, D. B. (2005). Highly nonrandom features of synaptic connectivity in local cortical circuits. *PLoS Biol.*, *3*(3), e68.

Sporns, O. (2011). *Networks of the Brain*. MIT press.

Sporns, O. (2014). Contributions and challenges for network models in cognitive neuroscience. *Nat. Neurosci.*, *17*(5), 652–660.

Sporns, O., & Honey, C. J. (2006). Small worlds inside big brains. *Proc. Natl. Acad. Sci. U.S.A.*, *103*(51), 19219–19220.

Sporns, O., Honey, C. J., & Kötter, R. (2007). Identification and classification of hubs in brain networks. *PLoS ONE*, *2*(10).

Sporns, O., Tononi, G., & Edelman, G. M. (2000). Theoretical neuroanatomy: relating anatomical and functional connectivity in graphs and cortical connection matrices. *Cerebral Cortex*, *10*(2), 127–141.

Sporns, O., & Zwi, J. D. (2004). The small world of the cerebral cortex. *Neuroinformatics*, *2*(2), 145–162.

Stephan, K. E., Kamper, L., Bozkurt, A., Burns, G. A., Young, M. P., & Kötter, R. (2001). Advanced database methodology for the Collation of Connectivity data on the Macaque brain (CoCoMac). *Philos. Trans. R. Soc. Lond., B, Biol. Sci.*, *356*(1412), 1159–1186.

Stephens, G. J., Honey, C. J., & Hasson, U. (2013). A place for time: the spatiotemporal structure of neural dynamics during natural audition. *J. Neurophysiol.*, *110*(9), 2019–2026.

Stepniewska, I., Collins, C. E., & Kaas, J. H. (2005). Reappraisal of DL/V4 boundaries based on connectivity patterns of dorsolateral visual cortex in macaques. *Cerebral Cortex*, *15*(6), 809–822.

Stratford, K., Tarczy-Hornoch, K., Martin, K., Bannister, N., & Jack, J. (1996). Excitatory synaptic inputs to spiny stellate cells in cat visual cortex. *Nature*, *382*(6588), 258–261.

Super, H., & Roelfsema, P. R. (2005). Chronic multiunit recordings in behaving animals: advantages and limitations. *Prog. Brain Research*, *147*, 263–282.

Super, H., Spekreijse, H., & Lamme, V. A. (2001). Two distinct modes of sensory processing observed in monkey primary visual cortex (V1). *Nat. Neurosci.*, *4*(3), 304–310.

Tehovnik, E. J. (1996). Electrical stimulation of neural tissue to evoke behavioral responses. *The Journal of Neuroscience Methods*, *65*(1), 1–17.

Tehovnik, E. J., Slocum, W. M., Carvey, C. E., & Schiller, P. H. (2005). Phosphene induction and the generation of saccadic eye movements by striate cortex. *J. Neurophysiol.*, *93*(1), 1–19.

Tehovnik, E. J., Slocum, W. M., & Schiller, P. H. (2003). Saccadic eye movements evoked by microstimulation of striate cortex. *Eur. The Journal of Neuroscience*, *17*(4), 870–878.

Tiesinga, P., Fellous, J. M., & Sejnowski, T. J. (2008). Regulation of spike timing in visual cortical circuits. *Nature Reviews Neuroscience*, *9*(2), 97–107.

Tsodyks, M., Kenet, T., Grinvald, A., & Arieli, A. (1999). Linking spontaneous activity of single cortical neurons and the underlying functional architecture. *Science*, *286*(5446), 1943–1946.

Uhlhaas, P. J., Pipa, G., Lima, B., Melloni, L., Neuenschwander, S., Nikolić, D., & Singer, W. (2009). Neural synchrony in cortical networks: history, concept and current status. *Front Integr Neurosci*, *3*, 17.

Ullman, S. (1995). Sequence seeking and counter streams: a computational model for bidirectional information flow in the visual cortex. *Cerebral cortex*, *5*(1), 1–11.

Van Essen, D. C. (2004a). Organization of visual areas in macaque and human cerebral cortex. In L. Chalupa, & J. Werner (Eds.) *The visual neurosciences*, (pp. 507–521). Cambridge, Massachusetts: MIT Press.

Van Essen, D. C. (2004b). Surface-based approaches to spatial localization and registration in primate cerebral cortex. *Neuroimage*, *23 Suppl 1*, 97–107.

Van Essen, D. C. (2005). A population-average, landmark-and surface-based (PALS) atlas of human cerebral cortex. *Neuroimage*, *28*(3), 635–662.

Van Essen, D. C., Drury, H. A., Dickson, J., Harwell, J., Hanlon, D., & Anderson, C. H. (2001a). An integrated software suite for surface-based analyses of cerebral cortex. *J Am Med Inform Assoc*, *8*(5), 443–459.

Van Essen, D. C., Glasser, M. F., Dierker, D. L., & Harwell, J. (2012a). Cortical parcellations of the macaque monkey analyzed on surface-based atlases. *Cerebral Cortex*, *22*(10), 2227–2240.

Van Essen, D. C., Glasser, M. F., Dierker, D. L., & Harwell, J. (2012b). Cortical parcellations of the macaque monkey analyzed on surface-based atlases. *Cerebral Cortex*, *22*(10), 2227–2240.

Van Essen, D. C., Harwell, J., Hanlon, D., & Dickson, J. (2005). Surface-based atlases and a database of cortical structure and function. In S. Koslow, & S. Subramaniam (Eds.) *Databasing the brain: From data to knowledge (Neuroinformatics)*, (pp. 369–388). Hoboken, NJ: John Wiley & Sons, Inc.

Van Essen, D. C., Lewis, J. W., Drury, H. A., Hadjikhani, N., Tootell, R. B. H., Bakircioglu, M., & Miller, M. I. (2001b). Mapping visual cortex in monkeys and humans using surface-based atlases. *Vision research*, *41*(10), 1359–1378.

van Kerkoerle, T., Self, M. W., Dagnino, B., Gariel-Mathis, M. A., Poort, J., van der Togt, C., & Roelfsema, P. R. (2014). Alpha and gamma oscillations characterize feedback and feedforward processing in monkey visual cortex. *Proc. Natl. Acad. Sci. U.S.A.*, *111*(40), 14332–14341.

Vangkilde, S., Coull, J. T., & Bundesen, C. (2012). Great expectations: temporal expectation modulates perceptual processing speed. *J Exp Psychol Hum Percept Perform*, *38*(5), 1183–1191.

Venables, W. N., & Ripley, B. D. (2002). *Modern applied statistics with S*. Springer.

Vezoli, J., Falchier, A., Jouve, B., Knoblauch, K., Young, M., & Kennedy, H. (2004). Quantitative analysis of connectivity in the visual cortex: extracting function from structure. *The Neuroscientist*, *10*(5), 476–482.

von Stein, A., Chiang, C., & Konig, P. (2000). Top-down processing mediated by interareal synchronization. *Proc. Natl. Acad. Sci. U.S.A.*, *97*(26), 14748–14753.

Vragović, I., Louis, E., & Diaz-Guilera, A. (2005). Efficiency of informational transfer in regular and complex networks. *Physical Review E*, *71*(3), 036122.

Wallisch, P., & Movshon, J. A. (2008). Structure and function come unglued in the visual cortex. *Neuron*, *60*(2), 195–197.

Walsh, V., & Cowey, A. (1998). Magnetic stimulation studies of visual cognition. *Trends in Cognitive Sciences*, *2*(3), 103–110.

Walsh, V., & Cowey, A. (2000). Transcranial magnetic stimulation and cognitive neuroscience. *Nature Reviews Neuroscience*, *1*(1), 73–79.

Wang, H. P., Spencer, D., Fellous, J. M., & Sejnowski, T. J. (2010). Synchrony of thalamocortical inputs maximizes cortical reliability. *Science*, *328*(5974), 106–109.

Wang, Q., & Burkhalter, A. (2013). Stream-related preferences of inputs to the superior colliculus from areas of dorsal and ventral streams of mouse visual cortex. *The Journal of Neuroscience*, *33*(4), 1696–1705.

Wang, X. J. (1998). Calcium coding and adaptive temporal computation in cortical pyramidal neurons. *J. Neurophysiol.*, *79*(3), 1549–1566.

Wang, X. J. (2002). Probabilistic decision making by slow reverberation in cortical circuits. *Neuron*, *36*(5), 955–968.

Wang, X. J. (2008). Decision making in recurrent neuronal circuits. *Neuron*, *60*(2), 215–234.

Wang, X. J. (2013). The prefrontal cortex as a quintessential "cognitive-type" neural circuit. In D. T. Stuss, & R. T. Knight (Eds.) *Principles of Frontal Lobe Function*, (pp. 226–248). Cambridge, Massachusetts: Cambridge University Press.

Watson, A. B., & Pelli, D. G. (1983). QUEST: a Bayesian adaptive psychometric method. *Percept Psychophys*, *33*(2), 113–120.

Watts, D. J., & Strogatz, S. H. (1998). Collective dynamics of 'small-world' networks. *Nature*, *393*(6684), 440–442.

Wong, K. F., & Wang, X. J. (2006). A recurrent network mechanism of time integration in perceptual decisions. *J. Neurosci.*, *26*(4), 1314–1328.

Yoshioka, T., Levitt, J. B., & Lund, J. S. (1992). Intrinsic lattice connections of macaque monkey visual cortical area V4. *The Journal of Neuroscience*, *12*(7), 2785–2802.

Young, M. P. (1993). The organization of neural systems in the primate cerebral cortex. *Proc. Biol. Sci.*, *252*(1333), 13–18.

Zeki, S. (2003). The disunity of consciousness. *Trends in Cognitive Sciences*, *7*(5), 214–218.

Appendix A

Connectivity data

Connectivity data used in the model of chapter 6 . For more detail on the dataset, see chapter 2. Pathways are listed alphabetically by target area, then source area.

Pathway	FLN	SLN
1 → 2	9,5378357528578E-03	0,926470588
3 → 2	2,4580966407181E-01	0,759106039
12 → 2	6,6566145358487E-03	0,218612818
13 → 2	1,8117212520747E-04	0,064516129
31 → 2	2,9221310517334E-05	1
44 → 2	5,6104916193281E-04	0,270833333
24b → 2	5,8442621034668E-05	0
24c → 2	2,4545900834561E-04	0
24d → 2	8,1819669448535E-05	0,214285714
46d → 2	1,1688524206934E-05	1
7A → 2	5,8442621034668E-06	1
7B → 2	2,0688687846273E-03	0,11299435
7op → 2	2,1097786193515E-03	0,301939058
9/46v → 2	1,0829417677724E-02	0,562331355
AIP → 2	1,8935409215232E-03	0,114197531
ENTORHINAL → 2	1,5253524090048E-03	0,049808429
F1 → 2	4,4416391986348E-04	0,578947368
F3 → 2	5,9027047245015E-04	0,326732673
F4 → 2	1,1424363559857E-01	0,429506855
F5 → 2	1,5010402786544E-01	0,465581685
Gu → 2	7,9598849849218E-03	0,067547724
INSULA → 2	3,0267433433855E-02	0,136319753
LB → 2	1,7532786310400E-05	0
LIP → 2	1,6130163405568E-03	0,27173913
MB → 2	9,3508193655469E-05	0,5
OPAI → 2	2,1623769782827E-04	0,594594595
OPRO → 2	7,7319587628866E-03	0,083900227

Pathway	FLN	SLN
PERIRHINAL → 2	8,2988521869229E-04	0
ProM → 2	4,4188465764313E-02	0,314905436
SII → 2	3,5938705379059E-01	0,466126777
TEa/ma → 2	7,5975407345069E-05	0
TEav → 2	1,5195081469014E-04	0,038461538
TEMPORAL POLE → 2	4,7338523038081E-04	0
VIP → 2	5,8442621034668E-06	0
1 → 5	2,5109067512005E-03	0,575
2 → 5	3,6345375223628E-02	0,810880829
3 → 5	3,2076833746587E-02	0,587084149
12 → 5	1,2554533756003E-04	0
23 → 5	8,8572235648599E-02	0,384833451
31 → 5	2,0087254009604E-03	0,0625
24a → 5	6,2772668780013E-05	1
24b → 5	1,2554533756003E-02	0,245
24d → 5	6,0261762028813E-03	0,09375
29/30 → 5	2,9503154326606E-03	1
46d → 5	1,8831800634004E-04	1
7A → 5	1,5056024606886E-01	0,304982281
7B → 5	1,1393239383572E-02	0,143250689
7m → 5	1,8204073946204E-03	0,275862069
7op → 5	1,0153479175167E-01	0,423493045
AIP → 5	1,0043627004802E-03	0,4375
ENTORHINAL → 5	3,7663601268008E-04	0
F1 → 5	3,3686952700794E-01	0,540389453
F2 → 5	1,1757320862496E-01	0,298451682
F3 → 5	4,4599981168199E-02	0,18156228
F5 → 5	6,8422208970214E-03	0,036697248
F6 → 5	3,5152694516807E-03	0,071428571
F7 → 5	3,1386334390007E-04	0
INSULA → 5	9,2275823106619E-03	0,326530612
LIP → 5	2,9503154326606E-03	0,510638298
MB → 5	3,7663601268008E-04	0,166666667
MIP → 5	1,6320893882803E-03	0,615384615
MST → 5	3,1386334390007E-04	0,6
PERIRHINAL → 5	1,2554533756003E-04	0
STPi → 5	2,0087254009604E-03	0,625
TEa/ma → 5	2,5109067512005E-04	0
TEMPORAL POLE → 5	2,5109067512005E-04	0
TPt → 5	6,2144942092213E-03	0,267676768
VIP → 5	1,6823075233044E-02	0,388059701
9 → 10	1,1153485576990E-01	0,471183421
11 → 10	2,8314514511659E-02	0,398714378
12 → 10	6,3900328380751E-02	0,489613152

Pathway	FLN	SLN
13 → 10	2,6451196813803E-02	0,501618363
14 → 10	2,0970970221437E-01	0,469684457
23 → 10	7,7145474298362E-03	0,451920246
25 → 10	1,6995410784411E-02	0,362431021
31 → 10	7,9941459614097E-04	0,650894982
32 → 10	4,2016910602875E-02	0,491756499
44 → 10	2,2537797271495E-05	0
24a → 10	6,6345077596112E-04	0,148241798
24b → 10	1,7885651602368E-03	0,21048803
24c → 10	6,4323395770498E-03	0,340993689
24d → 10	1,3496712750603E-04	0,057291667
29/30 → 10	1,2577204164066E-03	0,309012339
45A → 10	4,2729265291065E-03	0,330334346
45B → 10	8,3637491895447E-04	0,41904238
46d → 10	1,8685112525539E-01	0,505907476
46v → 10	9,6127463982966E-02	0,466492827
7A → 10	1,6783914537329E-04	0,739583333
7op → 10	1,0210280731669E-05	0,75
8B → 10	1,8648939227281E-02	0,318170783
8l → 10	4,3848389857641E-04	0,267180736
8m → 10	5,7168830934116E-03	0,369415002
8r → 10	3,0769454383626E-04	0,112418831
9/46d → 10	1,1234449871600E-02	0,282879737
9/46v → 10	2,3336486909282E-05	0,166666667
CORE → 10	3,5586189475662E-04	0,410343555
DP → 10	1,1238750771815E-04	0,930232558
ENTORHINAL → 10	2,2160593339142E-04	0,068518519
F1 → 10	1,5586520776832E-06	1
F2 → 10	6,5099769738437E-05	0,111111111
F3 → 10	1,7188273472306E-06	0
F4 → 10	7,1063346992896E-06	0,333333333
F5 → 10	1,1230915082877E-05	0,3
F6 → 10	4,5913244518638E-05	0,110576923
F7 → 10	2,0211008424320E-03	0,221069395
FST → 10	1,1299639242753E-04	0,589285714
INSULA → 10	3,0390679560949E-04	0,054835289
IPa → 10	1,7857100873589E-04	0,476646505
LB → 10	1,0624096562648E-03	0,401677856
LIP → 10	5,2596476704062E-06	0,333333333
MB → 10	9,0226448336584E-04	0,274998439
MIP → 10	2,5525701829172E-06	1
MST → 10	5,1564820416919E-06	0,333333333
OPAI → 10	5,2166900148820E-04	0,144312011
OPRO → 10	2,7791428074764E-02	0,269966264

Pathway	FLN	SLN
Parainsula → 10	4,4446296152696E-04	0,054441434
PBc → 10	2,7900150464521E-03	0,622457851
PBr → 10	2,6299937751119E-02	0,597892043
PERIRHINAL → 10	3,6043685703110E-04	0,134338871
PGa → 10	1,9709029480038E-03	0,538553966
PIP → 10	2,0420561463337E-05	0,375
Pro.St. → 10	1,8107132855689E-03	0,494741601
STPc → 10	4,6569331454718E-03	0,694722245
STPi → 10	2,0526960525347E-02	0,575341959
STPr → 10	3,4788465527240E-02	0,556717445
TEa/ma → 10	2,0835861007825E-04	0,348511905
TEa/mp → 10	1,1589249174842E-05	0,666666667
TEad → 10	9,6722630051941E-06	0,75
TEav → 10	5,3993137188329E-05	0,435515873
TEMPORAL POLE → 10	2,8715177503395E-02	0,441398403
TEpd → 10	9,1075290327449E-06	0,833333333
TEpv → 10	1,2963031930040E-05	0,083333333
TH/TF → 10	1,2006743139224E-03	0,126679419
V2 → 10	7,2285264159668E-06	0,666666667
1 → 24c	2,7691626052282E-05	0
2 → 24c	2,2430217102348E-03	0,290123457
3 → 24c	5,2614089499335E-04	0,315789474
5 → 24c	2,5573216659282E-02	0,429344884
9 → 24c	1,3347363757200E-02	0,752074689
10 → 24c	1,5230394328755E-04	0,272727273
11 → 24c	4,1537439078423E-05	0
12 → 24c	2,0768719539211E-02	0,978666667
23 → 24c	2,3994793974302E-02	0,594345066
31 → 24c	3,1845369960124E-04	0,260869565
32 → 24c	1,9384138236597E-03	0,778571429
44 → 24c	1,6033451484271E-02	0,888601036
24a → 24c	4,3614311032344E-03	0,571428571
24b → 24c	1,1847862206469E-01	0,631880332
24d → 24c	1,0162826761187E-01	0,567983651
29/30 → 24c	4,1537439078423E-05	1
45B → 24c	8,3074878156845E-05	0,5
46d → 24c	4,8460345591493E-04	0,857142857
46v → 24c	2,3122507753655E-03	0,526946108
7A → 24c	7,9613424900310E-03	0,40173913
7B → 24c	4,3198936641560E-03	0,503205128
7m → 24c	1,9522596366859E-02	0,746099291
7op → 24c	3,4891448825875E-03	0,412698413
8B → 24c	4,2866637128932E-02	0,725775194
8l → 24c	8,3074878156845E-05	0,666666667

Pathway	FLN	SLN
8m → 24c	2,7691626052282E-05	1
8r → 24c	2,7691626052282E-05	0
9/46d → 24c	5,1091050066460E-03	0,848238482
9/46v → 24c	7,4767390341161E-04	0,592592593
CORE → 24c	2,7691626052282E-05	0
F1 → 24c	1,1173571112096E-02	0,82527881
F2 → 24c	4,9111098803722E-02	0,782351283
F3 → 24c	1,1504486043420E-01	0,785293056
F4 → 24c	3,0737704918033E-03	0,846846847
F5 → 24c	2,2125609215773E-02	0,769086358
F6 → 24c	2,6207354895879E-01	0,778529163
F7 → 24c	8,0471865307931E-02	0,643324157
INSULA → 24c	1,7487261852016E-02	0,750593824
IPa → 24c	2,7691626052282E-05	0
LB → 24c	2,7691626052282E-05	0
LIP → 24c	2,2153300841825E-04	0,375
MIP → 24c	8,2382587505538E-03	0,628571429
MST → 24c	1,6614975631369E-04	0,75
OPRO → 24c	6,3690739920248E-04	0,391304348
ProM → 24c	2,2014842711564E-03	0,748427673
SII → 24c	2,7968542312805E-03	0,544554455
STPc → 24c	1,5230394328755E-04	0,272727273
STPi → 24c	4,1537439078423E-05	0
STPr → 24c	2,7691626052282E-05	0
TEpv → 24c	2,7691626052282E-05	0
V6 → 24c	1,3845813026141E-04	0,4
V6A → 24c	8,0582631812140E-03	0,778350515
VIP → 24c	1,3845813026141E-04	0,3
2 → 46d	1,6735141286430E-05	0
3 → 46d	2,9286497251253E-05	1
9 → 46d	1,1816264883816E-01	0,619480933
10 → 46d	7,6521433532203E-02	0,593712411
11 → 46d	2,6525198938992E-03	0,670347003
12 → 46d	3,4348877490398E-03	0,175395859
13 → 46d	3,8490824958790E-04	0,347826087
14 → 46d	2,2425089323817E-03	0,436567164
23 → 46d	1,2664318168506E-02	0,599273208
31 → 46d	1,0208436184722E-03	0,770491803
32 → 46d	1,6065735634973E-03	0,408854167
44 → 46d	6,6940565145721E-05	0,75
24a → 46d	1,3388113029144E-04	0,5
24b → 46d	6,6940565145721E-05	0,25
24c → 46d	3,0960011379896E-03	0,335135135
24d → 46d	1,6735141286430E-05	0

Pathway	FLN	SLN
29/30 → 46d	3,4056012517886E-03	0,566339066
45A → 46d	1,4894275744923E-03	0,505617978
46v → 46d	5,9162908232853E-02	0,537939325
7A → 46d	5,1878937987934E-04	0,903225806
7m → 46d	7,5308135788936E-04	0,888888889
7op → 46d	1,6735141286430E-05	0
8B → 46d	3,8976144056096E-02	0,486474882
8l → 46d	6,6940565145721E-05	0
8m → 46d	3,6633224275996E-02	0,502055733
8r → 46d	4,1837853216076E-03	0,256
9/46d → 46d	5,9593838120978E-01	0,416807077
9/46v → 46d	1,1714598900501E-04	0,428571429
DP → 46d	2,5939468993967E-04	1
ENTORHINAL → 46d	1,6735141286430E-05	0
F1 → 46d	6,6940565145721E-05	0,5
F2 → 46d	1,3388113029144E-04	0
F3 → 46d	1,6735141286430E-05	1
F4 → 46d	3,3470282572861E-05	0
F5 → 46d	5,0205423859291E-05	0
F6 → 46d	3,3470282572861E-03	0,41
F7 → 46d	7,4304027311751E-03	0,418918919
INSULA → 46d	1,6735141286430E-05	1
LIP → 46d	3,3470282572861E-05	0,5
MIP → 46d	1,6735141286430E-05	0
MST → 46d	1,6735141286430E-05	1
MT → 46d	1,6735141286430E-05	1
OPRO → 46d	3,8490824958790E-04	0,043478261
Parainsula → 46d	3,3470282572861E-05	1
PBc → 46d	1,8408655415073E-04	0,181818182
PBr → 46d	4,6858395602005E-04	0,142857143
PERIRHINAL → 46d	3,3470282572861E-05	0
PGa → 46d	2,9788551489846E-03	0,445224719
STPc → 46d	4,4724665087985E-03	0,63797942
STPi → 46d	1,3316988678677E-02	0,496072887
STPr → 46d	5,8572994502506E-04	0,057142857
TEMPORAL POLE → 46d	1,6735141286430E-05	0
TEO → 46d	1,6735141286430E-05	1
TEOm → 46d	1,6735141286430E-05	1
TEpd → 46d	6,6940565145721E-05	0
TEpv → 46d	3,7654067894468E-05	0,444444444
TH/TF → 46d	8,3675706432152E-05	0
V2 → 46d	2,2592440736681E-03	0,655555556
V3 → 46d	1,1714598900501E-04	0,714285714
V6A → 46d	7,5308135788936E-05	0,777777778

Pathway	FLN	SLN
VIP → 46d	1,6735141286430E-05	0
2 → 7A	1,8277692989591E-05	0
5 → 7A	1,0025314604791E-02	0,387420237
9 → 7A	8,2249618453159E-05	0,222222222
12 → 7A	6,3971925463568E-05	0
13 → 7A	4,5694232473977E-05	0
23 → 7A	1,1300183690815E-01	0,412939749
31 → 7A	6,9775092987763E-02	0,412966601
24a → 7A	8,2249618453159E-04	0,233333333
24b → 7A	5,0263655721375E-04	0,345454545
29/30 → 7A	2,2472423530702E-02	0,548596991
45A → 7A	1,3616881277245E-03	0,718120805
45B → 7A	1,3708269742193E-04	0,4
46d → 7A	1,4814070168063E-02	0,676742751
46v → 7A	1,4622154391673E-04	0
7B → 7A	4,7522001772936E-04	0,057692308
7m → 7A	2,1613371960191E-02	0,420718816
8B → 7A	7,4481598932583E-03	0,440490798
8l → 7A	4,6608117123457E-04	0,490196078
8m → 7A	5,3919194319293E-04	0,305084746
9/46d → 7A	2,9518474178189E-03	0,442724458
9/46v → 7A	3,8200378348245E-03	0,473684211
DP → 7A	2,0763459236175E-02	0,231514085
ENTORHINAL → 7A	4,3775074710070E-03	0,018789144
F1 → 7A	1,0966615793755E-04	1
F2 → 7A	7,1008837264560E-03	0,725868726
F3 → 7A	5,0263655721375E-04	0,563636364
F5 → 7A	1,3251327417453E-03	0,965517241
F7 → 7A	1,5536039041152E-04	0,235294118
FST → 7A	8,4260164682014E-03	0,455531453
INSULA → 7A	1,2885773557662E-03	0,375886525
IPa → 7A	2,1933231587509E-03	0,125
LB → 7A	1,8277692989591E-05	0
LIP → 7A	1,3123383566526E-01	0,581128134
MB → 7A	6,3971925463568E-05	0,714285714
MIP → 7A	3,6555385979182E-05	0
MST → 7A	1,3891960556739E-01	0,612130781
MT → 7A	5,4833078968773E-05	1
PERIRHINAL → 7A	3,9205651462672E-03	0,20979021
PGa → 7A	1,0875227328807E-02	0,324369748
PIP → 7A	3,1985962731784E-04	0,4
STPc → 7A	1,3635158970235E-02	0,658847185
STPi → 7A	4,1673140016267E-02	0,523464912
STPr → 7A	2,5223216325635E-03	0,641304348

Pathway	FLN	SLN
TEa/ma → 7A	3,9297039927620E-04	0
TEa/mp → 7A	4,4232017034810E-03	0,462809917
TEav → 7A	9,1388464947954E-05	0
TEMPORAL POLE → 7A	3,2899847381264E-04	0
TEO → 7A	2,1384900797821E-03	0,623931624
TEOm → 7A	2,3029893166884E-03	0,781746032
TEpd → 7A	2,7964870274074E-03	0,065359477
TEpv → 7A	7,8356469846376E-02	0,362374621
TH/TF → 7A	8,5905157051077E-04	0,223404255
TPt → 7A	1,6584264734105E-01	0,543064969
V1 → 7A	1,8277692989591E-05	0
V2 → 7A	3,6555385979182E-05	0,5
V3A → 7A	3,6555385979182E-05	0,5
V4 → 7A	3,0432358827669E-03	0,801801802
V6 → 7A	1,2794385092714E-04	0,142857143
V6A → 7A	7,9023605640496E-02	0,442003007
VIP → 7A	8,2249618453159E-05	0,666666667
2 → 7B	3,0754954596673E-03	0,879310345
5 → 7B	2,1793597136608E-02	0,578467153
12 → 7B	1,0074898919600E-03	0,407894737
23 → 7B	5,4616557300988E-03	0,422330097
44 → 7B	2,7175714191025E-03	0,658536585
24b → 7B	1,9089282163452E-03	0,194444444
24c → 7B	3,9769337840525E-05	0
24d → 7B	1,6703121893020E-03	0,436507937
45B → 7B	3,4466759461788E-04	0,807692308
46v → 7B	6,7607874328892E-04	0,529411765
7A → 7B	3,9726917213495E-01	0,534303257
7m → 7B	1,8625306555313E-02	0,592882562
7op → 7B	1,5160071584808E-01	0,482423924
8m → 7B	1,8559024325578E-04	0,714285714
9/46d → 7B	2,5187247298999E-04	0,473684211
9/46v → 7B	1,2699675217074E-02	0,854906054
AIP → 7B	2,6804533704514E-02	0,581107814
F1 → 7B	9,4120766222576E-04	0,704225352
F2 → 7B	2,9296745542520E-03	0,266968326
F3 → 7B	1,1665672433221E-03	0,659090909
F4 → 7B	1,1917544906211E-02	0,819799778
F5 → 7B	3,6627560151123E-02	0,786102063
INSULA → 7B	1,4568834095579E-02	0,101910828
LB → 7B	1,4449526082057E-03	0,963302752
LIP → 7B	5,7771591436336E-02	0,633088573
MB → 7B	5,0374494597998E-04	0,105263158
MIP → 7B	7,1399217869689E-02	0,649090234

Pathway	FLN	SLN
MST → 7B	1,2964804136011E-02	0,800613497
MT → 7B	1,6968250811957E-03	0,84375
PBc → 7B	5,3025783787367E-05	0,5
PERIRHINAL → 7B	7,9538675681050E-05	0
PGa → 7B	5,4351428382051E-04	0,756097561
ProM → 7B	6,6282229734208E-04	0,5
SII → 7B	5,3171604692782E-02	0,515582149
STPc → 7B	9,8893086763439E-03	0,76541555
STPi → 7B	7,9538675681050E-05	0,666666667
STPr → 7B	1,5907735136210E-04	0
TEa/ma → 7B	3,0489825677736E-04	0
TEpv → 7B	5,3025783787367E-05	0,5
TH/TF → 7B	1,5907735136210E-04	0,166666667
TPt → 7B	1,2805726784649E-02	0,341614907
V2 → 7B	3,9769337840525E-05	1
V6A → 7B	1,3786703784715E-03	1
VIP → 7B	6,0555445085173E-02	0,548380035
1 → 7m	1,5483471394287E-04	1
2 → 7m	1,1910362610990E-05	1
3 → 7m	2,9775906527474E-05	1
5 → 7m	7,1104864787608E-03	0,685929648
9 → 7m	4,8236968574508E-04	0,327160494
11 → 7m	2,9775906527474E-05	0
12 → 7m	4,1686269138464E-05	0,5
13 → 7m	2,3820725221979E-05	0,25
14 → 7m	2,0843134569232E-05	0
23 → 7m	9,1173825787126E-02	0,548073155
25 → 7m	2,3820725221979E-05	0,25
31 → 7m	2,6768539968199E-02	0,651167964
32 → 7m	3,5731087832969E-05	0
44 → 7m	1,6674507655386E-04	0,392857143
24a → 7m	1,0957533602111E-03	0,10326087
24b → 7m	1,0144651353910E-02	0,259465806
24c → 7m	1,6495852216221E-03	0,093862816
24d → 7m	9,1322705319763E-03	0,613628953
29/30 → 7m	5,6544446495674E-03	0,203791469
45B → 7m	1,1314844480440E-04	0,315789474
46d → 7m	4,2936857212618E-03	0,721220527
46v → 7m	5,7795034569827E-03	0,735703246
7A → 7m	7,8480356834464E-02	0,608491103
7B → 7m	5,9551813054948E-06	1
7op → 7m	5,4192149880003E-04	0,703296703
8B → 7m	3,8399009057831E-02	0,496588089
8l → 7m	5,7765258663300E-04	0,546391753

Pathway	FLN	SLN
8m → 7m	1,8574210491838E-02	0,500160308
8r → 7m	3,6803020467958E-03	0,656957929
9/46d → 7m	2,1581577051113E-02	0,645419426
9/46v → 7m	1,2386777115429E-03	0,764423077
AIP → 7m	3,1264701853848E-04	0,733333333
DP → 7m	1,3428933843891E-02	0,689135255
ENTORHINAL → 7m	4,1686269138464E-05	0,142857143
F1 → 7m	3,0669183723298E-04	0,72815534
F2 → 7m	3,1693474907844E-02	0,505824878
F3 → 7m	1,6734059468441E-03	0,790035587
F5 → 7m	2,9775906527474E-05	0
F6 → 7m	1,8997028364529E-03	0,147335423
F7 → 7m	1,3414045890627E-02	0,555604883
FST → 7m	5,3596631749454E-05	0,222222222
INSULA → 7m	1,5483471394287E-04	0,5
IPa → 7m	1,3696917002638E-04	0,47826087
LB → 7m	3,3349015310771E-04	0,5
LIP → 7m	3,1068180870767E-02	0,692064405
MB → 7m	3,0966942788573E-04	0,673076923
MIP → 7m	2,7361080508096E-02	0,605180107
MST → 7m	7,9915555529088E-02	0,51227691
MT → 7m	9,1412033039346E-04	0,921824104
PBc → 7m	9,7069455279566E-04	0,564417178
PBr → 7m	5,9551813054948E-06	0
PERIRHINAL → 7m	1,7865543916485E-04	0,266666667
PGa → 7m	6,2529403707696E-04	0,266666667
PIP → 7m	4,7671226350486E-03	0,785758901
Pro.St. → 7m	1,6078989524836E-04	0,814814815
STPc → 7m	1,1675132949423E-02	0,360112216
STPi → 7m	8,9327719582423E-05	0,133333333
STPr → 7m	5,9551813054948E-05	0
TEa/mp → 7m	1,7865543916485E-05	0,666666667
TEpd → 7m	5,9551813054948E-06	1
TEpv → 7m	5,8063017728575E-04	0,138461538
TH/TF → 7m	5,8360776793849E-04	0,142857143
TPt → 7m	3,6981675907123E-03	0,495169082
V1 → 7m	2,6798315874727E-05	0,666666667
V2 → 7m	1,4500866478880E-03	0,718685832
V3 → 7m	1,7865543916485E-05	1
V3A → 7m	1,7270025785935E-04	0,931034483
V4 → 7m	3,6624365028793E-04	0,918699187
V6 → 7m	2,3225207091430E-03	0,938461538
V6A → 7m	4,3377838388290E-01	0,588319685
VIP → 7m	8,3819176874840E-03	0,685612789

Pathway	FLN	SLN
9 → 8B	1,7650127723052E-01	0,620599054
10 → 8B	1,3197018120829E-01	0,572930393
11 → 8B	1,2706607977184E-02	0,682481752
12 → 8B	2,2445249127580E-02	0,679063361
13 → 8B	1,1238082724346E-02	0,68088033
14 → 8B	5,5456150995312E-03	0,512195122
23 → 8B	6,5349373751270E-03	0,620342992
25 → 8B	1,5458160556185E-04	0,15
31 → 8B	7,0721084544545E-04	0,803278689
32 → 8B	3,3992495063050E-02	0,659845384
44 → 8B	5,4103561946646E-05	0,571428571
24a → 8B	2,5390028713533E-03	0,476407915
24b → 8B	8,1425860729702E-03	0,50450878
24c → 8B	9,3707369291591E-02	0,632299571
24d → 8B	1,3912344500566E-04	0,444444444
29/30 → 8B	5,3717107932742E-04	0,143884892
45A → 8B	2,7824689001132E-04	0,166666667
45B → 8B	4,7920297724172E-04	0,459677419
46d → 8B	3,9959345037737E-02	0,477369439
46v → 8B	3,9170978849372E-02	0,489739542
7A → 8B	8,8884423198062E-04	0,72173913
7m → 8B	2,6510745353857E-03	0,711370262
8l → 8B	9,3521871364917E-04	0,727272727
8m → 8B	4,9095117926442E-02	0,559508816
8r → 8B	5,8354556099597E-04	0,304635762
9/46d → 8B	8,6998527610207E-02	0,616915423
9/46v → 8B	1,4685252528375E-04	0,684210526
CORE → 8B	1,5458160556185E-05	0,5
DP → 8B	1,0434258375425E-04	0,925925926
ENTORHINAL → 8B	1,5458160556185E-04	0
F1 → 8B	7,7290802780923E-06	0
F2 → 8B	8,5019883059015E-05	0,090909091
F4 → 8B	3,0916321112369E-05	0
F5 → 8B	7,7290802780923E-06	0
F6 → 8B	6,5488497196276E-02	0,618198985
F7 → 8B	1,5122718472115E-01	0,576714709
FST → 8B	2,2027878792563E-04	0,894736842
INSULA → 8B	1,0047804361520E-04	0
IPa → 8B	7,1107538558449E-04	0,597826087
LB → 8B	2,7051780973323E-05	0,285714286
LIP → 8B	5,7195194057883E-04	0,878378378
MB → 8B	3,8645401390462E-05	0
OPAI → 8B	2,6278872945514E-04	0,941176471
OPRO → 8B	5,4103561946646E-03	0,542857143

Pathway	FLN	SLN
Parainsula → 8B	6,1832642224738E-05	0
PBr → 8B	3,5167315265320E-04	0,714285714
PERIRHINAL → 8B	3,4780861251415E-05	0
PGa → 8B	3,9688827228004E-03	0,632911392
SII → 8B	7,7290802780923E-06	1
STPc → 8B	5,4103561946646E-05	0,714285714
STPi → 8B	1,4376089317252E-02	0,673924731
STPr → 8B	1,9137202768557E-02	0,541195477
TEa/ma → 8B	9,2748963337108E-05	0,75
TEa/mp → 8B	3,0916321112369E-05	0,75
TEad → 8B	1,5458160556185E-05	1
TEMPORAL POLE → 8B	8,9966494436994E-03	0,193728522
TH/TF → 8B	2,9756959070655E-04	0,090909091
V4 → 8B	7,7290802780923E-06	1
2 → 8l	2,0417121798340E-04	0,45
3 → 8l	2,4500546158008E-04	0,583333333
5 → 8l	6,1251365395020E-05	0,166666667
9 → 8l	2,5725573465909E-03	0,174603175
10 → 8l	5,3084516675684E-04	0,076923077
11 → 8l	5,4105372765601E-04	0,264150943
12 → 8l	2,1376726522862E-02	0,291786055
13 → 8l	3,6648733628020E-03	0,077994429
14 → 8l	6,1251365395020E-05	0,666666667
23 → 8l	5,6147084945435E-04	0,545454545
25 → 8l	5,1042804495850E-05	0,4
31 → 8l	7,1459926294190E-05	0,285714286
32 → 8l	1,0208560899170E-04	0,5
44 → 8l	1,9253345855835E-02	0,365853659
24a → 8l	4,1753014077605E-03	0,562347188
24b → 8l	2,3071347632124E-03	0,331858407
24c → 8l	2,4296374940025E-03	0,390756303
24d → 8l	1,0514817726145E-03	0,436893204
29/30 → 8l	2,4500546158008E-04	0,5
45A → 8l	1,2454444296987E-02	0,3
45B → 8l	6,8397358024439E-02	0,381492537
46d → 8l	3,8966076952132E-02	0,272727273
46v → 8l	1,1055871453801E-02	0,167128347
7A → 8l	1,7558724746572E-03	0,255813953
7B → 8l	3,0625682697510E-05	0,666666667
7m → 8l	1,2250273079004E-04	0,083333333
7op → 8l	1,1229416989087E-04	0,545454545
8B → 8l	2,0611084455424E-02	0,251609708
8m → 8l	4,1541696866993E-01	0,498709852
8r → 8l	1,2335004134467E-01	0,59985103

Pathway	FLN	SLN
9/46d → 8l	1,0147309533775E-02	0,211267606
9/46v → 8l	2,4745551619588E-02	0,296617162
AIP → 8l	1,0208560899170E-04	0,4
CORE → 8l	6,5334789754688E-04	0,109375
DP → 8l	6,0230509305103E-04	0,779661017
ENTORHINAL → 8l	2,8583970517676E-04	0,25
F1 → 8l	1,4087814040855E-03	0,195652174
F2 → 8l	1,8987923272456E-02	0,195698925
F3 → 8l	2,2458833978174E-04	0,090909091
F4 → 8l	5,4207458374593E-03	0,224105461
F5 → 8l	1,2658615514971E-02	0,318548387
F6 → 8l	2,3275518850108E-03	0,350877193
F7 → 8l	2,6072664536480E-02	0,258026625
FST → 8l	3,2769480486336E-03	0,563862928
Gu → 8l	1,3169043559929E-03	0,046511628
INSULA → 8l	9,3102075400431E-03	0,101973684
IPa → 8l	1,9906693753382E-03	0,307692308
LB → 8l	3,8792531416846E-04	0,315789474
LIP → 8l	2,9186275610727E-02	0,504372158
MB → 8l	1,9192094490440E-03	0,106382979
MIP → 8l	8,1668487193360E-05	0,375
MST → 8l	5,6963769817369E-03	0,422939068
MT → 8l	2,1346100840165E-02	0,487804878
OPAI → 8l	5,8188797125269E-04	0,157894737
OPRO → 8l	4,3998897475423E-03	0,085846868
Parainsula → 8l	3,2667394877344E-04	0,15625
PBc → 8l	2,0008779362373E-03	0,428571429
PBr → 8l	8,3710199373194E-04	0,146341463
PERIRHINAL → 8l	1,0208560899170E-04	0,8
PGa → 8l	4,8694835489041E-03	0,406708595
PIP → 8l	3,4300764621211E-03	0,755952381
ProM → 8l	1,7456639137581E-03	0,070175439
SII → 8l	1,2046101861021E-03	0,177966102
STPc → 8l	1,1535673816062E-02	0,324778761
STPi → 8l	5,8699225170228E-03	0,151304348
STPr → 8l	1,1229416989087E-03	0,109090909
TEa/ma → 8l	1,1229416989087E-04	0,090909091
TEa/mp → 8l	1,0208560899170E-04	0,8
TEad → 8l	3,0625682697510E-05	1
TEav → 8l	1,3271129168921E-04	0,384615385
TEMPORAL POLE → 8l	4,0834243596680E-04	0,2
TEO → 8l	1,4700327694805E-03	0,833333333
TEOm → 8l	2,6236001510867E-03	0,883268482
TEpd → 8l	1,5312841348755E-04	0,533333333

Pathway	FLN	SLN
TEpv → 8l	1,2658615514971E-03	0,612903226
TH/TF → 8l	1,2658615514971E-03	0,548387097
TPt → 8l	4,2875955776514E-04	0,404761905
V1 → 8l	8,1668487193360E-05	0,75
V2 → 8l	3,5729963147095E-03	0,928571429
V3 → 8l	4,9103177925008E-03	0,925155925
V3A → 8l	4,9001092316016E-04	0,8125
V4 → 8l	1,2781118245761E-02	0,95686901
V4t → 8l	2,9604826607593E-04	0,689655172
V6A → 8l	2,1437977888257E-04	0,047619048
VIP → 8l	1,7048296701614E-03	0,305389222
2 → 8m	4,8548992001554E-05	0
3 → 8m	2,4274496000777E-05	0,5
5 → 8m	8,4960736002719E-05	0,571428571
9 → 8m	2,0390576640652E-03	0,220238095
10 → 8m	2,0876066560668E-03	0,011627907
11 → 8m	1,8205872000583E-04	0,133333333
12 → 8m	7,1245645762280E-03	0,2879046
13 → 8m	3,4712529281111E-03	0,213286713
14 → 8m	9,7097984003107E-05	0,375
23 → 8m	2,6701945600854E-04	0,272727273
31 → 8m	3,6411744001165E-05	0,333333333
32 → 8m	2,9129395200932E-04	0,083333333
44 → 8m	1,5414304960493E-02	0,393700787
24a → 8m	7,0396038402253E-04	0,206896552
24b → 8m	1,0073915840322E-03	0,120481928
24c → 8m	2,3667633600757E-03	0,205128205
24d → 8m	3,6411744001165E-04	0,366666667
29/30 → 8m	1,2137248000388E-04	0
45A → 8m	2,5949436224830E-02	0,536014967
45B → 8m	1,2403053731597E-01	0,55553381
46d → 8m	1,1071597625954E-01	0,305634729
46v → 8m	3,3438118241070E-02	0,401451906
7A → 8m	1,6021167360513E-03	0,303030303
7B → 8m	7,2823488002330E-04	0,666666667
7m → 8m	5,4617616001748E-04	0,511111111
7op → 8m	5,7045065601825E-04	0,468085106
8B → 8m	1,7210617664551E-02	0,157263752
8l → 8m	1,8360015050188E-01	0,577047663
8r → 8m	6,9825587746234E-02	0,487919346
9/46d → 8m	3,7406998337197E-02	0,369565217
9/46v → 8m	9,1684771394934E-02	0,473391581
AIP → 8m	9,1029360002913E-04	0,413333333
CORE → 8m	6,9182313602214E-04	0,228070175

Pathway	FLN	SLN
DP → 8m	2,0633321600660E-04	0,705882353
ENTORHINAL → 8m	6,0686240001942E-05	0
F1 → 8m	8,2533286402641E-04	0,294117647
F2 → 8m	2,1580026944691E-02	0,20303712
F3 → 8m	2,3060771200738E-04	0,263157895
F4 → 8m	3,8924154337246E-02	0,304957905
F5 → 8m	1,4686070080470E-02	0,353719008
F6 → 8m	1,2622737920404E-03	0,125
F7 → 8m	1,0638297872340E-01	0,282373075
FST → 8m	2,8765277760920E-03	0,270042194
Gu → 8m	1,3350972800427E-04	0,363636364
INSULA → 8m	2,8643905280917E-03	0,283898305
IPa → 8m	9,7097984003107E-05	0,125
LB → 8m	1,1530385600369E-03	0,336842105
LIP → 8m	6,2142709761989E-03	0,24609375
MB → 8m	1,7113519680548E-03	0,163120567
MIP → 8m	1,2137248000388E-05	1
MST → 8m	1,9419596800621E-03	0,44375
MT → 8m	6,9182313602214E-04	0,596491228
OPAI → 8m	6,0686240001942E-05	0
OPRO → 8m	1,6992147200544E-04	0,142857143
Parainsula → 8m	1,2137248000388E-04	0,1
PBc → 8m	5,1340559041643E-03	0,250591017
PBr → 8m	1,1773130560377E-03	0,18556701
PERIRHINAL → 8m	2,4274496000777E-05	0
PGa → 8m	4,1266643201321E-03	0,297058824
PIP → 8m	3,6411744001165E-05	0
ProM → 8m	5,8258790401864E-04	0,395833333
SII → 8m	7,5250937602408E-04	0,370967742
STPc → 8m	3,3668725953077E-02	0,26964672
STPi → 8m	1,3994246944448E-02	0,209019948
STPr → 8m	1,4321952640458E-03	0,050847458
TEa/ma → 8m	3,6411744001165E-05	0,666666667
TEa/mp → 8m	1,5778422400505E-04	0,153846154
TEMPORAL POLE → 8m	1,3350972800427E-04	0,181818182
TEOm → 8m	2,4274496000777E-05	0,5
TEpd → 8m	3,6411744001165E-05	0,333333333
TEpv → 8m	1,2137248000388E-05	0
TH/TF → 8m	1,2137248000388E-05	0
TPt → 8m	8,4960736002719E-05	0,142857143
V2 → 8m	1,2137248000388E-04	0,2
V3 → 8m	4,8548992001554E-05	0,25
V3A → 8m	1,2137248000388E-05	0
V4 → 8m	1,0923523200350E-04	1

Pathway	FLN	SLN
V4t → 8m	1,4564697600466E-04	0,583333333
V6A → 8m	5,8258790401864E-04	0,4375
VIP → 8m	7,0396038402253E-04	0,344827586
2 → 9/46d	4,6591809159950E-05	0,833333333
5 → 9/46d	9,7066269083229E-04	0,824
9 → 9/46d	2,4289863175387E-02	0,588075448
10 → 9/46d	7,8856637003215E-03	0,574101428
11 → 9/46d	2,5625495037972E-04	0,545454545
12 → 9/46d	7,1984345152122E-03	0,292880259
13 → 9/46d	6,9887713739925E-04	0,138888889
14 → 9/46d	5,4357110686608E-05	0,285714286
23 → 9/46d	8,2156890152045E-03	0,491493384
31 → 9/46d	2,7287269564677E-02	0,515936255
32 → 9/46d	3,1061206106633E-05	0
44 → 9/46d	9,4620199102331E-03	0,405826836
24a → 9/46d	6,2898942365932E-04	0,172839506
24b → 9/46d	5,1639255152278E-04	0,248120301
24c → 9/46d	3,0362328969234E-03	0,413043478
24d → 9/46d	5,5133640839274E-04	0,338028169
29/30 → 9/46d	5,4395937194241E-03	0,309778729
45A → 9/46d	2,0050008541832E-02	0,522269558
45B → 9/46d	4,2398546335554E-03	0,518315018
46d → 9/46d	1,9572442497942E-01	0,559769887
46v → 9/46d	9,6806131482085E-02	0,434805278
7A → 9/46d	7,2993834350588E-04	0,723404255
7B → 9/46d	1,1104381183121E-03	0,573426573
7m → 9/46d	3,4695367221109E-02	0,698075201
7op → 9/46d	8,3865256487909E-04	0,555555556
8B → 9/46d	7,0974855953657E-02	0,596389497
8l → 9/46d	1,4703598440727E-02	0,53340375
8m → 9/46d	2,2153240460327E-01	0,581418581
8r → 9/46d	5,8682383636957E-02	0,623064708
9/46v → 9/46d	1,6835173709795E-02	0,528597786
CORE → 9/46d	1,5530603053317E-05	0
DP → 9/46d	4,6591809159950E-05	0,666666667
F1 → 9/46d	5,4357110686608E-05	0,285714286
F2 → 9/46d	2,1863206448306E-02	0,507369917
F3 → 9/46d	3,5720387022628E-04	0,391304348
F4 → 9/46d	9,3688362919132E-03	0,614173228
F5 → 9/46d	6,3675472518598E-04	0,5
F6 → 9/46d	9,6483871468729E-03	0,605633803
F7 → 9/46d	5,5929584245756E-02	0,633877126
FST → 9/46d	2,8731615648636E-04	0,554054054
Gu → 9/46d	2,3295904579975E-05	0

Pathway	FLN	SLN
INSULA → 9/46d	1,9801518892979E-03	0,215686275
LB → 9/46d	6,9887713739925E-05	0,333333333
LIP → 9/46d	2,4305393778440E-03	0,453674121
MB → 9/46d	2,2519374427309E-04	0,137931034
MIP → 9/46d	1,6307133205982E-04	0,857142857
MST → 9/46d	1,9568559847179E-03	0,373015873
MT → 9/46d	2,2519374427309E-04	0,413793103
OPAI → 9/46d	3,1061206106633E-05	0
OPRO → 9/46d	1,2968053549519E-03	0,140718563
Parainsula → 9/46d	1,3201012595319E-04	0,147058824
PBc → 9/46d	2,0150957461678E-03	0,531791908
PBr → 9/46d	5,3580580533942E-04	0,231884058
PERIRHINAL → 9/46d	7,7653015266583E-06	1
PGa → 9/46d	4,5815279007284E-04	0,406779661
PIP → 9/46d	1,5530603053317E-05	1
Pro.St. → 9/46d	2,0966314121977E-04	0,851851852
ProM → 9/46d	3,3002531488298E-04	0,094117647
SII → 9/46d	1,2036217366320E-04	0,548387097
STPc → 9/46d	2,5621612387209E-02	0,609031671
STPi → 9/46d	6,4917920762863E-03	0,522129187
STPr → 9/46d	1,5142337976984E-04	0,153846154
TEa/ma → 9/46d	1,1647952289987E-05	0
TEa/mp → 9/46d	7,7653015266583E-06	0
TEad → 9/46d	1,5530603053317E-05	0
TEav → 9/46d	7,7653015266583E-06	0
TEMPORAL POLE → 9/46d	1,1647952289987E-04	0,333333333
TEO → 9/46d	7,7653015266583E-06	0
TPt → 9/46d	8,3865256487909E-04	0,546296296
V2 → 9/46d	1,8131979064747E-03	0,687366167
V3 → 9/46d	4,6591809159950E-05	0,833333333
V4 → 9/46d	8,5418316793241E-05	0,818181818
V6 → 9/46d	1,0638463091522E-03	0,562043796
V6A → 9/46d	1,9032754041839E-02	0,793961648
VIP → 9/46d	7,6099954961251E-04	0,612244898
2 → 9/46v	1,7825877520645E-03	0,77184466
3 → 9/46v	3,4613354409020E-05	0,666666667
5 → 9/46v	6,9226708818040E-05	0,5
9 → 9/46v	4,3555137631350E-04	0,238410596
10 → 9/46v	2,3652458846164E-04	0,37804878
11 → 9/46v	5,4668908842847E-02	0,569250251
12 → 9/46v	1,2869822058514E-01	0,491752208
13 → 9/46v	1,3579972713139E-02	0,502973662
14 → 9/46v	4,6151139212027E-04	0,525
23 → 9/46v	1,2858861162951E-02	0,517048004

Pathway	FLN	SLN
31 → 9/46v	3,4613354409020E-05	0,333333333
32 → 9/46v	8,9417832223302E-05	0
44 → 9/46v	7,9933773115231E-02	0,523094688
24a → 9/46v	1,2864630055353E-02	0,461883408
24b → 9/46v	5,8381191103214E-03	0,403162055
24c → 9/46v	6,5996129073199E-03	0,38986014
24d → 9/46v	1,1999296195127E-03	0,620192308
29/30 → 9/46v	5,5064077972350E-03	0,299109481
45A → 9/46v	5,9431129520288E-02	0,462046205
45B → 9/46v	7,4649467675454E-03	0,420401855
46d → 9/46v	3,7324733837727E-02	0,659659969
46v → 9/46v	2,8408333741963E-01	0,587269515
7A → 9/46v	2,1973711157326E-02	0,616959832
7B → 9/46v	1,9669038642926E-02	0,642616219
7m → 9/46v	7,6726268939995E-04	0,398496241
7op → 9/46v	4,5574249971877E-04	0,525316456
8B → 9/46v	1,6395192205073E-02	0,506685433
8l → 9/46v	2,9998240487818E-03	0,257692308
8m → 9/46v	3,3955700675249E-02	0,597349643
8r → 9/46v	1,8691211380871E-03	0,401234568
9/46d → 9/46v	1,4254933124115E-02	0,60946985
AIP → 9/46v	1,9729612013142E-03	0,584795322
ENTORHINAL → 9/46v	2,3075569606013E-05	0
F1 → 9/46v	5,7688924015034E-05	0,4
F2 → 9/46v	5,0997008829290E-03	0,450226244
F3 → 9/46v	1,2201207429180E-03	0,472813239
F4 → 9/46v	1,4468382142970E-02	0,442583732
F5 → 9/46v	1,7283601634904E-02	0,453271028
F6 → 9/46v	7,9726092988777E-03	0,460202605
F7 → 9/46v	9,2648411968144E-03	0,424657534
FST → 9/46v	2,3075569606013E-05	0
Gu → 9/46v	8,0764493621047E-05	0,285714286
INSULA → 9/46v	1,0109983933635E-02	0,562910128
IPa → 9/46v	8,7629475578836E-03	0,45885451
LIP → 9/46v	1,5875991888937E-02	0,551598837
MB → 9/46v	2,3075569606013E-05	0
MST → 9/46v	5,6535145534733E-04	0,428571429
OPAI → 9/46v	1,6152898724209E-04	0,071428571
OPRO → 9/46v	4,7766429084448E-03	0,417874396
Parainsula → 9/46v	4,3266693011275E-05	0
PBc → 9/46v	2,0191123405262E-05	0
PBr → 9/46v	1,1537784803007E-05	0
PERIRHINAL → 9/46v	2,1575657581623E-03	0,181818182
PGa → 9/46v	5,2352698543643E-03	0,436363636

Pathway	FLN	SLN
ProM → 9/46v	8,9879343615423E-03	0,568677792
SII → 9/46v	2,2198697960985E-02	0,674116424
STPc → 9/46v	9,7494281585407E-04	0,556213018
STPi → 9/46v	7,0380487298341E-04	0,299180328
STPr → 9/46v	2,6248460426840E-04	0,340659341
TEa/ma → 9/46v	1,1180113474114E-02	0,468524252
TEa/mp → 9/46v	2,0072861111031E-02	0,557551372
TEad → 9/46v	2,3075569606013E-04	0,05
TEav → 9/46v	7,8456936660446E-04	0,058823529
TEMPORAL POLE → 9/46v	6,9226708818040E-04	0,083333333
TEOm → 9/46v	2,3075569606013E-05	1
TEpd → 9/46v	1,0384006322706E-04	0,444444444
TEpv → 9/46v	6,9226708818040E-04	0,220833333
TH/TF → 9/46v	6,0573370215785E-05	0
TPt → 9/46v	2,1575657581623E-03	0,486631016
V3 → 9/46v	1,1537784803007E-05	1
V6A → 9/46v	8,0764493621047E-05	0,714285714
VIP → 9/46v	3,4613354409020E-05	0,666666667
9 → DP	1,5899578263687E-05	1
12 → DP	3,9748945659216E-06	0
23 → DP	2,0311711231860E-03	0,189823875
31 → DP	2,1861920112569E-03	0,327272727
24b → DP	9,0627596103013E-04	0,342105263
24c → DP	2,7824261961451E-05	0
29/30 → DP	3,9748945659216E-04	0,63
45A → DP	1,5899578263687E-05	0,75
45B → DP	6,7573207620668E-04	0,788235294
46d → DP	7,5522996752511E-04	0,489473684
46v → DP	1,3117152067541E-04	0,090909091
7A → DP	1,1797487071655E-01	0,344642857
7m → DP	2,3451877938938E-04	0
8B → DP	1,1248951621558E-03	0,360424028
8m → DP	1,9317987590379E-03	0,516460905
8r → DP	4,4121329681730E-04	0,423423423
9/46d → DP	7,8305422948656E-04	0,365482234
ENTORHINAL → DP	4,6108776964691E-04	0,051724138
F2 → DP	1,5382841970117E-03	0,330749354
F4 → DP	1,5899578263687E-05	0
F5 → DP	1,5899578263687E-05	0
F7 → DP	6,4790781424523E-04	0,085889571
FST → DP	1,0370499922490E-02	0,266385588
INSULA → DP	3,9748945659216E-06	1
IPa → DP	7,7907933492064E-04	0,234693878
LIP → DP	2,0204389078580E-02	0,368089711

Pathway	FLN	SLN
MIP → DP	6,4870279315841E-03	0,251838235
MST → DP	5,1840574928750E-02	0,302100905
MT → DP	1,6242214175269E-01	0,481229504
PBc → DP	1,4309620437318E-04	0
PERIRHINAL → DP	3,9748945659216E-05	0,2
PGa → DP	8,9832617189829E-04	0,092920354
PIP → DP	3,7105640772879E-02	0,437279057
Pro.St. → DP	2,6631793591675E-04	0,208955224
STPc → DP	3,3786603810334E-04	0
STPi → DP	4,7698734791060E-05	0
STPr → DP	7,9497891318433E-06	1
TEa/ma → DP	3,6966519463071E-04	0,086021505
TEa/mp → DP	2,1464430655977E-04	0,037037037
TEad → DP	3,1799156527373E-05	0
TEav → DP	4,7698734791060E-05	0
TEO → DP	3,3786603810334E-04	0,152941176
TEOm → DP	7,8702912405248E-03	0,349494949
TEpd → DP	1,2163177371720E-03	0,166666667
TEpv → DP	2,6957734946081E-02	0,434974934
TH/TF → DP	1,7998322594493E-02	0,204946996
TPt → DP	9,5397469582119E-05	0,083333333
V1 → DP	1,1924683697765E-05	0
V2 → DP	7,9024878865088E-02	0,914994216
V3 → DP	5,0401663095886E-03	0,924290221
V3A → DP	3,2053549779592E-02	0,718998016
V4 → DP	3,3760766995655E-01	0,501371637
V4t → DP	7,9060652916181E-03	0,219205631
V6 → DP	2,0204389078580E-02	0,6791265
V6A → DP	3,8826770119923E-02	0,582207207
VIP → DP	9,1422575016198E-04	0,060869565
1 → F1	1,2154907543921E-03	0,888888889
2 → F1	1,2546565675892E-01	0,61966272
3 → F1	9,9265078275354E-03	0,517006803
5 → F1	1,0897774976647E-01	0,558917691
9 → F1	4,5018176088596E-05	0
23 → F1	3,2052941375080E-02	0,54494382
44 → F1	4,0516358479736E-04	0,333333333
24b → F1	4,2429630963502E-03	0,037135279
24c → F1	4,3217449045052E-03	0,114583333
24d → F1	2,0764633720865E-02	0,412466125
29/30 → F1	4,5018176088596E-05	0
7A → F1	3,6014540870877E-04	0,375
7op → F1	6,5951627969793E-03	0,233788396
8B → F1	3,6014540870877E-04	0,5

Pathway	FLN	SLN
8m → F1	4,5018176088596E-05	0
F2 → F1	4,0204607610323E-01	0,433306273
F3 → F1	2,2994158891653E-01	0,476824433
F4 → F1	2,9430632617919E-02	0,407265774
F5 → F1	9,0036352177192E-03	0,3
F6 → F1	7,7993990073492E-03	0,122655123
F7 → F1	3,3425995745782E-03	0,38047138
INSULA → F1	2,6560723892272E-03	0,610169492
MB → F1	3,1512723262017E-04	0,285714286
MST → F1	1,9132724837653E-04	0,470588235
ProM → F1	3,6014540870877E-04	0
STPc → F1	9,0036352177192E-05	0,5
3 → F2	5,8108498367886E-03	0,71686747
5 → F2	1,8762744051318E-02	0,734141791
12 → F2	1,2251791824554E-04	0
13 → F2	8,7512798746817E-05	0,1
23 → F2	8,3557220243461E-02	0,643485547
31 → F2	1,0501535849618E-04	1
44 → F2	6,3884343085176E-04	0,698630137
24a → F2	3,1504607548854E-04	0,277777778
24b → F2	2,1178097296730E-02	0,194628099
24c → F2	3,1242069152614E-02	0,392997199
24d → F2	1,3522477662358E-01	0,542583484
45B → F2	4,3756399373408E-05	1
46v → F2	4,5506655348345E-04	0,326923077
7A → F2	8,3399697205716E-03	0,389296957
7B → F2	5,2507679248090E-05	0,333333333
7m → F2	7,4735930129781E-03	0,791569087
7op → F2	1,2435568701923E-02	0,622800844
8B → F2	1,4002047799491E-04	0,25
8l → F2	1,7502559749363E-05	0
8m → F2	2,3628455661641E-04	0,592592593
8r → F2	2,6253839624045E-05	1
9/46d → F2	1,6627431761895E-04	0,578947368
9/46v → F2	2,5378711636577E-04	0,344827586
AIP → F2	5,2507679248090E-05	0,5
F1 → F2	1,6275630310933E-01	0,674588665
F3 → F2	3,3982970009364E-01	0,595951792
F4 → F2	4,1918630599725E-03	0,75782881
F5 → F2	4,1542325565114E-02	0,743206236
F6 → F2	7,5698570915996E-02	0,477109827
F7 → F2	2,4512334928983E-02	0,397001071
INSULA → F2	6,4759471072644E-03	0,433783784
IPa → F2	5,2507679248090E-05	0

Pathway	FLN	SLN
LIP → F2	7,0010238997453E-05	0,875
MB → F2	3,0629479561386E-04	0,342857143
MIP → F2	2,2053225284198E-03	0,773809524
MST → F2	4,0255887423536E-04	0,608695652
MT → F2	8,7512798746817E-06	0
OPRO → F2	2,1003071699236E-04	0,083333333
Parainsula → F2	9,6264078621498E-05	0
PBr → F2	6,1258959122772E-05	1
PERIRHINAL → F2	3,5005119498727E-05	0
PGa → F2	1,2251791824554E-04	0,642857143
ProM → F2	7,8761518872135E-05	0
SII → F2	5,2507679248090E-05	0
STPc → F2	3,7630503461131E-04	0,88372093
STPi → F2	4,4631527360877E-04	0,882352941
STPr → F2	4,3756399373408E-05	0,6
TEa/ma → F2	5,2507679248090E-05	0,5
TEMPORAL POLE → F2	2,6253839624045E-05	0
TPt → F2	1,3529478686258E-02	0,528460543
VIP → F2	7,8761518872135E-05	1
1 → F5	2,3988722433278E-03	0,6812749
2 → F5	1,9870976990897E-01	0,634610297
3 → F5	1,0016008410389E-02	0,603053435
5 → F5	9,5572599335770E-05	0,4
9 → F5	4,7786299667885E-05	0,4
10 → F5	9,0793969368982E-05	0,842105263
11 → F5	1,4813752897044E-04	0,193548387
12 → F5	1,1870116837503E-02	0,526972625
13 → F5	1,1468711920292E-04	0
14 → F5	1,4335889900366E-05	1
23 → F5	1,2424437913650E-04	0,384615385
25 → F5	4,7786299667885E-06	1
32 → F5	3,8229039734308E-05	0,75
44 → F5	2,2746278641913E-03	0,581932773
24a → F5	7,4068764485222E-04	0,206451613
24b → F5	1,2902300910329E-04	0,074074074
24c → F5	8,2813657324445E-03	0,502019619
24d → F5	4,8742025661243E-04	0,490196078
29/30 → F5	1,4335889900366E-05	0
45A → F5	2,8671779800731E-05	0
45B → F5	1,0512985926935E-04	0,272727273
46d → F5	9,5572599335770E-05	0,6
46v → F5	1,0990848923614E-04	0,391304348
7A → F5	7,1679449501828E-05	0,2
7B → F5	7,5636155114329E-02	0,667108921

Pathway	FLN	SLN
7m → F5	4,7786299667885E-06	1
7op → F5	3,3450409767520E-05	0,142857143
8B → F5	4,3007669701097E-05	0,666666667
8l → F5	8,2192435428763E-04	0,581395349
8m → F5	2,8671779800731E-05	1
8r → F5	2,5326738823979E-04	0,566037736
9/46d → F5	3,3450409767520E-05	0,285714286
9/46v → F5	2,7954985305713E-03	0,256410256
AIP → F5	3,2685828972833E-03	0,576023392
CORE → F5	5,2564929634674E-05	0,363636364
ENTORHINAL → F5	1,1468711920292E-04	0,25
F1 → F5	4,1669653310396E-03	0,79587156
F2 → F5	1,1038635223281E-03	0,445887446
F3 → F5	3,1104102453826E-02	0,69549854
F4 → F5	5,1501206604067E-01	0,569320987
F6 → F5	3,3450409767520E-05	0,428571429
F7 → F5	3,8229039734308E-05	1
Gu → F5	8,3100375122452E-03	0,199539965
INSULA → F5	6,0067378682532E-03	0,23150358
LB → F5	4,7786299667885E-05	0,8
LIP → F5	6,4989367548324E-03	0,473529412
MB → F5	2,8671779800731E-05	0,666666667
MIP → F5	4,7786299667885E-06	0
OPAI → F5	2,8671779800731E-04	0,233333333
OPRO → F5	5,5766611712422E-03	0,316195373
Parainsula → F5	2,3893149833943E-05	1
PBr → F5	3,8229039734308E-05	0,75
PERIRHINAL → F5	7,1679449501828E-05	0,333333333
ProM → F5	4,4369579241631E-02	0,312008616
SII → F5	5,7654170549304E-02	0,545296312
STPc → F5	4,7786299667885E-06	0
STPi → F5	1,9114519867154E-05	0,5
STPr → F5	3,8229039734308E-05	0
TEa/ma → F5	6,6900819535039E-05	0
TEa/mp → F5	1,9114519867154E-05	1
TEav → F5	1,1468711920292E-04	0,25
TEMPORAL POLE → F5	4,7786299667885E-05	0,4
TEOm → F5	1,4335889900366E-05	1
TEpd → F5	2,8671779800731E-05	0,333333333
TEpv → F5	4,7786299667885E-05	0,2
TH/TF → F5	9,5572599335770E-06	0
V1 → F5	5,2564929634674E-05	1
V2 → F5	3,3450409767520E-05	0,571428571
V3 → F5	4,7786299667885E-06	0

Pathway	FLN	SLN
V6 → F5	9,5572599335770E-06	0
V6A → F5	1,4335889900366E-05	1
1 → F7	1,1283879849247E-05	0
3 → F7	1,2412267834172E-04	0,545454545
5 → F7	4,5135519396989E-05	0,25
9 → F7	1,1576132337343E-01	0,619066186
10 → F7	1,4894721401007E-03	0,121212121
11 → F7	2,7081311638194E-04	0,5
12 → F7	1,2096319198393E-02	0,398320896
13 → F7	2,5840084854776E-03	0,445414847
14 → F7	2,2567759698495E-05	1
23 → F7	3,0387488434023E-02	0,680282213
31 → F7	4,8295005754779E-03	0,91588785
32 → F7	2,5952923653269E-04	0,217391304
44 → F7	1,0166775744172E-02	0,705882353
24a → F7	1,0787389135880E-02	0,302301255
24b → F7	6,4792038094378E-02	0,293974225
24c → F7	9,3543363950261E-02	0,411580217
24d → F7	1,8031639999097E-02	0,590738423
45A → F7	3,4348130261109E-02	0,671813403
45B → F7	6,3866759946740E-03	0,704946996
46d → F7	9,0271038793979E-04	0
46v → F7	1,4804450362213E-02	0,493140244
7A → F7	2,1890726907540E-03	0,5
7B → F7	5,6419399246237E-05	0,6
7m → F7	5,6193721649252E-03	0,925702811
7op → F7	3,8365191487441E-04	0,735294118
8B → F7	1,0376655909368E-01	0,379186603
8l → F7	3,1256347182415E-03	0,693140794
8m → F7	3,6909570986888E-02	0,555181902
8r → F7	2,2567759698495E-03	0,51
9/46d → F7	2,5072781025028E-02	0,451845185
9/46v → F7	3,7800997494979E-03	0,537313433
F1 → F7	3,1594863577893E-04	0,357142857
F2 → F7	9,8959626277899E-02	0,491220068
F3 → F7	1,0087788585227E-02	0,589485459
F4 → F7	2,7194150436686E-03	0,560165975
F5 → F7	2,0310983728645E-03	0,605555556
F6 → F7	2,4237773916183E-01	0,468482309
FST → F7	7,8987158944732E-05	0,857142857
INSULA → F7	2,0875177721108E-03	0,643243243
IPa → F7	2,9789442802013E-03	0,715909091
LIP → F7	4,4007131412065E-04	0,487179487
MB → F7	1,5797431788946E-03	0,442857143

Pathway	FLN	SLN
MST → F7	6,3189727155785E-04	0,75
OPRO → F7	1,0832524655277E-03	0,239583333
Parainsula → F7	5,6419399246237E-04	0,12
PBc → F7	2,2567759698495E-05	1
PBr → F7	2,5501568459299E-03	0,716814159
PERIRHINAL → F7	5,6419399246237E-05	0
PGa → F7	2,8322538421611E-03	0,812749004
ProM → F7	1,8054207758796E-04	0,375
SII → F7	4,5135519396989E-05	0,5
STPc → F7	1,8392724154273E-03	0,82208589
STPi → F7	1,1633680124574E-02	0,762366634
STPr → F7	6,5672180722620E-03	0,716494845
TEa/ma → F7	9,1399426778904E-04	0,925925926
TEa/mp → F7	2,2567759698495E-05	0
TEav → F7	6,7703279095484E-05	0,333333333
TEMPORAL POLE → F7	5,9804563201011E-04	0,547169811
TEO → F7	4,5135519396989E-05	0,5
TH/TF → F7	4,5135519396989E-05	1
TPt → F7	1,7377174967841E-03	0,74025974
V2 → F7	9,0271038793979E-05	0,625
VIP → F7	1,1283879849247E-05	1
1 → MT	2,9779009967035E-06	1
2 → MT	2,3823207973628E-05	0
23 → MT	1,1316023787473E-04	0,026315789
32 → MT	2,9779009967035E-06	0
24a → MT	1,0422653488462E-05	0
24b → MT	4,4668514950552E-06	0
29/30 → MT	1,7867405980221E-05	0,166666667
45A → MT	2,9779009967035E-06	0
45B → MT	5,0028736744618E-04	0,452380952
7A → MT	4,5264095149893E-04	0,661184211
8l → MT	2,2751163614814E-03	0,672774869
8m → MT	6,2833711030443E-04	0,407582938
8r → MT	8,0403326910994E-05	0,703703704
9/46d → MT	5,9558019934069E-06	1
9/46v → MT	3,8712712957145E-05	0,846153846
DP → MT	1,4645317101788E-02	0,837738918
F1 → MT	2,9779009967035E-06	0
F2 → MT	5,9558019934069E-06	0,5
F4 → MT	2,0845306976924E-05	0,142857143
F5 → MT	2,9779009967035E-06	0
FST → MT	6,1856959503524E-02	0,285865588
INSULA → MT	4,4668514950552E-05	0,066666667
IPa → MT	1,3326106960248E-03	0,055865922

Pathway	FLN	SLN
LB → MT	2,9779009967035E-06	1
LIP → MT	2,2867301753686E-02	0,529105352
MB → MT	8,0403326910994E-05	0,074074074
MIP → MT	1,1911603986814E-05	0
MST → MT	5,7428820721426E-03	0,186932849
OPRO → MT	2,9779009967035E-06	1
PBr → MT	1,7867405980221E-05	0
PERIRHINAL → MT	8,8741449701763E-04	0,003355705
PGa → MT	6,0659843302850E-03	0,039273441
PIP → MT	9,3223190701802E-03	0,614758026
Pro.St. → MT	8,9337029901104E-06	0,333333333
ProM → MT	2,9779009967035E-06	0
SII → MT	2,9779009967035E-06	0
STPc → MT	1,7807847960287E-03	0,050167224
STPi → MT	2,1738677275935E-04	0,02739726
STPr → MT	2,4269893123133E-04	0,012269939
TEa/ma → MT	2,2661826584913E-03	0,05781866
TEa/mp → MT	1,5056267439333E-02	0,324367089
TEad → MT	1,0601327548264E-03	0,016853933
TEav → MT	1,1584034877176E-03	0,005141388
TEMPORAL POLE → MT	2,3823207973628E-05	0
TEO → MT	3,8200513985712E-02	0,332709698
TEOm → MT	8,8449615404086E-02	0,362130496
TEpd → MT	1,3552427435997E-02	0,207866403
TEpv → MT	1,8906693428070E-02	0,234682627
TH/TF → MT	9,4131450505796E-03	0,165137615
TPt → MT	2,6801108970331E-05	0,444444444
V1 → MT	1,8994541507473E-02	0,890491495
V2 → MT	1,1946296533425E-01	0,94168235
V3 → MT	5,1044200984494E-02	0,896388775
V3A → MT	3,3516275717897E-02	0,863349622
V4 → MT	3,8092713969631E-01	0,615316062
V4t → MT	7,7112746309636E-02	0,470747249
V6A → MT	2,9779009967035E-06	1
VIP → MT	1,4949063003451E-03	0,513944223
9 → PBr	1,2528188423954E-03	0,281818182
10 → PBr	8,8722352566001E-03	0,596277279
11 → PBr	6,9474499441926E-04	0,245901639
12 → PBr	7,9383157559053E-03	0,665710187
13 → PBr	2,3347987517369E-03	0,309756098
14 → PBr	1,3667114644313E-04	0
23 → PBr	1,2821461925696E-02	0,278481013
25 → PBr	1,0278809138744E-03	0,12465374
31 → PBr	1,8592970547368E-03	0,355283308

Pathway	FLN	SLN
32 → PBr	2,6508507778866E-03	0,297529538
24a → PBr	1,3126124689643E-03	0,292841649
24b → PBr	1,0563540693834E-03	0,35309973
24c → PBr	1,1104530648505E-04	0,41025641
24d → PBr	2,2778524407189E-05	0
29/30 → PBr	8,0664449556958E-03	0,208965761
45A → PBr	3,7584565271862E-04	0,439393939
45B → PBr	5,6946311017972E-05	0,8
46d → PBr	4,1969431220246E-03	0,485074627
46v → PBr	8,6843124302408E-04	0,373770492
7A → PBr	2,2778524407189E-05	0,5
7m → PBr	2,1639598186829E-04	0,157894737
8B → PBr	9,2537755404205E-04	0,353846154
8l → PBr	2,8473155508986E-06	0
8m → PBr	4,4418122594018E-04	0,583333333
8r → PBr	2,8473155508986E-06	0
9/46d → PBr	4,1229129177012E-03	0,55801105
CORE → PBr	8,3671214778707E-02	0,532804737
DP → PBr	5,6946311017972E-05	1
ENTORHINAL → PBr	8,0436664312886E-03	0,01380531
F6 → PBr	2,2778524407189E-05	1
F7 → PBr	1,3382383089223E-04	0,680851064
FST → PBr	1,0250335983235E-04	0,555555556
INSULA → PBr	1,3296963622697E-03	0,310492505
IPa → PBr	5,4098995467074E-05	0
LB → PBr	5,0596797339468E-02	0,615700619
LIP → PBr	8,5419466526958E-06	1
MB → PBr	9,2295733582379E-02	0,533981182
MST → PBr	1,1673993758684E-04	0,634146341
OPAI → PBr	2,5455001025034E-03	0,454138702
OPRO → PBr	2,6536980934375E-03	0,03111588
Parainsula → PBr	7,6564315163664E-03	0,309408702
PBc → PBr	1,0483531126854E-01	0,587386947
PERIRHINAL → PBr	1,1360789048085E-03	0,037593985
PGa → PBr	2,4657752670782E-03	0,184757506
Pro.St. → PBr	6,3381244163003E-03	0,163971249
ProM → PBr	8,5419466526958E-06	0
STPc → PBr	5,2894580989044E-02	0,701458793
STPi → PBr	2,8422758023735E-01	0,565771415
STPr → PBr	6,7800277897998E-02	0,454308752
TEMPORAL POLE → PBr	1,4329684973007E-01	0,399964234
TH/TF → PBr	2,5537573176010E-02	0,242390456
TPt → PBr	7,4314935878454E-04	0,601532567
V2 → PBr	1,1389262203594E-05	1

Pathway	FLN	SLN
V4 → PBr	2,2778524407189E-05	0
1 → ProM	2,2093466409646E-05	1
2 → ProM	2,7517412413214E-02	0,551987154
3 → ProM	1,1046733204823E-04	0
9 → ProM	2,2093466409646E-05	0
11 → ProM	5,5233666024115E-05	0
12 → ProM	1,3129042413932E-01	0,643247791
13 → ProM	1,6238697811090E-03	0,159863946
44 → ProM	1,1068826671233E-02	0,52994012
24a → ProM	2,0215521764826E-03	0,459016393
24b → ProM	1,0494396544582E-04	0,421052632
24c → ProM	2,4634215046755E-03	0,35426009
24d → ProM	1,1599069865064E-04	0,619047619
46d → ProM	1,1046733204823E-05	1
46v → ProM	3,1483189633746E-04	0,596491228
7A → ProM	1,6570099807235E-05	0,666666667
7B → ProM	1,1101966870847E-03	0,611940299
7op → ProM	7,1803765831350E-05	0,230769231
9/46v → ProM	1,8077978889693E-02	0,650779102
AIP → ProM	4,2253754508448E-03	0,678431373
ENTORHINAL → ProM	2,2259167407718E-03	0,23325062
F1 → ProM	6,6280399228938E-05	0
F2 → ProM	1,1046733204823E-05	0,5
F3 → ProM	1,5354959154704E-03	0,791366906
F4 → ProM	3,1925058961938E-03	0,242214533
F5 → ProM	3,1432374661003E-01	0,760560905
Gu → ProM	1,7508519792984E-01	0,62213319
INSULA → ProM	2,4092925119719E-02	0,366345713
LIP → ProM	5,9652359306044E-04	0,611111111
MB → ProM	2,2093466409646E-05	0
OPAI → ProM	3,8939734547001E-03	0,239716312
OPRO → ProM	2,7511889046612E-02	0,304758081
PERIRHINAL → ProM	1,2261873857354E-03	0,018018018
PGa → ProM	2,2093466409646E-05	0
SII → ProM	2,4255312097830E-01	0,608370907
TEa/ma → ProM	1,1930471861209E-03	0,407407407
TEav → ProM	3,0930852973504E-04	0,232142857
TEMPORAL POLE → ProM	1,8945147446271E-03	0,221574344
2 → STPc	7,0964765993684E-05	0,2
5 → STPc	2,8385906397474E-05	1
9 → STPc	2,8385906397474E-05	0,5
10 → STPc	1,4476812262712E-03	0,411764706
12 → STPc	4,1301493808324E-03	0,329896907
13 → STPc	2,1786183160061E-03	0,185667752

Pathway	FLN	SLN
23 → STPc	3,1508356101196E-03	0,193693694
31 → STPc	1,7883121030408E-03	0,103174603
24b → STPc	4,6836745555832E-04	0,424242424
24c → STPc	1,4192953198737E-05	0
29/30 → STPc	3,4063087676968E-04	0
45A → STPc	2,8385906397474E-05	0
45B → STPc	7,6641947273179E-04	0,462962963
46d → STPc	7,1674413653621E-03	0,63960396
46v → STPc	3,0656778909272E-03	0,583333333
7A → STPc	1,4476812262712E-03	0,441176471
7B → STPc	2,2708725117979E-04	0,375
7m → STPc	4,2578859596210E-05	0
7op → STPc	8,2319128552674E-04	0,689655172
8B → STPc	7,9480537912926E-04	0,5
8l → STPc	5,1094631515453E-04	0,805555556
8m → STPc	7,2525990845545E-03	0,553816047
8r → STPc	4,9675336195579E-04	0,514285714
9/46d → STPc	2,2992584181954E-03	0,314814815
CORE → STPc	1,3298797147216E-02	0,779082177
DP → STPc	1,9870134478232E-04	0,785714286
ENTORHINAL → STPc	5,9610403434695E-04	0
F5 → STPc	1,0360855835078E-03	0,602739726
F6 → STPc	1,4192953198737E-05	1
F7 → STPc	7,2384061313558E-04	0,274509804
FST → STPc	6,2448994074442E-03	0,468181818
INSULA → STPc	2,0260440691197E-02	0,66619965
IPa → STPc	6,1881275946493E-03	0,338302752
LB → STPc	5,7197601390909E-02	0,660421836
LIP → STPc	2,8641379555051E-02	0,670961348
MB → STPc	2,2417769577405E-02	0,643241532
MST → STPc	1,8561544193308E-01	0,582199113
MT → STPc	7,3803356633431E-04	0,423076923
Parainsula → STPc	2,1999077458042E-04	0,129032258
PBc → STPc	9,2232906361991E-02	0,532199738
PBr → STPc	2,0153993542206E-02	0,210915493
PERIRHINAL → STPc	6,6706880034063E-04	0,042553191
PGa → STPc	1,2028527835929E-02	0,466076696
PIP → STPc	4,9107618067629E-03	0,705202312
Pro.St. → STPc	1,9870134478232E-04	0
STPi → STPc	4,0955185750275E-01	0,611415304
STPr → STPc	1,2397544619097E-02	0,155981683
TEa/ma → STPc	5,2513926835326E-04	0,135135135
TEa/mp → STPc	3,8320973636589E-04	0,296296296
TEad → STPc	7,6641947273179E-04	0,018518519

Pathway	FLN	SLN
TEav → STPc	3,9740268956463E-04	0,035714286
TEMPORAL POLE → STPc	3,8604832700564E-03	0,033088235
TEO → STPc	1,7031543838484E-04	0,5
TEOm → STPc	3,1224497037221E-04	0,159090909
TEpd → STPc	8,0899833232800E-04	0,280701754
TEpv → STPc	1,4334882730724E-03	0,108910891
TH/TF → STPc	9,3673491111663E-03	0,045454545
TPt → STPc	4,5985168363907E-02	0,607407407
V2 → STPc	3,9740268956463E-04	0,214285714
V3A → STPc	2,8385906397474E-05	1
V4 → STPc	1,3909094134762E-03	0,520408163
V6A → STPc	1,4192953198737E-05	0
VIP → STPc	5,6771812794947E-05	0
9 → STPi	4,5710961280738E-04	0,136363636
10 → STPi	2,3260645978994E-02	0,778472532
11 → STPi	3,1166564509594E-04	0,1
12 → STPi	5,7865921439480E-03	0,337522442
13 → STPi	2,0777709673063E-04	0,2
14 → STPi	1,3141901368212E-02	0,682213439
23 → STPi	4,4672075797085E-04	0,069767442
25 → STPi	2,6179914188059E-03	0,571428571
32 → STPi	3,3244335476900E-04	0,375
24c → STPi	1,3505511287491E-04	0
24d → STPi	4,1555419346125E-05	0
29/30 → STPi	4,1555419346125E-05	0
45A → STPi	3,7399877411513E-04	0
46d → STPi	3,5010440799111E-03	0,43620178
46v → STPi	2,5141028704406E-03	0,483471074
8B → STPi	2,0777709673063E-04	0,4
8m → STPi	4,1555419346125E-05	0
9/46d → STPi	1,9738824189410E-04	0,368421053
CORE → STPi	1,8159718254257E-02	0,870709382
F6 → STPi	8,3110838692251E-05	1
F7 → STPi	8,3110838692251E-05	1
Gu → STPi	4,1555419346125E-05	0
INSULA → STPi	6,0255358051882E-04	0,896551724
IPa → STPi	1,1219963223454E-03	0,407407407
LB → STPi	7,0020881598221E-02	0,809198813
LIP → STPi	4,1555419346125E-05	0,5
MB → STPi	1,0762853610646E-02	0,787644788
MST → STPi	6,8545664211434E-02	0,71354956
MT → STPi	4,1555419346125E-05	1
OPRO → STPi	5,8177587084576E-04	0,5
Parainsula → STPi	8,5188609659557E-04	0,146341463

Pathway	FLN	SLN
PBc → STPi	5,6369926343019E-02	0,805012901
PBr → STPi	3,3477045825239E-01	0,549962761
PERIRHINAL → STPi	4,1555419346125E-05	1
PGa → STPi	4,1555419346125E-03	0,375
Pro.St. → STPi	7,2721983855720E-05	0
STPc → STPi	2,2799380824252E-01	0,806433974
STPr → STPi	2,4954029317348E-02	0,302248127
TEa/ma → STPi	8,3110838692251E-05	0
TEa/mp → STPi	2,7011022574982E-04	0,461538462
TEav → STPi	1,6622167738450E-04	0,25
TEMPORAL POLE → STPi	1,2568436581236E-01	0,752851711
TEpd → STPi	1,4544396771144E-04	0,428571429
TH/TF → STPi	6,2333129019188E-04	0,766666667
TPt → STPi	8,3110838692251E-05	0,5
V4t → STPi	3,1166564509594E-05	0
9 → STPr	1,7132396871428E-03	0,746019108
10 → STPr	3,2955311179435E-02	0,655049669
11 → STPr	4,5995575040171E-03	0,40717675
12 → STPr	1,6844583516343E-02	0,597700219
13 → STPr	1,4567993518061E-03	0,344569288
14 → STPr	1,3000706574967E-02	0,488091491
23 → STPr	6,4792106002614E-04	0,334736842
25 → STPr	6,9948193596085E-03	0,366614665
32 → STPr	1,6177565835600E-03	0,52613828
44 → STPr	1,1457972429936E-04	0,238095238
24a → STPr	8,7298837561416E-04	0,4625
24b → STPr	1,3340353614854E-03	0,625766871
24c → STPr	2,7280886737943E-04	0,85
29/30 → STPr	1,3776847802661E-04	0,099009901
45A → STPr	2,1824709390354E-03	0,625
45B → STPr	8,0751424744310E-04	0,804054054
46d → STPr	1,0104840447734E-02	0,555615551
46v → STPr	8,9890521801521E-03	0,535204856
7A → STPr	1,9369429583939E-04	0,85915493
8B → STPr	6,0017950823474E-04	0,836363636
8l → STPr	4,9105596128297E-05	0,333333333
8m → STPr	3,5465152759325E-04	0,738461538
8r → STPr	6,0017950823474E-05	0,727272727
9/46d → STPr	1,0230332526728E-04	0,48
9/46v → STPr	5,3879751307436E-04	0,708860759
CORE → STPr	1,0066647206301E-03	0,319783198
DP → STPr	3,8193241433120E-05	0,714285714
ENTORHINAL → STPr	3,9448162223065E-03	0,060857538
F1 → STPr	1,0912354695177E-05	0,5

Pathway	FLN	SLN
F2 → STPr	1,6368532042766E-05	0,666666667
F4 → STPr	5,4561773475885E-06	1
F7 → STPr	5,1833684802091E-05	0,789473684
FST → STPr	2,3270596387465E-03	0,723329426
Gu → STPr	5,4561773475885E-06	0
INSULA → STPr	9,8484001123973E-04	0,318559557
IPa → STPr	2,0981729990152E-02	0,42894292
LB → STPr	7,3112776457686E-03	0,452985075
LIP → STPr	1,2412803465764E-04	0,901098901
MB → STPr	1,6856859915375E-02	0,496034957
MST → STPr	1,8851092735918E-02	0,645730825
MT → STPr	1,6368532042766E-05	0,833333333
OPAI → STPr	2,9736166544357E-04	0,394495413
OPRO → STPr	6,1982174668605E-03	0,320862676
Parainsula → STPr	6,3237095458551E-03	0,541846419
PBc → STPr	8,9208499633072E-03	0,528746177
PBr → STPr	1,9855847794477E-01	0,457098498
PERIRHINAL → STPr	9,7992945162690E-03	0,356069042
PGa → STPr	3,3195382982728E-02	0,53377712
Pro.St. → STPr	1,2685612333143E-04	0,086021505
STPc → STPr	3,0261323614063E-02	0,880279468
STPi → STPr	2,4014000551074E-01	0,606429991
TEa/ma → STPr	2,3892600605090E-02	0,401918246
TEa/mp → STPr	4,0239307938465E-03	0,341694915
TEad → STPr	6,2473230629888E-04	0,515283843
TEav → STPr	1,3798672512051E-02	0,511269276
TEMPORAL POLE → STPr	2,2652957111718E-01	0,500108387
TEO → STPr	5,4561773475885E-06	0
TEOm → STPr	2,1279091655595E-04	0,666666667
TEpd → STPr	9,5755912450178E-04	0,287749288
TEpv → STPr	1,6614060023407E-03	0,500821018
TH/TF → STPr	1,5371415632494E-02	0,366758364
TPt → STPr	1,3640443368971E-05	0,4
V2 → STPr	5,4561773475885E-06	1
V4 → STPr	2,7280886737943E-06	1
1 → TEO	2,5647601949218E-05	0
2 → TEO	3,8471402923827E-05	0
3 → TEO	1,2182610925878E-04	0,210526316
5 → TEO	2,5647601949218E-05	1
11 → TEO	1,2823800974609E-05	0
12 → TEO	2,3724031803026E-04	0,378378378
23 → TEO	1,2823800974609E-05	1
44 → TEO	1,2823800974609E-05	0,5
24a → TEO	7,6942805847653E-05	0

Pathway	FLN	SLN
24b → TEO	3,8471402923827E-05	0
24d → TEO	1,9235701461913E-05	0,333333333
45A → TEO	1,9235701461913E-05	0,666666667
45B → TEO	4,1677353167479E-04	0,507692308
46d → TEO	1,2823800974609E-05	0,5
46v → TEO	3,8471402923827E-05	0,5
7A → TEO	4,6165683508592E-04	0
7B → TEO	2,5647601949218E-05	1
7m → TEO	5,1295203898435E-05	0,375
8B → TEO	1,2823800974609E-05	0
8l → TEO	6,0848935624519E-03	0,749209694
8r → TEO	5,3859964093357E-04	0,797619048
9/46d → TEO	2,5647601949218E-05	1
9/46v → TEO	3,9112592972557E-04	0,672131148
DP → TEO	1,1669658886894E-03	0,263736264
ENTORHINAL → TEO	2,5647601949218E-05	1
F2 → TEO	6,4119004873044E-06	1
F5 → TEO	3,8471402923827E-05	0,833333333
F7 → TEO	4,4883303411131E-05	0,857142857
FST → TEO	6,9748653500898E-02	0,371943372
INSULA → TEO	1,2823800974609E-04	0,3
IPa → TEO	5,5847653244422E-03	0,117106774
LB → TEO	1,2823800974609E-05	1
LIP → TEO	7,8994614003591E-03	0,308441558
MB → TEO	3,8471402923827E-05	0
MIP → TEO	1,9235701461913E-05	0
MST → TEO	5,8348294434470E-04	0
MT → TEO	2,4397281354193E-02	0,424178712
Parainsula → TEO	4,4883303411131E-05	0,714285714
PBc → TEO	7,6942805847653E-05	1
PBr → TEO	5,1295203898435E-05	0,25
PERIRHINAL → TEO	1,7510900230828E-02	0,037715123
PGa → TEO	4,5460374454988E-03	0,039492243
PIP → TEO	1,7119774301103E-03	0,483146067
ProM → TEO	1,2823800974609E-05	1
STPc → TEO	1,9235701461913E-05	0
STPi → TEO	1,2823800974609E-04	0
STPr → TEO	1,3144395998974E-03	0,073170732
TEa/ma → TEO	1,5689920492434E-02	0,474049857
TEa/mp → TEO	2,9488330341113E-02	0,307675582
TEad → TEO	8,8035393690690E-03	0,23379461
TEav → TEO	1,5632213388048E-02	0,30680886
TEMPORAL POLE → TEO	3,1418312387792E-04	0,183673469
TEOm → TEO	4,0337265965632E-02	0,482753139

Pathway	FLN	SLN
TEpd → TEO	2,3132213388048E-01	0,349668764
TEpv → TEO	9,0760451397794E-02	0,304415401
TH/TF → TEO	1,4593485509105E-02	0,023725835
V2 → TEO	2,4615285970762E-02	0,936962751
V3 → TEO	1,2239676840215E-01	0,84252711
V3A → TEO	4,9371633752244E-04	0,337662338
V4 → TEO	2,5587330084637E-01	0,664085601
V4t → TEO	5,8668889458836E-03	0,520218579
3 → TEpd	5,0127072127844E-06	1
11 → TEpd	3,5088950489491E-05	0,142857143
12 → TEpd	1,8221190718471E-03	0,504814305
13 → TEpd	3,4086409046934E-04	0,566176471
23 → TEpd	7,5190608191766E-06	0
44 → TEpd	2,7569889670314E-05	0,272727273
24a → TEpd	2,7068618949036E-04	0,203703704
24b → TEpd	3,5088950489491E-05	0,142857143
45A → TEpd	9,4238895600347E-04	0,712765957
45B → TEpd	6,4864431333430E-03	0,675425039
46d → TEpd	1,5038121638353E-05	0
46v → TEpd	4,0853563784193E-04	0,429447853
7A → TEpd	2,0201210067521E-03	0,503722084
8l → TEpd	4,5941461605169E-03	0,725040917
8m → TEpd	2,5063536063922E-05	0,2
8r → TEpd	1,9198668624964E-03	0,596605744
9/46v → TEpd	1,4185961412180E-03	0,485865724
CORE → TEpd	7,5190608191766E-06	0
DP → TEpd	8,0203315404551E-05	0,6875
ENTORHINAL → TEpd	3,4337044407573E-04	0,102189781
F5 → TEpd	7,5190608191766E-06	0
F6 → TEpd	1,5038121638353E-05	0,666666667
FST → TEpd	1,0451494538655E-03	0,225419664
INSULA → TEpd	7,7696961798158E-05	0
IPa → TEpd	6,3460873313851E-03	0,178909953
LB → TEpd	1,5038121638353E-05	0
LIP → TEpd	2,8271668680104E-03	0,721631206
MB → TEpd	5,0127072127844E-06	0
MST → TEpd	1,0025414425569E-05	1
MT → TEpd	1,5038121638353E-05	0,333333333
OPAI → TEpd	1,0025414425569E-05	1
OPRO → TEpd	8,0203315404551E-05	0,125
Parainsula → TEpd	5,0127072127844E-06	0
PBr → TEpd	6,0152486553413E-05	0
PERIRHINAL → TEpd	3,5068899660640E-02	0,075471698
PGa → TEpd	4,4362458833142E-04	0,11299435

Pathway	FLN	SLN
PIP → TEpd	1,1027955868126E-04	0,863636364
Pro.St. → TEpd	5,0127072127844E-05	0,1
SII → TEpd	4,9375166045926E-04	0,223350254
STPc → TEpd	5,0127072127844E-06	0
STPi → TEpd	2,5063536063922E-05	0,2
STPr → TEpd	4,2858646669307E-04	0,204678363
TEa/ma → TEpd	6,5162687412591E-02	0,363206277
TEa/mp → TEpd	2,4381557247623E-01	0,46513636
TEad → TEpd	2,6857834610738E-01	0,516456854
TEav → TEpd	1,1495641451078E-01	0,448960014
TEMPORAL POLE → TEpd	1,1704671341852E-03	0,00856531
TEO → TEpd	1,3762638288060E-01	0,679736301
TEOm → TEpd	1,7424170271639E-02	0,70972382
TEpv → TEpd	3,8961266811367E-02	0,280411708
TH/TF → TEpd	1,6191044297294E-02	0,035913313
V2 → TEpd	1,7544475244745E-04	0,971428571
V3 → TEpd	1,9048287408581E-04	0,921052632
V3A → TEpd	3,5088950489491E-04	0,914285714
V4 → TEpd	2,7389432210654E-02	0,952964861
V4t → TEpd	5,7646132947021E-05	0,913043478
7op → V1	6,5905096660808E-05	0,333333333
8l → V1	2,1468411852533E-04	0,104211794
8r → V1	1,7786631567714E-06	0
CORE → V1	4,2051754745834E-05	0
DP → V1	4,9063704109749E-04	0,003960396
FST → V1	7,5312297246041E-03	0,020929381
IPa → V1	1,2313857972380E-03	0,017511521
LB → V1	6,3448131080336E-05	0,0625
LIP → V1	1,2873673033355E-03	0,009089382
MB → V1	3,7817339456986E-05	0
MST → V1	6,5738150991430E-03	0,008804324
MT → V1	5,8852547353403E-02	0,17323749
PBc → V1	1,1382275378941E-04	0,277631579
PERIRHINAL → V1	1,7577714727171E-03	0,007245872
PGa → V1	7,3423435952682E-04	0,003809524
PIP → V1	8,4924526827224E-04	0
STPc → V1	1,6535203572885E-03	0,036214364
STPi → V1	4,3213348360514E-04	0,081729544
STPr → V1	1,9369771090702E-05	0,047619048
TEa/ma → V1	7,0890811167129E-04	0,029216301
TEa/mp → V1	2,2680874902888E-03	0,021262233
TEad → V1	8,7616177276813E-04	0,005889244
TEav → V1	1,0588882801376E-03	0
TEO → V1	2,7034555509039E-02	0,096027815

Pathway	FLN	SLN
TEOm → V1	1,9236562760412E-03	0,009896034
TEpd → V1	3,6308239967448E-03	0,020500658
TEpv → V1	5,4083853413761E-03	0,001887834
TH/TF → V1	3,9719946601775E-03	0,005872348
TPt → V1	2,1968365553603E-05	0,5
V2 → V1	7,3215720618642E-01	0,420794741
V3 → V1	6,9065028226676E-03	0,067021339
V3A → V1	2,1819683414529E-03	0,004350808
V4 → V1	1,2773034369581E-01	0,296524615
V4t → V1	2,1677842611126E-03	0,0226497
8l → V2	1,0890779817564E-04	0,242494824
8m → V2	2,4677286850678E-05	0
DP → V2	4,2114875688123E-04	0,07456427
FST → V2	2,0717555878459E-03	0,070467797
IPa → V2	6,3458251791680E-05	0,37037037
LIP → V2	9,5378575411145E-04	0,049165866
MB → V2	9,4957803621252E-06	0
MST → V2	7,4575573857483E-04	0,018827292
MT → V2	3,5730857719322E-02	0,268649674
PBc → V2	1,7797236089235E-06	0
PERIRHINAL → V2	2,0439906879239E-04	0,035
PGa → V2	1,4951055262873E-04	0,023290986
PIP → V2	4,3631948303666E-04	0,006312959
STPc → V2	8,7402312540106E-05	0
STPi → V2	6,9467006530567E-05	0,074074074
STPr → V2	8,8986180446177E-06	0,4
TEa/ma → V2	5,7997652992224E-05	0
TEa/mp → V2	1,0611583615540E-04	0,052631579
TEad → V2	1,6961219731446E-04	0,016666667
TEav → V2	2,3769102964272E-04	0,014245014
TEO → V2	3,2741902063531E-03	0,091031056
TEOm → V2	1,6854781025118E-03	0,051366601
TEpd → V2	1,0526816058894E-03	0,032376273
TEpv → V2	1,1481025595005E-03	0,019217983
TH/TF → V2	1,7930916128961E-03	0,010029093
TPt → V2	9,3097907345239E-07	0
V1 → V2	7,6356223730682E-01	0,735960125
V3 → V2	3,1238140647928E-02	0,321376461
V3A → V2	1,9312040198189E-03	0,027455598
V4 → V2	1,5133149948425E-01	0,254470985
V4t → V2	1,1582296044833E-03	0,237627106
V6 → V2	5,3391708267706E-06	0
V6A → V2	2,6970963039015E-05	0,380952381
VIP → V2	1,3286758140691E-04	0,007575758

Pathway	FLN	SLN
45B → V4	3,5867334152066E-05	0,25
7A → V4	1,0464810449669E-04	0,043478261
8l → V4	2,4207994713175E-03	0,604238306
8r → V4	6,8780770344628E-05	0,473684211
9/46d → V4	3,6200405444541E-06	0
9/46v → V4	1,6040378980687E-05	0
DP → V4	9,7408023407786E-05	0
ENTORHINAL → V4	6,4661122861462E-05	0
FST → V4	1,2539858073290E-02	0,16589374
INSULA → V4	7,0174451501261E-05	0,483333333
IPa → V4	1,2701261851198E-03	0,062091503
LB → V4	1,0693585987125E-05	1
LIP → V4	2,6625532532375E-03	0,215392934
MST → V4	1,2603527647094E-04	0,043478261
MT → V4	8,4679357732758E-02	0,460765636
PERIRHINAL → V4	7,4835716107707E-03	0,000433651
PGa → V4	6,0217152820374E-04	0,025
PIP → V4	6,4856591269670E-04	0,148770492
STPc → V4	1,0793507374867E-04	0
STPi → V4	2,3230499375724E-04	0
STPr → V4	2,5658466770426E-04	0,074074074
TEa/ma → V4	5,4547180798177E-03	0,035564776
TEa/mp → V4	2,2449284298079E-02	0,155161842
TEad → V4	3,1292583691215E-03	0,01296461
TEav → V4	7,5662884184574E-03	0,024386682
TEO → V4	2,3781716795119E-01	0,4303798
TEOm → V4	1,6305260468223E-02	0,24841461
TEpd → V4	7,4878781327724E-02	0,274665301
TEpv → V4	2,7308084801295E-02	0,039024191
TH/TF → V4	1,4223869160405E-02	0,012066079
V1 → V4	1,3046690615096E-02	0,98172206
V2 → V4	3,9084645762747E-01	0,926048751
V3 → V4	2,9448962316775E-02	0,659411144
V3A → V4	1,0019538572105E-04	0
V4t → V4	4,3923223589269E-02	0,439250155